Doctoral theses at NTNU, 2016:237

Gerhard Henning Olsen

Ferroelectric Tungsten Bronzes

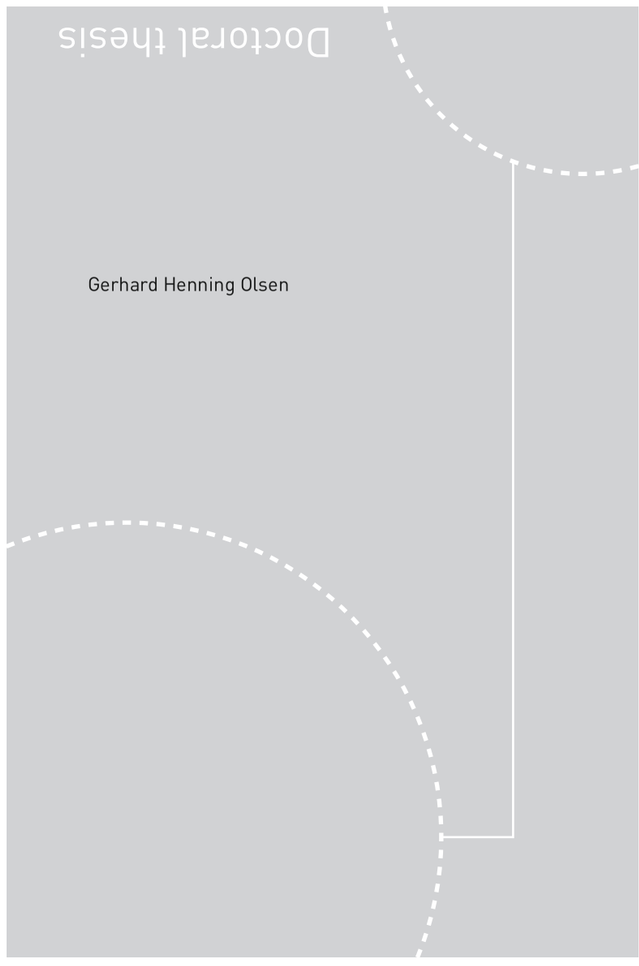

ISBN 978-82-326-1812-5 (printed ver.)
ISBN 978-82-326-1813-2 (electronic ver.)
ISSN 1503-8181

NTNU
Norwegian University of
Science and Technology

NTNU
Norwegian University of
Science and Technology
Thesis for the Degree of
Philosophiae Doctor
Faculty of Natural Sciences and Technology
Department of Materials
Science and Engineering

Doctoral theses at NTNU, 2016:237

NTNU
Norwegian University of
Science and Technology

Gerhard Henning Olsen

Ferroelectric Tungsten Bronzes

Thesis for the Degree of Philosophiae Doctor

Trondheim, September 2016

Norwegian University of Science and Technology
Faculty of Natural Sciences and Technology
Department of Materials Science and Engineering

NTNU
Norwegian University of
Science and Technology

NTNU
Norwegian University of Science and Technology

Thesis for the Degree of Philosophiae Doctor

Faculty of Natural Sciences and Technology
Department of Materials Science and Engineering

ISBN 978-82-326-1812-5 (printed ver.)
ISBN 978-82-326-1813-2 (electronic ver.)
ISSN 1503-8181

IMT-report 2016:231

Doctoral theses at NTNU, 2016:237

Printed by NTNU Grafisk senter

Preface

This thesis has been submitted to NTNU, Norwegian University of Science and Technology, in partial fulfilment of the requirements for the academic degree Philosophiae Doctor.

The work described herein has been performed at NTNU between August 2012 and July 2016, including a four months stay with the Materials Theory group at ETH Zurich from January to April 2015. The work has been supervised by Professor Tor Grande (main advisor) and Associate Professor Sverre Magnus Selbach (co-advisor) at the Department of Materials Science and Engineering, and by Professor Henrik Koch (co-advisor) at the Department of Chemistry (all at NTNU).

The project has been funded jointly by the Faculty of Natural Sciences and Technology at NTNU, and the Research Council of Norway (NFR) as part of the strategic project "From molecules to process applications" (NFR project no. 209337). Computational resources have been provided by the Norwegian metacenter for High Performance Computing (Notur) through the project NN9264K.

All experimental work has been performed by the author, with the exception of the neutron diffraction experiments which were performed by Dr. Magnus Helgerud Sørby at Institute for Energy Technology, Kjeller, Norway. All computational work has been performed by the author. Calculations have been done on the Abel Cluster at the University of Oslo, and on the Euler Cluster at ETH Zurich.

Parts of this thesis have been published, and the scientific papers are included in Appendix A. The author of this thesis has been the main contributor to all papers, but all co-authors have been involved in the writing of the manuscripts.

Trondheim, August 26, 2016
Gerhard Henning Olsen

Acknowledgements

It is now nearly four years since I started as a PhD candidate, and nine years — a third of my life at the time of writing — since I moved to Trondheim and started my chemistry studies at NTNU. Looking back, it has been a fantastic period in my life, and I feel privileged to have had this opportunity. I am grateful to many people, and I will start by warmly thanking my main advisor, Tor, for taking me in and coaching me through these last four years. You have been a wonderful advisor, scientifically and personally, and I would gladly do another PhD with you if I had the chance. I am also very happy that I got to be a part of the brand new computational division of our research group, and my co-advisor Sverre deserves acknowledgement for leading this effort. I would also like to thank my second co-advisor, Henrik, for first introducing me to the wonders of quantum chemistry, which eventually led me to pursue a (mainly) computational PhD.

In the spring of 2015, I spent four months visiting the Materials Theory research group at ETH Zurich under the guidance of Professor Nicola Spaldin, and I am very grateful for this generous opportunity. During my time in Zurich, I learned computational techniques and ways of thinking that have influenced my work a lot. I specifically want to thank Dr. Uli Aschauer, now at the University of Bern, for teaching me to appreciate phonons — they have without doubt become my favourite quasi-particles!

One of the things I have enjoyed most about my scientific training, is that it has included teaching and scientific outreach. In the spring of 2014, I got the opportunity to give lectures in first-year Inorganic Chemistry at NTNU. This is one of the most rewarding things I have ever done, and I am very grateful to Tor, who trusted me with this responsibility. In addition, I have had the great pleasure of being co-advisor to the brilliant MSc students Astrid Marthinsen, Trond Brandvik and Solveig Stubmo Aamlid. I have learned so much from our collaboration and discussions!

I took my initial steps into the world of density functional theory together with Zhaohui, who was my first office mate. I think we learned enormously much from each other during those two years, and not just about DFT — for one thing, I don't think I would ever have dared to taste a Chinese century egg if not for you! My second office mate, Sandra, has accompanied me in exploring both mountain tops and potential energy surfaces, and I am grateful both for our numerous coffee-fueled, whiteboard-assisted science discussions, and for our friendship.

My years at NTNU have been very enjoyable. I am looking back with happiness at group meetings, DoktorandØl gatherings, internal seminars, department parties, Thursday lunches, Friday lectures, and casual conversations in the hallways of K1 and K2. Thanks to all of my colleagues for being a part of this wonderful community,

thanks to Høiskolens Chemikerforening, thanks to my family and friends in Trondheim and elsewhere, and finally — thanks to my parents, who always do everything they can to help me achieve my goals. I really appreciate it.

Science isn't about why,
it's about why not!

Cave Johnson

Summary

Ferroelectric materials are everywhere in the modern society, from consumer electronics to car engines. Applications cover a whole range of devices such as sensors, actuators and transducers due to their dielectric or piezoelectric properties. Almost all technologically important ferroelectrics have the perovskite crystal structure, and the dominating material is lead zirconate titanate (PZT). In recent years, there has been an increasing desire to develop lead-free alternatives to PZT, although no definite replacement has yet emerged. Exploration of materials with other crystal structures is an attractive route towards finding lead-free alternatives. Ferroelectrics with tetragonal tungsten bronze (TTB) structure have been known for more than 60 years, including lead metaniobate, which is commercially available for high temperature piezoelectric sensor applications. In this work, ferroelectric tungsten bronzes were investigated by combining experiments with first-principles density functional theory (DFT) calculations. The principal goal was to obtain a fundamental understanding of the origin of polarization in this class of materials, which is expected to receive more attention in the years to come.

A major part of the thesis is focused on the materials strontium barium niobate (SBN) and lead metaniobate (PN). While they both have the TTB structure, they are different in terms of space group symmetry and orientation of polarization with respect to the structural framework. Moreover, the dielectric behaviour of SBN changes with the Sr/Ba ratio, with Ba-rich compositions being classical ferroelectrics and Sr-rich compositions relaxors. Despite the fact that this has been known for decades, the origin of this fundamental difference has so far not been investigated in depth. Both SBN and PN are "unfilled" TTBs, meaning that the structure contains a mixed occupancy of cations and vacancies. This creates a possibility for cation order–disorder phenomena. The energetics of cation ordering in SBN, approximated by the end components, SN and BN, and PN were investigated by first principles calculations, initially with focus on the paraelectric structures. A supercell approach was used to sample ten different possible cation configurations, as an approximation to the true, possibly disordered structure. A thermodynamic model was developed for cation interchange in tungsten bronzes, and this model predicts that cation ordering in the three compositions SN, BN and PN behave qualitatively different as a function of temperature. Importantly, it was concluded that Ba-rich, ferroelectric SBN compositions will probably be more strongly affected by the thermal history than Sr-rich relaxor compositions.

The next step in the investigation was the underlying mechanism behind the ferroelectric transition in SBN and PN. First-principles phonon calculations revealed an unstable polar mode in all the ten configurations of both SN and BN. The mode is similar to the soft mode causing spontaneous polarization in perovskite ferroelectrics

such as $BaTiO_3$ and $KNbO_3$. Some of the configurations were also found to have a second instability, a mode consisting of octahedral tilting in the xy plane of the TTB structure. In contrast to many ferroelectrics, this was not found to reduce the polarization, even for severely distorted structures. The possibilities for octahedral tilting are limited in the rigid TTB structure, and the structural framework cannot completely adapt to the different size of the Sr^{2+} and Ba^{2+} cations. This leaves Sr^{2+} with enough space so that it can displace under the application of an electric field, which is suggested to contribute to the diffuse dielectric response of Sr-rich SBN. In the case of PN, X-ray and neutron diffraction experiments were performed in order to provide reliable data on the ferroelectric crystal structure. Refinement of the cation distribution made it possible to concentrate further first principles calculation on only four relevant cation configurations, for which energies and spontaneous polarization were calculated. The polarization was found to be large and surprisingly robust against cation disorder. Nudged elastic band calculations were performed for the ferroelastic switching in PN, and high transition barriers were found. This is a likely reason why the observed spontaneous polarization in PN is lower than the calculated value.

SBN and PN are "unfilled" TTBs with cation–vacancy disorder. A number of "filled" TTBs were also examined computationally, both to isolate the order–disorder effects from other phenomena, and to extend the project to more general TTB materials. The series $K_4R_2Nb_{10}O_{30}$ with R = La, . . . , Gd, Bi was studied by first-principles phonon calculations, and it was found that while all are subject to the same polar instability as unfilled SBN, the size of the R^{3+} cation has a profound effect on an in-plane polar instability similar to the one found in PN. When R = Bi, this instability dominates and results in a net in-plane polarization. Comparison with materials where K is replaced by Tl revealed that the in-plane polarization is closely connected to the presence of lone pair cations on the perovskite-like A1 sites in the TTB structure. It is suggested that this is the mechanism behind the morphotropic phase boundary in the lead barium niobate system, for which very high piezoelectric response is achieved.

TTBs with partially reduced Nb are electrically conducting and have recently been shown to be promising for thermoelectric applications. $(Sr, Ba)_6Nb_{10}O_{30}$, the filled counterpart to the ferroelectric SBN system, has an interesting metal–insulator transition as the composition changes from the Ba to the Sr end component. As metallic systems are more challenging for DFT calculations than insulators, attention was given to the choice of functional used for $(Sr, Ba)_6Nb_{10}O_{30}$. The DFT+U approach was used, after calibration against computationally much more expensive hybrid functional calculations. Structural optimizations and phonon calculations were then performed, along with an analysis of the electronic structure. Consistent with experiments, filled $Ba_6Nb_{10}O_{30}$ was found to be dynamically stable in the tetrag-

onal aristotype symmetry, while filled $Sr_6Nb_{10}O_{30}$ has multiple instabilities which lead to an orthorhombic ground state with octahedral tilting and a larger unit cell. The electronic structure calculations were however inconclusive with respect to the metal–insulator transition associated with this structural distortion.

The final part of the thesis deals with the rhombohedral polymorph of PN, r-PN. At room temperature, PN is only metastable in the TTB structure, with r-PN being the thermodynamically stable structure. This polymorph has previously been thought to have less interesting properties, with little or no piezoelectric response. The previously reported space group symmetry, $R3m$, is polar, and initial calculations of the spontaneous polarization based on structural data from literature demonstrated a fairly high polarization. A polar–nonpolar phase transition, which could possibly be ferroelectric, was also observed by high-temperature X-ray diffraction, so it was decided to investigate further whether r-PN could have attractive functional properties. X-ray and neutron diffraction experiments were conducted in order to provide a better description of the crystal structure of r-PN at room temperature. This led to a complete re-investigation of the crystal structure, and it was concluded based on experimental and computational investigations that the space group symmetry of r-PN is $R3$, and not $R3m$ as previously reported. At the same time, the improved description of the crystal structure led to significantly less exciting predictions of spontaneous polarization, and additional dielectric characterization demonstrated that while the material indeed shows a polar–nonpolar phase transition at a high temperature of 780 °C, the structural transition has no impact on the dielectric permittivity and the material is not ferroelectric.

Finally, this work is a significant contribution to a platform for computational investigation of ferroelectric tungsten bronzes. It has been established that the ferroelectric polarization in the well known SBN system is driven by an unstable phonon similar to what is found in ferroelectric perovskites, and is suggested to be a general feature for most Nb-based TTBs. Only in certain cases, such as when the A1 site is occupied by a lone pair cation, the out of plane polarization mechanism is suppressed by a different driving force, leading to in-plane polarization.

Contents

1 Background

It is not an overstatement to claim that ferroelectricity is one of the cornerstones of today's technology-infested society. The fundamental property of a ferroelectric is the existence of a microscopic electric dipole moment, Figure 1.1(a), which can be reoriented by an applied electric field. Macroscopically, this gives rise to a switchable electric polarization which can be measured experimentally as a current, Figure 1.1(b). The effect was first discovered in 1921 in Rochelle salt, an organic salt which at the time was already known to be piezo- and pyroelectric.

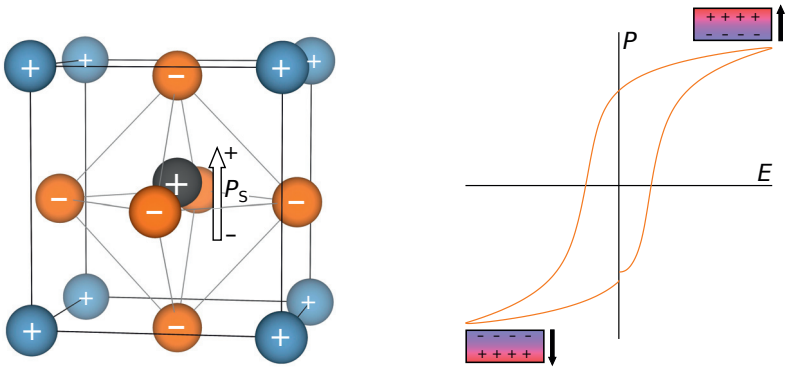

(a) (b)

Figure 1.1 — (a) Atomic arrangement for a typical ferroelectric with perovskite structure. The non-centrosymmetric arrangement of cations (+) and anions (–) gives rise to a microscopic dipole moment (P_S). (b) Typical characteristic of a ferroelectric material: Application of an electric field (E) produces a macroscopic polarization (P) that can be switched by reversing the orientation of the field. This gives rise to a hysteresis loop as shown.

One of the major milestones in ferroelectric history[1,2] was the invention of the barium titanate ceramic capacitor in the 1940s, whose very high dielectric constant was soon attributed to ferroelectricity. Other ferroelectric ceramics were soon discovered, such as lead metaniobate and alkali niobates which were both reported as ferroelectric for the first time in the 1950s. The attractiveness of ferroelectric ceramics is due to the fact that ceramics can be processed conveniently from principal oxide powders, which is beneficial for large-scale manufacturing. At the same time, the switchable polarization in a ferroelectric makes it possible to *pole* the ceramic by application of an electric field. This makes the polycrystalline ceramic macroscopically polar

and piezoelectric even though individual grains are randomly oriented. In many applications, it is therefore not actually the ferroelectric effect that is used directly, but ferroelectricity is necessary to bring about piezoelectricity in a polycrystalline material.

Ferroelectrics today are utilized in a wide range of applications.[2,3] One of the biggest applications on a per-weight basis is in sonar arrays for ships and submarines, where piezoelectric ceramics are used as transducers that both generate and detect ultrasonic waves. The same principle is used in ultrasonic imaging equipment used for physical health monitoring. In other cases, piezoelectric ceramics are utilized either as actuators (motors) or as sensors. Inkjet printers and fuel injection systems in internal combustion engines are examples of actuator applications where only the *converse* piezoelectric effect is used, while pressure sensors are a typical example of an application which utilizes the *direct* piezoelectric effect. Pressure sensors are used in a variety of situations, such as in the engines and tires of cars, or in connection with exploration of oil, gas and mineral resources. These environments frequently involve high temperatures, which limits the number of materials that can be used. Ferroelectric polarization disappears above the temperature known as the Curie point, T_C, which is therefore a theoretical upper limit for application of the piezoelectric ceramic. There are not too many ferroelectric materials suitable for high-temperature applications, and this is an obvious motivation for research on new high-temperature piezoelectrics.[4]

One of the most attractive materials for high-temperature piezoelectric applications today is lead metaniobate, $Pb_5Nb_{10}O_{30}$ (PN). PN was first discovered in 1953[5] and belongs to a class of materials with the tetragonal tungsten-bronze (TTB) crystal structure. These materials, many of which are ferroelectric, are remarkably flexible both structurally and chemically, and are considered the second most important class of ferroelectrics after perovskites.[3] Despite their popularity, however, a fundamental understanding of the mechanism behind their ferroelectric properties has not previously been presented. There are several reasons for this: First, lead metaniobate itself is not a thermodynamically stable material, as it is metastable at room temperature with respect to a rhombohedral polymorph.[6,7] Other TTB materials, that are apparently stable, are more complicated in terms of composition, as most are solid solutions with various degrees of disorder.[3,8] Second, the structural and chemical complexity of most TTBs has for a long time made computational investigations practically unfeasible. Fundamental studies of the much simpler perovskite structure has been guided by first-principles calculations for several decades, but only recently has this become possible for TTB.

The foundation for the present project was laid in 2008–2009 when Norwegian basic chemistry research was evaluated by a comittee appointed by the Research

Council of Norway.[9] In the report, the field of inorganic and materials chemistry was characterized as one of the strongest and best developed subfields of Norwegian chemistry research at the time of writing. On the other hand, the evaluation committee also recommended that the research groups involved in this field should seek to include more basic research in their profiles, and pointed out that applications of computational chemistry methods was under-represented in Norway. Especially for nanotechnology-related research, increased cross-disciplinary work involving computational methods was suggested as a promising way to go. At the Department of Materials Science and Engineering (DMSE) at NTNU, the activity related to ferroic materials was specifically mentioned as one of the most forward-looking research programs. In the follow-up report by representatives from the chemistry research institutions in Norway,[10] one of the recommendations was to establish strategic projects at each institution, in order to meet challenges pointed out in the evaluation. The strategic project "From Molecules to Process Applications" was subsequently created at NTNU, with the intention of including cross-disciplinary projects within ferroics and catalysis in collaborative subprojects between DMSE and the Departments of Chemistry and Chemical Engineering.

For the present subproject on ferroelectrics, the starting point was lead metaniobate (PN), a well-known TTB ferroelectric and one of the best high-temperature piezoelectric ceramics currently available. Its thermodynamic stability had recently been investigated,[7] sparking new interest in fundamental understanding of the material and the possibilities it offers. As a lead-free analogue to PN, strontium barium niobate, $(Sr_xBa_{1-x})_5Nb_{10}O_{30}$ (SBN), was included in the study. Despite having the same basic TTB crystal structure, PN and SBN are different in terms of spontaneous polarization, which lies in different directions with respect to the highly anisotropic crystal structure.[11] In addition to being a lead-free ferroelectric,[12,13] SBN has attractive electro-optical properties such as high second harmonic yield and good pyroelectric performance,[14] and also shows an interesting crossover from classic to relaxor-type ferroelectricity as the Sr/Ba ratio increases.[8] Since both materials fall within the group of "unfilled" TTBs,[15] cation–vacancy ordering is also a possibility, and likely to influence the mechanism for ferroelectricity in both. The origin of ferroelectricity in TTB oxides, and the influence of order–disorder phenomena, had not been investigated before. No computational work on TTBs was known at the time, which also motivated our interest in approaching PN and SBN by first-principles methods.

Aim of the work

The overall aim of this work was to gain a fundamental understanding of ferroelectricity in oxides with tetragonal tungsten-bronze (TTB) structure, focusing on lead metaniobate (PN) and strontium barium niobate (SBN). In particular, the study aimed to explain the difference in ferroelectric behaviour between PN and SBN, and why SBN changes from classical to relaxor ferroelectric upon changing the composition. Another important goal was to gain insight into the effect of cation order–disorder phenomena on the ferroelectric properties of TTB materials. Moreover, due to the structural complexity of TTBs, it was important to develop a practical computational strategy for these materials. Throughout the course of the project, lattice dynamics emerged as a particularly useful method, making possible the exploration of unstable phonon modes that lead to distorted, polar crystal structures.

The unfilled TTBs PN and SBN were investigated by first-principles density functional theory (DFT) calculations. Disordered systems pose certain challenges for DFT, so the true, disordered system was approximated by sampling the cation–vacancy configurations possible in a $1\times1\times2$ supercell. This led to a comprehensive study of the energetics of cation ordering, at first without addressing the polarization mechanism and thereby considering only the paraelectric state of PN and SBN. Based on the calculated energies associated with the cation configurations, a thermodynamic model was developed for cation interchange in TTBs. The energetics of cation ordering in PN and SBN and the thermodynamic model for TTBs is described in Chapter 4.

The polarization mechanism was investigated for BN and SN with TTB structure, the end members of the "unfilled" SBN system. Lattice dynamical calculations were performed for all configurations possible in the $1 \times 1 \times 2$ supercell, and unstable phonon modes were followed in order to identify the true zero-kelvin ground states. Chapter 5 gives an account of this ground state search, the resulting spontaneous polarization and the mechanism stabilizing it. For PN with TTB structure, phonon calculations proved less successful, so a slightly different strategy was chosen (Chapter 6). Diffraction data was applied to reinvestigate the crystal structure of ferroelectric PN. Based on the new insight in the structure, the most relevant cation configurations for PN were identified and spontaneous polarization was calculated along with the energy barrier for switching of ferroelectric and -elastic domains in PN. Based on these studies, the microscopic origins of the ferroelectric polarization in SBN and PN were identified.

In order to learn about the mechanism for ferroelectricity in PN as compared to SBN, a computational study was performed for a series of "filled" TTBs which do not suffer from the additional complexity of cation configurations. This made it possible to isolate the effects of lone pair cations (Tl^{+}, Pb^{2+}, Bi^{3+}) on different sites in the TTB

structure, thereby providing information on the role of the lone pairs in stabilizing an in-plane polarization in PN as compared to the out-of-plane polarization in SBN (Chapter 7). Closely related to this is a project concerning TTB niobates that are electric conductors due to a non-zero occupation of the *d* band when Nb is partially reduced from +5 to +4. This is exemplified by the system $(Sr_xBa_{1-x})_6Nb_{10}O_{30}$, which is the filled counterpart to the ferroelectric SBN system mentioned above. Starting from structural data provided by experimental collaborators, a lattice dynamics approach was used to investigate distortions possibly leading to a metal–insulator transition that has been found experimentally in this system. The investigation of filled SBN is described in Chapter 8.

The final part of the thesis, Chapter 9, concerns the less known rhombohedral polymorph of PN (r-PN), which was investigated in the early stages of the project. The motivation for studing r-PN, rather than the TTB polymorph (TTB-PN) which inspired the project, was to initiate first-principles calculations without the added complexity of cation–vacancy ordering, which is fundamental to the unfilled TTBs. Chapter 9 describes the investigation of structure and symmetry in r-PN at ambient conditions by a combined experimental and computational approach. In addition, the high-temperature properties of the r-PN polymorph are explored by structural and thermal characterization methods.

2 Introduction

2.1 Ferroelectricity

Characteristics and history

A ferroelectric material, as mentioned in Chapter 1, has a microscopic electric dipole moment which can be reoriented by application of an electric field (Figure 1.1). The switching of polarization is the defining property, and this imposes several requirements for the existence of ferroelectricity. First, the material must be a *dielectric*, or electric insulator, otherwise the applied electric field would just produce an ohmic current through the material. A subset of dielectrics are the *piezoelectric* materials, in which the crystal contains a unique polar axis. "Piezo" comes from the Greek word for pressure, and refers to the fact that an electric polarization builds up in these materials when pressure (mechanical stress) is applied. The piezoelectric effect also works the other way around: Application of an electric field produces mechanical strain (converse piezoelectric effect). In some piezoelectrics, an electric polarization spontaneously arises along this polar axis below a certain critical temperature, the Curie temperature, T_C. These materials are known as *pyroelectrics* because of the temperature-dependence of electric polarization. *Ferroelectrics* are a further subset of the pyroelectrics, and this hierarchy is shown in Figure 2.1. While piezo- and pyroelectricity can be predicted from the a material's crystal structure, ferroelectricity must be experimentally verified by testing for the existence of a hysteresis loop as in Figure 1.1b, which is the macroscopic signature of switching.

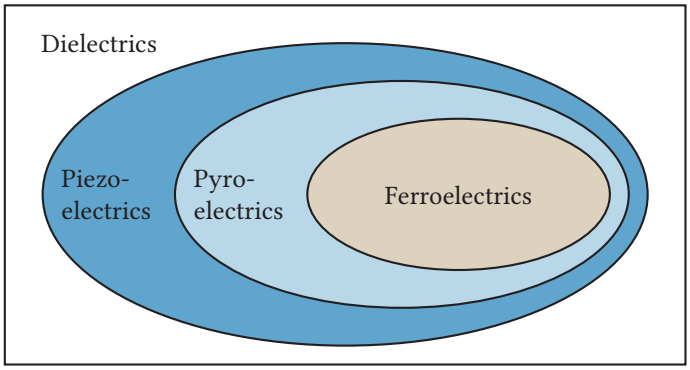

Figure 2.1 — Hierarchy of functional properties.

The discovery of ferroelectricity, interpreted as the first publication of an electric hysteresis loop, was made by Valasek in 1921 in the material Rochelle salt (sodium potassium tartrate, $NaKC_4H_4O_6 \cdot 4\,H_2O$).[16] Rochelle salt, being water soluble, is not well suited for applications of ferroelectricity. The same is also true for the second ferroelectric to be discovered, potassium dihydrogen phosphate (KH_2PO_4 or KDP),[17] which has a Curie temperature of $-150\,^{\circ}\mathrm{C}$.[1] The first truly useful ferroelectrics were developed from the 1940s, when ferroelectricity was first discovered in a ceramic material, barium titanate ($BaTiO_3$), and found to be the source of its very high dielectric constant.[18] It is hard to overstate the technological importance of this discovery. Ceramic materials can be conveniently processed from simple oxide powders such as $BaCO_3$ and TiO_2 in the case of $BaTiO_3$, which is key to feasible large-scale manufacturing. The individual grains of a ceramic body are more or less randomly oriented, so a pyroelectric (but not ferroelectric) material would lose its macroscopic polar properties if it were processed as a ceramic. The microscopically switchable polarization of a ferroelectric material, however, makes it possible to reorient the polarization in each grain by applying an electric field over the ceramic sample. This results in a net macroscopic polarization, and both piezo-, pyro- and ferroelectric properties in the ceramic. During the 1940s and early 50s, ceramic transducers based on $BaTiO_3$ were developed simultaneously in several labs around the world. Much of the development was for a long time kept secret because of World War II and the military applications of transducers, *e.g.*, in sonars.[1]

The technologically most important ferroelectric material today is lead zirconate titanate, $PbZr_{1-x}Ti_xO_3$ PZT,[19–22] a solid solution system first investigated in Japan in the 1950s.[23,24] PZT is usually made with a composition close to $x = 0.48$, where properties such as dielectric permittivity and piezoelectric coefficients are particularly high. This phenomenon has been attributed to a composition-dependent phase boundary, a *morphotropic phase boundary* (MPB), as shown in the PZT phase diagram, Figure 2.2(a).[19,25] The practically vertical phase boundary means that the ferro- and piezoelectric properties are stable over a wide temperature range. The drawback with PZT is the high content of lead, over 60 % by weight at the MPB composition, which is an environmental challenge since processing of lead-containing ceramics releases Pb to the environment, mainly in the form of the volatile oxide PbO.[22] In 2003, the European Parliament passed two directives that lay restrictions on the use and waste handling of electrical and electronic (EE) equipment within the European Union.[26,27] Specifically, the EU member states are from 2006 required to ensure that no new EE equipment on the market contains lead, mercury, cadmium, hexavalent chromium or certain types of aromatic organic compounds. However, exemptions are made for materials "if their elimination or substitution (…) is technically or scientifically impracticable",[26] but the intention is to continue the elimination as soon as there are

good alternatives. PZT components fall within this category, as there were at the time, and still are, no lead-free replacements that can match the piezoelectric properties of PZT. The EU directives have therefore sparked a huge research activity related to lead-free piezoelectrics over the last decade. A major catalyst for this research activity was a paper from researchers at Toyota laboratories in 2004, reporting bulk ceramics based on $K_{1-x}Na_xNbO_3$ (KNN) with piezoelectric properties close to those of PZT.[28] This was achieved through chemical modifications which were originally thought to produce an MPB similar to that in PZT. Later investigations have indicated that the enhanced properties were more likely because of a polymorphic (temperature-dependent) phase transition that was shifted towards room temperature.[22] Still, the MPB concept is commonly used as a guideline in the search for new lead-free piezoelectric materials, which is still a major research topic where we only recently have started seeing the large-scale implementation of new technologies, Figure 2.2(b).[29]

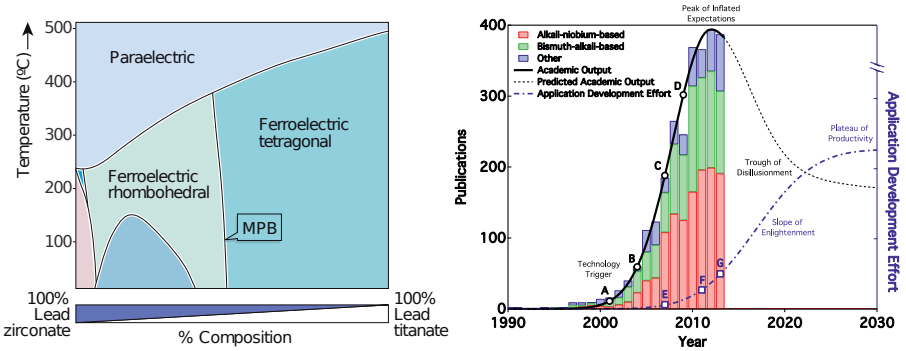

Figure 2.2 — (a) Phase diagram of the PZT system.[20] The nearly vertical morphotropic phase boundary (MPB) leads to good piezoelectric properties that are stable with temperature. (b) Research and development activity on lead-free piezoceramics up to 2014, demonstrating the time offset between research activity in terms of scientific publications (black curve) and transfer into application (blue). Adapted from Rödel *et al.*[29]

Ferroelectric phase transitions

Barium titanate has the perovskite structure, which was used as an example to illustrate the microscopic origin of the ferroelectric polarization in Figure 1.1(a). Many other early and important ferroelectrics, such as $KNbO_3$ and $PbTiO_3$, also have this structure, and almost all technologically important ferroelectric ceramics up until today are perovskites (one notable exception is the TTB-type oxide lead metaniobate, $Pb_5Nb_{10}O_{30}$, which is utilized as a high-temperature piezoceramic). The technological importance of perovskites has to a large extent also influenced our fundamental understanding of ferroelectricity. During the 1950s and 60s, fundamental research became directed towards understanding the origin of ferroelectricity in perovskites. Helen Megaw was the first to solve the crystal structure of $BaTiO_3$, and described how it transforms from a paraelectric cubic structure to a tetragonal structure with polarization along [001] upon cooling through the ferroelectric Curie temperature, T_C. Further cooling leads to subsequent transitions to orthorhombic (polarization along [110]) and rhombohedral ([111] polarization) structures.[30] Megaw realized at an early stage that the polarization arises mainly due to displacement of Ti^{4+} relative to the other ions in the direction of the spontaneous polarization, and that partial covalent bonding is important for stabilizing these microscopic dipoles.[31]

The picture of a ferroelectric phase transition in which an atom, such as Ti^{4+} in $BaTiO_3$, displaces away from a symmetric position to create a dipole, is known as the *displacive limit*.[32] Originally, all perovskite ferroelectrics were thought to be of this kind. The other limiting case is known as the *order–disorder limit*, where the atom is never in a centrosymmetric position, but the displacement can be randomly directed or preferentially in one direction. This is exemplified by KDP, in which spontaneous polarization arises from alignment of dipoles that exist also in the paraelectric state. A cartoon of the displacive and order–disorder cases in shown in Figure 2.3. Usually, a phase transition will show some signature of both types. Thermodynamic properties is one way to distinguish them experimentally: In a displacive phase transition, the entropy change will be due to the different vibrational (phonon) properties of the two phases, whereas the entropy change for an order–disorder transition is mainly configurational in origin.[32]

The displacive picture is the foundation for one of the most influential microscopic descriptions of ferroelectric phase transitions, namely the *soft mode theory* introduced by Cochran in 1959.[33,34] Soft mode theory treats the ferroelectric transition as a temperature-dependent vibrational mode or phonon. The mode is a stable lattice vibration in the paraelectric state, but when approaching T_C from above, the phonon frequency goes to zero, a phenomenon known as mode softening. Below T_C, the mode no longer corresponds to a dynamic lattice vibration, but instead to a

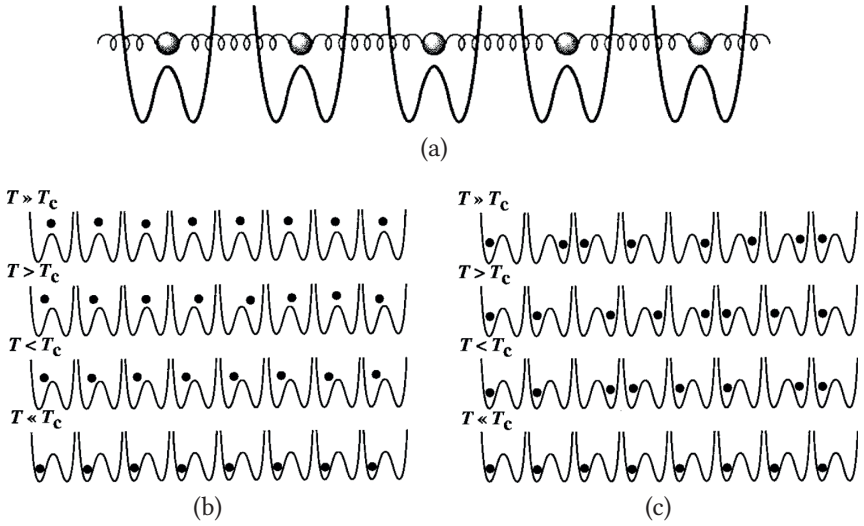

Figure 2.3 — (a) Model system for illustrating the ferroelectric phase transition. The balls represent cations that create dipoles when displaced from their centrosymmetric positions, such as Ti^{4+} in $BaTiO_3$. The springs represent ionic interactions with neighbouring cations, which favour a cooperative distortion. The double-well potentials represent covalent interactions with neighbouring anions, favouring local off-centering of the cations. (b) Displacive limit: Long-range ionic interactions dominate over local covalency. Above T_C, all atoms are vibrating around the central position, and below T_C they cooperatively displace towards the same side of the double-well. (c) Order–disorder limit: Local covalent interactions dominate over long-range ionic forces. At all temperatures, atoms are displaced towards one side of the double-well. Above T_C, the distribution is random. Below T_C, one side of the double-well is preferentially occupied over the other. Adapted from Dove.[32]

permanent distortion with the same atomic displacement pattern as the soft mode in the paraelectric phase.[35] Softening of an optical zone centre phonon gives rise to a polar and possibly ferroelectric transition such as in $BaTiO_3$, while a soft zone boundary mode results in an antiferrodistortive transition as seen in $SrTiO_3$.[36]

While the displacive picture originally seemed like a good description for $BaTiO_3$,[37] later studies revealed that the transition in fact is mainly of order–disorder nature.[38–41] Evidence suggests that even in the paraelectric state of $BaTiO_3$, the centrosymmetric cubic structure is just an average, and that Ti^{4+} is always displaced along one

of the body diagonals of the unit cell. In the paraelectric state, all the eight ⟨111⟩ displacements are equally and randomly occupied. In the tetragonal state, only the four displacements with a positive z component ([111], [1$\bar{1}$1], [$\bar{1}$11] and [$\bar{1}\bar{1}$1]) are occupied, yielding an average [001] displacement and a macroscopic polarization in the same direction. In the orthorhombic phase, two of eight directions are occupied (*e.g.*, [111] and [11$\bar{1}$] for an average [110] displacement), and only in the rhombohedral phase is the crystal completely ordered, with all displacements along [111]. This behaviour is predicted by the vibronic theory of ferroelectricity, first introduced by Bersuker in 1966.[42] Within this theory, distortions from high symmetry (such as local off-centering of the B cation in perovskites) is explained by the second-order Jahn–Teller (SOJT) or pseudo-Jahn–Teller (PJT) effect, essentially an energy-lowering contribution from additional covalent bonding.[43] The different phase transitions are governed by the correlation between the individual displacements. The theory correctly predicts the observed phases in $BaTiO_3$, and it has even been suggested that vibronic theory casts doubt on the very existence of displacive phase transitions.[44] Even in $PbTiO_3$, which for a long time was thought to be purely displacive, a significant order–disorder component is found.[45] Still, even strongly order–disorder-type ferroelectrics show a certain temperature variation in the atomic positions, and in general a ferroelectric transition should be thought of as intermediate between the displacive and order–disorder limits.

In the context of theoretical frameworks for description of ferroelectrics, *Landau theory* is also worth mentioning.[46] This phenomenological theory, which is also known as Landau–Devonshire theory after Devonshire who popularized its use on ferroelectrics,[47–49] is a general framework for describing the equilibrium behaviour of a system with a phase transition, making it possible to predict a range of macroscopic properties from a relatively small set of measured values. In the case of a ferroelectric, the state of the material is characterized by the polarization, P, which is a macroscopic order parameter (OP) for the ferroelectric transition. It is also possible to employ a microscopically defined OP, such as the distortion mode amplitude for a polar distortion.[50] Regardless of which OP is chosen, it describes a symmetry change associated with the phase transition, and is defined so that it is zero in the paraelectric state and non-zero in the ferroelectric state. The fundamental postulate of Landau theory is that the free energy of a system close to the phase transition can be described by a polynomial expansion in the OP:[46]

$$\mathcal{F} = \frac{1}{2}aP^2 + \frac{1}{4}bP^4 + \frac{1}{6}cP^6 + \ldots - EP,$$

where $a, b, c, \ldots$ are fitting parameters, E the electric field, and odd-numbered terms in the series have been dropped according to symmetry requirements ("up" and

"down" polarization states, represented by $+P$ and $-P$, must have the same energy). The goal is to simplify this expansion as much as possible, while still describing essential properties of the system. The coefficient a is taken to be linearly dependent on temperature, $a = a_0(T - T_0)$ with T_0 the phase transition temperature, while the other coefficients are taken as positive and independent of T. Truncating the series after the 4th order term, the *Curie–Weiss law* for dielectric susceptibility (reciprocal permittivity) in the paraelectric phase follows:

$$\frac{1}{\varepsilon} = \frac{1}{P/E} = \frac{1}{a_0(T - T_0)},$$

implying a divergence in susceptibility as T_0 is approached. By minimizing $\mathcal{F}$, it follows that $P = 0$ in the paraelectric phase and that $P = \sqrt{(a_0/b)(T_0 - T)}$ in the ferroelectric phase. Such a phase transition, where the order parameter goes continuously to zero upon approaching the transition temperature, is termed a *second-order phase transition*. If also a 6th order term is included in the Landau expansion and b is allowed to be negative, a *first-order phase transition* is predicted. In this case, P drops suddenly to zero instead of vanishing continuously, and a temperature hysteresis is predicted, precisely as observed in the prototype ferroelectric $BaTiO_3$. The essential physics of ferroelectrics can thus be described by a small number of parameters. A natural next step in the analysis would be to include coupling between polarization and strain,[51,52] which makes it possible to predict for example how clamping of a ferroelectric (if the material is grown as a thin film on a substrate) can shift the phase transition temperature or even change the order of the transition.[46] The parameters $(a, b, c, \ldots)$ can be found by fitting the expressions derived from $\mathcal{F}$ to experimental values, and have been tabulated for many common ferroelectrics.[53] In recent years, first-principles methods have enabled the direct calculation of energies, thereby providing data from "computer experiments" for fitting the Landau coefficients. Curiously, while the formalism of Landau theory is based on a series expansion and thus expected to be valid only in the close vicinity of T_0, experience has shown that it can provide a good description of phase transitions (especially displacive) over a wide temperature range.[32,54]

In recent years, computational methods have considerably enhanced the understanding of ferroelectric materials. One of the milestones was Cohen's 1992 report on the origin of ferroelectricity in perovskite oxides,[55] which compared the mechanisms stabilizing ferroelectric polarization in $BaTiO_3$ and $PbTiO_3$ by first-principles calculations. By calculating the potential energy surfaces for tetragonal and rhombohedral distortions at difference lattice parameters, it was shown that rhombohedral displacement of Ti^{4+} lowers the energy for both materials in the absence of lattice strain. For increasing tetragonal strains, the tetragonal distortions become gradu-

ally more favoured over the rhombohedral. In $PbTiO_3$, the experimental tetragonal strain is large enough ($c/a = 1.06$, as compared to $c/a = 1.01$ in $BaTiO_3$) that the tetragonally distorted structure becomes the stable ground state. The large strain in $PbTiO_3$ can in turn be traced back to covalent interactions between Pb 6*s* and O 2*p* orbitals. In $BaTiO_3$, the corresponding interactions between Ba 5*d* and O 2*p* are almost purely ionic, and the lattice strain is smaller. Cohen's work thus gave solid support to the order–disorder model for $BaTiO_3$, while at the same time addressing the role of *lone pair cations* such as Pb^{2+} in stabilizing ferroelectric distortions. This type of "A-site driven ferroelectricity" is especially interesting in the context of *multiferroics*, materials in which electric, magnetic and/or elastic order coexists (most commonly ferroelectricity and antiferromagnetism).[56] In analogy to the role of Pb^{2+} in $PbTiO_3$, the $6s^2$ lone pair on Bi^{3+} has been shown to play a central role in the ferroelectric distortion in the multiferroic perovskites $BiMnO_3$ and $BiFeO_3$.[57,58] For this reason, replacement of Pb with Bi is frequently one of the guidelines employed for exploration of new lead-free ferroelectric materials.[22]

Relaxor ferroelectrics

Relaxor ferroelectrics, or simply *relaxors*, are a subgroup of ferroelectric materials which encompasses many of the ferroelectric TTBs.[15] The first studies on relaxors were conducted in the Soviet Union by Smolenskii and co-workers,[59–61] and these materials, characterized among other things by a diffuse phase transition, later came to be known as *dirty displacive ferroelectrics*.[62,63] The term "relaxor ferroelectrics" was popularized by L. Eric Cross and co-workers at Penn State University,[8,64,65] and comes from the observation that the properties of relaxors are governed by the time scale of dielectric relaxation in the materials.[13,66] * The interest in relaxors escalated in the late 1990s after the discovery of ultrahigh electromechanical response in relaxor-based single crystals, with piezoelectric coefficients an order of magnitude higher than in conventional PZT-based piezoceramics.[68]

The distinction between relaxors and classic ferroelectrics is traditionally made from the viewpoint of dielectric response: While a classic ferroelectric has a sharp and clear peak in dielectric permittivity at the ferroelectric phase transition, a relaxor is characterized by a *diffuse phase transition*. The dielectric response of a relaxor is also dependent on measurement frequency, as shown in Figure 2.4 for a range of solid solutions between the ferroelectric $BaTiO_3$ and the relaxor $LaMg_{1/2}Ti_{1/2}O_3$ (BT–LMT). The phase transition becomes increasingly diffuse when LMT is introduced to BT.

*Some authors reserve the term "relaxor ferroelectric" for solid solutions between relaxors and ferroelectrics,[67] but such a distinction is not made in the present work.

Because of the frequency dispersion in dielectric response, the Curie temperature is not well defined for a relaxor, and the peak permittivity temperature T_m is instead reported. T_m for a relaxor typically follows the phenomenological Vogel–Fulcher (VF) relation:[69,70]

$$f = f_0 \exp\left[-\frac{E_a}{k_B(T_m - T_f)}\right],$$

where E_a is an activation energy, f_0 is an attempt frequency, and T_f is referred to as the freezing temperature (interpreted as T_m at zero frequency). The VF relation was initially applied to magnetic spin glasses,[71] and its successful application to relaxors has led to the term "dipole glass" as a relaxor analogue to the magnetic counterpart.[72] VF behaviour, together with a criterion for the profile of the $\varepsilon(T)$ curve, has even been suggested as a definition of relaxor ferroelectricity.[73]

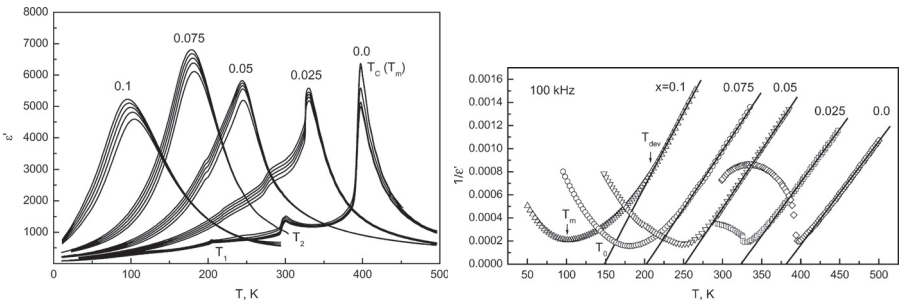

Figure 2.4 — (a) Temperature dependence of dielectric permittivity for measurement frequencies of 1×10^2 to 1×10^6 Hz (top to bottom curve for each composition). The numbers denote x in the solid solution $(1 - x)$BT–xLMT, so a higher x means more pronounced relaxor behaviour. (b) Temperature dependence of reciprocal dielectric permittivity for measurements at 1×10^5 Hz and the same compositions as in panel a. Solid lines show fits to the Curie–Weiss law, which does not describe the dielectric response well for relaxors. Adapted from Salak *et al.*[74]

In classic ferroelectrics, the divergence in dielectric permittivity upon cooling through T_C is associated with a structural phase transition from a non-polar paraelectric to a polar ferroelectric phase of lower symmetry. For example, the ferroelectric transition in $BaTiO_3$ is a structural transition between phases with average space group symmetries $Pm\bar{3}m$ (cubic) and $P4mm$ (tetragonal), and is a typical first-order transition that involves both atomic displacements and lattice strain. In contrast, the average structure of the prototype perovskite relaxor lead magnoniobate,

$PbMg_{1/3}Nb_{2/3}O_3$ or PMN, is well described by space group $Pm\bar{3}m$ at all temperatures, with Mg and Nb randomly distributed and no long-range symmetry break on cooling through T_m.[75] On a local scale, however, a symmetry break occurs at the Burns temperature, T_d, the temperature at which *polar nano-sized regions (PNRs)* start to form. Inside each PNR, the symmetry is lowered and the material is polar, but there is no long-range correlation beyond a few unit cells, and the material appears on average non-polar (perovskite relaxors are for this reason sometimes referred to as "pseudo-cubic"). This is manifested in macroscopic properties that depend on $P^2 \neq 0$ (when averaged over a suitable volume and time), such as the refractive index and linear thermal expansion. T_d typically lies far above T_f, for PMN they are around −50 °C and 350 °C, respectively.[66,76,77] Between T_d and T_f, the PNRs are dynamic and reorientable, while below T_f they are static and frozen in a glass-like phase.[72,76]

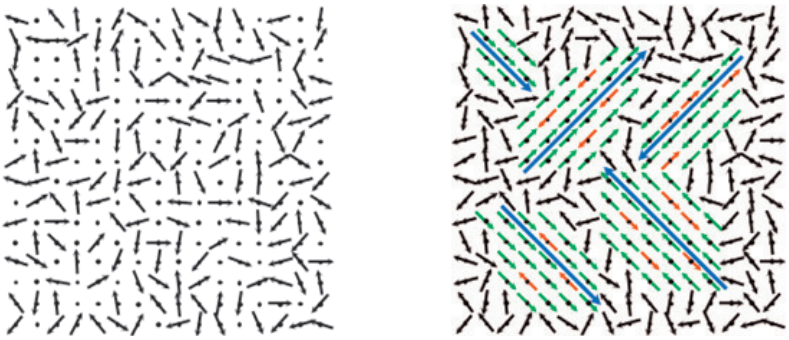

(a) (b)

Figure 2.5 — (a) Paraelectric state of an order–disorder ferroelectric, for example $BaTiO_3$. Individual unit cells may have polar displacements, but there is no correlation and the average structure is non-polar. A similar disorder has been reported for the paraelectric state of the prototype relaxor PMN.[75] (b) Relaxor below T_d, showing polar nano-regions (PNRs) where polarization is correlated over a few unit cells, but not on a length scale of micrometers as in ferroelectric domains. Each PNR is polar (long blue arrows), but when averaged over a sufficiently large volume the net polarization is zero. Illustrations from Bokov and Ye.[73]

The concept of order and disorder is central to relaxors. A clear demonstration of this was provided in 1980 by Nava Setter and L. Eric Cross, who studied the effect of B-site cation order on the diffuseness of the ferroelectric phase transition in $PbSc_{1/2}Ta_{1/2}O_3$ (PST).[64,78] PST is particularly suitable for the study of B-site order–disorder phenomena. First, the 1:1 ratio between Sc and Ta facilitates simple rock salt

ordering of the cations, which can be conveniently observed by X-ray diffraction due to the significant difference in atomic number between Sc and Ta. At the same time, the ionic charges of +3 and +5 are not so different that electrostatic forces induce a strong tendency for ordering (which is the case for $PbMg_{1/2}W_{2/3}O_3$, with charges of +2 and +6). The radius difference between the cations is of importance, since too different radii will favour ordering through elastic interactions, while too similar radii might lead to disorder no matter how long the material is annealed (this is the case for $BaFe_{1/2}Nb_{1/2}O_3$). The A-site cation size also plays a role, since a smaller A-site cation will make the size difference between the B-site cations more important. All things considered, it turns out that PST is "just right",[79] and that the degree of order can be tuned by thermal treatment: Quenching a sample from high temperature will freeze in a disordered B-site cation distribution, while annealing at elevated temperature for several hours induces ordering of Sc^{3+} and Ta^{5+} in a chequerboard pattern. The transition from B-site cation disorder to order is evident from the X-ray diffractograms shown in Figure 2.6(a), and is reflected in a change in dielectric response from relaxor to classic ferroelectric, as shown in Figure 2.6(b).

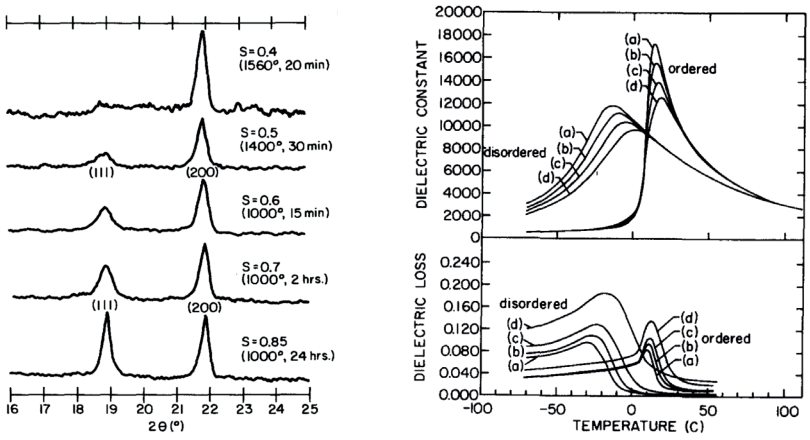

Figure 2.6 — (a) X-ray diffraction patterns of PST powders with various degrees of B-site cation order. The order parameter S, calculated from intensity ratios of X-ray diffraction lines, is 0 for perfect disorder and 1 for perfect order. After Setter and Cross.[78] (b) Dielectric permittivity and loss for ordered ($S = 0.80$) and disordered ($S = 0.35$) PST single crystals, measured at frequencies from 1×10^3 Hz to 1×10^6 Hz [(a)–(d) in the figure]. After Setter and Cross.[64]

Relaxors continue to attract attention, mainly due to the ultrahigh piezoelectric response found in single crystals of PMN–PT, a solid solution of PMN and $PbTiO_3$.[68] In line with the previously mentioned interest in more environmentally friendly piezoelectrics, also lead-free relaxors have attracted some attention.[12,13,80] In particular, there has been a huge interest in developing solid solution systems similar to PMN–PT, but featuring lead-free relaxors and ferroelectrics.[81] One of the promising candidates in this respect is the $Bi_{1/2}Na_{1/2}TiO_3$–$BaTiO_3$ (BNT–BT) system, of which single crystals with high piezoelectric coefficients have been made.[82,83] Lead-free relaxors are of interest also for other purposes, such as thermoelectricity. For example, the partially reduced SBN system, $(Sr, Ba)_5Nb_{10}O_{30-\delta}$, has shown an enhanced Seebeck coefficient for compositions in the relaxor regime.[84] Despite their many promising and useful properties, however, relaxors are still far from being fully understood. Being intimately linked to disorder on different length scales, the phenomenon of relaxor ferroelectricity is inherently complex. This is especially a challenge for computational investigations, where true disorder is hard or impossible to implement properly. Often, one must resort to replacing disordered systems by much simpler model systems for the calculations to be feasible.[85] Cation ordering has been studied in lead-free perovskite relaxors such as BNT and related compositions,[86,87] while molecular dynamics calculations have been used with some success to correlate the polar and chemical order in the prototype relaxors PMN and PSN.[88–90] More complicated structures and chemical compositions, as is the case for many relaxors, represent a big challenge for computational studies.

2.2 Tetragonal tungsten-bronze-type ferroelectrics

Crystal structure and subtypes

Tungsten bronzes *sensu stricto* are non-stoichiometric oxides with the general formula A_xWO_3, where A is a metal cation and $x < 1$. They are metallic oxides with a bronze-like lustre as shown in Figure 2.7(a), hence their name. Tungsten bronzes exist in three basic structure types, all of which are based on corner-sharing WO_6 octahedra. The structure type which is the main focus of this work is the tetragonal tungsten bronze (TTB) structure, shown in Figure 2.7(b). The other possible structures are the perovskite tungsten bronze [PTB; Figure 2.8(a)], essentially an A-deficient perovskite; and the hexagonal tungsten bronze [HTB; Figure 2.8(b)]. Which structure type is the most stable depends both on the size of the metal cation and on x. Tungsten bronzes in the broad sense, *sensu lato*, is used for a large group of oxides, mainly niobates and tantalates, that crystallize with structures similar to the actual tungsten oxides. Most of them are not metallic, but rather insulators due to the d^0 electron configuration

of Nb^{5+} and Ta^{5+}, and for this reason they are more conveniently referred to as *tungsten-bronze-type* oxides or *bronzoïds*.[91]

While both the TTB and perovskite structures are based on corner-sharing BO_6 octahedra, the connectivity is more complex in TTB, resulting in several different sites that can accomodate cations. The aristotype unit cell with space group symmetry $P4/mbm$ is shown in Figure 2.7(b), where sites corresponding to the general formula $(A1)_2(A2)_4C_4(B1)_2(B2)_8O_{30}$ are marked. The A1 sites, with a coordination number of 12, are similar to the A sites in perovskites and form square-shaped channels along the tetragonal c direction. The A2 sites form pentagonal channels, formally 15-coordinated, while the C sites form triangular channels.[94] The A1 and A2 sites can be occupied by a variety of metal cations, such as alkali and alkali earth elements, p-block elements such as Pb and Bi, or rare earth elements. The C sites are narrow and can only accommodate small cations such as Li^+ or Nb^{5+}, thus making possible a Nb:O

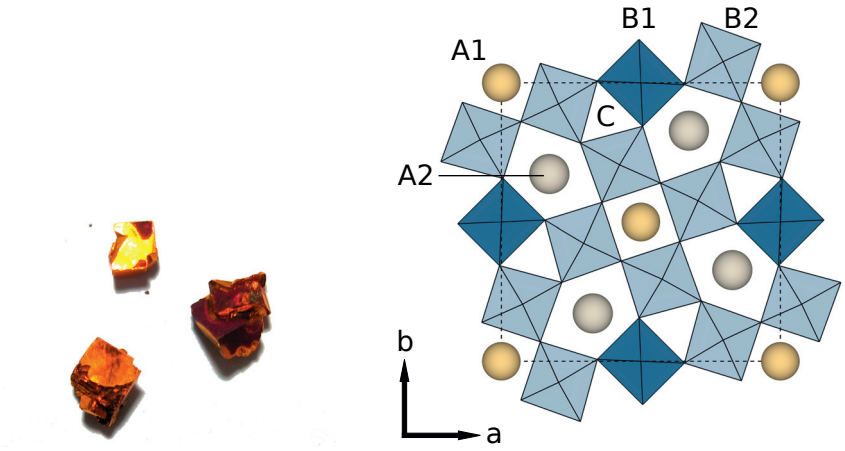

(a) (b)

Figure 2.7 — (a) Crystals of sodium tungsten bronze (Na_xWO_3), showing their bronze-like colour and lustre. The longest crystal edge is approximately 5 mm. Local colour variations are due to different Na concentration in different parts of the crystals.[a] (b) Projection along c of the TTB crystal structure in the aristotype space group symmetry $P4/mbm$, with the unit cell marked by a dashed line. The general formula is $(A1)_2(A2)_4C_4(B1)_2(B2)_8O_{30}$; cation sites are marked in the figure (A1, A2 and C at $z = 0$, B1 and B2 at $z = ½$).

[a] Image source: Wikimedia Commons, user *Brammers* (public domain).

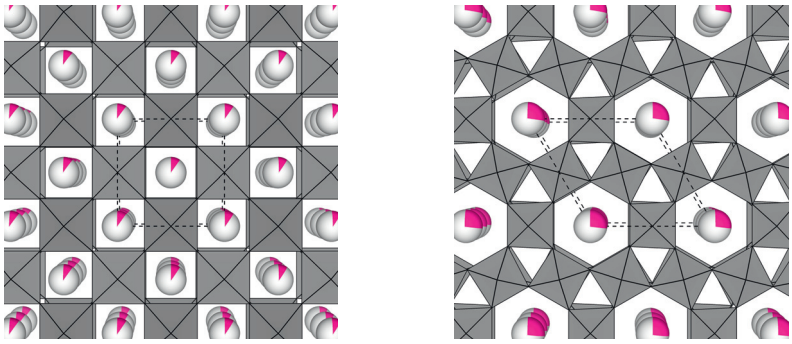

(a) (b)

Figure 2.8 — (a) Perovskite tungsten bronze (PTB) structure, exemplified by $Na_{0.10}WO_3$ with space group symmetry $P4/nmm$.[92] (b) Hexagonal tungsten bronze (HTB) structure, exemplified by $Rb_{0.27}WO_3$ with space group symmetry $P6_3/mcm$.[93] Both are projections along c, and in both panels the relevant unit cell is marked with a dashed black line. Partially coloured spheres show the average occupancy of the alkali metal cation.

ratio higher than 1:3.[95–97] The tetragonal tungsten-bronze structure can be derived from the perovskite structure by rotation of blocks of octahedra, as shown in Figure 2.9. This illustration shows that unlike the perovskite structure, the TTB structure can not be constructed from regular, undistorted octahedra. The TTB unit cell marked in Figure 2.9(b) contains 10 octahedra from the original perovskite structure, so the unit cell parameter is $a_t = \sqrt{10}a_0$ where a_0 is the corner-to-corner length of an undistorted octahedron (the unit cell parameter of a cubic perovskite).

A plethora of chemical compositions can be accommodated in the TTB framework. Starting from the general formula $(A1)_2(A2)_4C_4(B1)_2(B2)_8O_{30}$ and assuming first that all B1 and B2 cations are Nb^{5+} or Ta^{5+}, it can be seen that the cations on the A1 and A2 sites (and C, if present) must have a total ionic charge of +10 in order to meet the requirement of electroneutrality. As a first step, three main classes of TTBs can be distinguished based on cation occupancy:[15] *Filled* TTBs where all six A1 and A2 sites are occupied, as in $Ba_4Na_2Nb_{10}O_{30}$ (BNN); *stuffed* TTBs where also the four C sites are occupied, $K_6Li_4Nb_{10}O_{30}$ (KLN) being the best known example; and *unfilled* TTBs, where some of the A1 and A2 sites are vacant, as in $Pb_5Nb_{10}O_{30}$ (PN) with five out of six sites occupied. Most of the filled TTBs have A1/A2 cations with different charges, such as Ba^{2+} and Na^+ in BNN. A deviation from the ideal 4:2 stoichiometry will be compensated for by cation vacancies, so for Ba-rich BNN, $Ba_{4+x}Na_{2-2x}Nb_{10}O_{30}$, there

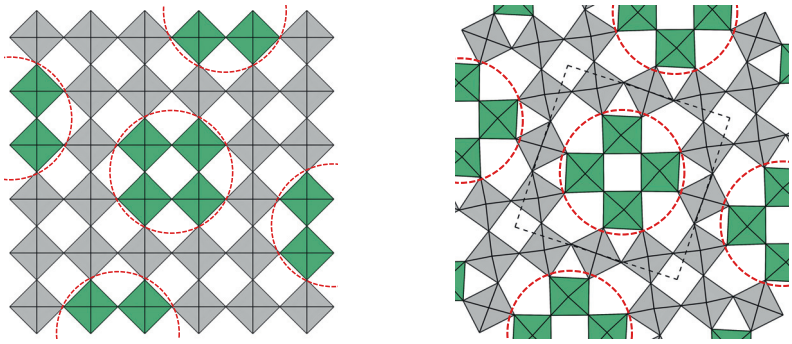

Figure 2.9 — Relation between the perovskite and TTB structures. (a) Perovskite structure consisting of corner-sharing BO_6 octahedra. The TTB structure is obtained by a 45° rotation of the blocks in green colour (rotation marked by dashed circle). (b) TTB structure (projection along the tetragonal *c* direction) after rotation of the perovskite blocks, with a dashed black line marking the TTB unit cell. Adapted from Ngai.[98]

are $6 - x$ cations and x vacancies distributed between the 6 sites.[99] There are many other mechanisms enabling the chemical flexibility of TTB compounds, several of which can occur simultaneously, and a non-exhaustive overview is given in Table 2.1.

A consequence of the chemical flexibility is that TTBs are relatively easy to synthesise as phase pure materials. At the same time, this also gives them a tendency to show up as undesired secondary phases in systems with lower tolerance for non-stoichiometry. A well-known example of this is the $K_{1-x}Na_xNbO_3$ (KNN) system, where secondary phases with TTB structure have a tendency to show up during sintering. The TTB secondary phase in KNN has the general formula $K_{10-5x}Nb_{10+x}O_{30}$, with specific compositions of $K_{5.83}Nb_{10.83}O_{30}$,[104,105] $K_{5.75}Nb_{10.85}O_{30}$[96] and $K_{5.45}Nb_{10.91}O_{30}$[97] having been reported. If one assumes that there must be between 4 and 6 K^+ cations in the TTB unit cell, so that at least the four A2 sites are fully occupied by K, the solid solution range is limited to $0.8 < x < 1.2$. Haugen *et al.*[106] suggested that this TTB phase forms as a consequence of potassium volatility during sintering of KNN. Using the general formula for the TTB phase, the formation reaction (simplified with $KNbO_3$ in place of KNN) is:

$$(10 + x)KNbO_3 \rightleftharpoons K_{10-5x}Nb_{10+x}O_{30} + 3xK_2O\,(g)$$

This reaction explains both the formation of the TTB phase and the differing composi-

Table 2.1 — Examples of the chemical flexibility of TTB compounds with general formula $(A1)_2(A2)_4C_4(B1)_2(B2)_8O_{30}$. One or two simple examples, generally regarded as prototypes, are given for each of the unfilled, filled and stuffed TTB families. The non-stoichiometric TTBs listed below can be related to one of the prototypes by a chemical mechanism such as cation substitution (s.). The solid solution ranges are $0 < x < 1$ unless otherwise specified, and vacancies are explicitly included in the formulae as □.

Type of non-stoichiometry	Example compound/system	Ref.
Simple (prototype) TTBs:		
Unfilled	$Pb_5\square Nb_{10}O_{30}$	[5]
Filled	$Ba_4Na_2Nb_{10}O_{30}$	[99]
Stuffed	$K_6Li_4Nb_{10}O_{30}$	[95]
Non-stoichiometric TTBs:		
Heterovalent s. of A1/A2	$(Pb_{1-x}Ba_x)_5\square Nb_{10}O_{30}$	[11]
Heterovalent s. of Nb	$Pb_5\square(Nb_{1-x}Ta_x)_{10}O_{30}$	[100]
Aliovalent s. of A1/A2	$Ba_{4+x}Na_{2-2x}\square_xNb_{10}O_{30}$	[99]
Aliovalent s. of Nb	$Ba_{5+x}\square_{1-x}Nb_{10-2x}Ti_{2x}O_{30}$	[101]
Reduction of Nb	$Ba_{5+x}\square_{1-x}Nb^{V}{}_{10-2x}Nb^{IV}{}_{2x}O_{30}$	[102]
Substitution of O	$Ba_{4-x}Na_{2+x}Nb_{10}O_{30-x}F_x \quad (0 < x < 2)$	[103]
O vacancies	$Ba_4La_2Nb_{6-2x}Ti_{4+2x}O_{30-x}\square_x$	[15]
Nb on C	$K_{10-5x}Nb_{10+x}O_{30} \qquad (0.8 < x < 1.2)$	[96]

tions reported by various authors. The phase diagram of the pseudobinary Nb_2O_5–K_2O system shows the TTB phase $K_{5.75}Nb_{10.85}O_{30}$ as a line compound,[107] although in light of the above it seems clear that it is actually a solid solution range.[96,105]

A both intriguing and comprehensively studied aspect of the TTB structure is the existence of incommensurately modulated superstructures.[15,108,109] A modulated structure is characterised by being based on an underlying periodic lattice, or substructure, while the actual atomic positions are displaced periodically with respect to this substructure, thereby forming a modulated structure or superstructure. In one dimension, the position of atom n in the superstructure can be expressed as

$$x_n = an + u\left[1 - \cos\left(2\pi\frac{an}{\lambda_m}\right)\right],$$

where a is the lattice parameter of the underlying structure, u is the amplitude and λ_m the wavelength of the modulation. If $\lambda_m = ca$ with c a *rational* number (simple fraction), the modulation is said to be *commensurate* and the atomic positions in the

superstructure will periodically coincide with the underlying substructure. If, on the other hand, c is an *irrational* number, there is no true periodicity in the structure, and any supercell description will only be an approximation. This is known as an *incommensurate* modulation of the underlying structure. In diffraction experiments, this gives rise to additional reflections, known as superstructure or satellite reflections. Diffraction from ordinary crystalline materials occurs under fulfilment of the Laue condition, which in one dimension can be written $Q = ha^*$ where Q is the wave vector transfer, $a^* = 2\pi/a$ is the reciprocal lattice parameter and h is an integer. The diffraction pattern of a modulated structure is described by a condition of the form

$$Q = ha^* \pm q \pm 2q \pm 3q \pm \ldots,$$

where $q = 2\pi/\lambda_m$ is the modulation vector that describes the position in reciprocal space of the satellite reflections relative to the ordinary Bragg reflections (an equivalent definition of incommensurateness is to say that $q = c'a^*$, with c' irrational).[110,111] Incommensurately modulated superstructures have been observed in many TTBs, and their existence has also been empirically correlated with ferroelectricity.[15]

Prototype TTB ferroelectrics

The early history of bronzoïds, or tungsten-bronze-type oxides, begins in 1953 with the discovery by Goodman of the General Electric Company of ferroelectricity in lead metaniobate, $Pb_5Nb_{10}O_{30}$ (PN).[5] This tungsten-bronze-type polymorph of PN will be referred to as TTB-PN in what follows. The crystal structure of ferroelectric PN was not determined at the time of its discovery, but based on X-ray diffraction data, the author reported a highly anisometric orthorhombic unit cell containing 40 formula units of $Pb(NbO_3)_2$, corresponding to a $2 \times 2 \times 2$ supercell of the aristotype cell). The discovery of TTB-PN was the first report of a ferroelectric ceramic with a general formula other than ABO_3, although not the first non-perovskite, as $LiNbO_3$ and $LiTaO_3$ were known. In 1956, M. H. Francombe (also General Electric) reported that PN can exist in another polymorph of rhombohedral symmetry (in the following referred to as r-PN),[6] also without knowing the structure in detail. This polymorph was obtained by firing the ceramics at temperatures around 1200 °C, while temperatures in excess of 1250 °C were necessary to achieve the ferroelectric polymorph reported by Goodman.[5] At the same time, Francombe redetermined the lattice parameters of TTB-PN to correspond to a $\sqrt{2} \times \sqrt{2} \times 2$ supercell of the aristotype. In 1957, the first unit cell data on the paraelectric structure were reported by Roth,[112] who identified the tetragonal unit cell which is now referred to as the aristotype, and suggested that the space group in the paraelectric state was probably $P4/mbm$. For

the ferroelectric state, Roth reported a $\sqrt{2} \times \sqrt{2} \times 1$ supercell, claiming no evidence for a doubled c parameter as found by Goodman and Francombe. In light of today's knowledge about the polymorphism and metastability of PN,[7] it is interesting to note that from the very beginning, lead metaniobate was doped in order to stabilize the ferroelectric polymorph. Goodman[5] had added up to 2.5 % of TiO_2, ZrO_2 or a mixture of the two, reportedly as a means to avoid water absorption by the PN ceramics, although it probably had the added effect of stabilizing the ferroelectric polymorph as well. Roth[112] stated that while a pure PN sample had transformed completely to the rhombohedral polymorph at 700 °C, a sample doped with 2 % $ZrTiO_4$ retained the "high-temperature" (TTB) structure.

In 1958, Francombe and Lewis[113] published the first high-temperature X-ray and dielectric study on PN. This seminal work established that the structure of TTB-PN in the paraelectric state is similar to the structure of the tetragonal alkali tungsten bronzes, with the ferroelectric transition in PN at 560 °C consisting of a distortion in the tetragonal [110] direction accompanied by a doubling of c. The topic of partial occupancy for Pb^{2+} was discussed, although no conclusion could be drawn regarding possible cation site preference. The polarization was determined to be confined to the xy plane [Figure 2.10(a)], introducing the then-new concept of "two-dimensional ferroelectricity". The discontinuous change in lattice parameters [Figure 2.10(b)] pointed to a first-order phase transition, and to a ferroelectric mechanism involving a change in Pb–O covalency in the A1 sites, although the lack of data on atomic positions and site occupancies made further conclusions difficult.

Francombe again followed up on this work in 1960 with a study on the TTB solid solution systems $(Pb, Ba)_5Nb_{10}O_{30}$ (PBN) and $(Ba, Sr)_5Nb_{10}O_{30}$ (SBN).[11] A peak in ferroelectric properties was found in the PBN system for 40 % Ba, which coincides with a minimum in T_C [Figure 2.11(a)] and a change from orthorhombic to tetragonal symmetry in the ferroelectric state [Figure 2.11(b)], effectively identifying what is now commonly known as a morphotropic phase boundary.[19] The author suggested that the pure TTB-PN has too large ferroelectric strain to be easily switched by normal electric fields at room temperature, but this is gradually relieved when Ba is substituted for Pb, leading to the improved properties of solid solutions over pure PN. This work contains the first claim that also SBN has the same TTB-type structure as PN, and it is suggested that SBN is polar along c as it is tetragonal both above and below T_C for all compositions. The author states that SBN and PBN have very similar properties, although the ferroelectricity is weaker in SBN. A similarity to the perovskites $BaTiO_3$ and $PbTiO_3$ is pointed out, and it is suggested that Pb might be the origin of the difference also between the TTBs.

In 1968–71, a series of three papers on lead-free TTB ferroelectrics[94,95,99] was published by researchers at Bell Telephone Laboratories. The papers considered composi-

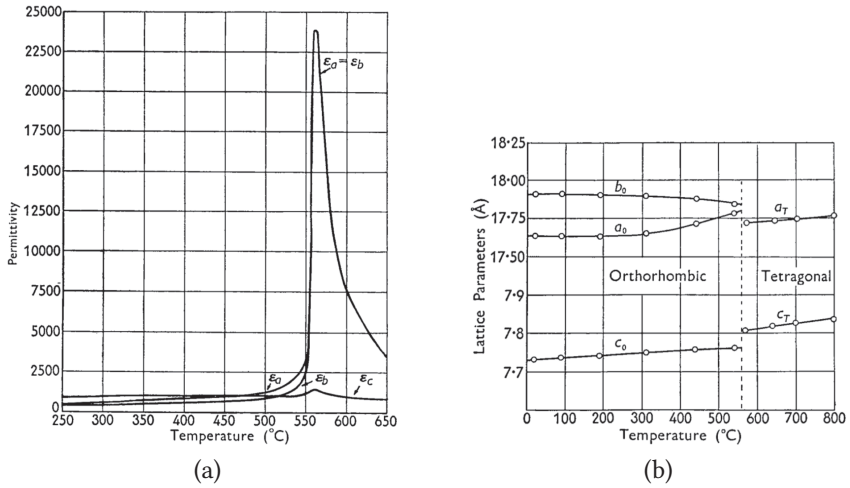

Figure 2.10 — High-temperature data on PN: (a) Dielectric permittivity, (b) lattice parameters.[113]

tions from the three solid solution systems $Sr_{5x}Ba_{5-5x}Nb_{10}O_{30}$ (SBN),[94] $Ba_{4+x}Na_{2-2x}Nb_{10}O_{30}$ (BNN)[99] and $K_{6-x-5y}Li_{4+x}Nb_{10+y}O_{30}$ (KLN).[95] The paper on SBN represents the first proper solution of the SBN crystal structure, with data on atomic positions and occupancies indicating that only Sr occupies the square A1 sites [Figure 2.12(a)]. The space group symmetry was determined as $P4bm$ in the ferroelectric state and $P\bar{4}b2$ in the paraelectric state. This result was commented upon as somewhat suprising since the two space groups do not have a group–subgroup relation, which is usually the case for ferroelectric transitions,[114] and strictly required if the transition is second-order. It was also deemed necessary to introduce split positions for the apical oxygens [oxygens above and below Nb along z, Figure 2.12(a)] in order to get a good fit of thermal displacement parameters, pointing to some kind of disordered structure. BNN and KLN were by and large described as similar to SBN in having a polar [001] axis and being tetragonal both above and below T_C. The KLN paper in addition represents the first report of a TTB with occupied C sites.

After Francombe's thorough work in 1960, only a few contributions have been made to the understanding of structure and polarization mechanism in TTB-PN. A French group published extensive single crystal X-ray data on atomic positions in the 1970s,[115,116] confirming that lead preferentially occupies the A2 sites, where they are significantly distorted towards the sides of the channels. Two supercells are suggested: An "average" cell of space group symmetry $Cm2m$ and dimensions $\sqrt{2}\times\sqrt{2}\times1$ referred

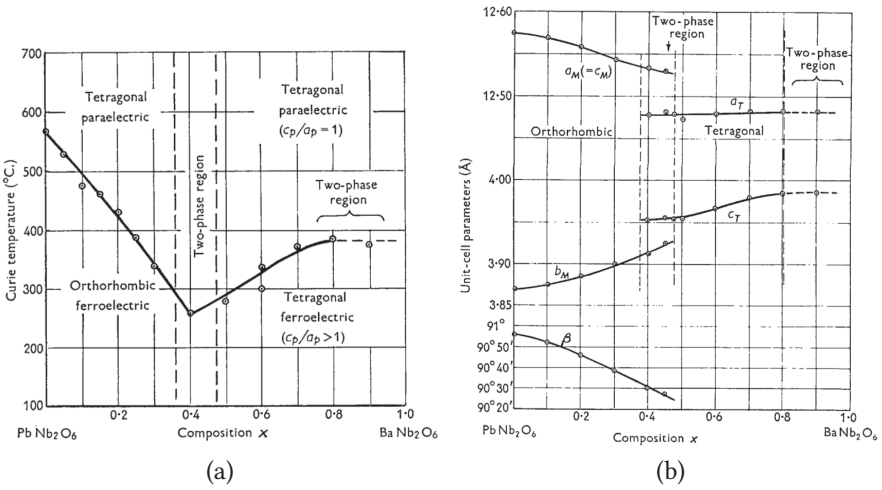

Figure 2.11 — Data on the PBN solid solution system. The variation with composition of (a) Curie temperature and (b) lattice parameters point to a morphotropic phase boundary at 37.5 to 47.5 % Ba content.[11]

to the aristotype, and a "true" cell of $Bb2_1m$ symmetry and dimension $2\sqrt{2} \times \sqrt{2} \times 2$. The two cells are related through ordering of Pb in the A2 channels, with the average cell expressed with split positions for Pb at A2 [Figure 2.12(b)].[115] The structures were analysed in terms of the displacement of Pb and Nb from their reference positions, chosen as the middle of the A1 and A2 sites. A comparison between TTB-PN and the lead-free TTBs SBN and BNN revealed that in all three compounds, Nb is displaced inside the NbO_6 octahedra in the direction of spontaneous polarization, while only in TTB-PN are the A2 cations displaced in the same direction (Figure 2.13).[116] The study did, however, not comment on the displacement of Pb in the A1 sites, which was suggested by Francombe as a key factor in the mechanism for ferroelectricity in TTB-PN,[11] and did also not comment on the extent to which the A2 displacements are actually involved in the ferroelectric transition.

The r-PN polymorph has received little attention through the years since its discovery, presumably due to it showing "no evidence of ferroelectric behaviour".[6] In 1966–67, Mahé published data on the lattice parameters, space group symmetry and atomic positions of r-PN.[117,118] This was the first solution of the crystal structure of r-PN, revealing that the structure is fundamentally different from TTB, containing "dimers" of two and two NbO_6 octahedra sharing an edge [Figure 2.14(a)]. The space group symmetry was determined as $R3m$, a polar space group, but the consequences

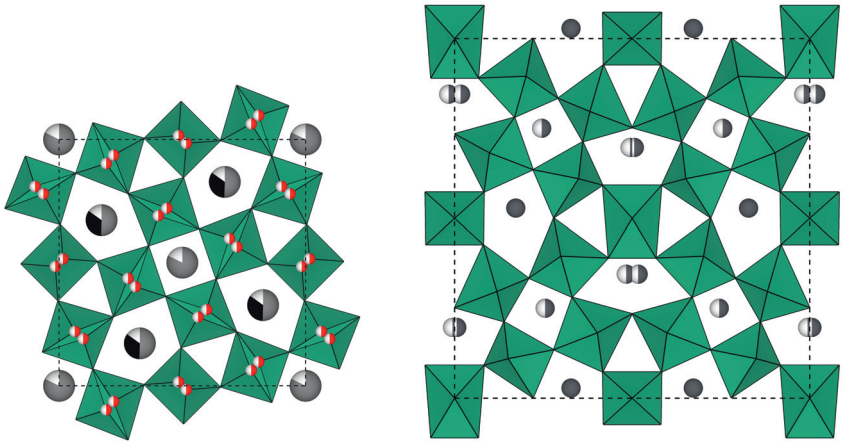

(a) (b)

Figure 2.12 — (a) Crystal structure of SBN with $x = 0.75$ as reported by Jamieson *et al.*,[94] projection along the tetragonal axis of the *P*4*bm* unit cell (dashed line). Split positions are used for the apical oxygens, which are shown explicitly as red and white spheres. Sr and Ba is represented by grey and black, respectively. (b) "Average" crystal structure of TTB-PN as reported by Labbé *et al.*[115] Projection along the tetragonal axis of the paraelectric structure, dashed line shows the *Cm*2*m* unit cell. Grey and white spheres denote positions halfway occupied by Pb, which occurs both on the A1 sites and the split A2 sites used for the simplified description of Pb ordering.

of this for possible functional properties of r-PN were not investigated further. In 1985, a Soviet work investigated solid solutions based on r-PN,[119] claiming evidence for piezoelectric activity in poled r-PN and of hysteretic behaviour in the solid solutions. Moreover, the temperature dependence of lattice parameters and dielectric response [Figure 2.14(b)] showed evidence for a polar–nonpolar phase transition from *R*3*m* to $R\bar{3}m$ at 815 °C, pointing to a possible ferroelectric transition. Again, in light of today's knowledge about PN, it is more likely that the solid solutions of r-PN contained a certain amount of the TTB-PN polymorph stabilized by doping, and that this is what gave rise to the hysteretic behaviour reported.

The transition from classic ferroelectric to relaxor behaviour in SBN was first pointed out by Glass in 1969 in connection with investigation of the material's pyroelectric properties,[14,120] although the term "relaxor" had not yet come into use. The same phenomenon was later reported for $K_{2-2x}Sr_{4+x}Nb_{10}O_{30}$ by Burns,[63] who had introduced the term "dirty displacive ferroelectrics" for disordered ferroelectrics

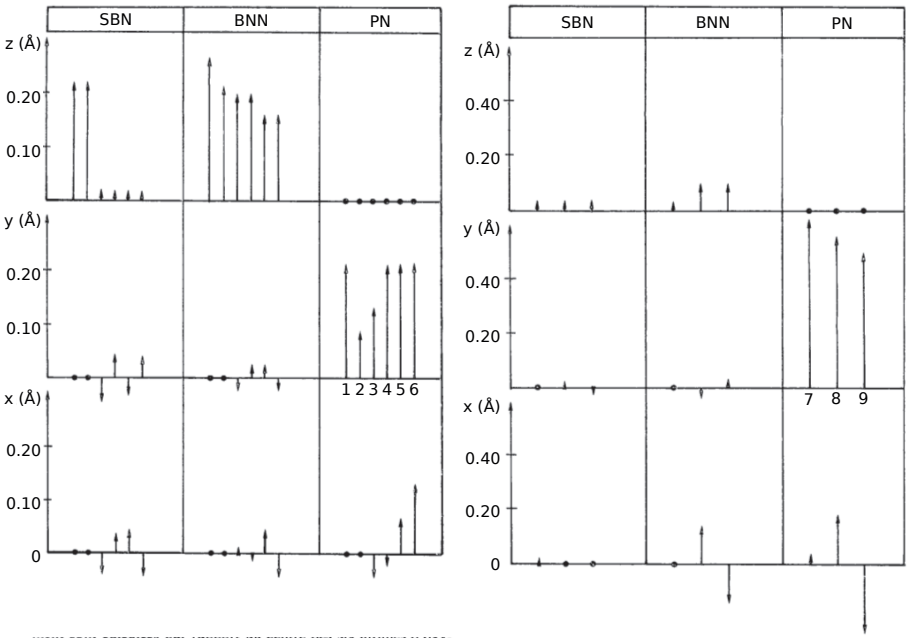

Figure 2.13 — Analysis of atomic displacements in three TTBs, after Labbé *et al.*[116] Left panel shows the displacements of Nb in the NbO_6 octahedra, right panel shows the displacements of the A2-site cations away from the center of the channel. Each panel shows the displacements of metal cations in SBN, BNN and PN (left to right), in the x, y and z directions (bottom to top).

with diffuse phase transition behaviour.[62] A different aspect of disorder in TTBs was brought to attention in 1981, when Schneck and co-workers reported on incommensurately modulated structures first in BNN[121] and soon after in SBN.[108] According to the authors, the first structural model of SBN reported by Jamieson *et al.*[94] corresponds to the average crystalline structure, while the true structure consists of an incommensurate modulation which is reflected in the average structure by the split oxygen positions [Figure 2.12(a)]. They suggested that incommensurate modulations are intrinsic to the TTB oxide family, an idea which seems to have some merit. A review from 2015 by Zhu and co-workers showed an empirical correlation between the existence of modulated structures (both commensurate and incommensurate) and classic ferroelectric behaviour[15] (Figure 2.15).

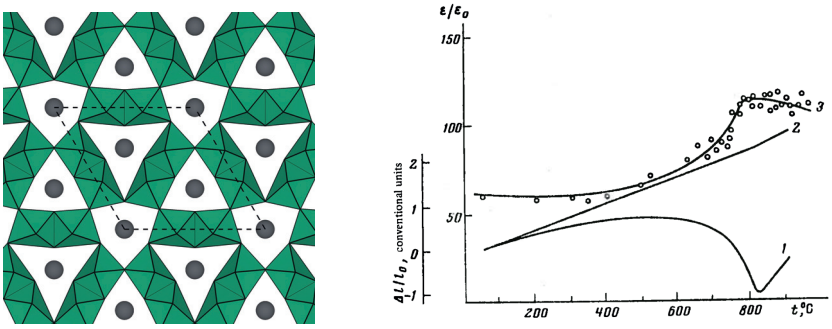

(a) (b)

Figure 2.14 — (a) Crystal structure of r-PN as reported by Mahé in 1967,[118] showing "dimers" built from two heavily distorted edge-sharing NbO_6 octahedra. Projection of one octahedral layer along the trigonal axis (hexagonal [001] direction), dashed line showing the base of the hexagonal unit cell. The crystal structure is built up by stacking the [001] layers in an ABCABC… pattern. (b) Temperature-dependent lattice parameters and dielectric response of r-PN as reported by Lopatin *et al.*,[119] pointing to a polar–nonpolar phase transition at 815 °C.

Filled TTBs

Filled TTBs, in which all A1 and A2 sites are occupied, are of particular interest in the context of computational studies, as these do not suffer from the complication of order–disorder phenomena such as in for example unfilled SBN. The prototypical filled TTB compound is BNN, which has attracted much attention also because of its incommensurately modulated crystal structure.[99,108,121,122] The fact that many TTBs have incommensurately modulated structures causes challenges for computational investigations based on periodic boundary conditions. A family of filled, insulating TTBs which has not been reported to show this behaviour, is the series $K_4R_2Nb_{10}O_{30}$ (KRN in what follows) with R = La, . . . , Gd, Bi, a group of TTBs which has attracted comparatively little attention.[123,124] Figure 2.16 shows phase transition temperatures reported for the KRN system, with some ambiguity regarding which transitions are actually taking place. Scott *et al.* only reported a single dielectric "anomaly" [Figure 2.16(a)],[123] while Neurgaonkar and co-workers reported that the KRN compounds go through a sequence of two transitions, where the upper is a ferroelectric transition similar to that found in SBN and other TTBs with polarization along z, and the lower is a ferroelastic transition to an orthorhombic space group.[124] As evident from Figure 2.16, the transition temperatures depend strongly on the size of R^{3+}. A deviation from

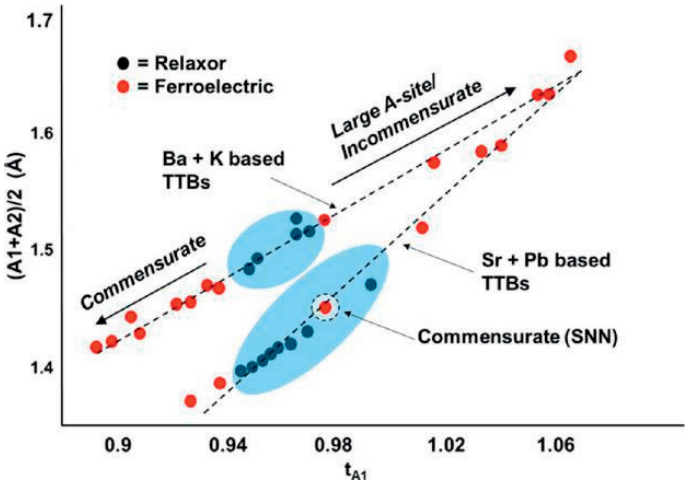

Figure 2.15 — Empirical map by Zhu *et al.*,[15] showing how different mechanisms promote ferroelectricity in TTBs. A *large* average A-site cation size increases the polarizability of the B-site cation by stretching the B–O bonds, which increases ferroelectric distortions (and also favours incommensurately modulated structures). A *low* A1-site tolerance factor (t_{A1}), which correlates with the average A-site cation size, also promotes ferroelectricity since it leads to commensurate modulations which are associated with long-range order. In between, relaxor behaviour dominates.

this trend is found for the compound with R = Bi (KBiN; not included in Figure 2.16), for which T_C has been reported in the range 360 to 420 °C,[125–127] despite Bi^{3+} having a very similar ionic radius to La^{3+} (r^{VI} = 1.03 Å and 1.032 Å, respectively[128]). The crystal structure of KBiN is also debated: Sugai and Wada[125] reported a tetragonal room-temperature crystal structure with a doubled c parameter, while Shimazu and co-workers indicated a weakly orthorhombic distortion ($a \approx b$).[126] Neurgaonkar and co-workers state in their review of TTB single crystal growth that KBiN has only one phase transition, at 420 °C, from 4/*mmm* to *mm*2 point group symmetry.[127] The transition is first order and has no ferroelastic contribution, but the material shows strong longitudinal and transverse ferroelectric effects. These partially contradictory reports leave a less than clear picture of both the structure and properties of the KRN series, with particularly high uncertainty for KBiN.

Another family of filled TTBs which has attracted attention recently, is the system $Sr_xBa_{6-x}Nb_{10}O_{30}$ with $0 < x < 6$, the filled counterpart to unfilled ferroelectric SBN. In this system, a metal–insulator transition has been shown to follow a change of

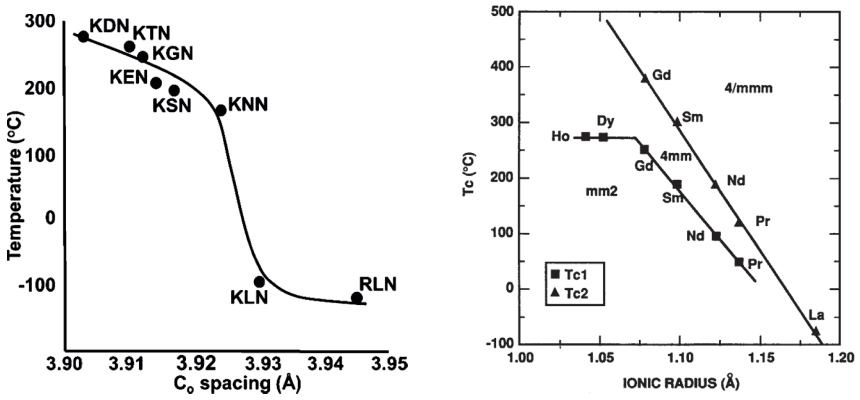

Figure 2.16 — (a) Dielectric anomaly temperatures for KRN (R = La, Nd, Sm, . . . , Dy) and $Rb_4La_2Nb_{10}O_{30}$ (RLN), plotted versus the c_0 spacing of the tetragonal unit cell. Original data from Scott *et al.*,[123] redrawn by Zhu *et al.*[15] (b) Phase transition temperatures in the KRN system plotted versus the ionic radius of R (linearly dependent on c_0 down to R = Gd). The upper transition (T_{C2}) is the paraelectric–ferroelectric transition, while the lower transition (T_{C1}) is a ferroelectric–ferroelastic phase transition. After Neurgaonkar *et al.*[124]

the Sr/Ba ratio, which is also accompanied by a change in crystal structure.[102] Since there are six divalent cations occupying the A1 and A2 sites, two of the ten Nb^{5+} cations are reduced to Nb^{4+} to maintain electric neutrality. Because of the partially occupied d band, the compounds are electrically conducting. Filled BN is metallic in the sense that the resistivity decreases with decreasing temperature, while for $x \geqslant 4$ it diverges at low temperature, pointing to an insulating ground state. Kolodiaznyi and colleagues[102] found that the filled SBN compositions with $x = 0, \ldots, 5$ crystallize in the aristotype space group $P4/mbm$, while for the Sr end member, the orthorhombic space group $Amam$ was assigned to a $\sqrt{2} \times 2\sqrt{2} \times 2$ supercell. Filled SN shows signatures of structural phase transitions at 720 K and 1072 K, which are suggested to be linked to the metal–insulator transition in the filled SBN system. No computational investigations have been made to support the experimental findings.

As mentioned previously, the search for lead-free ferroelectrics is one of the main motivations for investigation of TTBs,[13,80] but in recent years materials with TTB structure have been investigated also with respect to other more or less exotic properties. Multiferroic materials have experienced something of a renaissance in the

last decade,[129–131] and TTBs have to some extent been explored as a playground for multiferroicity.[132,133] One example is $K_{6-x}Fe_{10}F_{30}$ with $x \approx 0.1$, a TTB fluoride which shows partial Fe^{II}/Fe^{III} ordering.[134] Among TTB oxides, SBN-based materials with partially reduced Nb have been suggested as n-type semiconductors for thermoelectric applications.[84,135–137] The TTB oxide $Ba_2Bi_2Nb_{10}O_{30}$ has been investigated as a potential oxide ion conductor,[138] and even superconductivity has been reported in the partially reduced $Ba_6Nb_{10}O_{30}$.[102] It seems that TTBs are an "up and coming" class of functional materials, and that more and more interesting properties will be discovered in TTBs in the near future. A common feature for the investigations done on TTBs up until now, is a lack of computational work. With the steadily increasing capabilities of modern computational materials science, this situation is likely to change.

2.3 Density functional theory

The fundamentals and applications of density functional theory are well documented in numerous textbooks and review papers,[139–144] and the same goes for its historic development and future prospects.[145–148] The remainder of this chapter is in no way intended as a complete overview of the wondrous world of density functional theory, but rather as a low-level introduction to a few concepts important for this project.

Fundamentals

The fundamental behaviour of atoms, molecules and solids is described by quantum mechanics (QM). At the heart of QM is the notion that a system, be it a single atom or a piece of chalk, is completely described by its *wave function*. The wave function is a complex function of the coordinates of all the particles in the system, meaning that a system with N particles (counting all atomic nuclei and electrons) is described by a $3N$-dimensional wave function. From this function, all possible information about the system can be extracted. The (stationary) wave function, Ψ, is obtained by solving the *Schrödinger equation* (SE) for the system:

$$\hat{H}\Psi(\mathbf{r}_1, \mathbf{r}_2, \ldots, \mathbf{r}_N) = E\Psi(\mathbf{r}_1, \mathbf{r}_2, \ldots, \mathbf{r}_N)$$

Here, $\hat{H}$ is the Hamilton operator, which specifies all possible interactions in the system, and E is the energy. This is an eigenvalue problem: The energy is an eigenvalue of the Hamiltonian, with the wave function as the corresponding eigenstate. Solving this $3N$-dimensional non-linear eigenvalue problem is hard to say the least, and approximations must be made in all non-trivial cases. The first level of approximation is usually the *Born–Oppenheimer approximation*:[149] Since the electrons are

much lighter and faster than the atomic nuclei, it suffices to solve the *electronic SE* for the system, in which the nuclei are regarded as stationary and the wave function only depends on the electronic coordinates. The nuclear coordinates enters the Hamiltonian as parameters, giving a separate Hamiltonian for each nuclear configuration. Even within this approximation, the mathematical problem is formidable, since the interactions between electrons turn the electronic SE into a many-body problem. Only for single-electron systems (such as the hydrogen atom or the H_2^+ molecular ion) is it possible to solve the equation analytically, while for all systems containing two or more electrons, approximate solutions must be found by numeric methods.

Even though the roots of density functional theory (DFT) can be traced back to the late 1920s,[150,151] DFT as we know it today originated in 1964, when Hohenberg and Kohn published a ground-breaking paper stating what has been come to known as the Hohenberg–Kohn theorems.[152] Briefly stated, they say that *(i) There is a one-to-one mapping between the Hamiltonian $\hat{H}$ and the ground state electron density $\rho(\mathbf{r})$; (ii) There exists a universal functional of the electron density which has the ground state energy of the system as its minimum.* This result is not trivial. The electron density is the square modulus of the wave function, $\rho = |\Psi|^2 = \langle\Psi|\Psi\rangle$, so ρ is obviously determined by $\hat{H}$, in which the nuclear coordinates enter. The insight of Hohenberg and Kohn was that the converse statement also holds, meaning that the 3-dimensional electron density is just as complete a description of the system as the $3N$-dimensional wave function. The second part of the theorem states that it is possible to obtain the ground state electron density by minimizing a *universal functional* of the electron density. An energy functional F is a mathematical expression which takes in the electron density $\rho(\mathbf{r})$ and produces the single number $E = F[\rho(\mathbf{r})]$. The drawback is of course that we do not know the formulation of F, and even if we did, the minimization procedure would most likely lead to a mathematical problem just as heavy as solving the full SE.

The first practical procedure for tackling the DFT problem was formulated by Kohn and Sham in 1965,[153] one year after the Hohenberg–Kohn theorem. The Kohn–Sham formalism, on which all modern DFT calculations are based, tackles the many-body problem by a mean-field approach: Instead of considering interactions between all the electrons, each electron interacts with the average of all the others. This makes it possible to separate the electronic SE for a system of N electrons into N smaller equations, each of which gives a single-particle wave function, or orbital, ϕ:

$$\hat{H}_{\mathrm{KS}}\phi_i(\mathbf{r}) = \varepsilon_i\phi_i(\mathbf{r})$$

The Kohn–Sham orbitals ϕ_i are eigenstates of the Kohn–Sham Hamiltonian $\hat{H}_{\mathrm{KS}}$, each with a Kohn–Sham energy ε_i as its corresponding eigenvalue. The Kohn–Sham

orbitals are wave functions for an artificial set of non-interacting electrons. In this sense, neither the orbitals nor their energies are physically meaningful on their own,[†] and the orbitals in principle only serve to calculate the total electron density:

$$\rho(\mathbf{r}) = 2\sum_i |\phi_i(\mathbf{r})|^2$$

The Kohn–Sham Hamiltonian consists of several contributions to the total energy:

$$\hat{H}_{\mathrm{KS}} = T_{\mathrm{kin}} + V_{\mathrm{ext}} + V_{\mathrm{H}} + V_{\mathrm{XC}},$$

The terms on the right represent the kinetic energy of the electrons, the external potential from the atomic nuclei, the interaction with the average of all the electrons (known as the Hartree potential), and the exchange–correlation (XC) potential. The Hartree potential includes an unphysical self-interaction, since the average potential an electron "sees" also includes a contribution from the electron itself. A correction for this,[155] and miscellaneous other QM effects such as the eponymous exchange and correlation, is grouped into the XC potential, the functional derivative of the exchange–correlation energy functional:

$$V_{\mathrm{XC}} = \frac{\delta E_{\mathrm{XC}}[\rho(\mathbf{r})]}{\delta\rho(\mathbf{r})}$$

The E_{XC} term is in principle the only unknown term in Kohn–Sham DFT, which would therefore be an exact theory if the exact XC functional were known. It is not, and even if it were, it would most likely lead to infeasibly heavy calculations, so in practice, simpler expressions for E_{XC} are used. The simplest is the local density approximation (LDA), a family of XC functionals which depend only on the density at each point in space, $E_{\mathrm{XC}}^{\mathrm{LDA}} = F[\rho(\mathbf{r})]$. A more sophisticated approach is to also include a dependency on the density gradient at each point, which leads to the generalized gradient approximation (GGA) family of functionals, $E_{\mathrm{XC}}^{\mathrm{GGA}} = F[\rho(\mathbf{r}), \nabla\rho(\mathbf{r})]$. Once an appropriate XC functional is chosen, the total energy of the system is obtained from the electron density:

$$E_{\mathrm{tot}} = E_{\mathrm{known}}[\rho(\mathbf{r})] + E_{\mathrm{XC}}[\rho(\mathbf{r})],$$

where "known" terms correspond to the kinetic energy, external potential and Hartree terms in the KS Hamiltonian. The XC part includes everything else, The KS equations must be solved iteratively or *self-consistently*: An initial charge density determines

[†]This distinction is most of all philosophical — the Kohn–Sham orbitals frequently resemble "real" orbitals as obtained by wave function-based methods such as Hartree–Fock.[154]

the initial KS Hamiltonian, which gives an initial set of KS orbitals. These are used to calculated a new charge density, and the total energy is calculated. The process is then repeated starting from the new charge density, and this continues until the difference in E_{KS} is sufficiently small between successive iterations.

The LDA and GGA functionals constitute the lowest two levels in the hierarchy of XC functionals,[156,157] as shown in Figure 2.17. The hyper-GGA family, also known as

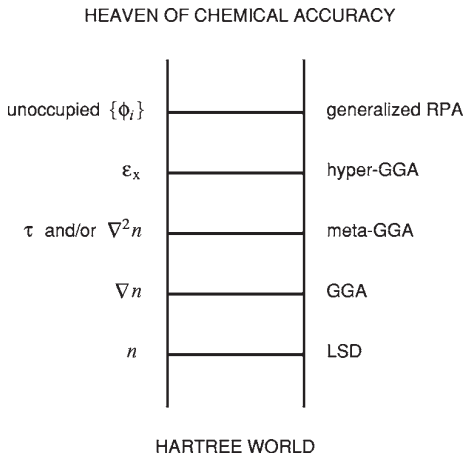

Figure 2.17 — The ladder of density functional approximations to the XC energy, as visualized by Perdew *et al.*[157] Symbols and abbreviations: LSD, local spin density (n); GGA, generalized gradient approximation; τ, kinetic energy density; ε_x, exact exchange; RPA, random phase approximation. Each rung of the ladder includes the components of the lower ones, plus additional complexity which potentially increases the accuracy, but also the computational cost.

hybrid functionals, are worthy of special mention. They result from replacing a part of the exchange energy in a density functional with *exact exchange* resulting from a Hartree–Fock (HF) calculation. By adjusting the amount of exact exchange, and possibly also combining LDA and GGA functionals for the DFT part of the exchange and/or correlation energies, a wide variety of hybrid XC functionals can be created.[158] A popular parametrisation of the mixing is

$$\begin{aligned} E_{\mathrm{XC}} = {} & E_{\mathrm{X}}^{\mathrm{LDA}} + A(E_{\mathrm{X}}^{\mathrm{HF}} - E_{\mathrm{X}}^{\mathrm{LDA}}) + (1-A)B(E_{\mathrm{X}}^{\mathrm{GGA}} - E_{\mathrm{X}}^{\mathrm{LDA}}) \\ & + E_{\mathrm{C}}^{\mathrm{LDA}} + C(E_{\mathrm{C}}^{\mathrm{GGA}} - E_{\mathrm{C}}^{\mathrm{LDA}}), \end{aligned}$$

where the XC functional is decomposed into exchange (X) and correlation (C) contributions, and A, B and C are mixing parameters introduced by density functional constructor Axel Becke.[159] One of the most popular density functionals in molecular chemistry is a hybrid functional known as B3LYP,[160,161] in which Becke's exchange functional (B88)[162] is combined with the correlation functional of Lee, Yang and Parr (LYP)[163] according to the mixing parameters $A = 0.20$, $B = 0.90$ and $C = 0.81$ as determined by fitting to empirical data such as atomization energies and ionization potentials for a wide range of atoms and small molecules.[159] The most popular GGA functional for solids is the Perdew–Burke–Ernzerhof (PBE) functional,[164] and by combining this with 25 % exact exchange ($A = 1/4$, $B = C = 1$), the result is a hybrid functional known as PBE0.[165,166] This latter type of hybrid, with no empirically determined parameters except those already present in the GGA ($A = 1/4$ is fixed *a priori*[165]), is appealing, as some have considered the "hyperparametric disorder" of functionals such as B3LYP to be unfortunate and counter to the spirit of the original, pure density functional theory.[167]

Range-separated hybrid functionals are a more recent innovation which intends to improve on the computational efficiency of hybrid functionals by splitting the exchange part of V_{XC}, which has the form of a Coulomb potential, $1/r$, into a long-range and a short-range part (the latter known as a *screened Coulomb potential*). There is no unique mathematical recipe for this separation, but a popular choice is the following:

$$V_{\mathrm{X}}(r) \sim \frac{1}{r} = \frac{\operatorname{erf}(\mu r) + \operatorname{erfc}(\mu r)}{r} = V_{\mathrm{X}}^{\mathrm{LR}}(x;\mu) + V_{\mathrm{X}}^{\mathrm{SR}}(x;u),$$

where $\operatorname{erf}(x)$ and $\operatorname{erfc}(x)$ denote the error function and complementary error function, respectively, which by definition sum to one.[‡] It turns out that accurate results can be achieved by replacing only the short-range part of V_{X} by exact exchange, while the long-range part, which would otherwise lead to very expensive HF calculations, can be evaluated in the usual way (LDA or GGA). The "short-rangedness" of $V_{\mathrm{X}}^{\mathrm{SR}}$ is characterised by the range-separation parameter μ, which has the dimension of reciprocal length. The effect of μ on the screened Coulomb potential is shown in Figure 2.18. The original range-separated hybrid functional was devised by Heyd,

[‡]

$$\operatorname{erf}(x) = \frac{2}{\sqrt{\pi}} \int_0^x e^{-t^2} \mathrm{d}t$$
$$\operatorname{erfc}(x) = \frac{2}{\sqrt{\pi}} \int_x^\infty e^{-t^2} \mathrm{d}t = 1 - \operatorname{erf}(x)$$

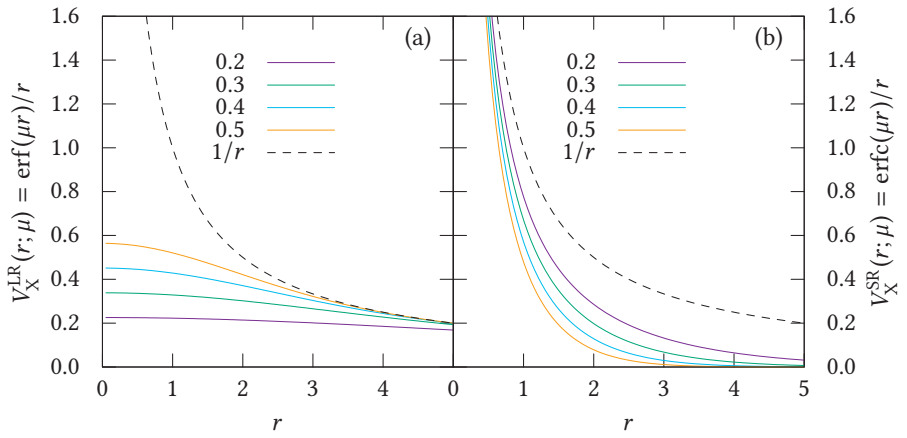

Figure 2.18 — Separation of the Coulomb interaction, $1/r$, into a long-range (a) and a short-range (b) part. The separation is characterized by a range-separation parameter, μ, with the dimension of reciprocal length. Graphs with the same μ (same colour) in a and b sum up to $1/r$, as shown by the dashed line.

Scuseria and Ernzerhof (HSE).[168] The first version is known as HSE03, and uses the PBE functional with 25 % HF exchange and a range separation parameter of $\mu = 0.283\ \text{Å}^{-1}$. A later revision, HSE06,[169] recommends $\mu = 0.207\ \text{Å}^{-1}$. The limiting cases of $\mu = 0$ and $\mu = \infty$ correspond to PBE0 and PBE, respectively, and HSE with finite values of μ can be regarded as an interpolation between these two.[169]

The main advantage of hybrid functionals is that they often provide an improved description of the electronic band gap for solids. For almost all materials, DFT calculations severely underestimate the band gap, in certain semiconductors by as much as half of the experimental value.[143] The hybrid functionals do, however, lead to significantly more costly calculations, even for range-separated hybrids. A popular and inexpensive solution to the band gap problem in DFT is the so-called DFT+U approach (also known as LDA+U, PBEsol+U and so on, depending on which functional is used), where an on-site Coulomb repulsion, U, is added to the Hamiltonian for electrons occupying narrow bands, such as the d band in transition metal oxides. This corrects for the previously mentioned self-interaction error inherent to mean-field approaches such as DFT. The Coulomb interaction U can in principle be calculated self-consistently,[170,171] but in practice it often enters as an empirical parameter which is determined by fitting to experimental data, for example on band gaps, magnetic

moments or lattice parameters. Alternatively, a hybrid functional calculation can be performed initially, and the results can be used to determine U for use in further calculations which would be infeasible with hybrid functionals.[172]

The long list of available functionals, as well as the possibility to combine both LDA and GGA functionals with various degrees of exact exchange at different range-separations, means that there are in principle infinitely many functionals to choose from. A recent example is the HSEsol functional,[173] created by replacing PBE in HSE06 with PBEsol, with the intention to improve on HSE06 for lattice parameters and bond lengths of solids in the same way as PBEsol improves on PBE, while also giving good electronic properties. There have even been attempts at combining hybrid functionals with DFT+U, with the motivation that these methods should be seen as complementary rather than mutually exclusive options.[174] Despite all these efforts, a functional that works equally well for both structural and electronic properties for a large number of solids remains elusive. Purpose-specific tailoring of functionals is a pragmatic solution,[158] even though the large number of adjustable parameters brings about certain challenges in itself.

DFT in modern materials science

"The calculation of a wavefunction took about two afternoons, and five wavefunctions were calculated on the whole, giving the ten points of the figure."[175]

The preceding quote, from a 1933 publication by Wigner and Seitz, refers to a calculation of the energy of sodium metal as a function of the lattice constant. Today, this type of calculation is a routine exercise which can be performed on a modern smartphone.[§] A lot has happened in the last two to three decades, which is reflected in a rapidly growing number of DFT publications, as shown in Figure 2.19. The use of DFT in solid-state chemistry and materials science has taken off at a later time than molecular chemistry, but is quickly catching up. A further perspective on the historical development of DFT for solids is provided by Figure 2.20, which shows the lattice parameter of silicon calculated by different DFT codes and implementations of the PBE exchange–correlation functional. This simultaneously illustrates the concepts of precision and accuracy in computer experiments: *Precision* refers to the comparability of results obtained by different calculations and/or software packages, while *accuracy* refers to how close computational results come to experimental values. The former can be thought of as the reproducibility of the computer experiments, in analogy to laboratory experiments, and has improved significantly over the 20 years since

[§]The open-source electronic structure software suite QUANTUM ESPRESSO,[176] for example, has been successfully implemented on both cellphones and videogame consoles.[177,178]

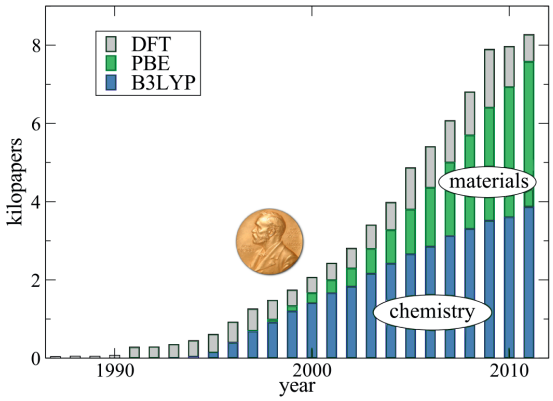

Figure 2.19 — Annual number of DFT publications, resolved into molecular ("chemistry") and solid-state ("materials") systems based on the citation of the B3LYP[160,161] and PBE[164] functionals, respectively (unit: kilopapers). Gold medal represents the 1998 Nobel prize to Walter Kohn and John Pople.[179,180] From [145].

the release of PBE in 1996. The accuracy has not improved in the same way, since it depends on the details of the functional, which are common to all the calculations. The PBE functional is known to overestimate the lattice parameter for most solids by 1 to 2 %, with the error increasing for heavier elements.[173,182] This should not be seen as a problem for the use of PBE, since comparison between different solids may still give realistic trends in properties.

Density functional calculations have been of immense importance for the fundamental understanding of ferroelectric materials.[183] As mentioned previously, one of the major milestones in understanding the origins of ferroelectricity was made with Cohen's electronic structure calculations for the perovskites $PbTiO_3$ and $BaTiO_3$ in the early 1990s,[55,184] which coincides in time with the onset of DFT publications shown in Figure 2.19. As is also the case for experimental studies, most of the computational work on ferroelectrics has focused on perovskites, although first-principles studies have been conducted also for materials such as for example the $LiNbO_3$[185,186] and $YMnO_3$ structural families,[187,188] Aurivillius,[189–191] Dion–Jacobson[192,193] and Ruddlesden–Popper phases,[194–196] and other types of layered perovskites.[197] In several cases, these fundamental studies have led to increased understanding also of more general phenomena than ferroelectricity: $YMnO_3$, for example, is a typical *improper ferroelectric*,[198,199] in which the polar distortion mode is not the energy-lowering mode that actually drives the transition (or, from a more

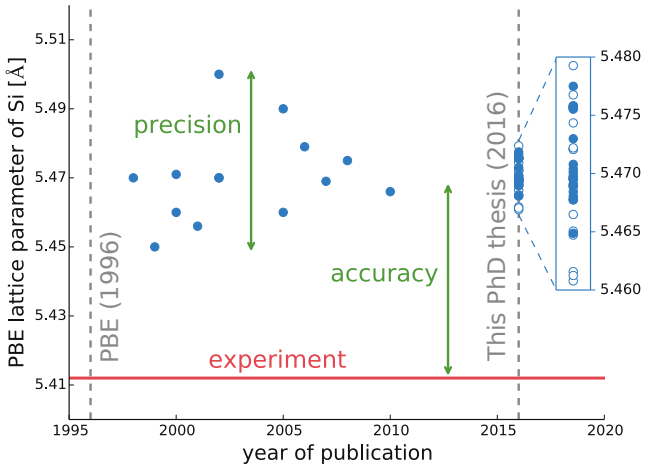

Figure 2.20 — Precision and accuracy of DFT calculations, here exemplified by the lattice parameter of silicon as calculated by different DFT codes using the PBE exchange–correlation functional. The *precision* has improved significantly over the 20 years since PBE was released (vertical dashed lines), meaning that the computer experiments are becoming increasingly reproducible. The *accuracy* is determined by the details of the functional (in this case, PBE overestimates the lattice parameter of Si). Adapted from [181].

macroscopic viewpoint, the spontaneous polarization is not the primary order parameter of the transition). In $YMnO_3$, the spontaneous breaking of symmetry occurs via a non-polar zone boundary mode, and polarization arises as a secondary effect.[187] Even more sophisticated is the concept of *hybrid improper ferroelectricity*, exemplified by $Ca_3Mn_2O_7$ with Ruddlesden–Popper structure.[194] In this case, ferroelectricity arises from a combination of *two* non-polar octahedral tilt modes, which may or may not condense at the same temperature. The insight gained from fundamental studies on ferroelectrics, be they perovskites or more exotic structures, plays a central role in the ongoing search for new multiferroic materials.[56–58,131,200–202]

Lattice dynamics and spontaneous polarization

Two computational topics deserve special mention: Lattice dynamical characterisation of ferroelectric instabilities, and calculation of spontaneous polarization in periodic structures. *Lattice dynamics* is the study of vibrations in a crystalline solid.

In a periodic lattice, each atom vibrates around its equilibrium position under the influence of forces governed by chemical bonds to other atoms (illustrated in the phase transition model in Figure 2.3). The possible vibrations of the crystal lattice can be decomposed into periodic "displacement waves", also knows as *phonons*. Provided that inter-atomic forces can be accurately described within the harmonic approximation, phonons can be obtained as eigenvectors of the *dynamical matrix*, the matrix of second derivatives of the energy with respect to periodic displacements of the atoms. The calculation of phonons is therefore a linear algebra problem which can be solved very efficiently once the energy is calculated for a given atomic displacement[32,203,204] Phonon calculations represent a computational approach to the soft mode theory of ferroelectricity developed in the 1960s: By performing phonon calculations for the high-symmetry paraelectric phase of a ferroelectric, such as a cubic perovskite, certain phonons will show up as unstable, which is manifested in imaginary vibration frequencies. If the eigenvector of the phonon is "frozen in", the energy of the system is lowered, and the result is a distorted structure of lower symmetry. By repeating the process until no further unstable phonons are found, the dynamically stable ground state structure can be reached. This is a systematic way of exploring energy-lowering distortions when starting from a high-symmetry crystal structure, such as a cubic perovskite, and can be used to predict if a hypothetical compound would undergo a displacive phase transition to a lower symmetry[32,194,204–208]

Spontaneous polarization in periodic structures represents a particular challenge for first-principles calculations, and the formulations necessary for implementing it in modern density functional codes were developed relatively late, in the early 1990s.[209,210] Several reviews exist of the modern theory of polarization,[211–214] and only an illustration of the basic problem will be given here.

The *macroscopic* interpretation of polarization is the surface charge per unit area, $|\mathbf{P}| = Q/A$, as illustrated in Figure 1.1(b). *Microscopically*, the polarization of a system is usually interpreted as the dipole moment per unit volume, $\mathbf{P} = \mathbf{d}/V$. For a finite system, such as a molecule or cluster, the polarization is straightforwardly calculated as

$$\mathbf{P} = \frac{1}{V} \sum_i q_i \mathbf{r}_i,$$

for a collection of point charges q_i at positions $\mathbf{r}_i$. This is referred to as the ionic limit, and for a continuous charge distribution, the above expression is generalized by an integral. A conceptual problem arises, however, when attempting to transfer this formulation to a periodic (infinite) system. As an example, the top panel of Figure 2.21 shows a one-dimensional chain of alternating anions and cations, spaced regularly so as to produce a centrosymmetric structure. The polarization of this system is

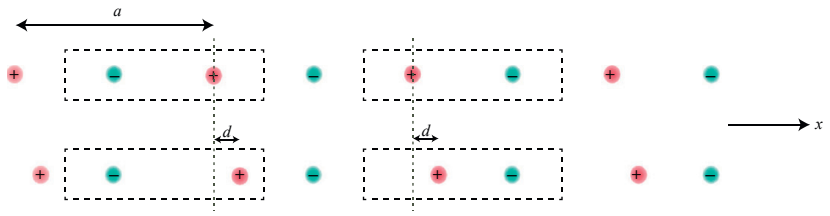

Figure 2.21 — One-dimensional chain of alternating anions and cations with lattice parameter a. The top panel shows a centrosymmetric and non-polar structure, while in the lower panel the cations have moved a distance d in the $+x$ direction, producing a polar structure. Different unit cells can be chosen (dashed lines), giving different microscopic dipole moments, even for the centrosymmetric structure. However, the *change* in polarization, $\Delta P = (1/a)\sum_i q_i \Delta x_i$, is the same in both cases ($\Delta P = d/a$ for $q = \pm 1$). Figure from [214].

ill defined: There is no uniquely defined unit cell for the system (the dashed lines show two possible choices), and hence also no unique microscopic dipole moment. However, a *change* in polarization is well defined, as shown in the bottom panel of Figure 2.21. The cations have now moved a distance d, producing a net polarization along x, and the corresponding change in polarization can be found from, again in the ionic limit,

$$\Delta P = \frac{1}{a}\sum_i q_i \Delta x_i,$$

which yields the same result for both the unit cells shown. The key point is that the *absolute* value of **P** is meaningless for a periodic structure, and that polarization must always be evaluated as a *change* with respect to a suitable reference structure (typically the paraelectric phase for a ferroelectric). The polarization is calculated as a so-called geometric phase or *Berry phase* of the wave funtion,[215,216] which can be an independent-particle Kohn–Sham or Hartree–Fock wave function,[217,218] or, in principle, the full many-body wave function.[219] The mathematics of the Berry phase method leads to the polarization being calculated modulo an arbitrary number of "polarization quanta":

$$P_i = P_{0,i} \pm nP_{q,i},$$

where $P_{q,i}$ is the polarization quantum in direction i and n is an integer. $P_{q,i}$ is determined by the crystal structure, and is generally of the same magnitude as $\mathbf{P}_s$ for a typical ferroelectric. The polarization is in other words multivalued, a concept referred to as the *polarization lattice*. The practical consequence of this is that a number

of calculations must be performed for structures that gradually transform between the polar (ferroelectric) state and a non-polar (paraelectric) reference state, in order to ensure that the same value of n is used for both end points when calculating ΔP. This is illustrated in Figure 2.22, which shows the detailed calculation of spontaneous polarization for the ferroelectric perovskite $BiFeO_3$.

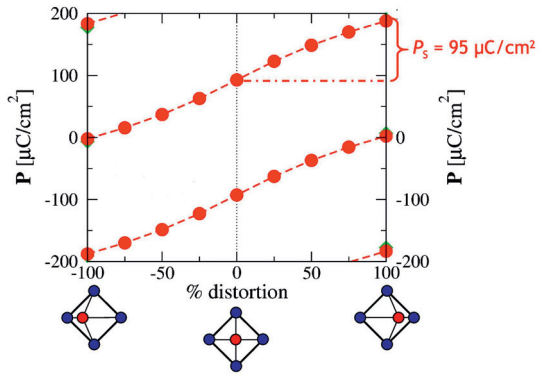

Figure 2.22 — Calculation of spontaneous polarization of $BiFeO_3$ using the modern theory of polarization. Polarization is calculated with respect to a gradual transformation between the ferroelectric state (±100 %) and a non-polar reference state (0 %). The dashed lines represent different branches of the polarization lattice, separated by the polarization quantum. The spontaneous polarization, $\mathbf{P}_s$, is extracted as the change in polarization along a single branch from 0 to 100 %. From [131].

Complementary to the direct calculation of spontaneous polarization is the calculation of *Born effective charges* (BECs).[220,221] The BEC tensor of atom i is defined as the derivative of the polarization in direction β with respect to displacement of the atom in direction α:

$$Z^*_{i,\alpha\beta} = \frac{\partial P_\beta}{\partial u_{i,\alpha}}.$$

The BECs are often anomalously large (significantly larger than the nominal ionic charges) in a structure that is dynamically unstable with respect to a lower-symmetry phase. For example, the titanium cation in cubic $BaTiO_3$ has a BEC of +7.25, almost twice the nominal ionic charge of +4. Similarly, the oxygen anions, with a nominal charge of −2, have a BEC of −5.71 for displacement in the direction of the Ti–O bonds.[221] The interpretation of this is that when cubic $BaTiO_3$ distorts into the polar

tetragonal phase, the additional covalent Ti–O bonding arises through electron transfer from O 2*p* orbitals to the formally empty Ti 3*d*. This leads to a larger net charge transfer than what would result from only the displacement of cations with nominal ionic charges. Large BECs are therefore considered to be a strong indicator for the existence of ferroelectricity. One advantage of this strategy is that calculation of BECs for the high-symmetry paraelectric phase does not require detailed knowledge about the ferroelectric phase. Hypothetical compounds, for example ABO_3 perovskites, can therefore be conveniently screened for large BECs in search of potentially new ferroelectric materials.

3 Methods

3.1 Computational details

General

All first-principles calculations in this work were performed with the Vienna Ab-initio Simulation Package (VASP, versions 5.3.2–5.4.1).[222–225] All calculations employ the projector augmented wave (PAW)[226,227] potentials supplied with VASP. The specific potentials are listed in Table 3.1 with the name used in the VASP potential library, and the corresponding valence electron configurations. The potentials used for f-block elements (lanthanides) include the f orbitals as core states in order to speed up convergence.

Table 3.1 — Valence electron configurations for the PAW potentials used in the density functional calculations.

Potential	Valence e^- config.
O	$2s^2 2p^4$
Nb_sv	$4s^2 4p^6 4d^3 5s^2$
K_sv	$3s^2 3p^6 4s^1$
Ti_sv	$3p^6 3d^2 4s^2$
Sr_sv	$4s^2 4p^6 5s^2$
Ba_sv	$5s^2 5p^6 6s^2$
La	$5s^2 5p^6 5d^1 6s^2$
Ce_3, …, Sm_3	$5s^2 5p^6 5d^1 6s^2$
Eu_3, Gd_3	$5p^6 5d^1 6s^2$
Tl_d	$5d^{10} 6s^2 6p^1$
Pb_d	$5d^{10} 6s^2 6p^2$
Bi_pv	$5p^6 5d^{10} 6s^2 6p^3$

Integrals in reciprocal space were approximated by sampling on a Monkhorst–Pack (MP) grid,[228] and wave functions were expanded in plane waves up to a certain energy cut-off. Both the energy cut-off and the density of the MP grid were tested for convergence in all new geometries, with respect to properties such as lattice parameters and total energies. In general, a $2 \times 2 \times 6$ MP grid was sufficient for a TTB unit cell of 12 Å × 12 Å × 4 Å. The energy cut-off is mainly determined by the oxygen potential used, which requires a minimum of 400 eV. 550 eV was generally found to give well converged results.

Most calculations employ the PBEsol functional,[229] which is a version of the Perdew–Burke–Ernzerhof (PBE) functional[164] optimized for solids, and typically improves on PBE for equilibrium properties such as lattice parameters and bond lengths. All calculations on insulating TTBs also use strictly non-spin-polarized calculations. For the conducting TTBs with a partially occupied *d* band, Chapter 8, both spin-polarized and non-spin-polarized calculations were performed with the range-separated hybrid functional HSEsol.[173] HSEsol is based on PBEsol and uses 25 % Hartree–Fock exchange and a range separation of $\mu = 0.207\,\text{Å}^{-1}$. Non-spin-polarized PBEsol+U calculations were used as a less computationally expensive alternative to HSEsol in order to facilitate structural relaxations and phonon calculations for conducting TTBs. The implementation of PBEsol+U follows the standard Dudarev scheme,[230] with the effective on-site Coulomb interaction $U_{\text{eff}} = U - J$ determined by fitting PBEsol+U results to HSEsol results for the electronic band gap.

Crystal structures and charge densities were visualized with VESTA[231] unless otherwise specified. Online tools from the Bilbao Crystallographic Server[232–234] were used throughout, and specific programs are cited as appropriate.

Structural optimization

Optimization of crystal structures was performed by relaxing atomic positions and/or lattice parameters until the Hellmann–Feynman forces[235] acting on all ions were below a certain threshold. For energetic comparisons, a force-based convergence criterion of $10^{-2}\,\text{eV}\,\text{Å}^{-1}$ was typically used, while a stricter criterion of $10^{-4}\,\text{eV}\,\text{Å}^{-1}$ was found to be necessary for calculation of phonon frequencies in TTBs. Relaxations were done either by a conjugate gradient algorithm[236] or by the quasi-Newton method.[237] For relaxations involving change of the supercell volume, the procedure was repeated until convergence occurred in a single ionic step, so as to minimize the effect of Pulay stress.[238]

Energy barriers

Nudged elastic band (NEB) calculations[239] were used to estimate energy barriers for diffusion, such as the transitions between cation configurations in BN and SN (Chapter 4), and for ferroelastic switching in PN (Chapter 6). The NEB method considers several intermediate "images" between the start and end points of the transition, and searches for the minimum energy path (MEP) between the end points by simultaneously optimizing the images along the transition path. Each image is constrained with respect to its neighbours by "spring forces" acting between the images. In cases where the transition path was simple and more or less symmetric,

the climbing image NEB (CINEB) method[240,241] was used. This is a variation on standard NEB in which the highest-energy image along the path (the middle image for a simple, symmetric path with one maximum) is brought to an energy maximum, which therefore converges to the exact saddle point and finds the correct transition barrier. The atomic positions for each image are relaxed until the forces on the ions are less than a certain force-based criterion[242] (typical criteria used for 90-atom cells were 0.05 eV $Å^{-1}$ for single-atom diffusion and 0.3 eV $Å^{-1}$ for ferroelastic switching). Reference calculations for ferroelastic switching were also performed for the simple perovskite $PbTiO_3$. In this case, the climbing image variation of the generalized solid-state NEB (SSNEB) method[243] was used in addition to standard CINEB. In SSNEB, both the atomic positions and the lattice parameters are optimized along the MEP, while subjected to spring forces between the images as in regular CINEB.

Electronic structure

Atom-resolved densities of states (DOSes) were calculated by projecting the total DOS onto atom-centered spherical regions with volumes equal to the Bader volumes[244–246] (referred to as "Bader spheres" in what follows). Projection in Bader spheres was done to ensure that the atom-resolved DOSes sum to the total DOS as closely as possible, which is not necessarily the case when projecting onto the PAW spheres or spherical regions determined by tabulated ionic radii.* This scheme also makes it possible to use different radii for the same cation on the A1 and A2 sites in the TTB structure, which have different coordination numbers and therefore different radii. Atomic charges were determined by the actual Bader analysis, where atomic charges are determined by integration of the charge density inside the non-spherical Bader volumes.[246] Spontaneous polarization was calculated by the Berry phase method[209,210] as implemented in VASP. Finally, the Born effective charge (BEC) tensor[221] was obtained using the linear response routines in VASP,[248] which is an implementation of density functional perturbation theory.[249]

Lattice dynamics

Phonon calculations were performed by the finite displacement method as implemented in the PHONOPY code,[204,250] with displacements of 0.01 Å used for calculation of the force constants. Unstable modes in high-symmetry structures were manifested

*Projection of DOSes directly onto the non-spherical, space-filling Bader regions can in principle produce atom-resolved DOSes that sum exactly to the total DOS.[247] However, this is a non-standard feature in VASP, and introduces possible ambiguity if orbital-resolved DOSes are created by further projection onto spherical harmonics.

as phonons with imaginary frequency. To obtain the dynamically stable ground state when starting from high-symmetry structures, the unstable modes were "followed" by systematically displacing atoms along the mode eigenvector (hereafter referred to as "freezing in" the mode), and relaxing the structure again until no further instabilities were found.[196,208,251]

3.2 Experimental work

Powder synthesis and sintering of dense ceramics

Lead metaniobate with TTB structure (Chapter 6) was synthesized by dissolving PbO (99.999 %, this and all other chemicals from Sigma-Aldrich) in nitric acid and mixing in stoichiometric amounts of Nb_2O_5 (99.99 %). 2 mol % $CaTiO_3$ [in the form of stoichiometric amounts of $CaCO_3$ (99.95 %) and TiO_2 (anatase, 99.8 %)] was added to the slurry in order to stabilize the TTB phase with respect to the rhombohedral phase.[7] The slurry was dried under reduced pressure in a rotavapor, and the powder heated to 400 °C at a rate of 25 °C h^{-1} and held at this temperature for 2 hours in order to decompose nitrates. The resulting oxide powder was pressed into 25 mm pellets and fired twice at 850 °C for 2 hours, with crushing and re-pressing between the firings. After this, the powder was ball-milled in ethanol with 5 mm ZrO_2 balls for 15 hours, and finally fired at 1250 °C for 1 hour to obtain phase-pure ferroelectric lead metaniobate. The main reaction is

$$5\,PbO + 5\,Nb_2O_5 \longrightarrow Pb_5Nb_{10}O_{30},$$

and the added $CaTiO_3$ is incorporated into the structure as a solid solution:

$$\left(1 - \frac{x}{5}\right) Pb_5\square Nb_{10}O_{30} + 2x CaTiO_3 \longrightarrow Pb_{5-x}Ca_{2x}\square_{1-x}\,Nb_{10-2x}Ti_{2x}O_{30},$$

where □ explicitly denotes a vacant A1/A2 position. A doping level of 2 mol %, corresponding to $x = 0.01$ in the above equation, gives a nominal stoichiometry of $Pb_{4.99}Ca_{0.02}Nb_{9.98}Ti_{0.02}O_{30}$ for the powder sample. Acceptor doping on the B1/B2 sites is charge compensated by cation excess on the A1/A2 sites, with a total A-site cation occupancy of 5.01 at the given doping level. It can be noted that the solubility limit for $CaTiO_3$ in TTB-PN is at least ten times higher than this.[7]

Powders of lead metaniobate with rhombohedral structure, Chapter 9, were prepared by conventional solid-state synthesis. PbO (99.999 %) and Nb_2O_5 (99.99 %) powders were mixed in equimolar amounts with a mortar and pestle, uniaxially pressed into 25 mm pellets and fired at 850 °C for 2 hours in a sealed alumina crucible.

The pellets were crushed down, and pressing and firing was repeated twice, for a total of three 2-hour firings at 850 °C. The sample was finally crushed to a powder and annealed for 30 minutes at 550 °C prior to structural analysis in order to remove possible strain from the crushing.

Dense ceramic samples of r-PN were prepared for dielectric impedance spectroscopy and dilatometry (Chapter 9). Fine-grained r-PN powder was first prepared by a solid state reaction as described above, where a single calcination step at 850 °C (2 hours) was performed, followed by ball milling in ethanol with 5 mm ZrO_2 balls for 100 hours and sieving the powder to 250 µm. A 10 mm pellet was uniaxially pressed at 30 MPa and cold-isostatically pressed at 2 kbar before sintering at 1140 °C for one hour in a sealed alumina crucible with sacrificial PN powder. The final density was 92 % of the theoretical value. A 5 mm cylindrical pellet was prepared in the same way for dilatometry, with similar final density.

Diffraction and structure refinement

Room temperature powder X-ray diffraction (XRD) was performed with a Siemens D5005 diffractometer set up in Bragg–Brentano geometry with θ–2θ scan mode. Cu $K\alpha_1$ X-rays (λ = 1.5406 Å) were provided from a primary graphite monochromator, and data were collected with a Braun position sensitive detector (PSD) scanning a 2θ range of 5°–110° with a step size of 0.015°. For TTB-PN, Chapter 6, a series of 12 two-hour scans were collected, and merged using the Bruker AXS Eva software suite prior to structural refinement. For r-PN, Chapter 9, a single scan was collected over 24 hours.

Powder neutron diffraction data were collected at room temperature with the PUS diffractometer installed at the JEEP II reactor at Institute for Energy Technology in Kjeller, Norway.[252] Two separate experiments were performed, on TTB-PN (Chapter 6) and r-PN (Chapter 9). Neutrons were provided from a vertically focusing Ge monochromator, with wavelengths of 1.5537 Å and 1.5555 Å, respectively, for the two experiments. Data were collected in a 2θ range of 10°–130° in steps of 0.05° with two detector banks, each with 6 horizontally stacked ^{3}He-filled PSD tubes covering a 2θ range of 20°.

High-temperature XRD (HTXRD) was performed with a Bruker AXS D8 Advance equipped with a high-temperature stage. The instrument was set up in Bragg–Brentano geometry with θ–θ scan mode, using Cu $K\alpha$ radiation and a Våntec-1 PSD. The HTXRD experiments on TTB-PN (Chapter 6) were performed at temperatures up to 700 °C, with heating provided from a radiant heater surrounding the alumina sample holder. The 2θ range was 20°–75° with a step size of 0.015°. Two separate HTXRD experiments were performed on r-PN (Chapter 9). The first used a radiant

heater to reach temperatures up to 850 °C with the same parameters as above, while the second experiment covered temperatures up to 1100 °C. In the latter, the powdered sample was dispersed in ethanol and spread out on a platinum (Pt) strip which was directly heated by an electric current. A 2θ range of 10°–90° was covered in steps of 0.015° in the Pt heater experiment.

The HTXRD temperatures were calibrated by recording diffractograms of powdered α-Al_2O_3 (corundum) over the same temperature ranges as in the main experiments, and extracting the lattice parameters for corundum by the Pawley method. Polynomial expressions for the lattice parameters of corundum as a function of temperature, given in ref. [253], were inverted in order to provide the temperature as a function of the lattice parameters. In this way, each HTXRD scan of corundum gave two calculated temperatures, one from each of the a and c lattice parameters, and the average value was used as the "real" temperature. The nominal and real temperatures were correlated through a second-order polynomial expression, which was finally used to correct the nominal temperatures in each HTXRD experiment.

Rietveld refinements were done with the Bruker AXS Topas 4.2 and Topas 5 software packages. The background intensity was fitted to a Chebychev polynomial of minimal degreee, and peak shapes were fitted to Pearson type VII (X-ray data) or Thompson–Cox–Hastings pseudo-Voigt profiles (neutron data). Lattice parameters and atomic positions were refined according to the atomic degrees of freedom dictated by the space group symmetry. Thermal displacement factors were refined isotropically. Structural data used as starting point for the refinements were taken from literature, and are given in Appendix B. For the HTXRD experiments on TTB-PN and r-PN, lattice parameters were obtained by Pawley fitting, without doing a full Rietveld refinement of the crystal structure.

Dielectric characterisation

The dense r-PN ceramic pellet was grinded with #1200 SiC paper down to a thickness of 0.92 mm, while ensuring that the top and bottom surfaces were parallel. The sample was cleaned in an ultrasonic bath with ethanol for 15 minutes, and electroded with platinum ink (Metalor Technologies UK Ltd, United Kingdom) which was dried at 120 °C. The dielectric characterisation was performed with a Novocontrol Alpha-A impedance analyser (Novocontrol Technologies GmbH, Germany). The sample was mounted in a Probostat sample cell (Norecs AS, Norway) configured in 2-electrode 4-wire setup and connected to the analyzer mainframe via a Novocontrol ZG4 test interface. The sample cell was heated to 1000 °C in a vertical tubular furnace at a rate of 2 °C min^{-1}, with a small flow of synthetic air through the cell during measurements. The dielectric response was measured at an AC field amplitude of 1 V.

Thermal analysis

Thermal expansion of a sintered r-PN ceramic was measured up to 900 °C with a Netzsch DIL 402C dilatometer (Netzsch-Gerätebau GmbH, Germany) with heating and cooling rates of 5 °C min^{-1} and a small flow of synthetic air during measurements. An alumina standard (Netzsch) was used for calibration. Differential thermal analysis (DTA) of an r-PN powder sample was performed with a Netzsch STA 449 C *Jupiter* thermal analyzer using the same temperature program as the dilatometric study.

4 Energetics of cation ordering in unfilled TTBs

The content of this chapter is based on ref. [254].

4.1 Results

Configurational energy landscape

An analysis is made of the different orderings possible in $A\mathrm{Nb_2O_6}$-type tungsten-bronzes. Starting with a single unit cell containing 45 atoms (5 formula units of $A\mathrm{Nb_2O_6}$), there are 6 sites among which to distribute 5 cations (or, equivalently and more convenient, six sites among which to distribute 1 vacancy). The four pentagonal (P) sites are equivalent, as are also the two square (S) sites, see Figure 4.1(a), so for a single unit cell, there are only two unique configurations.

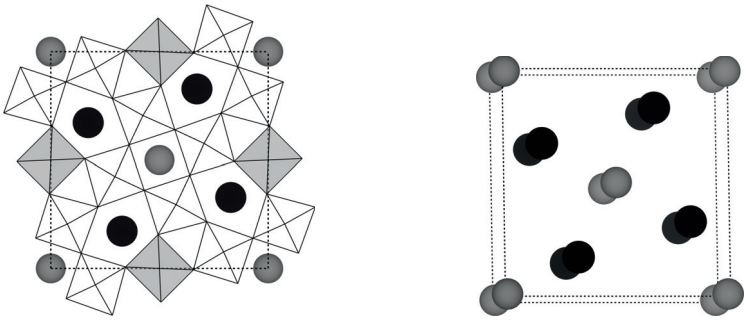

(a) (b)

Figure 4.1 — (a) Projection along the *c* axis of the tetragonal tungsten-bronze unit cell in the *P*4/*mbm* aristotype. The A1 and A2 sites are represented by grey and black spheres, respectively, while the B1 and B2 sites are shown as grey and white octahedra. (b) Supercell with a doubled *c* axis, showing only the A1 and A2 sites with the same colors as in (a).

A more realistic approach is to look at the possible configurations in a $1 \times 1 \times 2$ *supercell*, by doubling the unit cell along *c*. In such a cell, there are a total of 12 A-sites (pentagonal and square), as shown in Figure 4.1(b). Among these 12 sites, there are 10 atoms and 2 vacancies to be distributed. Focusing on the distribution of vacancies, the possible configurations can be counted and named according to the following scheme:

- The two vacancies can be distributed between square and pentagonal sites in three ways: Both pentagonal (PP), both square (SS), or one of each (SP).
- If the first vacancy is located on a square site, there are three possible ways to place the second vacancy on another square site: On the other square site in the same layer; diagonally in the layer above; or directly above the first. Hence, there are three SS configurations.
- If the first vacancy is located on a pentagonal site, there are five possible ways to place the second vacancy on another pentagonal site: Two in the same layer (next to the first or diagonally opposite from it); the same two positions in the layer above; or directly above the first. Hence, there are five PP configurations.
- If the first vacancy is located on a square site and the second on a pentagonal, they can either be in the same layer, or in different layers. Hence, there are two SP configurations.
- A triplet [*hkl*] is used to describe the (approximate) vector between the two vacancies. For example, two pentagonal vacancies within the same layer can be designated as PP[100] or PP[110] configurations, depending on whether the vacancies are "nearest neighbours" within the unit cell, or diagonally opposite from each other, respectively.

This scheme leads to a total of 10 unique configurations for each composition. These are summarized in Table 4.1, which gives the systematic name for each configuration, and the local space group symmetry arising from the cation ordering.[255] As the table shows, the five PP configurations lead to local orthorhombic space group symmetries, the three SS configurations preserve the tetragonal symmetry (with SS[110] even preserving the aristotype space group $P4/mbm$), and the two SP configurations lead to local monoclinic symmetry. The 10 configurations for a $1\times1\times2$ supercell also include the two configurations possible for a single unit cell: PP[001] is identical to a single unit cell with the vacancy on a pentagonal site, while SS[001] is identical to a single unit cell with the vacancy on a square site. The scheme can in principle be extended to even larger supercells, such as $1\times1\times3$ or $1\times1\times4$. The $1\times1\times2$ cell employed here leads to a manageable number of configurations and good computational efficiency.

The total energy of BN, SN and PN in all 10 configurations considered above is shown in Figure 4.2. Both the energy of the initial structures, and the energy after optimisation of atomic positions and lattice parameters, are shown. The two configurations that correspond to a single unit cell, PP[001] and SS[001], are the least energetically favourable among the initial structures, and for all three compounds, it

Table 4.1 — The 10 cation configurations possible for the $1\times1\times2$ supercell considered in this chapter, showing the systematic name, local space group symmetry, and a sketch of the configuration (cations represented by grey spheres, vacant sites white).

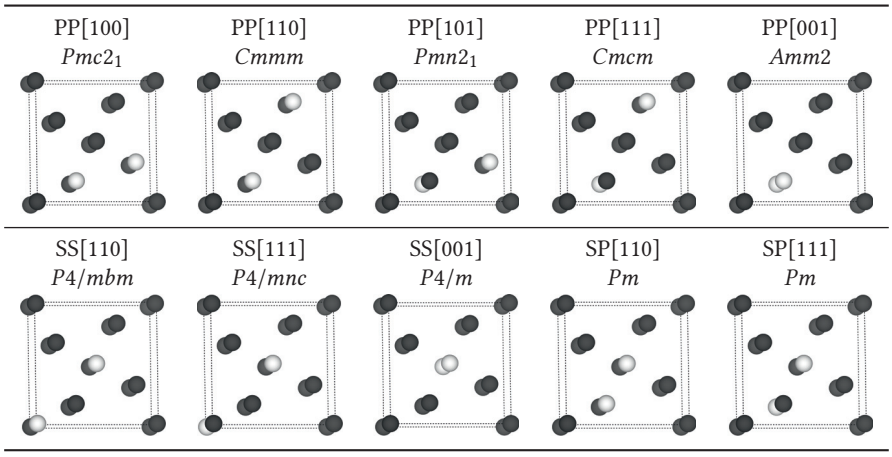

is one of these two configurations that has the highest energy initially. The relative energies of the configurations change, however, when ionic relaxation is taken into account. Especially for BN, the initial configurations of highest energy are the ones that gain most by relaxation, giving an overall energy landscape which is quite flat. Subsequent relaxation of the unit cell volume and change of lattice parameters does not contribute as much, as the main energy gain lies in the relaxation of the atomic positions.

For SN and PN, the energy landscape is not quite as flat as for BN, although for both compounds there are several configurations that are very close in energy. The effect of volume relaxation is even lower for SN and PN than for BN, contributing very little to the total energy gain upon optimization of the structure. The effect of ionic relaxation is significant, making the total energy gain larger, at the most around 3.8 eV. The energy for the fully relaxed structures is summarized in Figure 4.3(a), where dashed lines mark the range of energies for each composition. In general, there is no single configuration, or a few configurations, that stand out as significantly more plausible than the others for any of the three compounds.

The change in the unit cell volume following the relaxation of lattice parameters is shown in Figure 4.3(b). The volume change is positive in almost all cases, and as large as up to 2 % with respect to the initial volumes. Some trends are evident: For BN, the expansion is largest for the PP configurations, where Ba^{2+} completely

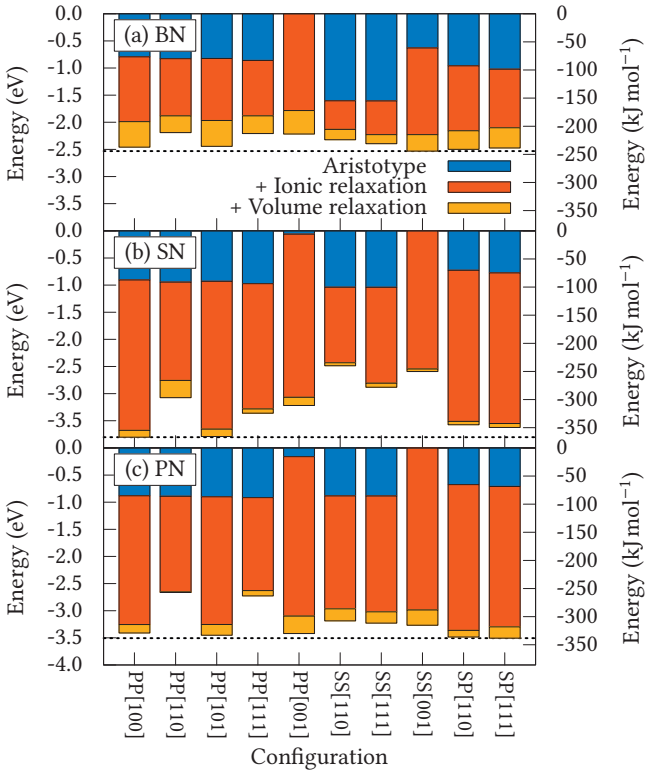

Figure 4.2 — Relative energy per unit cell ($A_5B_{10}O_{30}$) of the different configurations for (a) BN, (b) SN and (c) PN. The blue bars labeled "Aristotype" show the energies of the intial structures, with space group symmetry as described in Table 4.1. The red and yellow bars show the additional energy contribution from relaxation of atomic positions and unit cell volume, respectively. The zero level is set at the highest initial energy for each composition (configurations PP[001] or SS[001]).

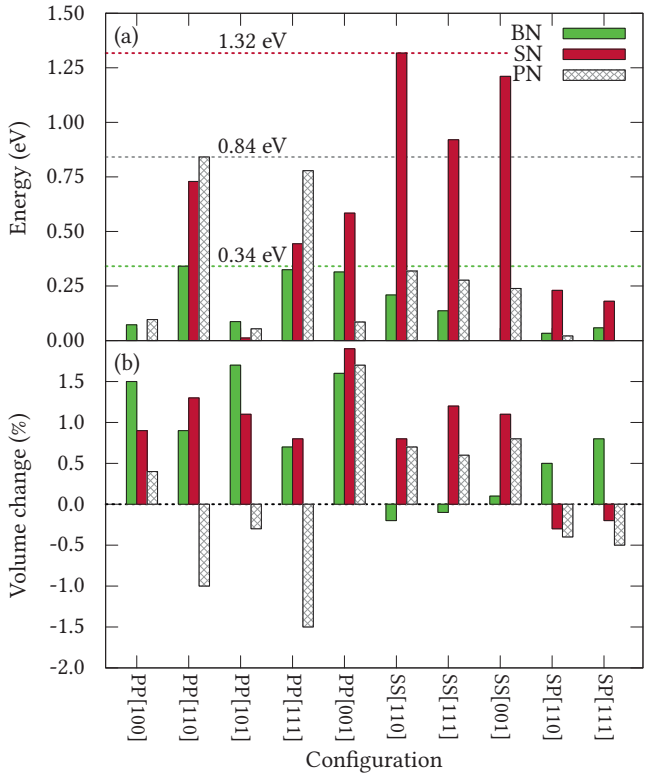

Figure 4.3 — (a) Relative energy per unit cell ($A_5B_{10}O_{30}$) of the fully relaxed structures, corresponding to the total energy shown in Figure 4.2. The lowest-energy structure is used as reference state for each compound (SS[001] for BN, PP[100] for SN and SP[111] for PN). Dashed lines mark the highest-energy configuration for each composition. (b) Volume change corresponding to the relaxed structures in (a), showing the difference in unit cell expansion associated with different cation configurations.

occupies the narrow square channels, and smaller and slightly negative for the SS configurations. This is as expected, as the large Ba^{2+} cations preferentially occupy pentagonal sites, and will expand the lattice if forced into the smaller square sites. A closer inspection of the lattice parameters shows that the volume change for BN comes from an expansion of the a and b parameters, and a contraction of c with respect to the initial values. Also for SN and PN, the a and b parameters mostly expand (the sole exception being PP[110] for PN, where they slightly contract), while the c parameter either expands or contracts.

Thermodynamic model

To gain further insight into the possibility of cation ordering, a thermodynamic model is developed. The model is an extension of the thermodynamic model devised by O'Neill and Navrotsky for the cation distribution in spinels.[256] The fundamental assumption, introduced by Schmalzried[257] and elaborated by Navrotsky and Kleppa,[258] is that the interchange of cations between two distinct sublattices can be viewed as a chemical equilibrium:

$$[Av](A_4)\mathrm{Nb_{10}O_{30}} \rightleftharpoons [A_{1+x}v_{1-x}](A_{4-x}v_x)\mathrm{Nb_{10}O_{30}}, \tag{4.1}$$

where $[A]$ denotes a cation A on an A1 or square site, and (A) denotes a cation A on an A2 or pentagonal site. A cation vacancy is denoted by v.* This introduces an interchange parameter, x, which ranges from 0 (all vacancies on square sites, i.e., SS configurations) to 1 (all vacancies on pentagonal sites, i.e., PP configurations). It is then assumed that the free energy of the cation interchange reaction (4.1) can be expressed as

$$\Delta G_{\mathrm{int}}(x) = \alpha x + \beta x^2 + RT \sum_s b_s \sum_i y_{i,s} \ln y_{i,s}, \tag{4.2}$$

where the last term on the right side is recognized as the entropy of mixing for an ideal solution, with $y_{i,s}$ being the fractional occupancy of species i on site s, and b_s the multiplicity of site s. This is a purely configurational entropy contribution, *i.e.*, it is assumed that all other entropy changes following reaction (4.1) are negligible. The enthalpy consists of two terms, one linear and one quadratic in the interchange parameter x, as was proposed by O'Neill and Navrotsky[256] as an extension of the original model by Navrotsky and Kleppa.[258] Effects of volume and non-configurational

*The use of lowercase v and i for vacancies and interstitials, respectively, is recommended in Norby's Kröger–Vink-compatible defect chemistry notation[259] in order to avoid ambiguous and/or hilarious situations when describing the defect chemistry of vanadium or iodine compounds such as VI_3. The same convention is used here.

entropy are neglected, and all configurations with same value of x are — for now — assumed to be degenerate. Differentiation of the entropy part shows that maximal configurational entropy is obtained for $x = 2/3$, in analogy to AB_2O_4 spinels, which also have a maximal configurational entropy for $x = 2/3$ when x is the fraction of B cations on tetrahedral sites (this is referred to as a random spinel). Continuing from (4.2), the entropy part can be written out as follows:

$$\begin{aligned}\Delta S_{\text{int}}(x) &= -R \sum_s b_s \sum_i y_{i,s} \ln y_{i,s} \\ &= -R \left\{ 2 \left[\frac{1+x}{2} \ln \frac{1+x}{2} + \frac{1-x}{2} \ln \frac{1-x}{2} \right] + 4 \left[\frac{4-x}{4} \ln \frac{4-x}{4} + \frac{x}{4} \ln \frac{x}{4} \right] \right\}\end{aligned} \tag{4.3}$$

Differentiation of (4.3) gives

$$\frac{\partial \Delta S_{\text{int}}}{\partial x} = -R \ln \frac{(1+x)x}{(1-x)(4-x)}. \tag{4.4}$$

For equilibrium conditions,

$$\frac{\partial \Delta G_{\text{int}}}{\partial x} = 0, \tag{4.5}$$

which, using the above result for the entropy part, evaluates to

$$\alpha + 2\beta x + RT \ln \frac{(1+x)x}{(1-x)(4-x)} = 0, \tag{4.6}$$

or, when rearranged:

$$\ln K = \ln \frac{x(1+x)}{(1-x)(4-x)} = -\frac{\alpha + 2\beta x}{RT}. \tag{4.7}$$

K in (4.7) can be recognized as the equilibrium constant for the simplified cation exchange reaction $[v]$ + (A) $\rightleftharpoons$ (v) + [A], using the same notation as in (4.1). Equation (4.7) gives the relation between temperature and degree of inversion once the enthalpy coefficients α and β are determined. This can be done experimentally by determining x from refinement of diffraction data at different T, given that it is possible to obtain data of sufficiently high quality at temperatures where the cation mobility is appreciable. Alternatively, as is done here, the parameters α and β can be determined by calculating the enthalpy term in (4.2) from first principles for cation configurations with different x.

As stated above, the thermodynamic model does not directly take into consideration the energy differences between configurations with the same value of the cation

interchange parameter x. In an attempt to meet this problem, the enthalpic part of Equation (4.2) was fitted to Boltzmann averages of the energies for each x:

$$\langle E \rangle(T) = \frac{\sum_n E_n e^{-E_n/k_B T}}{\sum_n e^{-E_n/k_B T}}, \tag{4.8}$$

where E_n is the energy of configuration n, and the sums are over configurations with the same value of x (i.e., the PP, SS and SP configurations are averaged separately). In this way, at zero kelvin the energies are identical to the single lowest energy for each x, while at finite temperatures there is also a contribution to the energy from population of configurations with higher energy. Fitting the energies of the fully relaxed structures to Equation (4.2) as described above leads to the plot shown in Figure 4.4(a). As is evident from this plot, the energies for each x spread out significantly, especially for the PP cases ($x = 1.0$), as was also seen in Figure 4.3a. Fits to Equation (4.2) for $T = 0$ K and $T = 1800$ K are both shown in Figure 4.4(a), in order to get an impression of how much the higher-energy configurations contribute for each x at finite temperatures. In general, this contribution is small, and α and β show very little variation with temperature.

The entropic part of (4.2) is purely configurational, and is shown in Figure 4.4(b). For comparison, the configurational entropy of a simple spinel is also given, and both are normalized with respect to the number of sites in the structure. It is noteworthy that both the spinel and the tungsten-bronze-type structure show a maximal configurational entropy for $x = 2/3$ with the definitions of x used here, which is therefore predicted to be the high-temperature limit of x in both structure types. However, the difference between maximum and minimum configurational entropy is almost three times larger for spinel than for the TTB structure. This is justified by the fact that a normal spinel ($x = 0$) can be defined as having zero configurational entropy, as both sublattices are fully occupied by only one cation. For the TTB structure, on the other hand, there is always a mixed occupancy between cations and vacancies on at least one of the sublattices, and so the configurational entropy is never zero. This means that there is less driving force for disordering in the TTB structure than in spinels, and that enthalpic effects can be expected to dominate the tungsten-bronze-type oxides also at higher temperatures.

Using α and β obtained above, the degree of cation interchange, x in (4.1), can be calculated as a function of temperature. The result is plotted in Figure 4.5, which also gives the temperature dependence of α and β (inset panel). For BN, both α and β are very small, which means that entropy is the main factor that governs the degree of cation inversion. BN therefore has a prominent temperature dependency, while both PN and SN, which have much more distinct minima in enthalpy [Figure 4.4(a)],

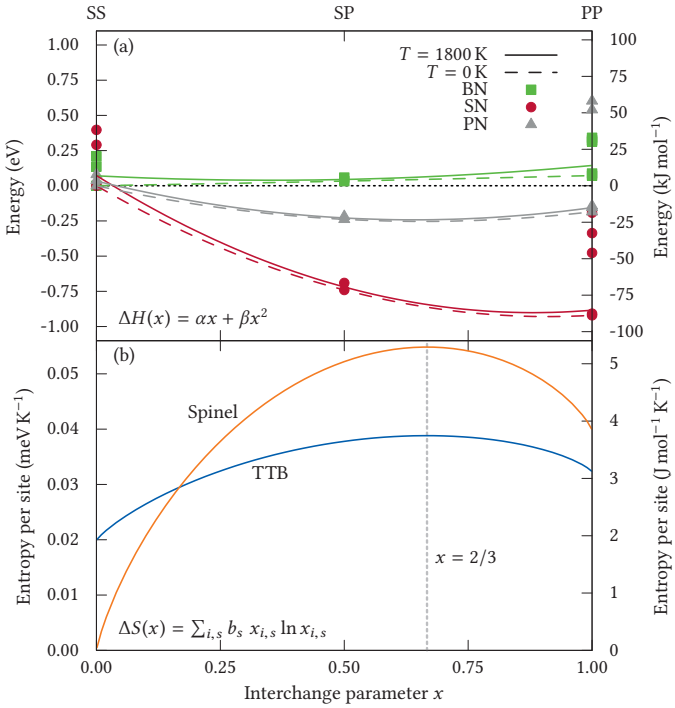

Figure 4.4 — (a) Total energies (points) plotted against the interchange parameter x as defined in reaction (4.1). $x = 0$ corresponds to the three SS configurations, $x = 0.5$ to the two SP, and $x = 1$ to the five PP configurations. Energy given in eV per unit cell, corresponding to reaction (4.1), with the lowest energy configuration at $x = 0$ used as reference. Lines show fits to the enthalpic part of Equation (4.2), where dashed lines represent zero temperature (only the lowest energy for each x is used) and dashed lines represent $T = 1800$ K through a Boltzmann average of the energies for each x. (b) Configurational entropy as a function of the degree of inversion for the TTB structure considered in this work, compared to the configurational entropy of a simple spinel. Values are normalized per site (three for spinel and six for TTB), to make it possible to compare the entropy between two structures with different stoichiometry. In both structures, maximal configurational entropy occurs at $x = 2/3$.

show only a weak dependency of x on temperature (Figure 4.5). As is also the case for spinels,[256] α and β are of similar magnitude, but with opposite sign (inset of Figure 4.5).

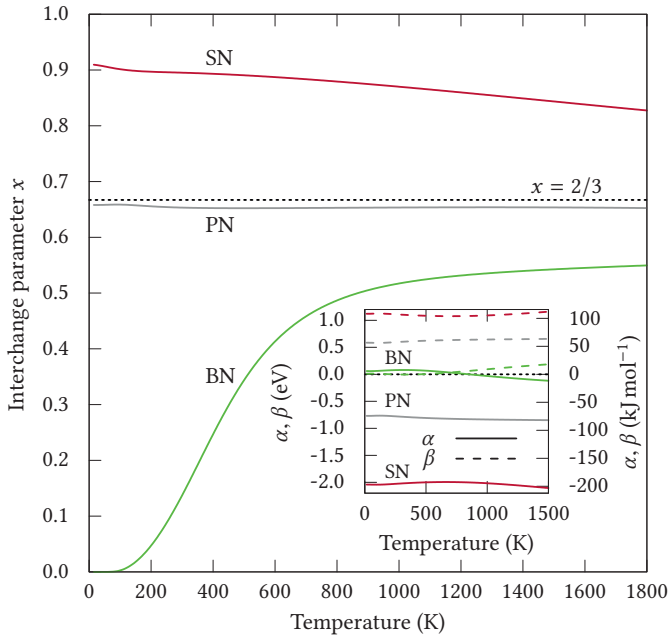

Figure 4.5 — Degree of cation interchange as a function of temperature for BN, SN and PN, calculated from Equation (4.7). The high-temperature limit $x = 2/3$, corresponding to maximal configurational entropy, is marked with a dotted black line. Inset plot shows the temperature dependency of the fitting parameters α (solid lines) and β (dashed).

Transition barriers

Due to the similarity in energetic stability between the different configurations, the energy barriers for transitions between some of these configurations were calculated in order to get an impression of how the configurations compare also kinetically. Two cases were considered, namely diffusion of A^{2+} cations in the two different types of

channels in the structure. To visualize these cases, the unit cell is shown again in Figure 4.6(a) (left panel) together with an alternative view emphasizing the pentagonal and square channels (right panel). Figure 4.6(b) shows a perspective view of the channel shapes, with grey and black arrows showing the diffusion paths through the square and pentagonal channels, respectively. Figure 4.6(c) shows the minimum energy path (MEP) for these two diffusion processes, where the end configurations are the PP[100] and PP[101] configurations for the pentagonal channel case, and SS[110] and SS[111] for the square channel case. As expected, the energy maximum midway along the path is higher for the square channel than for the pentagonal channel, as the square channels are narrower. In Figure 4.6(d), the height of the energy barriers are compared for the two cases in all three compositions, and the larger size of Ba^{2+} relative to Sr^{2+} and Pb^{2+} is again manifested in the increased transition barrier. The height of the barriers is significant, and dominates over the energy differences between the start and end points, as demonstrated in Figure 4.6(a).

4.2 Discussion

Possibility of cation ordering in TTBs

As Figure 4.3(a) shows, the energy differences between different cation configurations are quite small, with a maximal difference of 1.32 eV per unit cell (0.263 eV or 25.4 kJ mol^{-1} per formula unit) for fully relaxed SN, and less for the other compositions. This is somewhat unexpected, as Ba^{2+} is significantly larger than Sr^{2+} and Pb^{2+}, so especially the PP configurations, with more cations in the narrow square channels, would be expected to lie high in energy for BN. This is the case for the initial structures [blue bars in Figures 4.2(a) to (c)], where two of the SS configurations have a much lower energy than the others, as expected from atomic size considerations. After relaxation of the structure is taken into account, the energy landscape is relatively flat, with energy differences smaller for BN than for both SN and PN. The main contribution to this energy landscape flattening comes from the ionic movements [red bars in Figures 4.2(a) to (c)], and only to a lesser extent from volume change (yellow bars). Although the energetic contribution from volume change is larger for BN than for SN and PN, the volume change itself is not systematically larger for BN, as seen in Figure 4.3(b).

The flatness of the energy landscape, particularly for BN, is striking, see Figure 4.2. This difference in behaviour of BN relative to SN and PN can be rationalized from the relative size of the cations and the coordination environment inside the channels. The square channels are formally 12-coordinated and similar to the A-sites in ABO_3 perovskites. The pentagonal channels are formally 15-coordinated, although

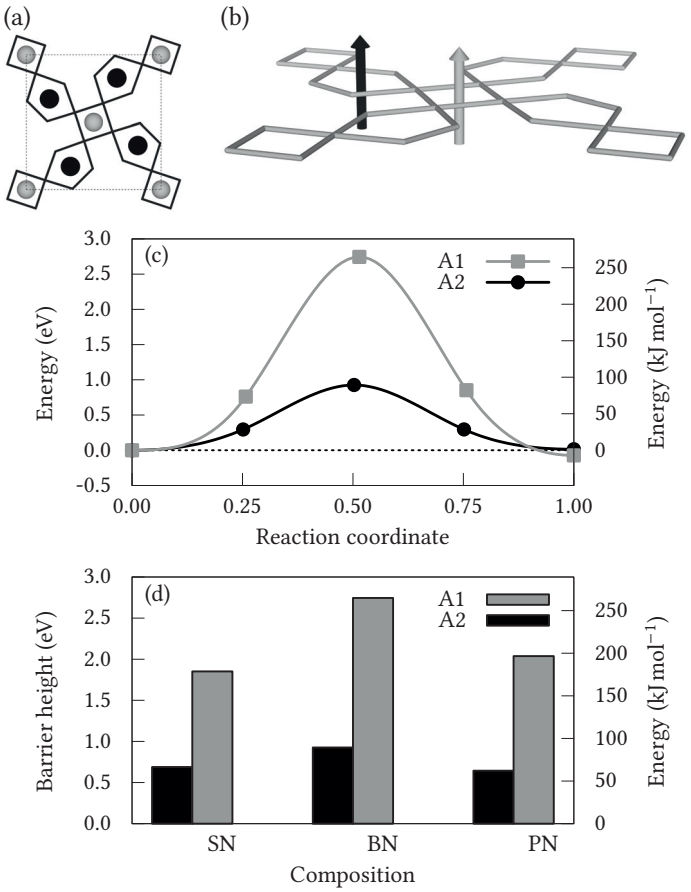

Figure 4.6 — (a) Projection of TTB unit cell along *c*, highlighting the shape of the channels considered for diffusion. (b) Perspective view of diffusion paths through the A1 (grey arrow) and A2 (black arrow) channels. (c) Minimum energy paths (MEPs) for cation diffusion through square (A1) and pentagonal (A2) channels in BN. The square channel diffusion is represented by the transition SS[110] to SS[111], while the pentagonal channel is represented by PP[100] to PP[101]. The dashed line marks the energy of the initial configuration in the diffusion process. (d) Comparison of the barrier heights for the MEPs for all three compositions.

in practice both the square and pentagonal coordination polyhedra are to some degree distorted and the effective coordination number is therefore less than the formal value. This distortion of A-site coordination polyhedra happens to a larger degree for Sr^{2+} and less for Ba^{2+}, since Sr^{2+} is significantly smaller than Ba^{2+} (ionic radii of 1.58 Å and 1.74 Å, respectively, when extrapolating Shannon values[128] to CN = 15). Sr^{2+} therefore has higher ability to shift towards an off-centered position in the channel, thus obtaining a smaller effective coordination number than Ba^{2+}. This enhanced ability to off-center and distort the structure enables the SN configurations to relax further towards their local energy minima than BN, where full relaxation is partially restricted by the large Ba^{2+} ions. In the case of Pb^{2+}, additional contributions may result from covalent bonding between Pb and O.

Although the energy differences shown in Figure 4.3(a) are small, the transition barriers between configurations are large, on the order of 1.0 to 2.5 eV. This is far above the thermal energy at synthesis conditions, which is on the order of 0.1 to 0.2 eV. In this work, only transitions corresponding to diffusion within the square or pentagonal channels have been considered, i.e., transitions that do not change the value of x. It is expected that since the channel cross-sections are larger than the openings between the channels, transitions that change x will have even higher barriers than those investigated at present.

Although these zero-kelvin DFT calculations indicate that the structure is not able to explore its entire configurational space, the situation might be very different at higher temperatures. During cooling from synthesis temperatures of typically 1300 to 1400 °C, it is possible that certain configurations are "frozen in" and persist to lower temperatures, where the different local space group symmetries (some of which are polar, cf. Table 4.1) can aid in the nucleation of the ferroelectric phase. This is similar to the scheme suggested for the lead-free perovskite relaxors studied by Gröting *et al.*,[86] where it was concluded that the small energy differences between different A-site configurations are not sufficient to create long-range order, but that short-range ordering may still be possible. Locally ordered regions that freeze in at high temperature in the paraelectric state, will most likely influence the nature of the ferroelectric ground state. For example, the relatively flat energy landscape predicted for BN might allow more of a long-range cooperativity in the ferroelectric phase, while the larger energetic differences between configurations of SN could lead to less long-range ordering in the ferroelectric state. This could in turn be an explanation for the tendency for SBN materials to become more relaxor-like for Sr-rich compositions. For PN, although more similar to SN in terms of energetics and cation radius, it is expected that the stereochemically active $6s^2$ lone pair on Pb^{2+} plays a significant role in the ferroelectric transition, and this might trump the contribution from energetics which would otherwise have made the material more similar to SN.

The volume change shown in Figure 4.3(b) is, in effect, the ΔV associated with reaction (4.1). Volume change for order–disorder processes has been addressed previously in the case of spinels.[260] In general, the order–disorder volume $\Delta V = V_{\text{disorder}} - V_{\text{order}}$ for spinels can be positive or negative, but more often positive, and largest (up to 5 %) when the disordering process involves changes in coordination numbers of the cations. Largely normal spinels such as $MgAl_2O_4$ tend to become more inverse with increasing pressure, and it has been observed that this compound disorders more with temperature under high-pressure conditions.[260,261] However, at ambient temperature, high pressure alone has only a negligible effect on the cation distribution,[262] which is also one of the assumptions in the thermodynamic model employed in this work.

Analogy to spinels and adaptation of O'Neill–Navrotsky model

As stated in the introduction, it should be possible to exploit the similarities between TTBs and spinels in the phenomenological analysis of order–disorder processes. A central question in this respect concerns the transferability of the O'Neill–Navrotsky model. First, it is assumed that non-configurational contributions to the entropy of reaction (4.1) are negligible. This works well for the interchange process in spinels, and the same assumption is made here. In addition to the configurational entropy, there could in principle be a contribution from change in vibrational entropy. Since the cation configurations differ with respect to local space group symmetry (Table 4.1), the number of vibrational modes will also be different, with more modes for configurations of lower symmetry. No attempt is made here to explicitly include this presumably small entropy contribution in the thermodynamic model.

Accepting the premise of configurational entropy only, the conceptually most important difference between TTB's and spinels is revealed by the entropy plot shown in Figure 4.4(b): Since at least one of the sublattices in TTB has a mixed occupancy for all x, the configurational entropy is never zero. In other words, there is no value of x for which the structure must necessarily be fully ordered. This is in contrast to spinels, where a normal spinel ($x = 0$) *must* be perfectly ordered, while an inverse spinel ($x = 1$) can be either ordered or disordered, depending on how the A and B cations distribute over the octahedral sites (the latter is not given by the value of x). Even a "random" spinel ($x = 2/3$) can have different degrees of order, even though the configurational entropy is at a maximum for this degree of inversion. For TTB's, however, any degree of inversion can have varying degrees of order, so there is no *a priori* reason for $x = 0$ to be defined as the ground state.

In light of the above considerations, it is clear that x in itself is not a measure of the degree of disorder, but should merely be though of as a parameter describing the distribution of cations between two sublattices. Order–disorder can take place on each

of these sublattices. In a spinel, a transition from normal to (partially or completely) inverse, must necessarily be accompanied by disorder, and so it is expected that the parameter α always be positive for spinels. This is indeed found to be the case,[256,263] so the negative values obtained for α for the TTB materials (inset of Figure 4.5) may seem counter-intuitive when compared to α values for spinels. However, once it is realized that reaction (4.1) is not in itself a disordering process, a negative α is not problematic: It merely reflects the fact that a cation interchange from the SS configurations towards the SP (and possibly PP) configurations is energetically favoured — to a large degree for SN; to a somewhat lesser degree for PN; and for BN, the flat energy landscape is reflected in the very small values of α and β.

Turning to the plot of x as a function of temperature (Figure 4.5), the different behaviour of BN, SN and PN can be understood in light of the above considerations. For BN, x increases with temperature, since the lowest-energy configuration at zero temperature has $x = 0$. The contribution from configurational entropy acts to push the structure towards a higher degree of cation interchange at higher temperature, similar to the behaviour of normal spinels. As the energy landscape for BN is so flat, the effect of entropy is large, and x rapidly approaches $2/3$ when the temperature increases. For SN, however, the energy differences between the configurations are much larger, with a pronounced enthalpy minimum at around $x = 0.9$, which does not change significantly with temperature, as shown in Figure 4.4(a). The effect of increased temperature is therefore to push x towards a slightly lower value, giving the behaviour of decreasing x shown for SN in Figure 4.5. PN is intermediate between BN and SN in terms of how deep the enthalpy minimum is (Figure 4.4), but as this minimum is located at around $x = 0.65$, very close to the high-temperature limit of $x = 2/3$, the temperature dependence of x becomes extremely weak for this compound, resulting in the almost flat curve for PN in Figure 4.5.

The use of a thermodynamic model provides a more complete picture of the behaviour of BN, SN and PN at realistic temperatures, as compared to simply calculating the zero-kelvin energy of the different configurations. It should be kept in mind that the transition barriers between configurations are high. The development of x with temperature (Figure 4.5) represents the true equilibrium state, while in reality the relaxation time for cation ordering will increase exponentially upon reduction of temperature, and a certain configuration will eventually freeze in, as has also been shown for spinels.[263] The main finding is that the preferred value of x differs significantly for BN and SN, which is likely connected to the gradual change in dielectric and ferroelectric properties with changing Sr/Ba-ratio in the SBN system. The strong temperature dependence of x for Ba suggests that changes in the cation configuration due to thermal history is most likely to occur at high Ba content.

In this study, only three different values of x have been sampled, namely 0 (the SS

configurations), 0.5 (SP) and 1 (PP), *via* a total of 10 configurations. These are all the possibilities accessible using a $1 \times 1 \times 2$ supercell, while a larger supercell would make it possible to sample more of configurational space (*e.g.*, a $1 \times 1 \times 3$ supercell would give access to configurations with $x = 0.33$ and $x = 0.67$, as well as more configurations with $x = 0$ and $x = 1$). However, already when using a $1 \times 1 \times 2$ supercell, a substantial variation can be seen between the energies for different configurations with the same x, and a sampling of more x values would not necessarily improve significantly on the model. At the same time, an advantage of larger supercells would be to remove artifacts from the periodic boundary conditions. The supercells used here contain two octahedral layers, and therefore have a repeat distance of nearly 8 Å along the shortest dimension (the c axis). Larger cells would be advantageous to eliminate all artificial ordering of vacancies, although it is not known if this contribution is significant. In any case, larger supercells would lead to many more configurations to investigate, and also make each configuration significantly more computationally demanding.

5 Ferroelectric polarization in SBN

The content of this chapter is based on ref. [264].

5.1 Results

Energy landscape including polarization

The initial study of cation order–disorder energetics, Chapter 4 and ref. [254], considered the high-symmetry *paraelectric* structures of $Ba_5Nb_{10}O_{30}$ (BN), $Sr_5Nb_{10}O_{30}$ (SN) and $Pb_5Nb_{10}O_{30}$ (PN). The investigation is now continued for BN and SN with emphasis on the dynamically stable *ground states*, including structural distortions such as ferroelectric polarization and octahedral tilting. The starting point is the relaxed paraelectric structures for BN and SN from Chapter 4, with Figure 5.1 showing again the aristotype TTB cell and the ten cation configurations possible in a $1 \times 1 \times 2$ supercell.

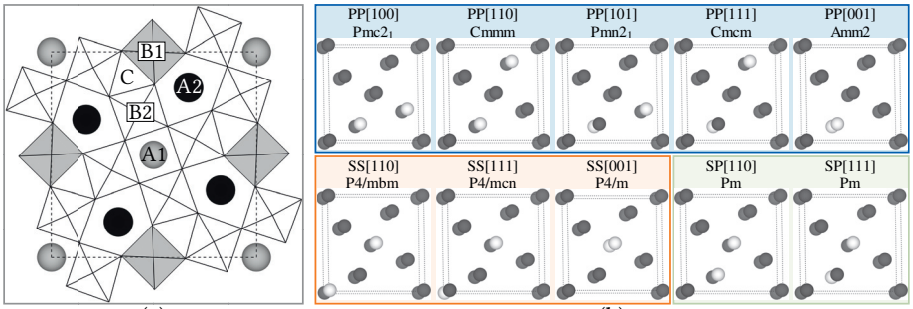

(a) (b)

Figure 5.1 — (a) Aristotype TTB structure, (b) Possible cation configurations for a $1 \times 1 \times 2$ supercell of an unfilled TTB, including local space group symmetry.

Phonon calculations for the paraelectric structures reveal imaginary frequency phonons, corresponding to structural instabilities, for all ten configurations of both BN and SN. The phonon with the highest imaginary frequency is in all cases a polar mode with Γ^- symmetry, corresponding to the displacement pattern illustrated in the left inset of Figure 5.2(a). The mode consists primarily of a cooperative displacement along the tetragonal c direction of all Nb ions relative to the surrounding oxygens in the NbO_6 octahedra. This is a polar mode, similar to the soft mode responsible for the ferroelectric transition in perovskite ferroelectrics, and produces a polarization along

c. Consistent with the imaginary frequency of the mode, the energy is lowered by freezing in the polar mode in all cases. The energy lowering as a function of mode amplitude[265] is shown in Figure 5.2(a) for BN and SN in the SS[001] configuration. A non-polar mode consisting of octahedral tilting around axes in the xy plane [Figure 5.2(a), right inset] is also present in all cases. This mode has a smaller imaginary frequency than the polar mode for both compounds in all configurations. The energy lowering associated with the tilt mode is significantly larger for SN than for BN, as shown in Figure 5.2(a). The tilt mode also lowers the energy more than the polar mode for SN, despite having a lower imaginary frequency. Simultaneous freezing-in of the polar and tilt modes, Figures 5.2(b) and (c), shows that the coupling between the modes is weak for both compounds.

In both compounds, the dynamically stable ground state for each configuration is systematically searched for by freezing in the polar mode, which always has the largest imaginary frequency of the unstable modes, at a mode amplitude close to the energetic minimum. The structures are then relaxed again, allowing the volume and cell parameters to change. After repeating the phonon calculations for the relaxed polar structures, no further instabilities are found in 9 of the 20 cases. In the remaining 11, a second, non-polar instability persists, its eigenvector qualitatively identical to the tilt-mode found in the paraelectric structures. After also freezing in this mode, relaxing the structures and repeating phonon calculations, the stable ground state structure is obtained for all configurations of both compounds. The relative energies of all the configurations are shown in Figures 5.3(a) and (b). The energy landscape is different for the two compounds: The SS[001] configuration has the lowest ground state energy for BN, while for SN the lowest energy is obtained for PP[100]. No single configuration has a substantially lower energy than the others, especially for SN, where PP[101] and SS[111] are particularly close in energy to the lowest-energy configuration. Consistent with the fixed-volume mapping of unstable modes shown in Figure 5.2, the energy relaxation following the polar distortion is more pronounced for BN, while the tilt mode has a larger impact on the ground state energy for SN. For SN there are large energy differences between the paraelectric structures, but the substantial contribution from tilt-mode distortions reduces these differences. The resulting spontaneous polarizations are shown in Figure 5.3(c) and compared to literature data. Several of the paraelectric reference structures have polar space group symmetries [Figure 5.1(b)], but none allow a polarization along z. The polarization reported in Figure 5.3(c) is the component along the tetragonal axis, P_z, which results from freezing in the unstable polar phonon. For the majority of the configurations, BN has a larger P_z compared to the same configuration for SN. 11 of the 20 ground state structures have tilt-mode instabilities, but the polar nature remains in all cases.

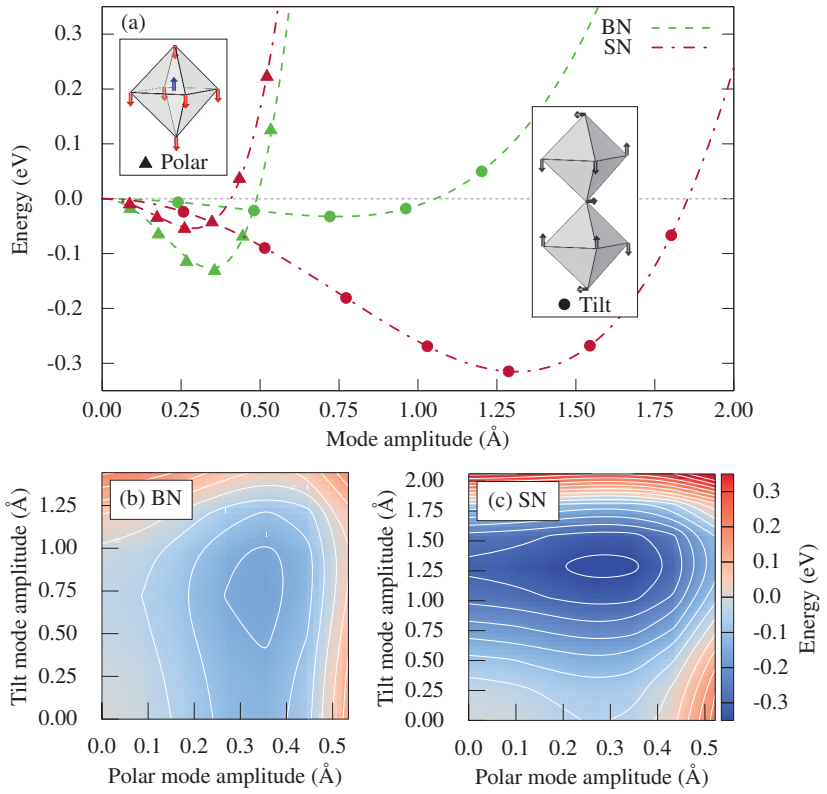

Figure 5.2 — (a) Potential energy curves for BN and SN in the SS[001] configuration, showing energy lowering from freezing in polar and tilt-mode instabilities independently from the paraelectric structure. Points show calculated energies, lines are polynomial fits to $\Delta E = \alpha Q^2 + \beta Q^4$ where Q is the mode amplitude.[265] Insets show the structural distortions associated with the phonons. (b) and (c) Contour plots for BN and SN, respectively, showing the weak coupling between the polarization and tilt modes (SS[001] configuration).

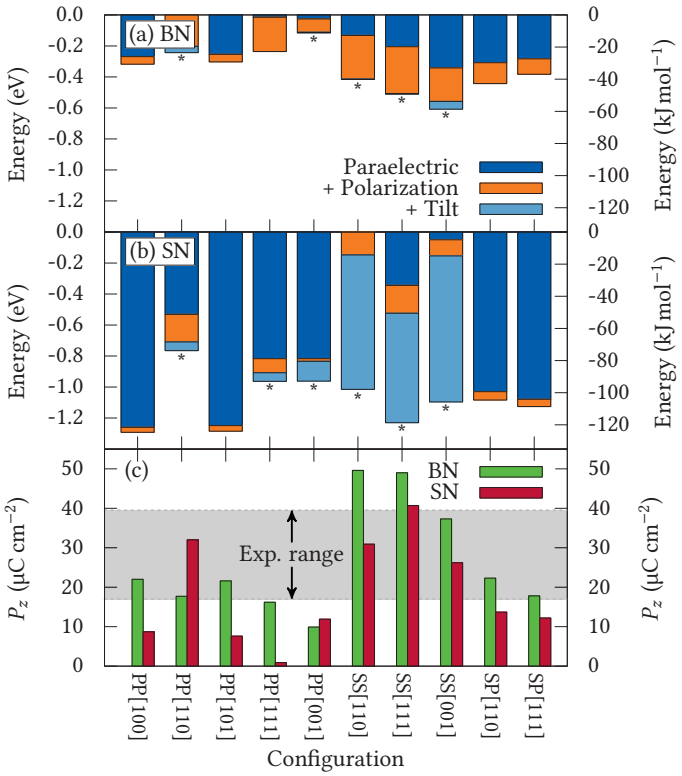

Figure 5.3 — Energy landscape for (a) BN and (b) SN, showing the stepwise energy lowering from freezing in the unstable phonons in sequence. All configurations have a polar instability ("Polarization"), while 11 of 20 (marked with *) have a secondary tilt-mode instability ("Tilt") after freezing in the polar mode. Energies are per 45-atom unit cell, with the zero level set to the highest-energy paraelectric structure ("Paraelectric"). (c) Spontaneous polarization for BN and SN in their fully relaxed ground states. P_z is the polarization along the tetragonal c direction. Shaded region marks values reported by Glass.[14]

Chemical bonding

At this point, focus is shifted to understanding the chemical bonding which stabilizes the polarization. The charge densities for the paraelectric and ground state structures for BN and SN in the SS[001] configuration are shown in Figures 5.4(a) and (b). This configuration is suitable for comparing the effects of polar and tilt-mode instabilities, in addition to being the true zero-kelvin ground state for SN. At the chosen isosurface value, a distinct "necking" can be seen between Nb and O in the direction of the polar distortion, pointing to a covalent bonding between the atoms. As further evidence for the role of Nb–O covalency, BECs are calculated for all configurations of both compounds in their paraelectric states (Table 5.1). Consistent with the charge density visualization in Figures 5.4(a) and (b), the BECs for Nb and O along c are large, exceeding +9 for Nb and −7 for oxygen, in comparison to their respective formal charges of +5 and −2. The values are similar to BECs reported for $KNbO_3$ and $NaNbO_3$, following the trend of Z^* being proportional to the formal charge of the B-site cation.[221,266] The variation in BEC between BN and SN is minor, pointing to a similar degree of Nb–O covalency in the two compounds, which is also indicated by their similar electronic densities of states, shown in Figure 5.5. For both compounds, the valence and conduction bands are composed of primarily O $2p$ and Nb $4d$ states, respectively. The polar distortion increases the band gap and makes the bands more compact, but apart from these subtle changes, the electronic structure changes little in the ferroelectric transition. There is little or no contribution from Ba or Sr states in the vicinity of the Fermi level, and the BECs for Ba and Sr are similar and close to the formal charge of +2. This demonstrates that Ba and Sr do not significantly change their covalency in the ferroelectric transition.

Table 5.1 — Diagonal components of the BEC tensor normal (Z^*_{xx}) and parallel (Z^*_{zz}) to the tetragonal z axis for BN and SN. Values are averaged over all ten configurations for each compound, and the number in parenthesis gives the uncertainty in the last digit in terms of standard deviation. Off-diagonal components of the BEC tensor are in all cases small.

		A	Nb	$O_\perp$	$O_\parallel$
BN	Z^*_{xx}	2.83(3)	8.2(6)	-4.0(3)	-1.60(6)
	Z^*_{zz}	2.69(3)	9.4(3)	-1.75(6)	-7.3(2)
SN	Z^*_{xx}	2.64(5)	8.1(5)	-3.9(2)	-1.55(4)
	Z^*_{zz}	2.52(7)	9.3(4)	-1.70(6)	-7.1(3)

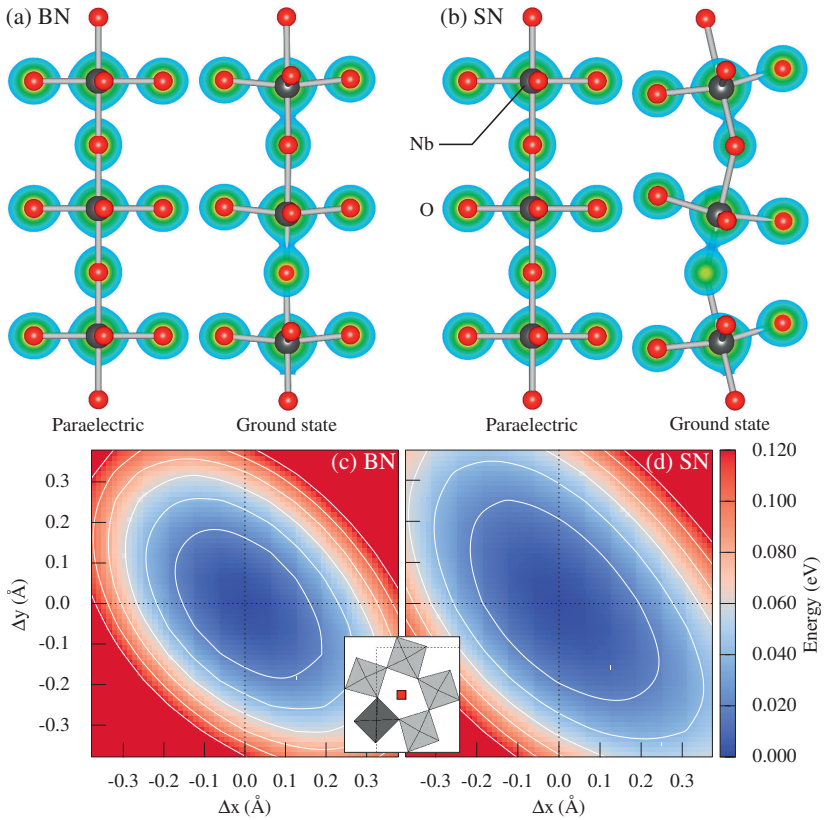

Figure 5.4 — (a) and (b) Charge density plots for $Ba_5Nb_{10}O_{30}$ (BN) and $Sr_5Nb_{10}O_{30}$ (SN) in paraelectric and ground state structures (isosurface value 0.15 eÅ^{-3}). (c) and (d) Potential energy surfaces for the A2-site cation in BN and SN in the paraelectric SS[001] configuration (energy per 45-atom unit cell). The reference position of the cation is in the middle of each plot, and the inset shows the location and size of the mapped area (red square).

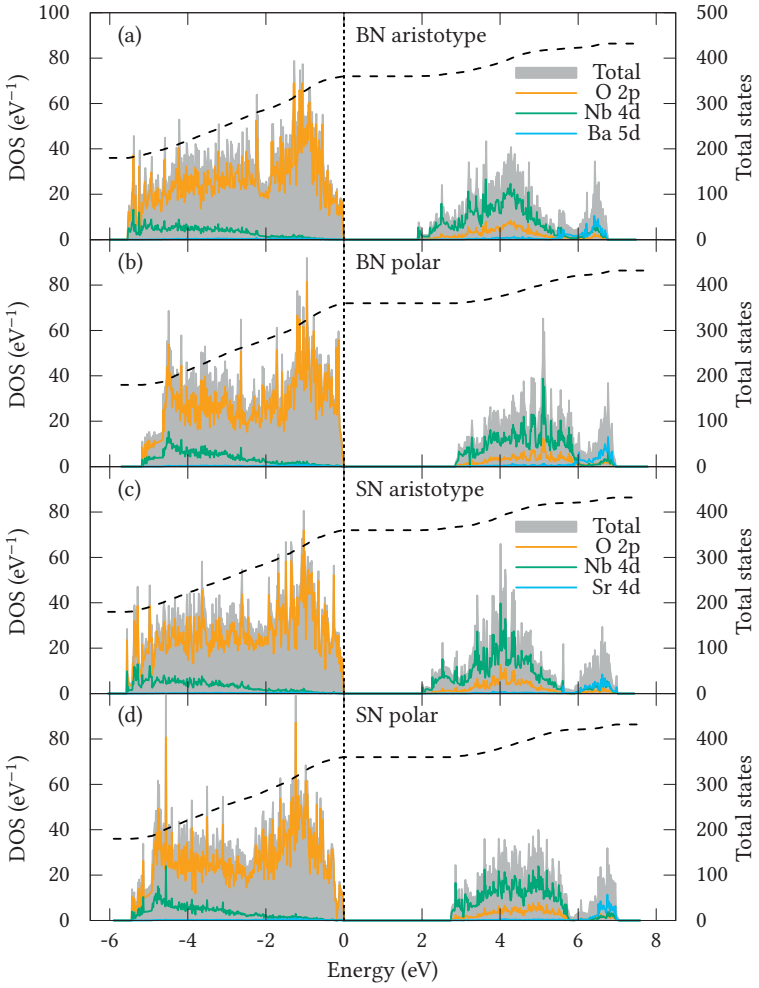

Figure 5.5 — (a) and (b) Electronic density of states for paraelectric states of BN and SN in the SS[001] configuration, normalized to one unit cell (45 atoms); (c) and (d) corresponding for the polar states. The polar distortion is increased to 200 % for the polar states in order to bring out possible differences. Energy is given relative to the Fermi level, with the total number of states (integrated DOS; dashed line) on the secondary axis.

5.2 Discussion

Ferroelectric mechanism

The results point to a conventional ferroelectric mechanism in which polarization arises from off-centering of d^0 Nb^{5+} ions in the NbO_6 octahedra, which is in turn stabilized by the resulting enhanced Nb–O covalency. Partial covalency is well known as the origin of ferroelectricity in perovskite oxides,[31,42,55] and is classified as a second-order Jahn–Teller effect.[267] The charge densities obtained for BN and SN [Figures 5.4(a) and (b)] are visually similar to those found experimentally for the prototype ferroelectrics $BaTiO_3$ and $PbTiO_3$,[268] and the large BECs found in this work are close to previous calculations for Nb and O in $KNbO_3$.[221] The interpretation of large BECs is that additional covalency associated with the polar distortion occurs through electron transfer from O 2*p* to the formally empty Nb 4*d* orbitals, thereby enhancing the charge transfer compared to simple ionic displacement with nominal charges. The calculated P_z [Figure 5.3(c)] show that the polarization is robust with respect to cation–vacancy disorder, and that a significant polarization persists for all ten configurations for both compounds. This is also evident from the charge densities [Figures 5.4(a) and (b)] which demonstrate that the off-centering of Nb^{5+} is significant even for the ground state of SN in the SS[001] configuration, where the tilt-mode amplitude is large. Octahedral tilting in TTBs is otherwise restricted by the connectivity in the xy plane, which prevents tilting around the z axis. Tilts around axes in the xy plane are however possible, and often lead to a $\sqrt{2}\times\sqrt{2}\times 2$ supercell relative to the aristotype,[91,123] in line with a recent group-theoretical analysis.[269] A $\sqrt{2}\times\sqrt{2}\times 2$ supercell was also reported for pure SN with TTB structure,[270] although for intermediate SBN compositions, doubling of the c parameter is not known to occur.

Relaxor behaviour

It is generally accepted that chemical or structural disorder is necessary for relaxor properties,[8] and both are possible in SBN due to Sr^{2+}, Ba^{2+} and vacancies occupying the same sublattices. In disordered perovskite relaxors, the two cations occupying the same sublattice are always aliovalent, examples being B-site disordered $PbMg_{1/3}Nb_{2/3}O_3$ (PMN)[8,89] and A-site disordered $Bi_{1/2}Na_{1/2}TiO_3$ (BNT).[13,86] In PMN and BNT the cation ratios are fixed by electroneutrality, whereas in SBN the A-site composition can be varied continuously, and relaxor properties emerge gradually for higher Sr content. This points to a different relaxor mechanism for SBN than for the perovskites. The possible role of the A-site cations in SBN is investigated by displacing Ba and Sr away from their relaxed positions in the A2 channels and

mapping the potential energy surface (PES) as shown in Figures 5.4(c) and (d). The PES is flatter for SN than for BN, which is explained by Sr^{2+} being smaller than Ba^{2+}. Due to the restrictions imposed by the octahedral connectivity, and the fact that not all cation configurations in SBN produce tilted ground states, the TTB structure cannot compensate for this by octahedral tilting. Based on this, it is suggested that Sr^{2+} is able to displace inside the A2 channels under application of an electric field, thereby producing an additional dielectric response which creates a diffuse phase transition for Sr-rich SBN. Sr preferentially occupies the A1 sites in SBN,[254,271] but for $x > 0.40$, Sr must also occupy A2 sites. For $x > 0.50$, the amount of Sr on A2 is high enough for this displacement effect to be appreciable, and it is proposed that this induces relaxor behaviour.

The mechanism suggested above is different from that in perovskite relaxors, where cation ordering determines the type of dielectric response.[78] Relaxor behaviour is often discussed in terms of polar nanoregions (PNRs), in which polar displacements are correlated over a length scale of a few unit cells.[73] The PNRs form at the Burns temperature, and are dynamic and reorientable down to the polar freezing temperature, as discussed in Chapter 2. The reorientation of dynamic PNRs contributes to the diffuseness of the phase transition. The atomic displacements suggested to be the origin of relaxor behaviour in this study might also very well be correlated, although this has not been specifically investigated. It is interesting to note that an in-plane dielectric anomaly has been observed at low temperatures (below 150 K) in several TTBs with out-of-plane polarization,[272] which could be related to a cation displacement effect as discussed above. In that case, it is natural to associate the reported dielectric anomaly with ordering of the in-plane cation displacements, while the different ability for Sr and Ba to displace would still explain the diffuse contribution to the ferroelectric transition. The properties discussed here should be generally applicable to TTB oxides with [001] polarization and possibilities for mixed and/or partial cation occupancy.

6 Ferroelectric lead metaniobate

6.1 Results

Crystal structure

The ferroelectric transition in $(Sr, Ba)_5Nb_{10}O_{30}$ (SBN) does not lead to a change of the unit cell size. In contrast, the unit cell for the ferroelectric phase of $Pb_5Nb_{10}O_{30}$ (TTB-PN) is a $\sqrt{2}\times\sqrt{2}\times1$ supercell with respect to the aristotype, a twofold increase of the unit cell size (see Figure 6.1).* A lattice dynamics-based analysis similar to that of SBN, Chapter 5, would therefore require larger supercells in the phonon calculations, in turn increasing the computational cost significantly, so the ferroelectric phase was instead investigated directly. Available data on the crystal structure of TTB-PN [shown previously in Figure 2.12(b)] were not of sufficient quality, so diffraction experiments were performed in order to provide a good starting point for the calculations.

Powder diffractograms of TTB-PN were recorded with X-ray and neutron radiation, and the structure was refined from both datasets simultaneously starting from literature data[115] (Appendix B). The refinement converged ($R_p = 8.29\,\%, R_{wp} = 10.70\,\%, \chi^2 = 1.46$) to the structure shown in Figure 6.1, for which the atomic positions are given in Table 6.1. Diffractograms and refined profiles for the X-ray and neutron data are presented in Figure 6.2. The refined structure appears less distorted than the previously reported structure,[115] as can be seen by comparing Figures 2.12(b) and 6.1. The NbO_6 octahedra are less deformed, and the square and pentagonal channels have a more regular shape. In the previous study,[115] the occupancy of Pb was not refined, but fixed at 0.5 for the square channels and the pentagonal channels with split positions. From the data in Table 6.1 it is seen that the actual occupations deviate only slightly from this, with Pb showing a clear preference for the pentagonal (A2) channels, resulting in a low occupancy for the square (A1) sites. The lattice parameters obtained in this work correspond well to those reported previously,[115] although the present values have around two orders of magnitude higher precision.

Spontaneous polarization

Based on the refined Pb occupancy (Table 6.1), only cation configurations where Pb is fully occupying the A2 sites were considered further for the computational investigations. This corresponds to the "SS" configurations studied in Chapters 4 and

*Possibly even more — a $2\sqrt{2}\times\sqrt{2}\times2$ unit cell has also been proposed,[115] implying an eightfold increase of the unit cell size.

Table 6.1 — Atomic positions for PN (space group *Amm*2, standard setting) based on joint refinement of X-ray and neutron diffraction data. WP, Wyckoff position; Occ., occupancy; B_{iso}, isotropic thermal displacement factors (constrained to be the same for all Nb, all O, and all Pb on A2 sites). Lattice parameters: $a = (3.871\,09 \pm 0.000\,10)$ Å, $b = (17.6483 \pm 0.0005)$ Å, $c = (17.9487 \pm 0.0005)$ Å.

Atom	WP	x	y	z	Occ.	B_{iso}
Pb1	4*e*	½	0.3246(2)	0.0222(5)	0.955(3)	0.44(6)
Pb2		½	0.0135(5)	0.1889(5)	0.478(2)	
Pb3		½	0.4818(4)	0.3373(5)	0.478(2)	
Pb4		½	0.2529(6)	0.2377(7)	0.590(7)	1.6(2)
Nb1	2*a*	0	0	0	1	0.42(3)
Nb2		0	0	0.4913(7)	1	
Nb3	4*d*	0	0.1840(4)	0.1055(6)	1	
Nb4		0	0.3172(4)	0.3869(5)	1	
Nb5		0	0.3961(4)	0.1762(6)	1	
Nb6		0	0.1162(4)	0.3150(6)	1	
O1	2*b*	½	0	0.9714(7)	1	1.17(3)
O2		½	0	0.4794(10)	1	
O3	4*e*	½	0.2009(5)	0.0966(7)	1	
O4		½	0.3323(5)	0.3774(6)	1	
O5		½	0.4019(5)	0.1657(7)	1	
O6		½	0.1146(5)	0.2902(7)	1	
O7	4*d*	0	0.0768(5)	0.0698(7)	1	
O8		0	0.1460(5)	0.2034(7)	1	
O9		0	0.2170(4)	0.9932(7)	1	
O10		0	0.2897(5)	0.1275(7)	1	
O11		0	0.4222(5)	0.0622(7)	1	
O12		0	0.0811(6)	0.4054(7)	1	
O13		0	0.2214(5)	0.3331(6)	1	
O14		0	0.3561(5)	0.2731(7)	1	
O15		0	0.4191(5)	0.3991(7)	1	
O16	2*a*	0	0	0.6943(9)	1	
O17		0	0	0.2708(8)	1	

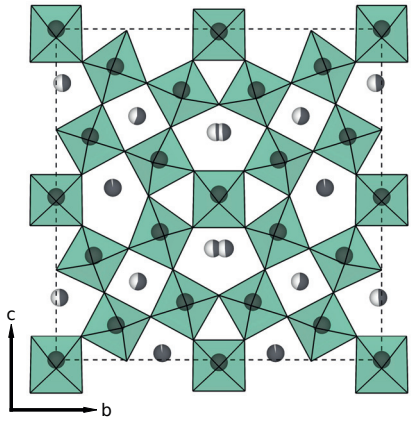

Figure 6.1 — Crystal structure of TTB-PN after joint refinement of X-ray and neutron diffraction data (space group *Amm*2). Grey spheres in channels: Pb (shading denotes occupancy), grey spheres in octahedra: Nb. Split positions are used for two of the Pb positions, as a simplified description of the "true" structure which has been reported to show ordering of Pb along *b*.[115]

5, although the $\sqrt{2} \times \sqrt{2} \times 1$ supercell used for PN creates four possible cases with this type of cation configuration, compared to the three SS cases considered for the $1 \times 1 \times 2$ supercell in the previous chapters. The cases, numbered 1 to 4, are presented in Table 6.2, along with the local space group symmetry introduced by the cation ordering (one monoclinic and three orthorhombic). The table can be compared to Table 4.1 in Chapter 4, which gives all the configurations possible for a $1 \times 1 \times 2$ supercell. As in the previous case, the local cation configuration lowers the space group symmetry to different symmetry classes: Configuration 1 is monoclinic (space group *Pm*), while configurations 2–4 are orthorhombic ($Pmc2_1$ and *Pmm*2).

The atomic positions were optimized for the four structures, with the split atomic positions used in the refinements replaced by single atoms in the mirror plane. Optimization of atomic positions was performed within the symmetry constraints imposed by the local space group symmetry as discussed above, while keeping the lattice parameters constant at the experimental values (Table 6.1). The resulting energy landscape is presented in Figure 6.3(a). Configurations 1 and 2 have the lowest energy, while the other two are significantly higher (0.5 eV per 90 atoms). The energy differences depend in part on the atomic degrees of freedom for each configuration, as dictated by the space group symmetry. Configuration 1 has the lowest symmetry, being mon-

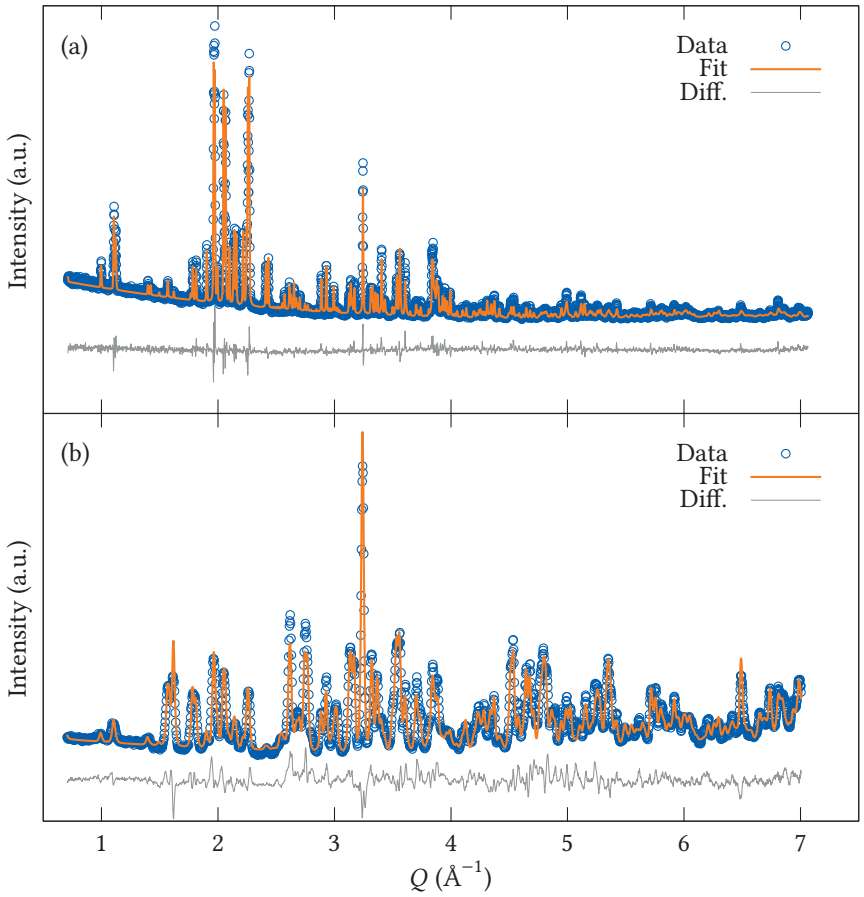

Figure 6.2 — (a) Powder X-ray and (b) powder neutron diffractograms for TTB-PN at ambient temperature, plotted as a function of the scattering vector ($Q = 2\pi/d$). Refinement profiles and difference curves are shown for simultaneous refinement of both datasets.

oclinic, although it is the orthorhombic configuration 2 that actually has the lowest energy. In practice, the energy difference between configurations 1 and 2 is on the order of 1 meV per atom, and close to the accuracy of the computational method, so configurations 1 and 2 should be regarded as equally favourable from an energetic point of view.

Table 6.2 — Cation configurations possible for the $\sqrt{2} \times \sqrt{2} \times 1$ supercell considered for PN (white spheres: vacancies). Local space group symmetry of each polar configuration is given (average symmetry *Amm*2).

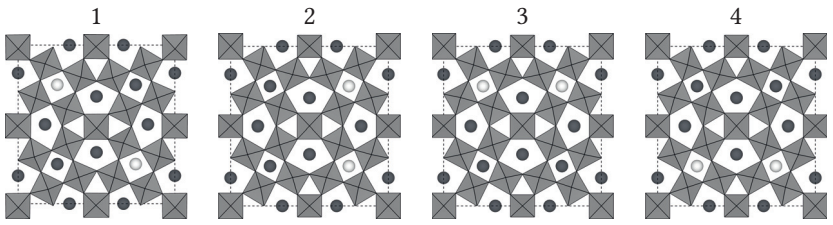

The TTB-PN structure has an in-plane polar distortion, which in turn leads to a ferroelectric polarization. Berry phase calculations of the spontaneous polarization for the relaxed structures revealed that the polarization is high, 109 μC cm^{-2} for all four cases [Figure 6.3(b)].[†] For configurations 2–4, which have orthorhombic space group symmetry (Table 6.2), the polarization lies strictly along *c* in the *Amm*2 cell. Details of the calculation for the lowest-energy configuration, configuration 2, are shown in Figure 6.4, with similar results obtained for the three other configurations. For configuration 1, which has monoclinic symmetry, the polarization is not confined to one of the unit cell axes, but can lie along any in-plane direction. In practice, the polarization is oriented to a large degree along *c* also for configuration 1, with a small component along *b* which leads to a net polarization vector that forms a 1.5° angle with *c*.

The mechanism that stabilizes the in-plane polarization in TTB-PN can be understood by inspecting the charge density, which is visualized for configuration 2 in Figure 6.5(a) and (b). It is readily seen that covalent Pb–O bonding, Figure 6.5(a), has a large influence on the structural distortion, and that Pb typically bonds more strongly to four of the surrounding oxygens. This leads to a substantial displacement of Pb inside both the square and pentagonal channels, while the displacement of Nb inside the NbO_6 octahedra, Figure 6.5(b), is less.

[†] At four significant digits, the values range from 108.5 to 109.4 μC cm^{-2}.

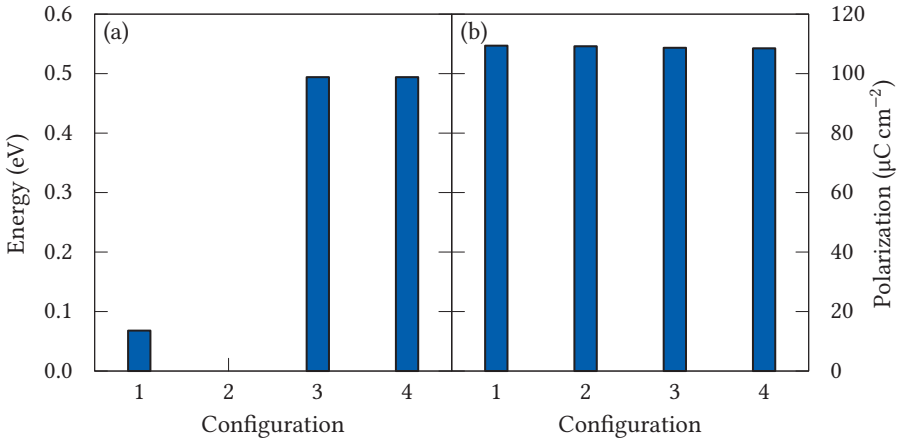

Figure 6.3 — Energy (a) and spontaneous polarization (b) of the four cation configurations considered in this work (Table 6.2), after optimizing atomic positions at constant experimental lattice parameters. Energies are given per 90-atom supercell and relative to configuration 2 which has the lowest energy.

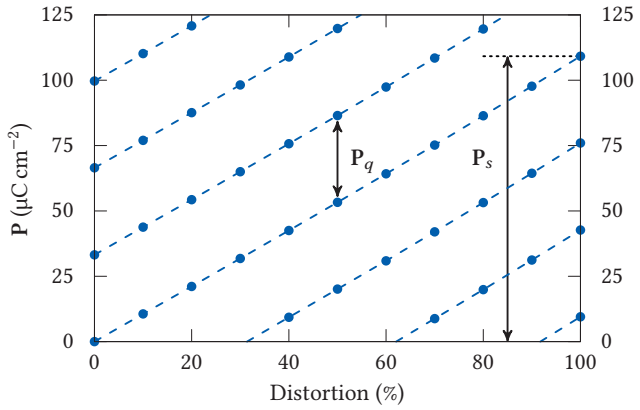

Figure 6.4 — Berry phase calculation of spontaneous polarization for TTB-PN (configuration 2, cf. Table 6.2). The spontaneous polarization, $\mathbf{P}_s$, is 109.2 μC cm^{-2} and the polarization quantum, $\mathbf{P}_q$, is 23.4 μC cm^{-2}. 0 % distortion refers to a centrosymmetric cell obtained by a pseudosymmetry search in space group *Cmmm*.[273]

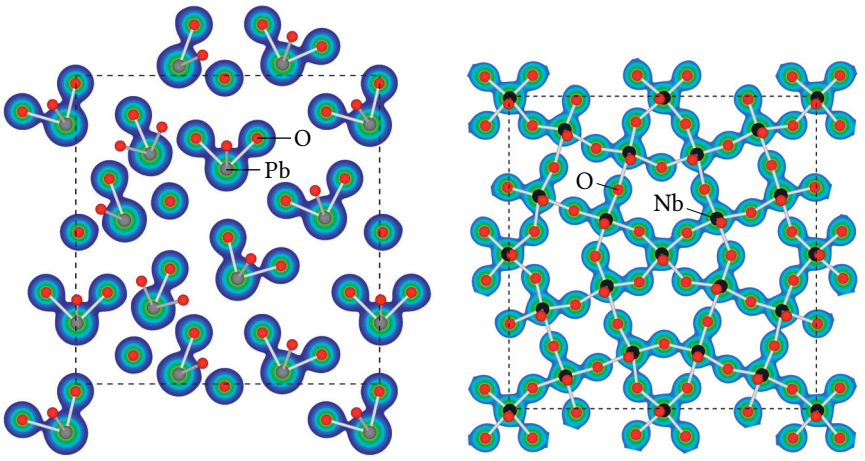

Figure 6.5 — Charge density sections for TTB-PN in configuration 2. (a) $z = 0$, showing the Pb–O interactions that lead to displacement of Pb inside the A1 and A2 channels; (b) $z = 1/2$, showing the Nb–O bonds defining the octahedra. Sections defined by isosurface values of 0.03 eÅ^{-3} and 0.10 eÅ^{-3}, respectively.

High-temperature lattice parameters

Finally, the high-temperature behaviour of TTB-PN was investigated by high-temperature X-ray diffraction. Selected diffractograms are presented in Figure 6.6, which shows how diffraction lines split as a consequence of the transition from tetragonal to orthorhombic symmetry as the temperature is lowered. The ferroelectric transition is seen to occur at $T_C = (595 \pm 5)$ °C, compared to literature values of 534 to 570 °C.[5,7,113] Lattice parameters were obtained by Pawley fitting with space group symmetry $P4/mbm$ above T_C and $Amm2$ below, as shown in Figure 6.7. The resulting lattice parameters are presented as a function of temperature in Figure 6.8(a). In the paraelectric phase with tetragonal symmetry, the two in-plane lattice parameters are identical ($a = b$). At T_C, the symmetry is reduced to orthorhombic $Amm2$, and the two in-plane lattice parameters become different ($c > b$). If the in-plane lattice parameters of the paraelectric phase are extrapolated below T_C, they overlap perfectly with the b parameter of the ferroelectric phase, as seen in Figure 6.8(a), and it is therefore natural to define the spontaneous strain using the b parameter as reference [Figure 6.8(b)]. The strain along the polar direction, c in $Amm2$, is as high as 1.7 % at room temperature (in comparison, the perovskite $KNbO_3$ has an orthorhombic strain of

around 1 % at room temperature[274]).

6.2 Discussion

Refinement of the crystal structure

The combination of X-ray and neutron diffraction data provides an overall more plausible description of the crystal structure than previously available data.[115,116,275] When the new structural data, Figure 6.1, is compared to that reported by Labbé, Figure 2.12(b), it is seen that especially the oxygen octahedra appear more regular, in the sense less deformed and strained, in the structure reported here. This is a consequence of the improved accuracy in oxygen positions achieved by including neutron diffraction data in the refinement. Since X-rays are scattered by the electron density, an element's X-ray scattering cross-section is determined by its atomic number. In the case of PN, oxygen contributes less to the scattered intensity compared to the much heavier elements Nb and Pb. This means that errors in the refined oxygen positions will have less impact on the quality of the Rietveld fit of the X-ray data, possibly leading to refined crystal structures that give a mathematically adequate fit despite being physically incorrect. In contrast, neutrons are scattered by the atomic nuclei, whose neutron scattering cross-sections are a more or less random function of atomic number (or, more precisely, isotope). The practical consequence is that also oxygen contributes significantly to the scattered intensity, in turn making the oxygen positions more accurate. This can be seen from the uncertainty in the oxygen positions in Table 6.1. In general, the accuracy is an order of magnitude better than oxygen positions determined solely from X-ray diffraction, such as the structural data for PN reported by Chakraborty and co-workers.[275] The same approach has been successfully used for the rhombohedral polymorph of PN (Chapter 9 and ref. [276]).

The starting point for the refinement was the crystal structure first reported for TTB-PN in 1973 by Labbé[115] and further elaborated in 1977.[116] In the original publications, the structural data is given in the $Cm2m$ setting of space group 38 in order to have c as the shortest unit cell edge in analogy to the $P4/mbm$ aristotype. Here, the ITA standard setting $Amm2$ is instead used (the two are related by $(a, b, c)_{Cm2m} = (b, c, a)_{Amm2}$). A key feature of the model is the use of split atomic positions for Pb in the pentagonal A2 channels. According to the works cited above, this makes it possible to describe the crystal structure by a $\sqrt{2} \times \sqrt{2} \times 1$ supercell (relative to the aristotype $P4/mbm$ unit cell), while the "true" cell is a four times larger $2\sqrt{2} \times \sqrt{2} \times 2$ supercell with space group symmetry $Bb2_1m$ (no. 36, $Cmc2_1$ in ITA standard setting). The two are related by ordering of Pb in the pentagonal channels, more specifically an alternating displacement in the in-plane direction normal to the polar axis (the

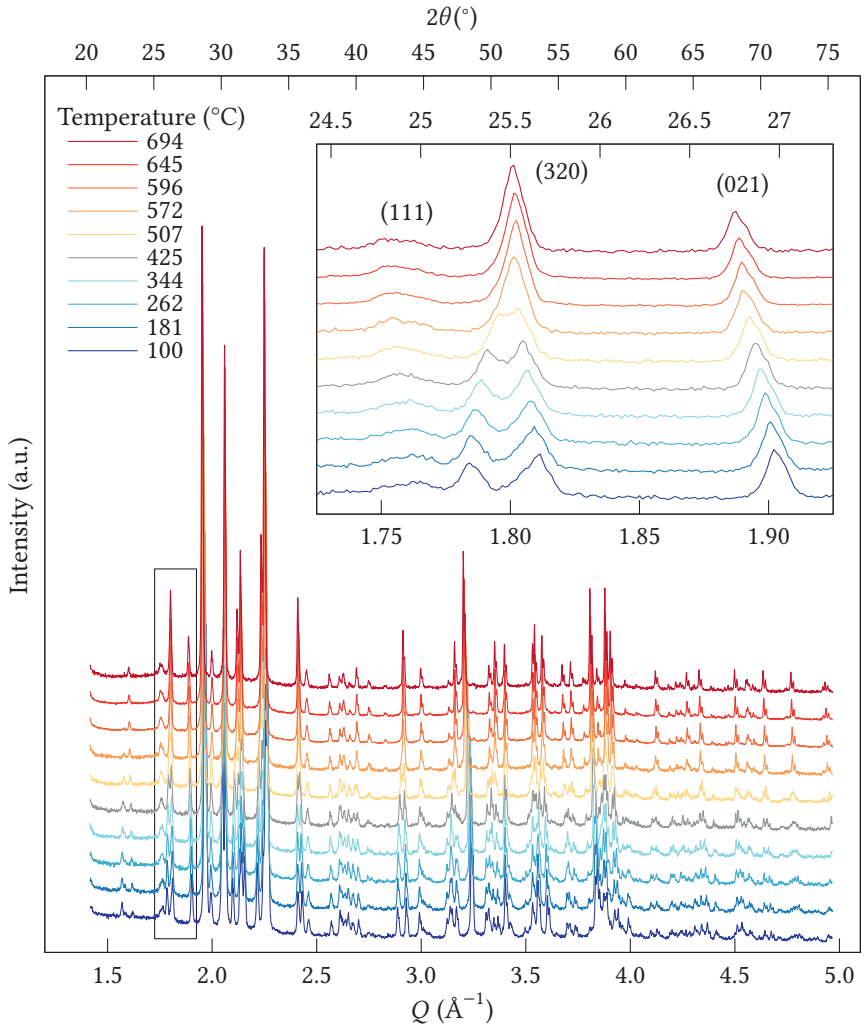

Figure 6.6 — Diffractograms of TTB-PN at different temperatures (calibrated against an alumina standard). 2θ scale for Cu $K\alpha$ radiation given on top axis. The inset shows a magnification of the dataset (marked with a rectangle; same units on the axes as the main plot). The ferroelectric phase transition at $T_C = (595 \pm 5)\,^\circ\mathrm{C}$ is manifested through splitting of certain peaks (indexed according to $P4/mbm$).

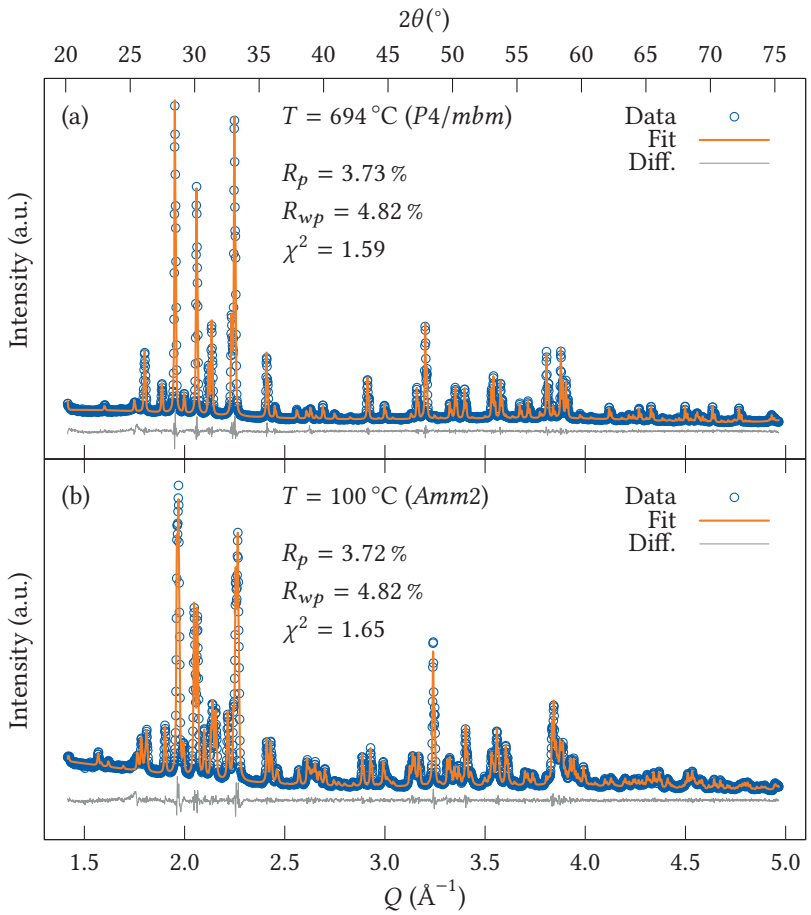

Figure 6.7 — Pawley fitting of X-ray diffractograms recorded at temperatures above (a) and below (b) the phase transition temperature for TTB-PN. 2θ scale for Cu$K\alpha$ radiation given on top axis.

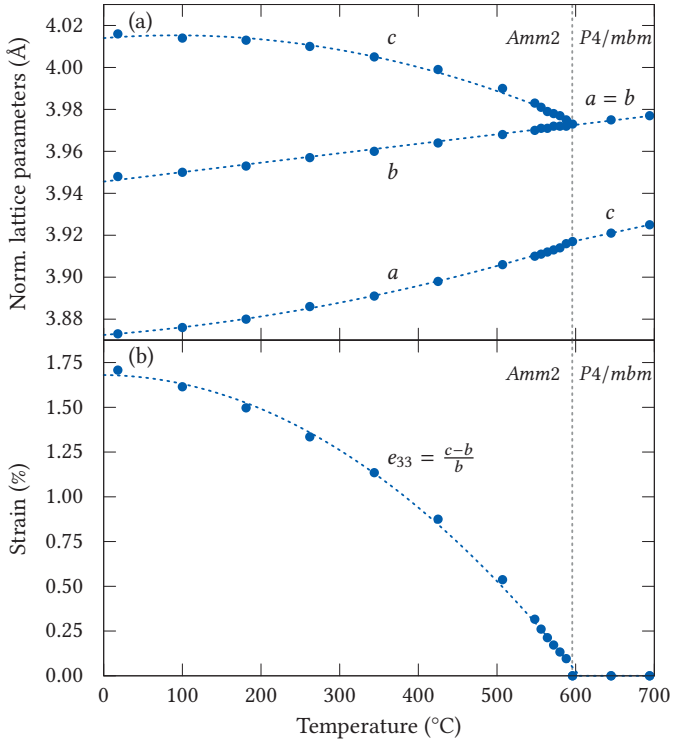

Figure 6.8 — (a) Temperature evolution of the lattice parameters for TTB-PN, as determined by the Pawley method. The ITA standard setting is used for space group *Amm*2, as defined in Figure 6.1 and Table 6.1. b and c are scaled by $1/(2\sqrt{5})$ so that all lattice parameters are related to the size of an NbO_6 octahedron. (b) Spontaneous strain in TTB-PN as a function of temperature. The vertical dashed line marks $T_C = 595\,°C$. Dashed lines through the data points are guides to the eye.

shortest of the two long edges). It is assumed here that this ordering of displacement is not crucial to the ferroelectric mechanism, which will be further discussed below.

Polarization and ferroelectric transition

Four specific cation configurations are investigated in detail, based on the structure refinement discussed above. In particular, the refinement of occupancy for Pb in the A1 and A2 channels makes it possible to identify the four configurations in Table 6.2 as the most relevant, as Pb strongly prefers to occupy the A2 sites, as was also pointed out by in the original works.[115,116] Interestingly, two of the configurations (1 and 2 in Table 6.2) have significantly lower energy than the others [Figure 6.3(a)], and are therefore, in principle, more likely to be the dominant configurations on a local level in TTB-PN. At the same time, all configurations have a high spontaneous polarization, which is practically the same, 109 μC cm^{-2}, for all four. As the calculated charge densities show, Figure 6.5, this is due to a combination of Pb–O and Nb–O bonding, which cooperatively create a polar in-plane distortion. The local coordination environment of Pb^{2+} is reminiscent of that in tetragonal $PbTiO_3$,[55,268] where Pb tends to displace towards, and bond to, four of the 12 oxygens it is coordinated by on the A sites. The structure and charge density in Figure 6.5 corresponds well to the analysis performed by Labbé (ref.,[116] results shown previously in Figure 2.13), which also concluded that displacement of both Nb^{5+} and Pb^{2+} in the in-plane direction are important contributions to the polarization in TTB-PN. This is in contrast to SBN and BNN, where the A2-site cations do not contribute significantly to polarization in the tetragonal *c* direction, even though the space group symmetry allows for it. The contribution to in-plane polarization from both Nb^{5+} and Pb^{2+} was also pointed out by Guo and co-workers,[277] who performed a similar analysis. An analysis in terms of Born effective charge (BEC), similar to what was done in Chapter 5, would likely have revealed anomalously high BECs for both Nb and Pb. This was not performed, as the present analysis focuses on the polar, ferroelectric structure, and not the paraelectric aristotype.

The calculated spontaneous polarization is significantly higher than experimental values, reported in the range 38 to 46 μC cm^{-2},[277] and it is natural to ask why. It is well known that piezoelectric properties of PN are improved by substituting Ba for Pb, with an MPB occurring at around 40 % Ba substitution.[11] This effect has been attributed to the fact that Ba^{2+}, being larger than Pb^{2+} (ionic radii of 1.61 Å and 1.49 Å for 12-fold coordination, respectively[128]), will expand the lattice and reduce the ferroelastic strain, in turn easing the domain switching. To test this hypothesis, nudged elastic band (NEB) calculations were performed for ferroelastic switching in TTB-PN. Starting from configuration 1, with monoclinic symmetry, it is possible to transform the

structure into itself by a 90° rotation followed by a translation. This transformation corresponds to the transition between two ferroelectric domains separated by a 90° domain wall, which are therefore also ferroelastic domains. The transition between 180° domains, which are ferroelectric but not ferroelastic, can similarly be performed by simply inverting the polar structure. NEB calculations were then used to estimate the energy barrier for the two transitions, leading to the minimal energy paths (MEPs) shown in Figure 6.9, which for comparison also includes calculations for similar switching in the tetragonal perovskite $PbTiO_3$ (PT). The barrier for 90° switching in PN is calculated to be as high as 0.18 eV per atom (16 eV for the 90-atom cell), which is around 30 times higher than the barrier for 90° switching in PT. The barrier for 180° domain switching in PN is similar in magnitude to the one for 90° switching, and also in this case almost an order of magnitude larger than for PT. For PT, both climbing image NEB (with fixed volume for each image) and solid-state climbing image NEB (with optimization of lattice parameters for each image) was performed (the latter was not applicable to TTB-PN, as it resulted in unphysically large deformation of the intermediate images).

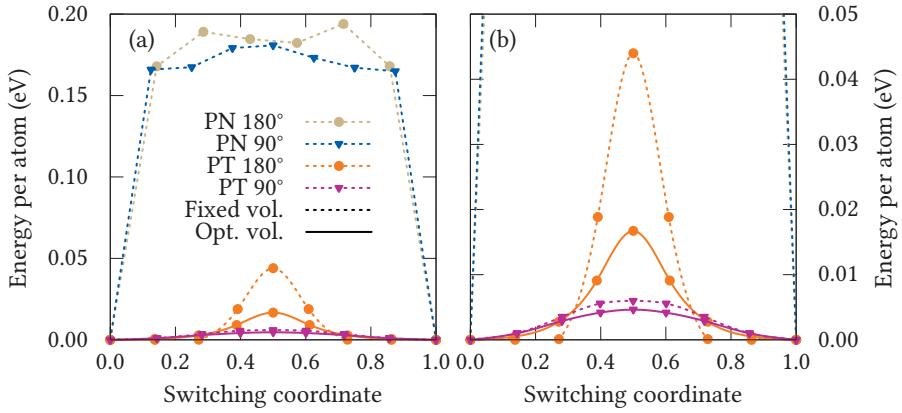

Figure 6.9 — (a) MEPs for domain switching in PN and $PbTiO_3$ (PT), in eV per atom for comparability between the materials. For PT, both fixed-volume NEB and solid-state NEB (with volume relaxation of each image) is included. (b) Zoom-in on the lower part of panel a.

The NEB calculations show a very high energy barrier for both 90° and 180° switching of TTB-PN, meaning that ferroelastic strain alone does not fully explain

the difficulty in switching. The calculated energy barriers should however be taken with some caution, as a liberal force-based convergence criterion of 0.3 eV Å^{-1} was necessary. Inspection of the relaxed intermediate images showed that the atoms do not displace smoothly between the end points of the switching path, which is an expected result based on the charge density, Figure 6.5(a). Pb tends to bond strongly (and non-centrosymmetrically) to oxygen,[55] which in this case prevents it from displacing "across" the pentagonal channels (as dictated by a linear interpolation between the start and end points), and instead keeps it in close contact with the oxygens along the channel wall. A denser spacing of images along the transformation path might have resulted in a smoother MEP, but probably not a significant lowering of the energy barriers. The fact that the domain switching does not only involve ionic displacement, but a significant breaking and re-forming of Pb–O bonds, is certain to contribute to the high switching barrier. This is probably also a reason why substitution of Ba for Pb relieves the switching barrier and improves the piezoelectric properties for TTB-PN. The Pb–O covalency contributes to the high polarization of the material, but is at the same time so strong that it significantly impedes the ferroelectric switching, whether or not the switching is also ferroelastic.

The spontaneous strain associated with the ferroelectric transition consists of an expansion of c while the b parameter develops linearly, Figure 6.8(a). This makes it natural to define the spontaneous strain, Figure 6.8(b), with reference to b. c is the polar direction, while b is the shorter of the long edges of the unit cell. In the model used for refinement of the structure, it is assumed that the alternating displacements of Pb along b do not take a significant part in the ferroelectric mechanism, so that their exact positions can be approximated by the split positions used here. This seems to be the case, since a sudden change in the Pb positions in the b direction would be expected to affect the b lattice parameter at T_C. This is not the case. The a parameter changes slope at T_C, although the effect is small compared to the change in c. The strain plot, Figure 6.8(b), shows a lattice strain that goes continuously to zero as T_C is approached from below. The strain does not follow the $\sqrt{T_C - T}$ dependency that would be expected from Landau theory for a purely ferroelastic second-order phase transition, where strain is the macroscopic order parameter. The ferroelectric transition in TTB-PN, on the other hand, is required to be first order, as $Amm2$ is not a direct subgroup of $P4/mbm$ (the complete group–subgroup sequence is $P4/mbm \rightarrow Cmmm \rightarrow Amm2$). There is therefore no guarantee that the spontaneous lattice strain behaves as a good macroscopic order parameter for the transition, as the strain must be coupled to at least one other polar mode.

7

Filled TTB insulators

7.1 Results

Structure and dynamical stability

The TTB structure, with general formula $(A1)_2(A2)_4C_4(B1)_2(B2)_8O_{30}$, is referred to as "filled" if all A1 and A2 sites, six in total, are occupied (Figure 7.1). For the compound to be electrically insulating, it is normally required that the B1 and B2 sites are occupied by d^0 cations such as Nb^{5+}, Ta^{5+} or Ti^{4+}. If all B1 and B2 sites (ten in total) are occupied by Nb^{5+}, which is the case for many TTBs, the principle of electroneutrality requires the A1 and A2 cations to have a total charge of +10. One example of such a filled, insulating TTB system is the series $K_4R_2Nb_{10}O_{30}$, hereafter referred to as KRN, with R = La, . . . , Gd, Bi. In this series, the cations order with K^+ on the A2 sites and the smaller R^{3+} on the A1 sites (for R = Tb, Dy, Ho, R^{3+} partially occupies the triangular C sites, and no stable TTB phase forms for R = Er, . . . , Lu).[124] The cation ordering makes the system convenient to study, as the actual cation distribution is compliant with the general TTB formula.

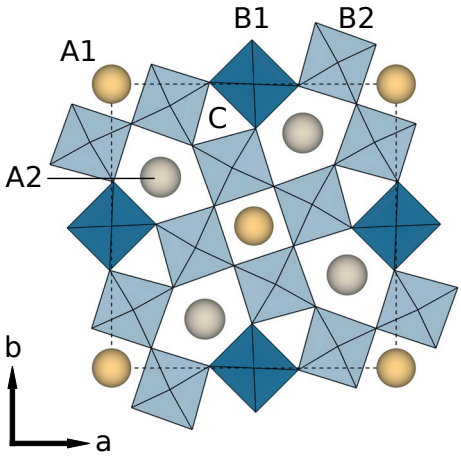

Figure 7.1 — Unit cell of the tetragonal tungsten bronze structure with aristotype space group symmetry $P4/mbm$ and general formula $(A1)_2(A2)_4C_4(B1)_2(B2)_8O_{30}$. In the KRN system, K^+ is on A2 while R^{3+} is on A1.

Due to a lack of experimental data on the KRN series, data for the unfilled,

insulating SBN system was used as the starting point. Lattice parameters and atomic positions were taken from the composition $(Ba_{0.67}Sr_{0.33})_5Nb_{10}O_{30}$ with space group symmetry $P4bm$ in the ferroelectric phase.[271] A "paraelectric" structure was obtained by searching for a pseudosymmetric structure with space group $P4/mbm$,[273] resulting in a unit cell with lattice parameters $a = b = 12.484$ Å and $c = 3.974$ Å which was used as the starting point for all subsequent calculations on KRN.

Lattice parameters and atomic positions were optimized for KRN with R = La, . . . , Gd, Bi,* under the symmetry constraints imposed by space group $P4/mbm$. Lattice parameters for the relaxed structures are shown in Figure 7.2. The lattice parameters and cell volume are plotted as a function of ionic radius of R^{3+} with coordination number (CN) 8, the largest CN for which ionic radii are tabulated for all R. The lattice parameters and cell volume generally follow the ionic radius, although the volume contracts slightly for Bi, which is mainly due to a contraction of the in-plane lattice parameter.

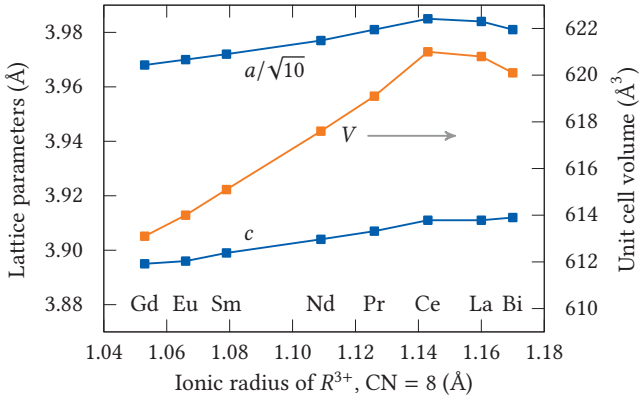

Figure 7.2 — Lattice parameters and volume for the KRN series. The in-plane lattice parameter is reported as $a/\sqrt{10}$, to make it directly comparable to the c parameter (both related to the size of an NbO_6 octahedron).

Phonon calculations, similar to the ones performed for unfilled BN and SN in Chapter 5, reveal several unstable modes for all compositions. The mode with the highest imaginary frequency is in all cases a polar mode which gives a polarization along z. It is similar to the polar mode in SBN, and is mainly due to relative

*R = Pm was not included, as its extreme radioactivity leads to it being completely deficient from the Earth's crust, and thus of limited experimental relevance.[278]

displacements of Nb in the NbO_6 octahedra. All compositions also have a second instability, which consists mainly of an in-plane displacement of K and *R* relative to the NbO_6 framework, resulting in an in-plane polarization which is similar to that seen in unfilled PN (Chapter 6). The imaginary frequency depends on the radius of *R* for both modes, and the squared frequency of both modes is presented in Figure 7.3 as a function of cation radius. The out-of-plane mode follows a strictly linear trend, while the in-plane mode shows a parabolic dependency on the cation radius. The trend is opposite for the two modes, in the sense that the largest *R* (La and Bi) cause the strongest out-of-plane instability, while the smallest *R* (Gd) gives the strongest in-plane instability. The only exception to this trend is the in-plane instability for KBiN, which in fact is the strongest of all the cases investigated.

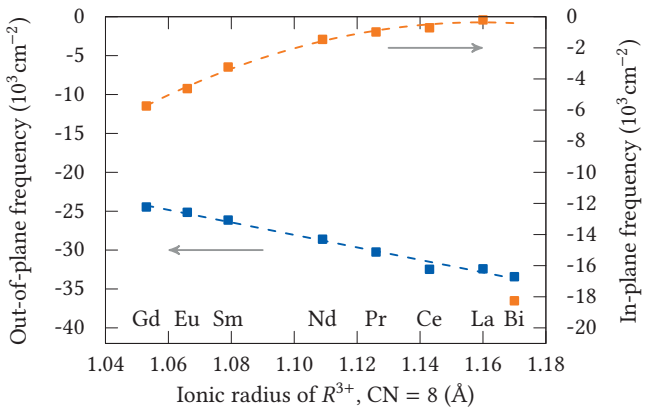

Figure 7.3 — Squared phonon frequencies for unstable polar phonons in KRN in the aristotype space group *P*4/*mbm*. Two phonons are included for each compound, one giving rise to a polarization along *z* (left axis) and the other in the *xy* plane (right axis). Dashed lines are guides to the eye. Note the deviation from the trend for the in-plane polar mode of KBiN.

Displacement of the atoms along the eigenvector of the out-of-plane polar mode (referred to as "freezing in" the mode) leads to lower energy for all compounds, as shown in Figure 7.4(a). Consistent with the phonon frequencies, Figure 7.3, the Bi compound experiences the largest energy lowering for this mode, and Gd the least. The behaviour follows the linear trend in phonon frequencies with ionic radius of R^{3+}, with only a slight deviation for KBiN. For the in-plane polar mode, Figure 7.4(b), the situation also mirrors the trend for the phonon frequencies: A slight tendency for

in-plane distortion is evident for KGdN, while the in-plane distortion in KLaN leads to no significant energy lowering within the computational uncertainty. KBiN deviates substantially from all other KRN compounds, with a significant energy lowering of around 0.16 eV per unit cell ($K_4R_2Nb_{10}O_{30}$).

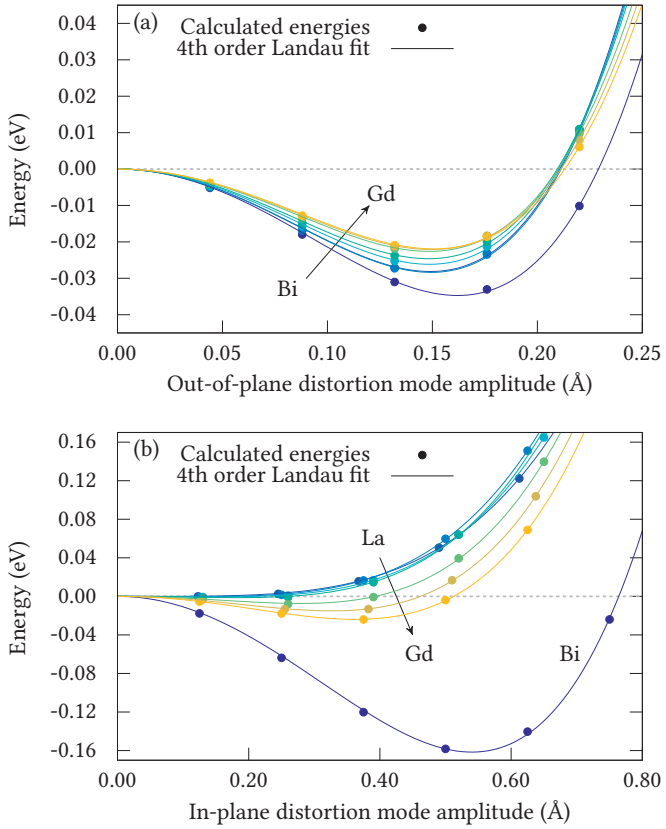

Figure 7.4 — Energy as function of mode amplitude for the polar out-of-plane (a) and in-plane (b) phonons in KRN. Note the different energy scales. Arrows indicate decreasing ionic radius.

Polarization and chemical bonding

The in-plane polar mode in KBiN was frozen in at an amplitude close to the energy minimum [Figure 7.4(b)], and the lattice parameters and atomic positions were relaxed. The resulting structure has an in-plane polarization, which was calculated to be $\mathbf{P}_s = 55\,\mu\text{C cm}^{-2}$, see Figure 7.5. This is a high polarization, comparable in magnitude to experimental data for PN (38 to 46 $\mu\text{C cm}^{-2}$[2277]), which is commercially available as a high-temperature piezoelectric. Similar to the analysis for PN in Chapter 6, the mechanism that stabilizes this polarization can be understood from the charge density. Figure 7.6 displays the structure and charge density for the relaxed KBiN structure, and covalent Bi–O bonds are clearly visible in the section containing Bi [panel (a)]. In addition, the Nb^{5+} cations are displaced in the same direction within the NbO_6 octahedra. The polarization therefore has contributions from displacement of both Bi^{3+} and Nb^{5+}, which mirrors the behaviour observed for PN (Chapter 6). K^+ is centrosymmetrically positioned in the A2 channels also in the polar structure [Figure 7.6(a)].

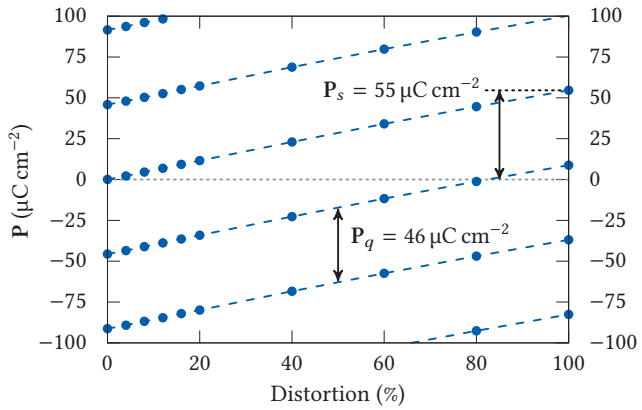

Figure 7.5 — Berry phase calculation for KBiN with in-plane polarization (compare with Figure 2.22). 100 % distortion corresponds to a structure with the in-plane polar mode frozen in and relaxed, 0 % distortion is a non-polar reference structure with space group $P4/mbm$. The polarization components along x and y were calculated separately and the net polarization found from $|\mathbf{P}| = \sqrt{P_x^2 + P_y^2}$, and accordingly for the polarization quantum.

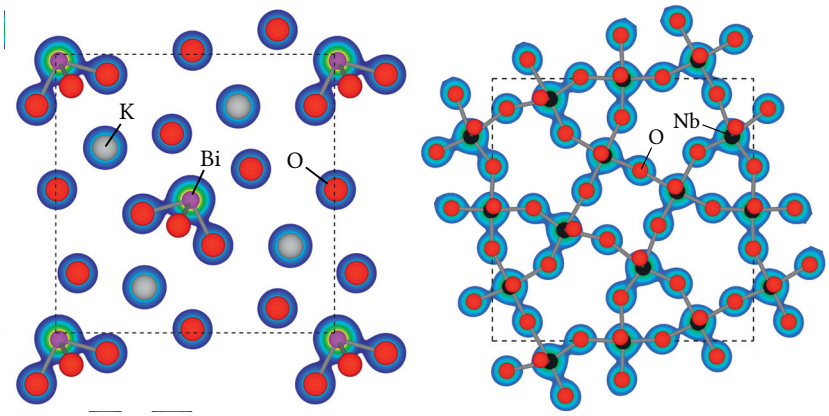

Figure 7.6 — Charge density sections for KBiN with in-plane polarization: (a) $z = 0$, showing the Bi–O interactions; (b) $z = 1/2$, showing the Nb–O bonds defining the octahedra. Sections defined by isosurface values of $0.14\,e\text{Å}^{-3}$ and $0.06\,e\text{Å}^{-3}$, respectively.

7.2 Discussion

Experimental significance

All calculations performed in this chapter are based on computationally optimized structures starting with experimental data for the structure of unfilled SBN.[271] This was done due to a lack of detailed structural data for the specific systems investigated, and is a reasonable approach given the rigidity of the octahedral framework in the TTB structure. There are, for example, very few degrees of freedom related to octahedral tilting in TTBs, as demonstrated by a recent group-theoretical analysis,[269] with only one tilt system possible within the rigid unit mode (RUM) picture. While the RUM picture is in itself an approximation, the octahedra in Nb-based TTBs are quite rigid due to the highly charged Nb^{5+}. The lattice parameters and volume, Figure 7.2, are mostly proportional to the radius of R^{3+} in KRN, indicating that the relaxed structures are reliable. At the same time, it must be kept in mind that in the current calculations, only phonons at the gamma point of the Brillouin zone are considered. This rules out the possibility of instabilities that lead to an increased unit cell, such as the $\sqrt{2}\times\sqrt{2}\times2$ cell commonly observed in TTBs.[123] Nevertheless, as ferroic transitions arise only from gamma-point instabilities, the present analysis should give a strong indication

of the ferroic properties.

The smooth, almost linear, variation in lattice parameters with R^{3+} radius for KRN compounds is contrasted by the variation in T_C as reported by Scott, Figure 2.16(a), where a large step is found between KNdN and KLaN. The same plot was redrawn by Zhu and colleagues in a recent review of structure–property relations in TTBs.[15] In the present work, unstable phonons are found for all compounds in the KRN system, with phonon frequencies varying smoothly with the radius of R^{3+} (Figure 7.3). Assuming that strongly negative frequencies imply large distortion mode amplitudes in the relaxed structures, this also implies a smooth variation in T_C, which is normally proportional to the distortion mode amplitude in displacive ferroelectrics.[279] This behaviour is in accordance with the T_C variation reported by Neurgaonkar, Figure 2.16(b), and it seems likely that the results reported by Scott are a consequence of inability to distinguish between the two transitions [$4/mmm \rightarrow 4mm$ at T_{C2} and $4mm \rightarrow mm2$ at T_{C1} in Figure 2.16(b)]. The trend seen in Figure 7.3 shows that for smaller R^{3+} cations, there is less difference in stability between the two modes, and a significant difference between T_{C1} and T_{C2} is to be expected. For larger R^{3+}, the in-plane mode frequency approaches zero, and the transition at T_{C1} presumably becomes difficult to observe.

Ferroelectric mechanism and role of lone pair cations

The out-of-plane polar mode seems to be an inherent feature of ferroelectric TTBs containing Nb. From previous computational work on unfilled TTBs (Chapter 5 and ref. [264]), it is known that a similar mode exists for all possible cation configurations in the unfilled SBN system, and hence can be described as robust with respect to cation–vacancy disorder. The results in this chapter point to the strongly unstable in-plane mode in KBiN being an exception, and closely linked to the presence of the lone pair cation Bi^{3+} on the A1 sites. To test this hypothesis, a comparison was made between KLaN and KBiN, and the corresponding compounds where K is replaced by Tl (TlLaN and TlBiN, respectively). K^+ and Tl^+ have similar ionic radii (1.64 Å and 1.7 Å, respectively[128]), but Tl^+ is similar to Pb^{2+} and Bi^{3+} in having a stereochemically active lone pair.[†] Relaxation and phonon calculations was performed in the same way for the Tl-containing compounds as for the KRN series. The squared phonon frequencies for the four compounds are plotted in Figure 7.7 (the data on KBiN and KLaN were also included previously in Figure 7.3). In general, TlLaN and TlBiN behave similarly to their potassium counterparts. The out-of-plane frequency is the

[†] Tl^+ is also extremely toxic,[280] making the cation substitution $K^+ \longrightarrow Tl^+$ interesting primarily as a pure computer experiment.

most strongly negative, and varies little between the four cation combinations. The in-plane frequency is almost zero for the La-containing compounds, and strongly negative for the Bi compounds, regardless of which cation occupies the A2 sites. The tendency for in-plane polar distortions is thus linked to the presence of the lone pair cation Bi^{3+} on the A1 sites.

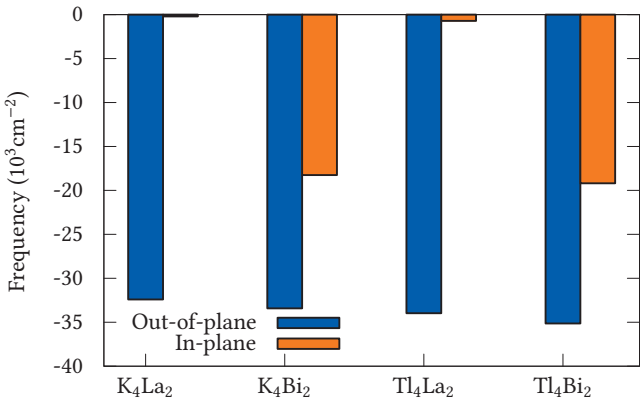

Figure 7.7 — Squared phonon frequencies for the four end members of the quaternary system $(K, Tl)_4(La, Bi)_2Nb_{10}O_{30}$. Note the dependency of the in-plane frequency on the presence of Bi at A1 sites.

The above results suggest that the presence of another lone pair cation, Tl^+, on the A2 sites, has no qualitative influence on the lattice dynamical behaviour. To expand further on this observation, the system $M_6Ti_2Nb_8O_{30}$ (MTN) with M = Ba, Sr, Pb was investigated in a similar manner. MTN is a group of filled TTBs with only one type of cation on the A1 and A2 sites, and the insulating nature of the compounds is ensured by substituting two out of ten Nb cations with Ti.[101] Under the assumption that Ti^{4+} and Nb^{5+} behave similarly (both being d^0 cations with six-coordinated radii of 0.605 Å and 0.64 Å, respectively[128]), the MTN system can be regarded as a model system that is similar to unfilled BN, SN and PN, but without the added complexity of cation–vacancy disorder on the A1 and A2 sites. Relaxation and phonon calculations for the MTN system resulted in the squared phonon frequencies plotted in Figure 7.8, which shows how the out-of-plane and in-plane phonon frequencies vary when Pb is gradually substituted for Ba and Sr in the $(Pb, Ba)_6Ti_2Nb_8O_{30}$ and $(Pb, Sr)_6Ti_2Nb_8O_{30}$ systems. The mixed compositions $Pb_2M_4Ti_2Nb_8O_{30}$ were created by placing Pb on the A1 sites and Sr or Ba on the A2 sites (*vice versa* for $M_2Pb_4Ti_2Nb_8O_{30}$), keeping the

cation distribution at all times in accordance with the general TTB formula. The MTN compositions studied are therefore not only different in terms of chemical composition, but also different in terms of cation configuration, and it is not necessarily obvious how to deconvolute these effects.‡

In analogy to the unfilled PN and SBN systems, the out-of-plane frequency for MTN [Figure 7.8(a)] is most strongly negative for the Ba/Sr-rich compositions, and least strongly negative for the Pb-rich. At the same time, the in-plane frequency [Figure 7.8(b)] reaches its most negative value for the compositions $Pb_2Ba_4Ti_2Nb_8O_{30}$ and $Pb_2Sr_4Ti_2Nb_8O_{30}$, that is, with 33 % Pb and 67 % Ba or Sr, and Pb occupying the A1 sites. The behaviour of the MTN system thus mirrors the behaviour of the KRN system with respect to the presence and localization of the lone pair cations Pb^{2+} and Bi^{3+} on the A1 sites. One contrasting point is that $Pb_6Ti_2Nb_8O_{30}$ [rightmost points in Figures 7.8(a) and (b)] does not have a particularly strong in-plane instability, while unfilled PN is known experimentally to have an in-plane polarization (see Chapter 6). One reason for this difference, as discussed above, could be the fact that only zone-center (gamma-point) phonon calculations have been performed for KRN and MTN, excluding instabilities that lead to an increase of the unit cell size. $Pb_6Ti_2Nb_8O_{30}$, like unfilled PN, has been reported to crystallize in a $\sqrt{2} \times \sqrt{2} \times 1$ supercell with space group symmetry *Amm*2,[284] and it is possible that phonons at other points in the Brillouin zone are required to properly describe the behaviour of these compounds.

The unfilled $(Pb, Ba)_5Nb_{10}O_{30}$ (PBN) system is similar to the $(Pb, Ba)_6Ti_2Nb_8O_{30}$ system (MTN with M = Pb, Ba), apart from the former having only Nb at the B sites and one vacant A site. The PBN system has been well characterized experimentally, owing to its morphotropic phase boundary (MPB) and corresponding peak in piezoelectric properties at 40 % Ba.[11] In light of the results discussed here, the location of the MPB in PBN is probably not directly determined by the chemical composition, but more likely by the cation distribution, in combination with the effect of cation size on the lattice parameters, as was also suggested by Francombe.[11] Starting from pure PN and gradually substituting Ba for Pb, the Ba^{2+} cations preferentially locate on the A2 sites, while Pb^{2+} remains on A1. This corresponds to a transition from the Pb_6 case towards the Pb_2M_4 case, without going *via* the cation distribution of the M_2Pb_4 case. The presence of Pb^{2+} on A1 sites ensures the possibility of in-plane distortion, while the lattice expansion from replacing Pb with Ba on A2 presumably makes

‡One possible strategy to eliminate the effect of cation configuration would be to employ the virtual crystal approximation (VCA) in the DFT calculations.[281] In this approach, "mixed" pseudopotentials are created by linear interpolation of pseudopotentials for reasonably similar elements. VCA has been used for phonon calculations in perovskite solid solutions such as $Pb(Zr, Ti)O_3$[282] and $(Ba, Sr)TiO_3$,[283] but the approach was not applicable here, as VCA-based force calculations with VASP are at the time of writing not fully supported by PHONOPY.

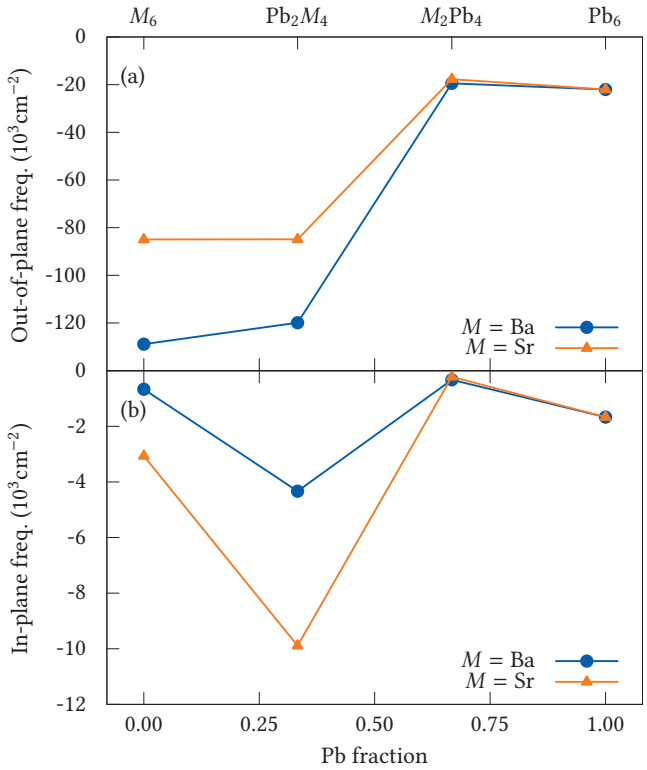

Figure 7.8 — Squared phonon frequencies for the out-of-plane (a) and in-plane (b) polar modes of the $(Pb, M)_6Ti_2Nb_8O_{30}$ systems with M = Ba, Sr. Stoichiometry is given on the bottom axis, and the cation distribution is indicated on the top axis.

the polarization switching process easier, as discussed in Chapter 6. The combined effect of this is to maximize the piezoelectric properties at the conventional MPB composition.

What is the origin of the in-plane distortion for compounds with A1-site lone pair cations? The charge density for KBiN, Figure 7.6, shows clear evidence for covalent bonds between Bi and O. In the paraelectric $P4/mbm$ structure, Bi is situated in a centrosymmetric position on the A1 sites, similar to the 12-coordinated A-site in a tetragonal perovskite. Displacement of the atoms along the eigenvector of the polar in-plane mode, followed by relaxation of atomic positions and lattice parameters, makes this coordination environment much less symmetric. In the relaxed structure, Figure 7.6(a), Bi is displaced towards four of the 12 oxygens in a square-pyramidal coordination, and the effective coordination number[§] goes from 11.9 to 5.4. This situation is reminiscent of $PbTiO_3$, in which the tetragonal ferroelectric polymorph has Pb and O arranged in a similar square-pyramidal coordination.[268] The Pb–O covalency which is responsible for this distortion was explained in Cohen's seminal paper on the origin of ferroelectricity in perovskites.[55] The same Pb–O coordination is found in the α polymorph of PbO, also known as red PbO or litharge[285] (and also in β-PbO (massicot), although more distorted[286]). The origin of the structural distortions in both α- and β-PbO have been investigated computationally,[287] and can in a similar manner to the $PbTiO_3$ case be traced to covalent interactions between the Pb 6*s* and O 2*p* orbitals.[288] This type of interaction therefore seems to be inherent to the lone pair cations Bi^{3+} and Pb^{2+}. The undistorted BiO_{12} polyhedron in aristotype KBiN is slightly elongated along *c*, with four short (2.60 Å) and eight longer (2.69 Å) bonds. The shorter in-plane bond lengths makes it much easier for an in-plane distortion to optimize chemical bonding than an out-of-plane distortion, and is manifested in a much larger "lone pair effect" for the in-plane mode than the out-of-plane mode [compare Figures 7.4(a) and 7.4(b)].

[§] The effective coordination number (ECoN) is based on the implementation in VESTA,[231] which is defined as follows:

$$\mathrm{ECoN} = \sum_i w_i, \quad w_i = \exp\left[1 - \left(\frac{l_i}{l_{\mathrm{av}}}\right)^6\right],$$

where w_i is the "bond weight" of bond i, l_i is the bond length, and l_{av} is the weighted average bond length in the given coordination polyhedron.

8

Partially reduced TTBs

8.1 Results

Electronic structure

$Ba_6Nb_{10}O_{30}$ ("filled" BN, abbreviated as f-BN in the following) has all A1 and A2 sites fully occupied by Ba^{2+}, and electroneutrality is preserved by partially reducing Nb. There are nominally two Nb^{4+} and eight Nb^{5+} per 46-atom unit cell, see Figure 8.1, corresponding to an average electron configuration of $d^{0.2}$ which opens up for possible electronic conductivity. It is not known whether the two electrons that occupy the conduction band localize preferentially on specific Nb atoms, or if they are delocalized. A metal–insulator transition has also been reported in the system $(Sr_xBa_{1-x})_6Nb_{10}O_{30}$ (f-SBN) for increasing Sr content,[102] and the mechanism for this is not known. In the following, hybrid functional and DFT+U calculations were used to find computational support for these experimental findings.

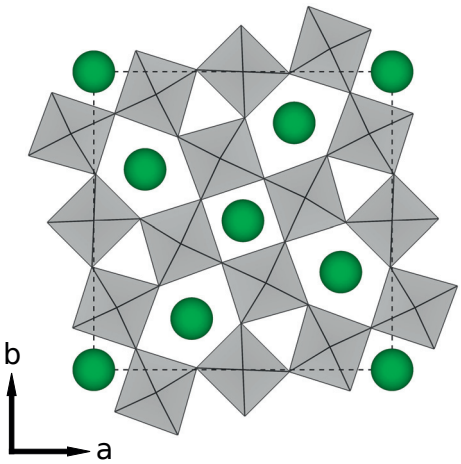

Figure 8.1 — Crystal structure of $Ba_6Nb_{10}O_{30}$ (f-BN), as reported by Kolodiaznyi *et al.* (space group symmetry $P4/mbm$).[102]

Hybrid functional calculations were performed for the reported crystal structure of f-BN,[102] shown in Figure 8.1. The results were used to calibrate less computationally expensive DFT+U calculations. A static, non-spin-polarized calculation resulted in an electronic band gap of 3.17 eV for f-BN (the term "band gap" is used for the energy

difference between the valence band maximum and the conduction band minimum, although there is a small occupation of the conduction band corresponding to the average electron configuration $d^{0.2}$). Similar calculations using DFT+U produced band gaps ranging from 2.1 to 3.4 eV when U_{eff} was varied from 0 to 12 eV, see Figure 8.2(a). A value of $U_{\text{eff}} = 10$ eV was found to reproduce the hybrid functional band gap. Relaxing the experimental structure in DFT+U calculations suggests a lower U_{eff} if experimental lattice parameters are used as the benchmark [Figure 8.2(b)], but the band gap-calibrated U value was chosen due to the focus on electronic rather than structural properties.

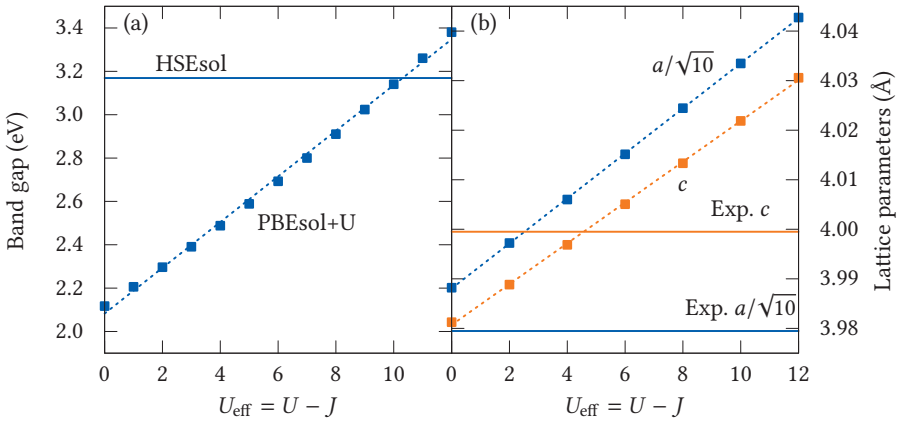

Figure 8.2 — Calibration of PBEsol+U calculations for f-BN, showing the effect of U_{eff} on electronic band gap (a) and lattice parameters (b). $U_{\text{eff}} = 10$ eV is necessary to reproduce the HSEsol band gap of 3.17 eV, while the lattice parameters suggest 0 to 5 eV. The term "band gap" refers here to the energy difference between the valence band maximum and the conduction band minimum, even though there are occupied states in the conduction band.

The charge density from spin-polarized hybrid functional calculations was analyzed according to the Bader partitioning scheme, Figure 8.3. The Bader analysis shows no support for charge ordering of the Nb d electrons between the B1 and B2 sites, as both the charges [Figure 8.3(a)] and radii [Figure 8.3(b)] are very similar for all Nb atoms. Four different Bader radii were used for each structure in the subsequent analysis: A1, A2, Nb and O, with the latter two calculated as averages of the values shown in Figure 8.3(b). The Bader radii were used to decompose the electronic density

of states (DOS) into atomic and orbital contributions. Orbital-projected DOSes for f-BN with experimental lattice parameters and atomic positions are shown in Figure 8.4. Panel (a) shows the spin-polarized DOS with ferromagnetic (FM) ordering of the spins along *c*. The corresponding non-spin-polarized DOS is shown in panel (b), both are obtained by hybrid functional calculations. The DOS obtained by DFT+U calculations after calibrating U versus the band gap of the non-spin-polarized hybrid functional calculations is shown in panel (c). All DOSes in Figure 8.4 were calculated using the experimental structure of f-BN reported by Kolodiaznyi *et al.*[102] (Figure 8.1). The FM ordering used in the spin-polarized calculations gave a lower total energy than any of the antiferromagnetic (AFM) orderings that were tested,* even though no net magnetic moment is found experimentally.[102] Based on the relatively symmetric spin-polarized DOS and the low electronic occupancy at the Fermi level, non-spin-polarized calculations were used for all subsequent calculations for f-BN and f-SN ($Sr_6Nb_{10}O_{30}$).

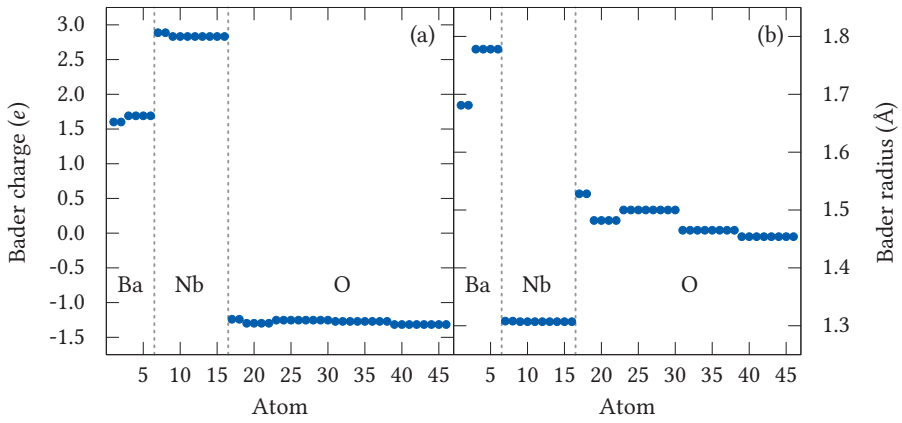

Figure 8.3 — (a) Bader charges and (b) Bader radii for f-BN at experimental geometry, obtained from spin-polarized hybrid functional calculations of the charge density. Notice the similar charge and radius on the Nb ions (atoms 7–16), and the different radii of Ba at A1 (atoms 1 and 2) and A2 (atoms 3–6) sites.

Full geometry optimization was performed for both compounds using DFT+U. For f-BN, the relaxation started from the crystal structure reported by Kolodiaznyi

*Both spin-polarized AFM and non-spin-polarized calculations give a higher energy of around 0.2 to 0.3 eV per 46 atoms compared to spin-polarized FM ordering.

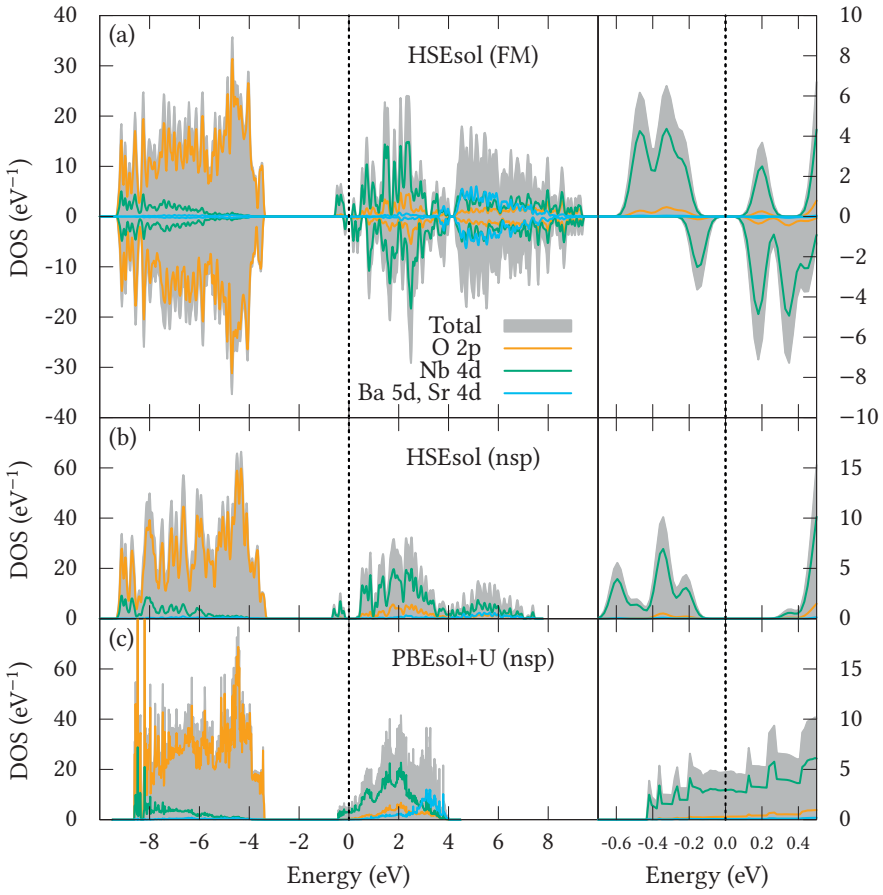

Figure 8.4 — Density of states for the experimental structure of f-BN[102] obtained by different methods: (a) Spin-polarized (ferromagnetic) hybrid functional calculations; (b) non-spin-polarized hybrid functional; (c) DFT+U. DOSes are normalized to 46-atom unit cells. Panels to the right show magnifications around the Fermi level, which is used as reference for the energy.

et al.,[102] which is given in the aristotype TTB unit cell with space group symmetry $P4/mbm$ (Figure 8.1). A corresponding tetragonal f-SN structure was obtained by using experimental atomic positions for f-BN and experimental lattice parameters for f-SN (Table 8.1), where the orthorhombic lattice parameters (o) are converted to tetragonal (t) by $a_t^2 = a_o b_o$. Consistent with Figure 8.2(b), the high U_{eff} employed here leads to an expansion of the lattice parameters for both f-BN and f-SN relative to the experimental data (Table 8.1).

Table 8.1 — Experimental and calculated lattice parameters for f-BN and f-SN during the mode following procedure. Experimental values are from Kolodiaznyi *et al.*,[102] and calculated values are reported with the same numerical precision as the experimental values. Space groups (SG) marked with an asterisk (*) correspond to larger supercells, for which the lattice parameters have been converted to "pseudo-tetragonal" parameters for easy comparison with $P4/mbm$.

f-BN				f-SN			
SG	a	b	c	SG	a	b	c
Experimental				Experimental			
$P4/mbm$	12.584		3.9995	$Amam^*$	12.379	12.350	3.8889
Calculated				Calculated			
$P4/mbm$	12.754		4.0220	$P4/mbm$	12.593		3.9834
				$Pbam$	12.680	12.623	3.9874
				$Pnma^*$	12.648	12.472	3.9323
				$P2_1/m^*$	12.623	12.568	3.9380
					($\gamma = 90.245°$)		

Dynamical stability

Phonons were calculated for f-BN and f-SN in space group $P4/mbm$ at the Γ and Z high-symmetry points of the Brillouin zone. This is assumed to capture any ferroic distortions, which arise from Γ-point instabilities, and any Z-point distortions that lead to doubling of the c parameter. f-BN is stable with respect to Γ-point distortions, while f-SN has a single unstable zone-center mode, Γ_2^+. The mode is non-polar and ferroelastic, and lowers the symmetry from tetragonal $P4/mbm$ to orthorhombic $Pbam$. The Γ_2^+ mode occurs as a stable vibration in f-BN, and its effect on the energy of f-BN and f-SN is shown in Figure 8.5(a). In addition, both compounds have a zone-boundary instability, Z_5^-, which doubles the c parameter and lowers the symmetry to

monoclinic $P2_1/m$. The effect of the Z_5^- mode amplitude on the energy of f-BN and f-SN is shown in Figure 8.5(b). For f-BN, the energy lowering is very small, bordering on the energy resolution limit of DFT, so f-BN is for all practical purposes considered to be dynamically stable in space group $P4/mbm$.

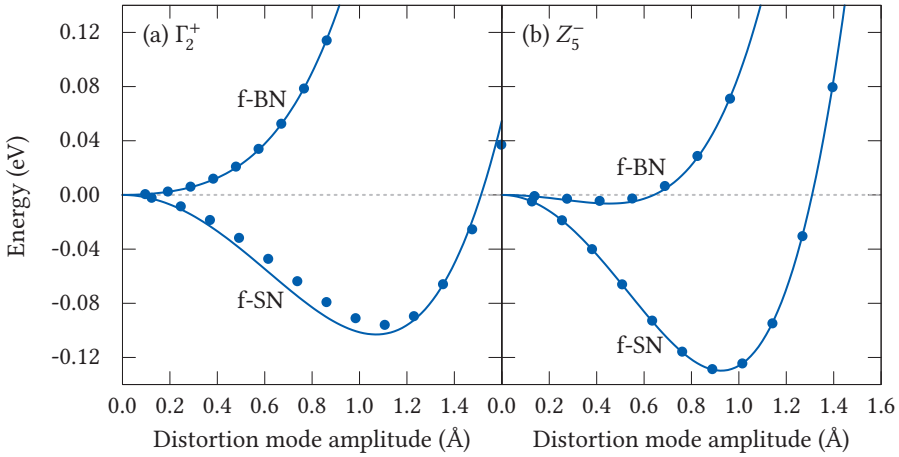

Figure 8.5 — Energy as function of mode amplitude (normalized to one unit cell)[265] for the zone-center (a) and zone-boundary (b) phonons considered in unfilled f-BN and f-SN. f-BN is dynamically stable in space group $P4/mbm$, while f-SN has instabilities that lead to orthorhombic distortion (Γ_2^+) and doubling of c through octahedral tilting (Z_5^-). Points are calculated energies, lines are fits to a Landau polynomial $\Delta E = \alpha Q^2 + \beta Q^4$.

f-SN was found to have significant instabilities both at the center and boundary of the Brillouin zone, and the ground state was searched for by "following" the unstable modes. The most strongly unstable mode in f-SN is the doubly degenerate Z_5^- [Figure 8.5(b)], although the energy relaxation for the Γ_2^+ mode is comparable [Figure 8.5(a)]. Relaxing the structure with Z_5^- frozen in at an amplitude close to the energy minimum resulted in a $1 \times 1 \times 2$ supercell with space group symmetry $P2_1/m$, which again has further instabilities at Z. If instead the Γ_2^+ mode is frozen into the $P4/mbm$ structure and relaxed, an orthorhombic cell with space group symmetry $Pbam$ results. This structure is stable with respect to Γ-point distortions, but has a further Z-point instability which leads to a $1 \times 1 \times 2$ cell with $Pnma$ symmetry. The $Pnma$ structure has no further instabilities and is therefore dynamically stable with respect to Γ- and Z-point distortions. In addition it has lower energy than the $P2_1/m$ structure, Figure 8.6, and is therefore considered the ground state structure for f-SN.

The group–subgroup relations between the space group symmetries are shown in the inset of Figure 8.6. Table 8.1 gives a comparison of the lattice parameters for all the structures considered. Atomic positions are given in Tables 8.2 and 8.3 for the dynamically stable ground state structures of f-BN and f-SN, respectively. The stable ground state for f-SN, *Pnma*, is visualized in Figure 8.7. Finally, the effect of the symmetry-lowering distortions on the electronic structure of f-SN is shown in Figures 8.8(b) to (d), which show the DOSes for f-SN relaxed in space groups *P*4/*mbm*, *Pbam* and *Pnma*, respectively, corresponding to the successive steps of the mode following procedure.

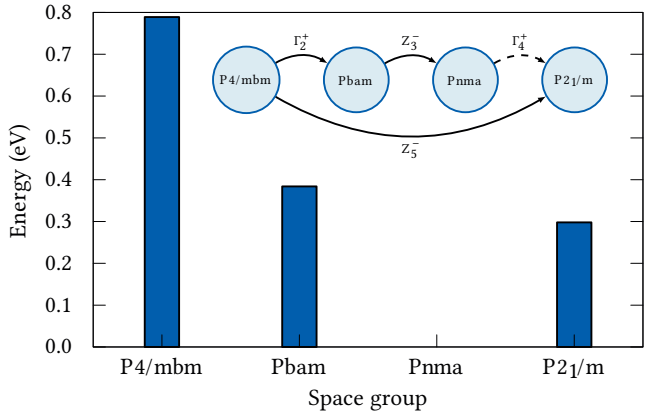

Figure 8.6 — Relative energy (per 46-atom unit cell) of f-SN following relaxation within the symmetry constraints of the relevant space groups. *P*4/*mbm* is the aristotype space group used as starting point, and *Pnma* is the dynamically stable ground state. Group–subgroup relations are shown in the inset diagram, with arrows marking energy-lowering distortions (the dashed arrow marks a distortion mode which does not lower the energy for f-SN).

8.2 Discussion

Choice of method and validity of results

Non-spin-polarized calculations were used for f-BN and f-SN despite the non-zero occupation of the conduction band in the partially reduced TTB compounds. This

Table 8.2 — Atomic positions for the dynamically stable structure of f-BN (space group symmetry $P4/mbm$).

Atom	WP	x	y	z
Ba1	2*a*	0	0	0
Ba2	4*g*	0.3318	$x + 1/2$	0
Nb1	2*c*	0	$1/2$	$1/2$
Nb2	8*j*	0.2877	0.5770	$1/2$
O1	2*d*	0	$1/2$	0
O2	4*h*	0.2212	$x + 1/2$	$1/2$
O3	8*i*	0.2930	0.5785	0
O4	8*j*	0.1569	0.4921	$1/2$
O5		0.4332	0.6397	$1/2$

Table 8.3 — Atomic positions for the dynamically stable structure of f-SN (space group symmetry *Pnma*).

Atom	WP	x	y	z
Sr1	4*c*	0.0008	$1/4$	0.4958
Sr2		0.3383	$1/4$	0.3104
Sr3		0.6322	$1/4$	0.6985
Nb1	4*a*	0	0	0
Nb2	8*d*	0.2134	0.0001	0.5783
Nb3		0.0815	0.0022	0.2922
O1	4*c*	0.5262	$1/4$	0.5237
O2	8*d*	0.2711	0.0247	0.7304
O3	4*c*	0.7663	$1/4$	0.4139
O4		0.1781	$1/4$	0.5877
O5		0.9499	$1/4$	0.7097
O6		0.1125	$1/4$	0.3070
O7	8*d*	0.3413	0.0437	0.4900
O8		0.0000	0.0310	0.1569
O9		0.0686	0.9590	0.6482
O10		0.1274	0.9799	0.4434

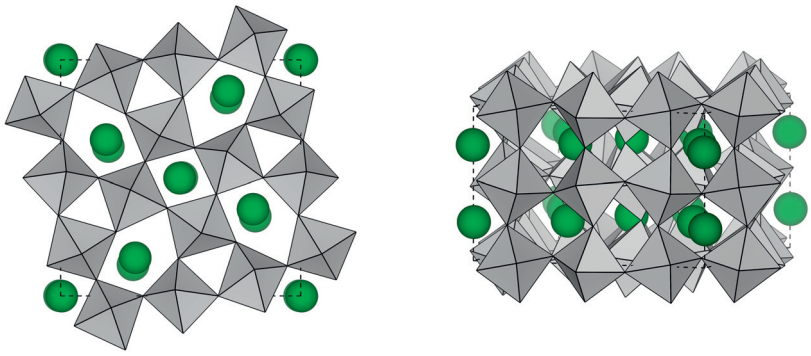

(a) (b)

Figure 8.7 — Visualization of the 1×1×2 *Pnma* supercell suggested as the dynamically stable ground state structure for f-SN: (a) "Top" view (projection along the pseudo-tetragonal axis); (b) perspective view which shows the tilted NbO_6 octahedra.

was the most convenient choice, since spin-polarized calculations would introduce an additional degree of freedom in the choice of magnetic ordering. Test calculations demonstrated that ferromagnetic (FM) ordering gives a lower total energy than the antiferromagnetic (AFM) orderings that were tested (both AFM and non-spin-polarized calculations give approximately 0.2 to 0.3 eV higher energy per 46 atoms than FM). On the other hand, experimental measurements have shown that the net magnetic moment is zero down to 1.5 K (and non-zero below due to the Meissner effect as the material becomes a superconductor),[102] so the magnetic ordering is in any case very weak. In addition, the local magnetic moments obtained in spin-polarized test calculations were found to be sensitive to changes in computational parameters, such as k-point density, type of electronic smearing, and even supercell size. The calculated magnetic structure is therefore also not very robust, which justifies the use of non-spin-polarized calculations. As stated above, the energy gain from spin-polarized calculations is low in comparison to non-spin-polarized calculations. This is consistent with the hybrid functional DOSes for f-BN [Figures 8.4(a) and (b)], which show a low density of states at the Fermi level. As an added benefit, non-spin-polarized calculations are less computationally costly than spin-polarized.

DFT+U calculations were used for all structural relaxations in this chapter. This was a choice of necessity, as the DFT+U calculations in this case performed around 50 times faster than the hybrid functional calculations, so the latter were in practice out of limits for structural optimization. The functionals used, PBEsol and HSEsol, are

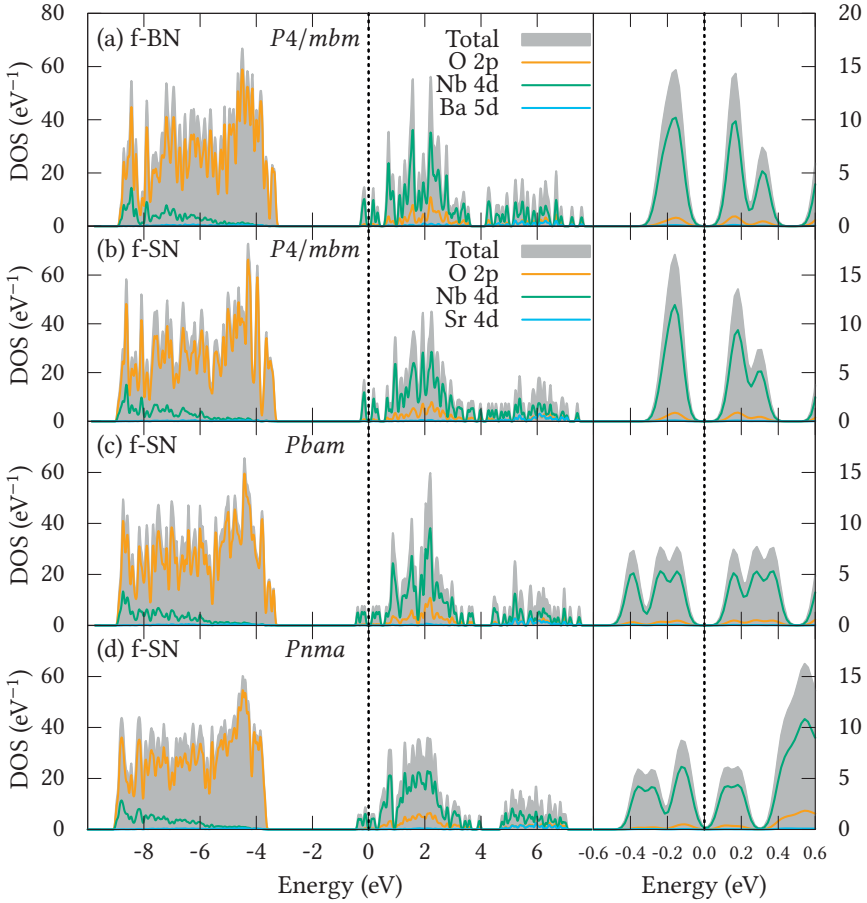

Figure 8.8 — Density of states for filled TTBs with optimized structures: (a) f-BN in space group *P*4/*mbm* (dynamically stable ground state); (b) f-SN in *P*4/*mbm*; (c) f-SN in orthorhombic *Pbam* (results from a Γ-point instability in *P*4/*mbm*); (d) f-SN in orthorhombic *Pnma* (dynamically stable ground state; results from a *Z*-point instability in *Pbam*). DOSes are normalized to 46-atom unit cells. Panels to the right show magnifications around the Fermi level, which is used as reference for the energy.

expected to give good correspondence in structural properties,[173] although it is not possible here to compare the effect on lattice parameters of the two functionals. The DFT+U calculations are calibrated against the electronic band gap obtained in hybrid functional calculations [Figure 8.2(a)], a choice made since the electronic (and not structural) properties are in focus in this work. Relaxations performed with DFT+U consistently lead to larger lattice parameters than the experimental values (Figure 8.2(b) and Table 8.1), although this would likely be the case also if hybrid functional calculations were used. The most notable difference between DFT+U and hybrid functional calculations is seen in the DOS for f-BN at experimental geometry (Figure 8.4), where the DFT+U calculation gives a non-zero DOS at the Fermi level (E_F), while a small gap opens up when the calculation is performed with HSEsol. In addition, the conduction band is much more compact within DFT+U, with a spread of around 4 eV above E_F. In hybrid functional calculations, the conduction band has an energy spread of up to 8 eV above E_F. The effect on the valence band is much smaller, which is not surprising since DFT is fundamentally a theory which describes occupied states, and the description of the unoccupied states in the conduction band should in any case be taken with caution, regardless of the level of theory within DFT.

DFT+U calculations were also used for all lattice dynamical calculations for f-BN and f-SN. Pre-relaxation to a force-based criterion of 10^{-4} eV Å^{-1} yielded well behaved phonons, with the expected zero-frequency acoustic branches at Γ in all cases. The fixed-volume energy profiles for the phonons of the $P4/mbm$ structures, Figure 8.5, follow the standard Landau polynomial form $\Delta E = \alpha Q^2 + \beta Q^4$ reasonably well. The small deviation for the Γ_2^+ mode in f-SN is most likely an effect of the fixed volume, since the mode is ferroelastic and leads to an orthorhombic strain of 0.5 % when the structure is relaxed (Table 8.1).

Consistency with experimental results

The mode following procedure followed here suggests the orthorhombic space group *Pnma* as the dynamically stable ground state for f-SN. Kolodiaznyi and colleagues[102] reported that single crystal and powder X-ray diffraction data of f-SN could be fitted "reasonably well" by using a $\sqrt{2} \times 2\sqrt{2} \times 2$ TTB supercell in the orthorhombic space group *Amam*. Fitting the same diffraction data to the 1×1×2 *Pnma* structure suggested here would be illuminating, since a detailed explanation of the choice of the *Amam* cell was not given in the work cited above. In order for lattice dynamics calculations to suggest a larger supercell, such as $\sqrt{2} \times 2\sqrt{2} \times 2$, it would be necessary to employ equally large supercells in the phonon calculations, which would again increase the computational effort. All phonon calculations performed in this work were performed with $1 \times 1 \times 2$ supercells, which limits the instability search to the Γ and Z points of

the Brillouin zone. The present approach still seems to describe much of the essential physics of the filled TTBs correctly, since it predicts f-BN to be stable in $P4/mbm$ and f-SN to have an orthorhombic distortion and a cell doubling along c. Despite this, there is of course a possibility that using larger supercells in the calculations would lead to the discovery of further instabilities than the ones presented here.

The structural properties of f-BN and f-SN are, at least on a qualitative level, well reproduced by the chosen computational procedure. The electronic properties are not known in as much detail, and one of the obvious questions to ask for a compound with a partially occupied conduction band is whether the d electrons are localized on particular Nb atoms. Bader charge analysis, Figure 8.3(a), does not support this, as Nb1 and Nb2 are calculated to have identical charges (the small difference in charge between Nb1 and Nb2 is within the accuracy limit of the method, since also Ba and O show small variations in charge between non-equivalent atomic positions). It is assumed that hybrid functional calculations give an improved description of electronic properties with respect to DFT+U, and the effect of the different levels of theory is easily seen by comparing the DOSes for f-BN calculated with the two methods [Figures 8.4(b) and (c)]. The DFT+U DOS predicts metallic behaviour, with a non-zero occupancy at E_F, while the hybrid DOS approaches zero, which can be attributed to an improved description of electron correlation. Still, even the hybrid functional results should be taken with caution, as metal–insulator transitions are in general not easily described by DFT.[†] The charge analysis in Figure 8.3 is performed for a spin-polarized charge density calculated with HSEsol, but this does still not predict charge ordering on Nb. It is of course possible that the d electrons actually are perfectly delocalized, corresponding to the average $d^{0.2}$ electron configuration dictated by the stoichiometry.

The electronic densities of states for f-BN and f-SN optimized in the $P4/mbm$ structure (Figures 8.8(a) and (b), respectively) are qualitatively more or less identical. In both materials, the DOS around the Fermi level is split in two bands, as shown in the magnified sections in Figure 8.8. In each case, the lower band contains the two d electrons, while the upper band is empty. The structural distortions in f-SN have the effect of splitting these bands further, as shown in the DOS for f-SN optimized in *Pbam* and *Pnma* (Figures 8.8(c) and (d), respectively). In the *Pnma* structure, the first band above E_F contains only a single empty state, and all higher-lying states are a part of the continuous conduction band. Anderson localization[295] has been

[†]This is a fundamental difficulty in all mean-field theories, DFT included, in which individual electron–electron interactions (correlation) are replaced by interactions between single electrons and the average electron density. One alternative is dynamical mean-field theory (DMFT),[289–292] which has been shown to be able to describe metal–insulator transitions (MITs) in strongly correlated materials such as VO_2[293] and $LaTiO_3$.[294]

suggested as the mechanism behind the metal–insulator transition in the filled SBN system [$(Sr, Ba)_6Nb_{10}O_{30}$ or f-SBN],[102] and also in the unfilled, reduced SBN system [$(Sr, Ba)_5Nb_{10}O_{30-\delta}$ or r-SBN].[84] For the latter, a schematic DOS was suggested based on the Anderson localization mechanism (Figure 8.9).

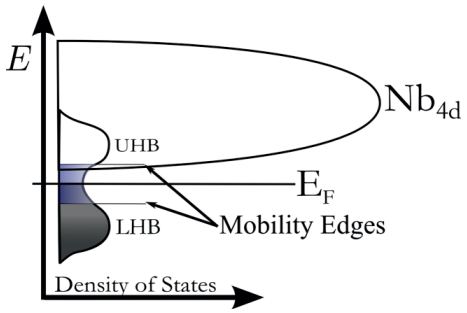

Figure 8.9 — Schematic DOS for oxygen-deficient r-SBN proposed by Bock and co-workers.[84] At low temperature, the material is an insulator due to *Anderson localization*:[295] Oxygen vacancies create an impurity band at E_F, which splits into upper (UHB) and lower Hubbard sub-bands (LHB). When the impurity states are disordered, the states at the edges of the sub-bands are localized, which makes the material insulating even though there is a non-zero DOS at the Fermi level.

The oxygen-deficient r-SBN is similar to f-SBN in the sense that both materials contain partially reduced niobium (in f-SBN, there are formally two d^1 Nb^{4+} and eight d^0 Nb^{5+} per 46-atom unit cell). In the work on r-SBN by Bock *et al.*,[84] the electronic structure is discussed in terms of defect states induced by the oxygen vacancies. In f-SBN, on the other hand, the "defect" with respect to stoichiometric, unfilled SBN ($(Sr, Ba)_5Nb_{10}O_{30}$) is an additional Sr^{2+} or Ba^{2+}, which is not disordered and does not directly influence the DOS in the vicinity of E_F. Instead, the material can be considered to be "electron doped", in the sense that only the occupancy of the conduction band is changed, without any additional defect states in or close to the band gap. The DOS close to E_F in f-BN and f-SN (Figure 8.8) does indeed bear resemblance to the sub-band structure shown schematically in Figure 8.9, and it can be noted that Anderson localization is possible in f-SN in light of the disordered distribution of Nb^{4+} suggested by the charge analysis.

9 Rhombohedral lead metaniobate

The content of this chapter is based on ref. [276].

9.1 Results

Diffraction experiments

Rhombohedral lead metaniobate, ($PbNb_2O_6$, abbreviated r-PN in the following), has attracted far less attention than the TTB polymorph. The initial report on r-PN in 1956 by Francombe[6] claimed that there was no evidence for any ferroelectric behaviour in the material. Much of the subsequent literature has therefore focused on avoiding formation of the r-PN phase and stabilizing the ferroelectric TTB-PN phase, which is thermodynamically metastable with respect to r-PN. The crystal structure of r-PN, shown in Figure 9.1, is not known to occur in other compounds except $PbRe_2O_6$[296] and possibly $PbTa_2O_6$.[100]

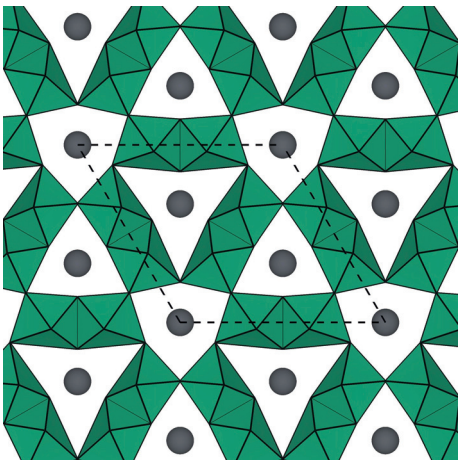

Figure 9.1 — Crystal structure of r-PN as reported by Mahé in 1967,[118] and used as starting point for the Rietveld refinement. Space group *R*3*m*, hexagonal setting, projection along *c* (unit cell marked by dashed line).

The initially reported space group symmetry *R*3*m* is polar, which in principle allows for functional properties such as pyro- and ferroelectricity. This was also suggested in 1985 by a Soviet group who found evidence for a polar–non-polar phase

transition in r-PN at 815 °C.[119] However, as the available structural data was of low quality, a re-examination of the crystal structure of r-PN was done in order to obtain a good starting point for computational investigations of possible functional properties.

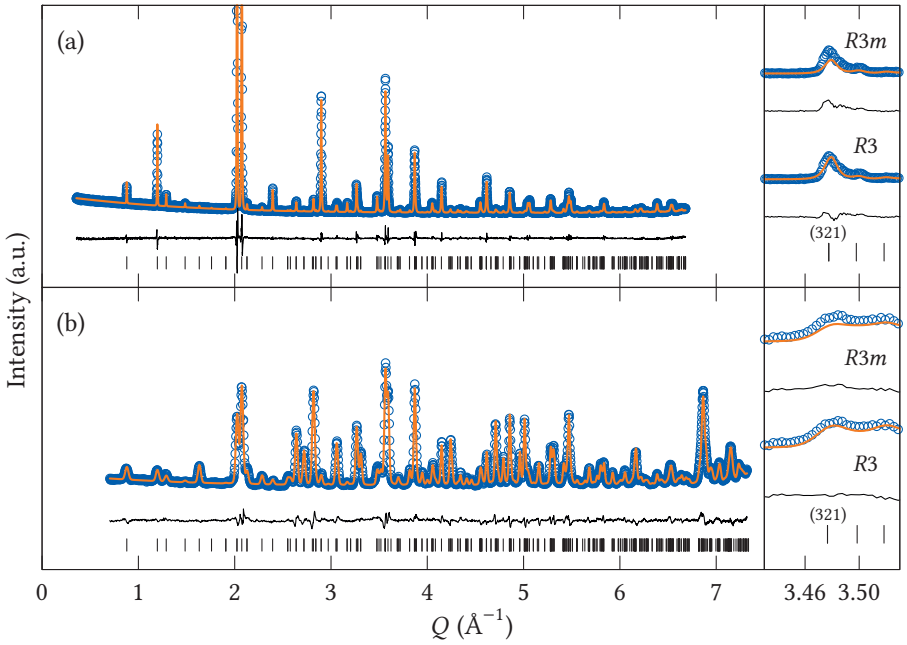

Figure 9.2 — (a) Powder X-ray and (b) powder neutron diffractograms, showing observed (blue circles) and calculated (orange line) intensity for space group $R3$, and their difference (black line) as a function of the scattering vector $Q = 2\pi/d$. Black tick marks show the position of individual Bragg reflections. Zoom-in to the right shows a comparison between refinements within space groups $R3$ and $R3m$.

Both X-ray and neutron diffraction experiments were performed on r-PN powder samples, and full Rietveld refinement was performed starting from the structural data reported by Mahé[118] (Appendix B). Five possible space group symmetries were considered: $R3$, $R\bar{3}$, $R32$, $R3m$ and $R\bar{3}m$. All five have the same selection rules for diffraction, so the distinction between the different candidate space groups relies only on the intensities of the Bragg reflections. X-ray and neutron diffractograms are shown in Figure 9.2 together with Rietveld refinements within space group $R3$, which gave the best fit both for the two datasets separately and for simultaneous

refinement. The goodness of fit for the different space groups is summarized in Table 9.1 together with lattice parameters from the refinements. Space group $R\bar{3}m$ yielded the worst fit, and gave rise to a systematic deviation for certain reflections between experimental data and the fit. Also the previously reported[117] space group $R3m$ gave systematic deviations for certain reflections, and a magnification of the representative (321) reflection is shown in the insets of Figure 9.2, comparing the fit for space group $R3m$ and $R3$. Similar deviations of comparable magnitude are apparent also in other reflections throughout the Q range, notably the $(1\bar{4}\bar{3})$ and $(03\bar{7})$ reflections at approximately $Q = 4.55\,\text{Å}^{-1}$ and $Q = 6.52\,\text{Å}^{-1}$, respectively. For space group $R3$, which gave the best fit, both the experimental (joint refinement of X-ray and neutron diffraction data) and the optimized atomic coordinates are given in Table 9.2. For all space groups, the refined structures show distinct differences from the previously reported structures, which have been refined in space group $R3m$.[118,275] The most pronounced difference is that the $NbO_{6/2}$ octahedra are far less deformed, with less variation in the Nb–O bond lengths (further discussed below).

Table 9.1 — Lattice parameters at room temperature, and quality of fit for joint refinement of X-ray and neutron data within each of the five space groups considered (estimated standard deviations in parenthesis). Literature values for $R3m$ (converted from hexagonal setting) are included at the bottom.

Space group	Lattice parameters		Quality of fit		
	a (Å)	α (°)	R_p(%)	R_{wp}(%)	χ^2
$R3$	7.17530(7)	93.9548(5)	6.62	9.05	1.89
$R\bar{3}$	7.17530(7)	93.9552(5)	6.85	9.29	1.94
$R32$	7.17508(9)	93.9566(6)	8.21	11.66	2.44
$R3m$	7.17521(8)	93.9555(6)	7.65	10.69	2.23
$R\bar{3}m$	7.17516(10)	93.9564(6)	8.51	11.93	2.49
$R3m$[117]	7.183	93.94			
$R3m$[275]	7.1654	93.908			

Computational results

Additional information on the relative stability of the different space groups is obtained from the calculated energies of the candidate structures. The energies of the possible structures are shown in Figures 9.3(a) to (c), corresponding to three different relaxation constraints. For full relaxation with no volume constraints, the volume after relaxation

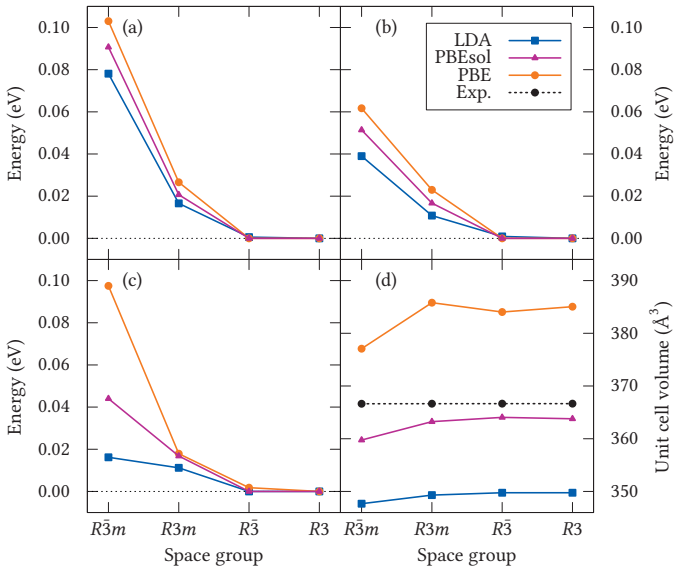

Figure 9.3 — Calculated energy per formula unit for each of the space groups considered, after ionic relaxation at (a) experimental lattice parameters; (b) relaxation of ions and lattice vectors at constant experimental volume; (c) unconstrained relaxation of ions and lattice vectors. (d) Relaxed unit cell volumes in comparison to the experimental value.

is shown in Figure 9.3(d). All energies are reported per formula unit of $PbNb_2O_6$, and given relative to the structure with the lowest symmetry, $R3$. The energy of the $R32$ structure is omitted from the figures, since this experimental structure relaxes into the higher-symmetry space group $R\bar{3}m$. Because of this apparent instability, and the relatively poor goodness of fit for Rietveld refinement within this space group (Table 9.1), $R32$ was not considered further as a plausible space group symmetry for r-PN at ambient temperature.

For the three space groups $R\bar{3}m$, $R3m$ and $R3$, the calculated energies correlate with the degree of symmetry, with $R\bar{3}m$ having the highest symmetry and the highest calculated energy, $R3m$ intermediate, and $R3$ the lowest. $R\bar{3}$, however, does not follow this trend: It has essentially the same energy as $R3$, while at the same time possessing a higher symmetry and merely half as many atomic degrees of freedom as $R3$ (Table 9.2). This result is the same for all the relaxation methods used. Lattice dynamical

calculations similarly show negligible difference between the dynamical stability of the $R\bar{3}$ and $R3$ structures, while the $R3m$ and $R\bar{3}m$ structures have instabilities which correlate with their higher energy.

Atomic positions for the $R3$ structure, both experimental (joint refinement) and after computational optimization (full relaxation with the PBEsol functional), are given in Table 9.2.

Table 9.2 — Atomic positions and unit cell parameters ($R3$, rhombohedral setting) based on joint refinement of diffraction data, and after geometry optimization by DFT calculations (PBEsol, unconstrained relaxation). B_{iso} are isotropic thermal displacement factors, constrained to be the same for all atoms of the same element.

	Experimental				Optimized		
Atom	x	y	z	B_{iso} (Å^2)	x	y	z
Pb1	0	0	0	1.48(3)	0	0	0
Pb2	0.3527(4)	0.3527(4)	0.3527(4)	1.48(3)	0.3527	0.3527	0.3527
Pb3	0.6889(5)	0.6889(5)	0.6889(5)	1.48(3)	0.6764	0.6764	0.6764
Nb1	0.5338(11)	0.2006(9)	0.8384(10)	0.06(3)	0.5403	0.1965	0.8405
Nb2	0.1531(10)	0.5117(8)	0.8068(9)	0.06(3)	0.1562	0.5122	0.8123
O1	0.404(2)	0.947(2)	0.678(2)	0.40(3)	0.403	0.959	0.678
O2	0.9617(14)	0.3878(14)	0.668(2)	0.40(3)	0.9501	0.3941	0.675
O3	0.760(2)	0.773(2)	0.065(2)	0.40(3)	0.772	0.772	0.058
O4	0.055(2)	0.053(2)	0.5216(14)	0.40(3)	0.058	0.058	0.5129
O5	0.571(2)	0.580(2)	0.293(2)	0.40(3)	0.581	0.581	0.294
O6	0.292(2)	0.294(2)	0.8515(12)	0.40(3)	0.295	0.295	0.8398
a (Å)	7.17530(7)				7.15572		
α (°)	93.9548(5)				94.0297		
V_{cell} (Å^3)	366.652(11)				363.551		

High-temperature behaviour

High-temperature X-ray diffraction (HTXRD) was used to characterize the crystal structure of r-PN at non-ambient temperatures. Two separate experiments were performed in order to cover a wide range of temperatures. Lattice parameters for both experiments, obtained by Pawley fitting at each temperature, are presented as a function of temperature in Figure 9.4. The hexagonal c parameter, which corresponds to the polar direction in space group $R3$, contracts up to a temperature of (780 ± 5) °C,

after which it expands again. The a parameter is less affected, but shows a clear change in slope at this temperature.

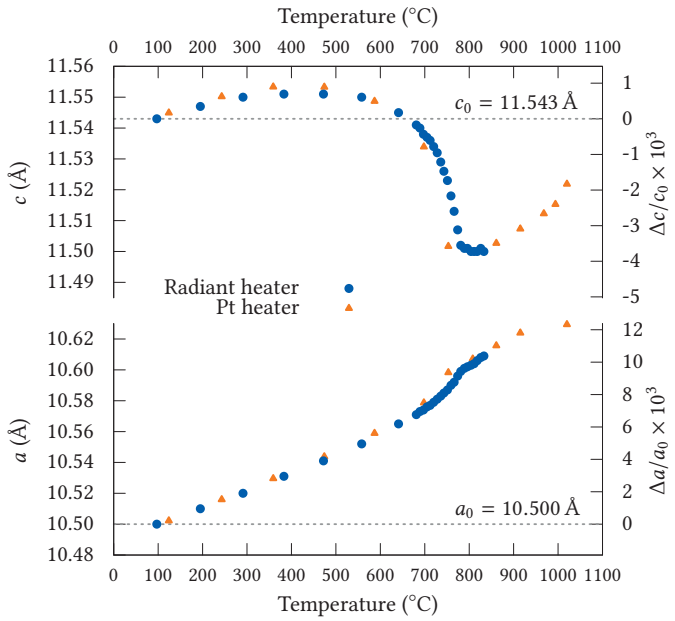

Figure 9.4 — Lattice parameters, obtained by Pawley fitting, for r-PN as a function of temperature (hexagonal setting). Space group $R3$ was used for fitting up to $T = 780$ °C, and $R\bar{3}m$ above. The relative change with respect to the ambient temperature lattice parameters (dashed lines) are given on the secondary axis.

The possible phase transition at 780 °C was investigated by dilatometry and differential thermal analysis (DTA). The results of the thermal characterization are presented in Figure 9.5. The DTA data, Figure 9.5(a), show an endothermic (exothermic) response during heating (cooling), in both cases at a temperature of (780 ± 5) °C, with little thermal hysteresis. The dilatometry data, Figure 9.5(b), demonstrate a significant thermal hysteresis, with a change in slope of the thermal expansion curve at around 800 °C upon heating, and at 520 °C during cooling.

Finally, dielectric impedance spectroscopy was used to check for a possible dielectric response associated with the phase transition. The relative dielectric permittivity is plotted in Figure 9.6, with emphasis on the temperature range where the phase

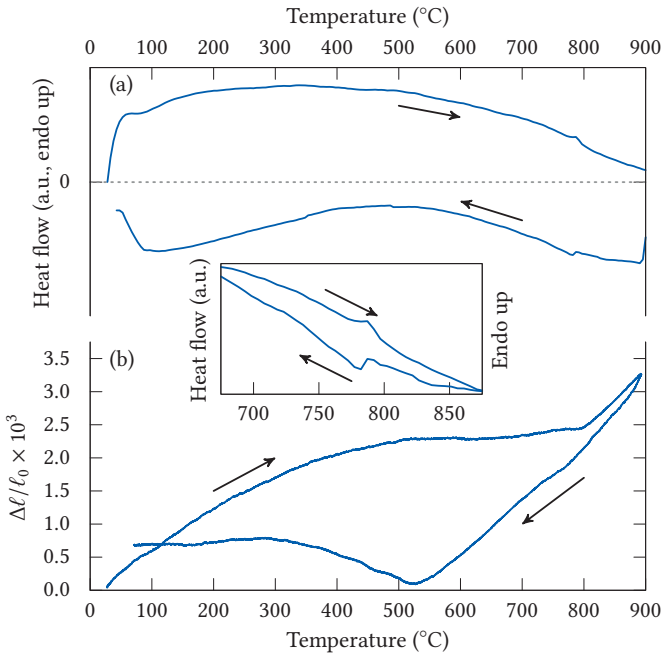

Figure 9.5 — Thermal analysis of r-PN. (a) DTA: Full heating and cooling curves are shown in main plot; inset shows a magnification of the relevant temperature range, with curves shifted in the y direction for easier comparison of peak positions (heating and cooling rate 5 °C min^{-1}). (b) Thermal expansion of a dense ceramic sample (heating and cooling rate 5 °C min^{-1}).

transition is observed by HTXRD, DTA and dilatometry. From room temperature and up to around 300 °C, the permittivity is constant at values of 100–1000 depending on measurement frequency. At higher temperatures, the dielectric response shows a monotonic increase, visible from around 500 °C in the main plot in Figure 9.6. This increase is presumably due to electrical conductivity, and the inset of Figure 9.6 demonstrates that the response is completely regular in the temperature range where the phase transition is expected. There is in other words no significant dielectric response associated with the phase transition. Dielectric loss data (not shown) did not contribute to additional knowledge about the material.

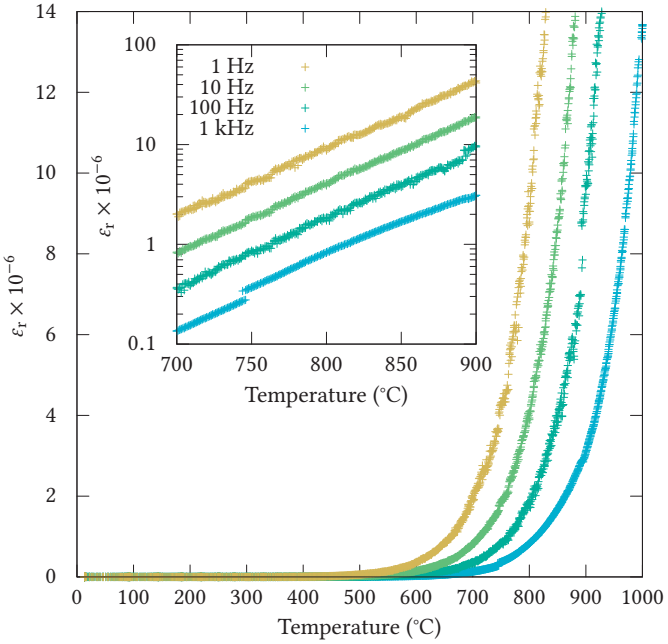

Figure 9.6 — Relative permittivity for r-PN as a function of temperature. Inset shows a logarithmic plot for the same temperature range as the inset of Figure 9.5.

9.2 Discussion

Space group symmetry at ambient temperature

Both refinement of the diffraction data and comparison of DFT energies point to either of $R\bar{3}$ or $R3$ as the most likely space group symmetries for r-PN at ambient conditions. This is in contrast to earlier works,[117,118] which conclude that the space group is $R3m$. Figure 9.7 gives the group–subgroup relations between the five space groups considered in this work. The path involving space group $R32$ can be excluded based on the poor Rietveld fit (Table 9.1) and the instability with respect to force-based geometry optimization.

The difference in quality of fit is quite small between $R3$ and $R\bar{3}$, as is evident from Table 9.1. A reasonable way of testing the statistical significance of this difference is by Hamilton's R-ratio test,[297,298] which is based on the well-known F-test. In the

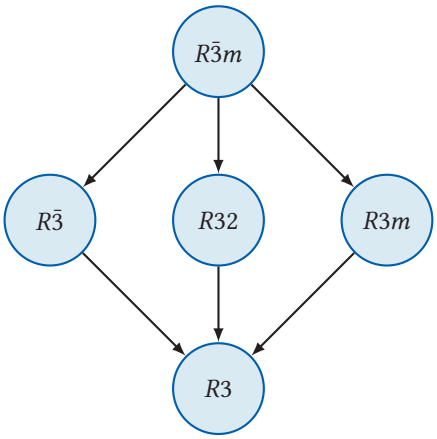

Figure 9.7 — Group–subgroup relations between the space group symmetries considered for r-PN.

present case, the ratio of R_{wp} factors for the $R\bar{3}$ and $R3$ refinements is $\mathcal{R} = 1.027$. For the joint refinement, the total number of (hkl) reflections is 730, with 60 parameters refined for $R3$ and 47 for $R\bar{3}$ (the difference of 13 corresponding to the difference in atomic degrees of freedom between the space groups). From Hamilton's table,[297] the value $\mathcal{R}_{13,670,0.005} = 1.023$ can be read off, meaning that the probability of $R3$ actually being a better model than $R\bar{3}$ for this particular refinement, is higher than 0.995. The same result is obtained if the X-ray and neutron diffraction data are refined and tested individually, so it is safe to conclude that $R3$ is a significantly better model than $R\bar{3}$.

In addition to the rhombohedral space group symmetries shown in Figure 9.7, refinements within further subgroups of $R3$ and $R\bar{3}$ could in principle also be included, *i.e.*, the trigonal groups $P3$ (143), $P3_1$ (144), $P3_2$ (145) and $P\bar{3}$ (147). $P3_1$ and $P3_2$, however, can be excluded, as the 3-fold screw axes are not compatible with the stacking pattern found in this structure (further described below). $P3$ and $P\bar{3}$, although possible from a structural point of view, do not yield a better fit than $R3$, despite a higher number of refined parameters for the trigonal groups. Based on this, there is no apparent reason not to keep the rhombohedral lattice centering, restricting the possible space groups to those shown in Figure 9.7.

A general observation for all energy calculations, is that $R\bar{3}m$ has the highest energy, $R3m$ intermediate, and $R\bar{3}$ and $R3$ are essentially at the same, lowest energy. This is true for all methods of geometry optimization, and for all functionals, as shown in Figures 9.3(a) to (c). In practice, the experimental $R3$ structure relaxes towards

$R\bar{3}$ symmetry, and the distinction between them is ultimately a matter of tolerance during the symmetry analysis.[255] For the constrained relaxations, Figures 9.3(a) and (b), the $R3$ structure is regarded as having $R\bar{3}$ symmetry for tolerances higher than $3 \cdot 10^{-4}$ if relaxed with PBE, and $3 \cdot 10^{-2}$ if relaxed with PBEsol. For the unconstrained relaxation, Figure 9.3(c), the threshold values are $5 \cdot 10^{-4}$ for LDA and $1 \cdot 10^{-3}$ for PBEsol. In other words, the structures relaxed using PBEsol give the largest structural differences between $R3$ and $R\bar{3}$, although the two space groups are hard to distinguish in all cases.

The graphs in Figure 9.3 confirm certain well-known properties of the functionals used.[182] LDA has an inherent tendency to over-bind, which is reflected in a relaxed cell volume which is smaller than the experimental volume by around 5 %, as seen in Figure 9.3(d). The PBE functional, on the other hand, slightly over-corrects this deviation, producing a unit cell volume which is around 5 % *larger* than the experimental value. The PBEsol functional is intended to improve on PBE for equilibrium properties of solids such as bond lengths and lattice parameters,[229] and the volume calculated with PBEsol comes very close to the experimental volume. This difference between the functionals is also reflected in the energies for the different space groups. As spontaneous polarization in solids requires a certain volume for the displacement of ions, the under-binding PBE functional is expected to favour polar space groups more than the over-binding LDA. For all calculations, PBE gives the largest energy difference between the polar $R3$ and the non-polar $R\bar{3}m$, and LDA the smallest. The effect of this is most pronounced for the unconstrained relaxations as shown in Figure 9.3(c).

While the diffraction data is convincing, $R3$ and $R\bar{3}$ are still so similar in structure and energy that care must be taken to properly distinguish between them. The difference between the space group symmetries $R3$ and $R\bar{3}$ is the presence of an inversion center in the latter, making the space group non-polar. This is obviously important for applications of the material, as for example pyro- and ferroelectricity requires a polar space group. A Soviet work from 1985 suggests that the rhombohedral $R3m$ polymorph transforms to the non-polar space group $R\bar{3}m$ at high temperatures,[119] based on the observed contraction of the polar axis (hexagonal [001] direction, rhombohedral [111] direction) upon heating to 815 °C, followed by regular thermal expansion. Such an anisotropic thermal expansion would be expected to accompany the transition from a polar to a non-polar space group, *e.g.*, from $R3m$ to $R\bar{3}m$ or from $R3$ to $R\bar{3}$, while a transition between two polar (or two non-polar) space groups is likely to be much more subtle. The anisotropic thermal expansion, Figure 9.4,suggests that the ambient-temperature space group is polar and that the high-temperature structure is non-polar. This, in addition to the statistical significance of the R_{wp} factors from the refinement, makes $R3$ the most probable space group symmetry for r-PN at ambient

temperature.

Description of the crystal structure

The main characteristic features of the crystal structure of r-PN are illustrated in Figure 9.8. Rhombohedral lead metaniobate is not a "layered" structure in the usual sense, although it is natural to picture it as being built from layers due to the anisotropy in crystal structure, polyhedral connectivity and bonding. The fundamental building blocks are *dimer* units, made up of two edge-sharing NbO_6 octahedra as shown in Figure 9.8(a). The dimers are corner-linked, creating layers or sheets as shown in Figure 9.8(b). The layers have a point group symmetry which is nearly hexagonal, although, as will be further discussed below, the point group symmetry of the crystal is trigonal due to the stacking sequence and the polyhedral connectivity between layers.

Three different kinds of rings of corner- and edge-sharing octahedra can be identified in the layers: One hexagonal, and two triangular rings that are symmetrically inequivalent. In Figure 9.8(b), the hexagonal ring (yellow) is in the middle, surrounded by six triangular rings (red and blue). Each of the triangular rings is pointing either up (red) or down (blue) within the plane of the figure, thereby distinguishing the two types. In a single layer of ideal hexagonal symmetry ($P6/mmm$), the two triangular rings would be equivalent. The layers are stacked as shown in Figure 9.8(c), with a repeating sequence of three layers. The rings in each layer form channels parallel to the hexagonal c axis. Lead cations are positioned inside these channels, between the layers. In the three-dimensional structure, every hexagonal ring has a triangular ring both above and below. This stacking sequence, with mixing of hexagonal and triangular rings, lowers the symmetry of the crystal from the ideal 6-fold, to the 3-fold symmetry observed. It can be noted that each of the three rings is associated with one of the three Wyckoff positions for lead in space group $R3$ (Table 9.2).

In addition to the stacking sequence, the polyhedral connectivity itself introduces tilts and distortions that prevent the ideal hexagonal symmetry from being realized. Between the layers, only corner-sharing connects the NbO_6 octahedra, whereas both corners and edges are shared within the layers. It is not possible to connect the layers as shown in Figure 9.8(c) without introducing symmetry-breaking distortions of the octahedra. The octahedral deformation in the crystal structure reported here is much less than reported in the previous work by Mahé.[118] He pointed out the large variation in Nb–O bond lengths, but remarked that this variation was not significant considering the experimental uncertainty in the oxygen positions. The uncertainty in oxygen positions in Mahé's work was on the order of 0.1 Å, while in the present work it is an order of magnitude less (Table 9.2), as a consequence of the neutron

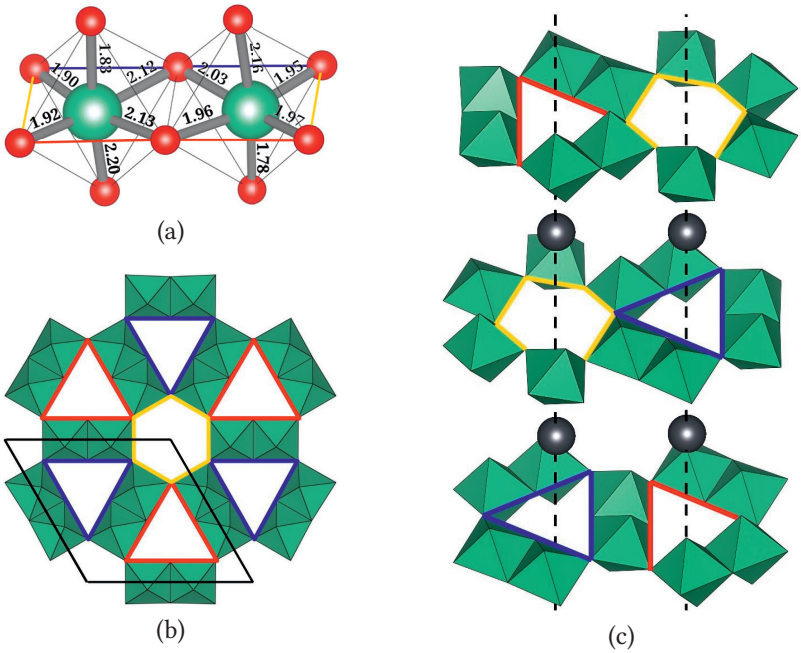

Figure 9.8 — Layered structure of PN: (a) Single dimer consisting of two edge-sharing NbO_6 octahedra. Experimental Nb–O bond lengths for space group $R3$ given in Å; edges coloured as in panels (b) and (c). (b) Single layer showing the hexagonal rings (yellow) and the two types of triangular rings (red and blue). Black line marks one hexagonal unit cell. (c) Stacking sequence. The layers are stretched apart in the hexagonal c direction for clarity. Lead ions (grey spheres) are situated inside channels formed by openings in the layers.

scattering cross section of oxygen being comparable to those of lead and niobium, hence improving the accuracy considerably.

Structures built from BO_6 dimer units are well known for niobates and tantalates of AB_2O_6 stoichiometry, with $A = \mathrm{Ca, Sr, Ba}$.[299] In particular, the hexagonal high-temperature form of $BaTa_2O_6$ bears a resemblance to the layer-like structure of r-PN described here,[300] with a combination of dimers and corner-sharing octahedra. The hexagonal $BaTa_2O_6$ structure is arguably even more complex than r-PN, containing both three-, five- and six-membered rings. Half of the TaO_6 octahedra in hexagonal $BaTa_2O_6$ share only corners with other octahedra, while in the r-PN structure, every NbO_6 octahedron is part of a dimer. The particular crystal structure found in r-PN is not commonly encountered, and is rather unique. It was not reported to exist for any other AB_2O_6 compounds in a recent review series,[301–304] although $PbRe_2O_6$ has previously been reported as isotypic with r-PN, with space group $R\bar{3}m$.[296] $PbTa_2O_6$ has also been reported to exist in a non-ferroelectric rhombohedral form,[100] analogous to r-PN, but no detailed structural study of this compound appears to have been conducted.

Possible ferroic phase transition

The presence of a polar space group symmetry ($R3$) in r-PN is interesting, since it is a requirement for pyro- and ferroelectricity. The HTXRD (Figure 9.4) and dilatometry data [Figure 9.5(b)] show that the polar axis contracts up to the phase transition temperature before it continues to expand, which suggests a polar–nonpolar transition. This was also suggested in 1985 by Lopatin and co-workers[119] based on dilatometry studies on a textured sample of r-PN [see Figure 2.14(b)], who hypothesized a transition from $R3m$ to $R\bar{3}m$ with 815 °C as the phase transition temperature. The thermal expansion, Figure 9.5(b), demonstrates that the same behaviour is also displayed by a dense ceramic with no particular texture. From the group-subgroup relations given in Figure 9.7, there are two possible such transitions: (i) $R3 \rightarrow R\bar{3}$ and (ii) $R3 \rightarrow R\bar{3}m$. Alternative (i) appears less likely, since the structural distortion separating these space group symmetries is small, and the transition would not be expected to appear as clearly in structural and thermal analysis. Alternative (ii) is not a direct group–subgroup transition, which implies that the transition cannot be of second order. A distinct thermal event is observed by DTA, 9.5(a), pointing to a first-order phase transition. A first-order $R3 \rightarrow R\bar{3}m$ transition is therefore plausible based on the present data, and the transition temperature is (780 ± 5) °C.

Upon cooling through the phase transition temperature, a spontaneous strain develops in the structure. The strain is confined to lie along the trigonal axis, meaning that there are only two possible polar domains. The strain is identical for these two

domains, which implies that the phase transition is co-elastic, but not ferroelastic.[52,54] The transition could still be ferroelectric if the spontaneous polarization could be switched 180° along the trigonal axis, but this does not seem to be the case based on the absence of any dielectric response at the phase transition temperature (Figure 9.6). The spontaneous polarization in the $R3$ structure near the phase transition is also likely to be low (on the order of $1\,\mu C\,cm^{-2}$ from test calculations) due to the small distortion from non-polar $R\bar{3}$ symmetry as discussed above. The claim by Lopatin and co-workers[119] of ferroelectric properties in r-PN is therefore not supported by the present data. A plausible explanation is that the solid solutions that were studied in the previous work were in reality not phase pure, but contained certain amounts of TTB-PN. The TTB phase has a high solid solubility, as discussed in Chapter 2, and would have been stabilized with respect to the rhombohedral phase by solid solution. This phenomenon was studied in detail by Sahini and co-workers,[7] who found that TTB-PN can be stabilized by addition of as little as 2 to 5 % of $BiTiNbO_6$, $Na_{1/2}Bi_{1/2}Nb_2O_6$, $K_{1/2}Bi_{1/2}Nb_2O_6$ or $CaTiO_3$ ($CaTiO_3$ being especially attractive as it does not simultaneously decrease T_C), eliminating the need to quench the samples in order to obtain the TTB phase. Lopatin and colleagues used the compositions $PbSb_2O_6$, $BiTiSbO_6$ and $PbTiWO_6$ (the latter not actually a stable phase in pure form) in concentrations of up to 16 %, 9 % and 40 %, respectively. It therefore seems likely that r-PN is not ferroelectric, and that previous claims of this is due to unintentional entropy stabilization of the TTB phase rather than ferroelectric properties of r-PN.

10 Conclusions and outlook

In this study several aspects of the tetragonal tungsten bronzes have been investigated by a combination of first principles density functional theory calculations and experiments. The major part of the work has focused on the "unfilled" metaniobates of barium, strontium and lead (SBN and PN). The possibility for cation and vacancy ordering in these tungsten bronzes was analysed by first-principles calculations, where it was found that the three compositions PN, BN and SN behave differently with respect to cation interchange between the A1 and A2 sublattices in the tungsten bronze. The energetics of the cation configurations was further applied in a thermodynamic model, originally devised for spinels, which predicted that the cation order in Ba-rich SBN compositions should depend most strongly on the thermal history. This is due to the configurational energy landscape being particularly flat for BN, while for SN and PN, the energy differences are large reducing the temperature dependence of cation interchange. For none of the three compounds are the energy differences large enough that long-range cation ordering is expected, but short-range order is likely and due to the large energy barriers between the different cation configurations the short-range order will be frozen in during material processing.

SBN and PN are both ferroelectric, but differ in terms of symmetry change and dielectric behaviour at the phase transition. SBN, represented by the end components BN and SN, was found to be ferroelectric due to a single polar instability, manifested as phonons with imaginary frequencies for all cation configurations that were investigated. This polar instability is robust with respect to cation disorder, and does not vanish for any cation configuration, although the absolute value varies significantly. The ferroelectric mechanism is similar to well-known perovskite ferroelectrics such as $BaTiO_3$, where the polar distortion is stabilized by covalent bonding between an octahedrally coordinated d^0 cation, such as Ti^{4+} or Nb^{5+}, and the surrounding oxygen anions. This mechanism, typically described as a second-order Jahn–Teller effect, is expected to be valid also for other Nb-based TTB ferroelectrics. In the case of PN, the nature of the ferroelectric distortion is determined by an in-plane distortion from the aristotype tetragonal structure. This is facilitated by the lone pair cation Pb^{2+}, which bonds strongly to oxygen, in a manner similar to tetragonal $PbTiO_3$. This creates a high spontaneous polarization for PN, calculated to be $109\,\mu C\,cm^{-2}$, which is stable with respect to cation disorder for the cation configurations that were examined. It was discussed that the high polarization and strain makes domain switching hard in PN, which explains why optimal piezoelectric properties are achieved for solid solutions where Pb is partially substituted by Ba.

Several "filled" TTBs were investigated as model compounds. The series $K_4R_2Nb_{10}O_{30}$ with R = La, . . . , Gd, Bi was investigated by lattice dynamics calculations,

and the main conclusion is that all compounds display two types of polar instabilities: One producing an out-of-plane polarization along the tetragonal axis, similar to SBN, and one producing an in-plane polarization, similar to PN. The out-of-plane instability dominates in all cases, except when R = Bi, where the in-plane polarization is stronger, and leads to a spontaneous polarization of 55 μC cm^{-2}. The polarization is stabilized by Bi–O covalent bonding in the A1 sites of the TTB structure, similar to the Pb–O covalency found in PN. Calculations where K^+ on the A2 sites was replaced by the lone-pair cation Tl^+ did not lead to additional in-plane distortion, demonstrating that this "lone-pair effect" is largely confined to the A1 sites in TTBs. When Bi^{3+} is combined with a large cation such as K^+, the size difference leads to cation ordering where Bi goes to the A1 sites, and the lone pair effect results in a ferroelectric distortion even though the concentration of lone pair cations is relatively low.

The TTB compounds $(Sr, Ba)_6Nb_{10}O_{30}$ with partly reduced Nb were also analysed by the first-principles lattice dynamics approach. In order to include possible effects of electron correlation related to the partially occupied conduction band, benchmark calculations were performed on experimental structures using a hybrid functional, and used to calibrate less computationally expensive DFT+U calculations. The latter was used for structural optimization and phonon calculations, which proved that the end component $Ba_6Nb_{10}O_{30}$ is dynamically stable in the aristotype structure, whereas $Sr_6Nb_{10}O_{30}$ has instabilities that lead to an orthorhombic ground state, both in accordance with experimental reports. Contrary to experiments, no evidence for a metal–insulator transition could be discerned from the calculations performed.

Finally, the rhombohedral polymorph of lead metaniobate (r-PN) was examined by a combination of diffraction experiments at ambient and elevated temperatures, thermal characterization and first-principles calculations. The main finding is that the space group symmetry at ambient temperature is $R3$, and not $R3m$ as previously reported. Evidence for a polar–nonpolar phase transition was found from high-temperature structural and thermal characterization. While this could in principle allow for ferroelectric properties, the data instead suggests that rhombohedral lead metaniobate is co-elastic, but not ferroelastic or -electric, and that previous reports of ferroelectricity in r-PN are most likely due to TTB impurities stabilized by solid solution.

From a materials point of view, this thesis provides new fundamental understanding of some of the most characteristic ferroelectric tungsten bronzes. Especially PN and SBN, and the mechanisms that stabilize ferroelectric polarization in these materials, were investigated in depth. The results, especially regarding the role of the lone pair cations, should be of general interest in the search for lead-free ferroelectrics. The cation order–disorder phenomena that are inherent to the TTB structure are also

a possible route towards new functionality, for example through suitable thermal treatment. From a computational viewpoint, the computer experiments performed in this project are original, as, to the best of the author's knowledge, no first-principles calculations on ferroelectric tungsten bronzes have been reported previously. The work has shown that both functional properties, such as ferroelectricity, and thermodynamic properties can be studied in depth using reasonable assumptions. In cases such as the partially reduced TTBs, which are particularly challenging for DFT calculations, there is still a lot left to be learned about computational methods, and the current work has demonstrated just one of several possible strategies.

The fundamental understanding of perovskite ferroelectrics has benefited enormously from the emergence of first-principles calculations during the last two to three decades. With computational power becoming ever more available, it is expected that also TTBs and other complex crystal structures will be the subject of more computational investigations in the years to follow.

References

[1] L. E. Cross and R. E. Newnham. "History of Ferroelectrics". *Ceramics and Civilization, Vol. III: High-Technology Ceramics—Past, Present and Future*. Westerville, OH: American Ceramic Society, 1987, pp. 289–305 (cited on pp. 1, 8).

[2] G. H. Haertling. "Ferroelectric Ceramics: History and Technology". *J. Am. Ceram. Soc.* 82.4 (Apr. 1999), pp. 797–818 (cited on pp. 1, 2).

[3] M. E. Lines and A. M. Glass. *Principles and Applications of Ferroelectrics and Related Materials*. OUP Oxford, 1977 (cited on p. 2).

[4] S. Zhang and F. Yu. "Piezoelectric Materials for High Temperature Sensors". *J. Am. Ceram. Soc.* 94.10 (Oct. 2011), pp. 3153–3170 (cited on p. 2).

[5] G. Goodman. "Ferroelectric Properties of Lead Metaniobate". *J. Am. Ceram. Soc.* 36.11 (Nov. 1953), pp. 368–372 (cited on pp. 2, 22–24, 85).

[6] M. H. Francombe. "Polymorphism in lead metaniobate". *Acta Crystallogr.* 9.8 (Aug. 1956), pp. 683–684 (cited on pp. 2, 23, 26, 119).

[7] M. G. Sahini, T. Grande, B. Fraygola, A. Biancoli, D. Damjanovic, and N. Setter. "Solid Solutions of Lead Metaniobate—Stabilization of the Ferroelectric Polymorph and the Effect on the Lattice Parameters, Dielectric, Ferroelectric, and Piezoelectric Properties". *J. Am. Ceram. Soc.* 97.1 (2014), pp. 220–227 (cited on pp. 2, 3, 24, 48, 85, 132).

[8] L. E. Cross. "Relaxor ferroelectrics". *Ferroelectrics* 76.1 (Dec. 1987), pp. 241–267 (cited on pp. 2, 3, 14, 76).

[9] E. Hey-Hawkins, R. J. Cava, D. Duprez, D. Fowler, T. K. Lindhorst, P. Madden, and G. Schembecker. *Basic Chemistry Research in Norway*. Technical report. The Research Council of Norway, 2009 (cited on p. 3).

[10] S. Skogestad *et al. Oppfølging av kjemievalueringen 2009. Rapport fra oppnevnt fagplanutvalg*. Technical report. Forskningsrådet, 2010 (cited on p. 3).

[11] M. H. Francombe. "The relation between structure and ferroelectricity in lead barium and barium strontium niobates". *Acta Crystallogr.* 13.2 (Feb. 1960), pp. 131–140 (cited on pp. 3, 22, 24, 26, 90, 101).

[12] J. Ravez and A. Simon. "Some Solid State Chemistry Aspects of Lead-Free Relaxor Ferroelectrics". *J. Solid State Chem.* 162.2 (Dec. 2001), pp. 260–265 (cited on pp. 3, 18).

[13] V. V. Shvartsman and D. C. Lupascu. "Lead-Free Relaxor Ferroelectrics". *J. Am. Ceram. Soc.* 95.1 (Jan. 2012), pp. 1–26 (cited on pp. 3, 14, 18, 31, 76).

[14] A. M. Glass. "Investigation of the Electrical Properties of $Sr_{1-x}Ba_xNb_2O_6$ with Special Reference to Pyroelectric Detection". *J. Appl. Phys.* 40.12 (Nov. 1969), pp. 4699–4713 (cited on pp. 3, 27, 72).

[15] X. Zhu, M. Fu, M. C. Stennett, P. M. Vilarinho, I. Levin, C. A. Randall, J. Gardner, F. D. Morrison, and I. M. Reaney. "A Crystal-Chemical Framework for Relaxor versus Normal Ferroelectric Behavior in Tetragonal Tungsten Bronzes". *Chem. Mater.* 27.9 (May 2015), pp. 3250–3261 (cited on pp. 3, 14, 20, 22, 23, 28, 30, 31, 99).

[16] J. Valasek. "Piezo-Electric and Allied Phenomena in Rochelle Salt". *Phys. Rev.* 17.4 (Apr. 1921), pp. 475–481 (cited on p. 8).

[17] G. Busch and P. Scherrer. "Eine neue seignette-elektrische Substanz". *Naturwissenschaften* 23.43 (Oct. 1935), pp. 737–737 (cited on p. 8).

[18] A. von Hippel, R. G. Breckenridge, F. G. Chesley, and L. Tisza. "High dielectric constant ceramics". *Ind. Eng. Chem.* 38.11 (Nov. 1946), pp. 1097–1109 (cited on p. 8).

[19] B. Jaffe, W. R. Cook, and H. L. Jaffe. *Piezoelectric ceramics*. Academic Press, 1971 (cited on pp. 8, 24).

[20] L. E. Cross. "Materials science: Lead-free at last". *Nature* 432.7013 (Nov. 2004), pp. 24–25 (cited on pp. 8, 9).

[21] K. M. Rabe, M. Dawber, C. Lichtensteiger, C. H. Ahn, and J.-M. Triscone. "Modern Physics of Ferroelectrics: Essential Background". *Physics of Ferroelectrics*. Topics in Applied Physics 105. Springer Berlin Heidelberg, 2007, pp. 1–30 (cited on p. 8).

[22] J. Rödel, W. Jo, K. T. P. Seifert, E.-M. Anton, T. Granzow, and D. Damjanovic. "Perspective on the Development of Lead-free Piezoceramics". *J. Am. Ceram. Soc.* 92.6 (June 2009), pp. 1153–1177 (cited on pp. 8, 9, 14).

[23] G. Shirane and A. Takeda. "Phase Transitions in Solid Solutions of $PbZrO_3$ and $PbTiO_3$ (I) Small Concentrations of $PbTiO_3$". *J. Phys. Soc. Jpn.* 7.1 (Jan. 1952), pp. 5–11 (cited on p. 8).

[24] E. Sawaguchi. "Ferroelectricity versus Antiferroelectricity in the Solid Solutions of $PbZrO_3$ and $PbTiO_3$". *J. Phys. Soc. Jpn.* 8.5 (Sept. 1953), pp. 615–629 (cited on p. 8).

[25] B. Jaffe, R. S. Roth, and S. Marzullo. "Piezoelectric Properties of Lead Zirconate-Lead Titanate Solid-Solution Ceramics". *J. Appl. Phys.* 25.6 (June 1954), pp. 809–810 (cited on p. 8).

[26] "Directive 2002/95/EC of the European Parliament and of the Council of 27 January 2003 on the restriction of the use of certain hazardous substances in electrical and electronic equipment". *Off. J. Eur. Union* 46.L37 (Feb. 2003), pp. 19–23 (cited on p. 8).

[27] "Directive 2002/96/EC of the European Parliament and of the Council of 27 January 2003 on waste electrical and electronic equipment (WEEE)". *Off. J. Eur. Union* 46.L37 (Feb. 2003), pp. 24–39 (cited on p. 8).

[28] Y. Saito, H. Takao, T. Tani, T. Nonoyama, K. Takatori, T. Homma, T. Nagaya, and M. Nakamura. "Lead-free piezoceramics". *Nature* 432.7013 (2004), pp. 84–87 (cited on p. 9).

[29] J. Rödel, K. G. Webber, R. Dittmer, W. Jo, M. Kimura, and D. Damjanovic. "Transferring lead-free piezoelectric ceramics into application". *J. Eur. Ceram. Soc.* 35.6 (June 2015), pp. 1659–1681 (cited on p. 9).

[30] H. D. Megaw. "Crystal structure of double oxides of the perovskite type". *Proc. Phys. Soc.* 58.2 (1946), p. 133 (cited on p. 10).

[31] H. D. Megaw. "Origin of ferroelectricity in barium titanate and other perovskite-type crystals". *Acta Crystallogr.* 5.6 (Nov. 1952), pp. 739–749 (cited on pp. 10, 76).

[32] M. T. Dove. "Theory of displacive phase transitions in minerals". *Am. Mineral.* 82.3-4 (1997), pp. 213–244 (cited on pp. 10, 11, 13, 41).

[33] W. Cochran. "Crystal Stability and the Theory of Ferroelectricity". *Phys. Rev. Lett.* 3.9 (Nov. 1959), pp. 412–414 (cited on p. 10).

[34] W. Cochran. "Crystal stability and the theory of ferroelectricity". *Adv. Phys.* 9.36 (1960), pp. 387–423 (cited on p. 10).

[35] P. C. Kwok and P. B. Miller. "Free Energy of Displacive Ferroelectrics". *Phys. Rev.* 151.2 (Nov. 1966), pp. 387–400 (cited on p. 11).

[36] R. Blinc. "The soft mode concept and the history of ferroelectricity". *Ferroelectrics* 74.1 (1987), pp. 301–303 (cited on p. 11).

[37] W. G. Spitzer, R. C. Miller, D. A. Kleinman, and L. E. Howarth. "Far Infrared Dielectric Dispersion in $BaTiO_3$, $SrTiO_3$, and TiO_2". *Phys. Rev.* 126.5 (June 1962), pp. 1710–1721 (cited on p. 11).

[38] R. Comès, M. Lambert, and A. Guinier. "The chain structure of $BaTiO_3$ and $KNbO_3$". *Solid State Commun.* 6.10 (Oct. 1968), pp. 715–719 (cited on p. 11).

[39] J. Harada, J. D. Axe, and G. Shirane. "Neutron-Scattering Study of Soft Modes in Cubic $BaTiO_3$". *Phys. Rev. B* 4.1 (July 1971), pp. 155–162 (cited on p. 11).

[40] G. Burns and F. H. Dacol. "Lattice modes in ferroelectric perovskites. III. Soft modes in $BaTiO_3$". *Phys. Rev. B* 18.10 (Nov. 1978), pp. 5750–5755 (cited on p. 11).

[41] B. Ravel, E. A. Stern, R. I. Vedrinskii, and V. Kraizman. "Local structure and the phase transitions of $BaTiO_3$". *Ferroelectrics* 206.1 (Feb. 1998), pp. 407–430 (cited on p. 11).

[42] I. B. Bersuker. "On the origin of ferroelectricity in perovskite-type crystals". *Phys. Lett.* 20.6 (Apr. 1966), pp. 589–590 (cited on pp. 12, 76).

[43] I. B. Bersuker. "Pseudo-Jahn–Teller Effect—A Two-State Paradigm in Formation, Deformation, and Transformation of Molecular Systems and Solids". *Chem. Rev.* 113.3 (Mar. 2013), pp. 1351–1390 (cited on p. 12).

[44] I. B. Bersuker. *Electronic Structure and Properties of Transition Metal Compounds: Introduction to the Theory*. John Wiley & Sons, Inc., 1996 (cited on p. 12).

[45] N. Sicron, B. Ravel, Y. Yacoby, E. A. Stern, F. Dogan, and J. J. Rehr. "Nature of the ferroelectric phase transition in $PbTiO_3$". *Phys. Rev. B* 50.18 (Nov. 1994), pp. 13168–13180 (cited on p. 12).

[46] P. Chandra and P. B. Littlewood. "A Landau Primer for Ferroelectrics". *Physics of Ferroelectrics*. Topics in Applied Physics 105. Springer Berlin Heidelberg, 2007, pp. 69–116 (cited on pp. 12, 13).

[47] A. F. Devonshire. "Theory of barium titanate". *Philos. Mag.* 40.309 (Oct. 1949), pp. 1040–1063 (cited on p. 12).

[48] A. F. Devonshire. "Theory of barium titanate—Part II". *Philos. Mag.* 42.333 (Oct. 1951), pp. 1065–1079 (cited on p. 12).

[49] A. F. Devonshire. "Theory of ferroelectrics". *Adv. Phys.* 3.10 (Apr. 1954), pp. 85–130 (cited on p. 12).

[50] J. M. Perez-Mato, D. Orobengoa, and M. I. Aroyo. "Mode crystallography of distorted structures". *Acta Crystallogr. A* 66.5 (Sept. 2010), pp. 558–590 (cited on p. 12).

[51] E. K. H. Salje. "Crystallography and structural phase transitions, an introduction". *Acta Crystallogr. A* 47.5 (Sept. 1991), pp. 453–469 (cited on p. 13).

[52] E. K. H. Salje, S. A. Hayward, and W. T. Lee. "Ferroelastic phase transitions: structure and microstructure". *Acta Crystallogr. A* 61.1 (Jan. 2005), pp. 3–18 (cited on pp. 13, 132).

[53] L.-Q. Chen. "Appendix A – Landau Free-Energy Coefficients". *Physics of Ferroelectrics*. Topics in Applied Physics 105. Springer Berlin Heidelberg, 2007, pp. 363–372 (cited on p. 13).

[54] E. K. H. Salje. *Phase Transitions in Ferroelastic and Co-elastic Crystals*. Cambridge University Press, Apr. 1993 (cited on pp. 13, 132).

[55] R. Cohen. "Origin of ferroelectricity in perovskite oxides". *Nature* 358 (1992), pp. 136–138 (cited on pp. 13, 39, 76, 90, 92, 103).

[56] N. A. Hill. "Why Are There so Few Magnetic Ferroelectrics?": *J. Phys. Chem. B* 104.29 (July 2000), pp. 6694–6709 (cited on pp. 14, 40).

[57] R. Seshadri and N. A. Hill. "Visualizing the Role of Bi 6s "Lone Pairs" in the Off-Center Distortion in Ferromagnetic $BiMnO_3$". *Chem. Mater.* 13.9 (Sept. 2001), pp. 2892–2899 (cited on pp. 14, 40).

[58] J. B. Neaton, C. Ederer, U. V. Waghmare, N. A. Spaldin, and K. M. Rabe. "First-principles study of spontaneous polarization in multiferroic $BiFeO_3$". *Phys. Rev. B* 71.1 (Jan. 2005), p. 014113 (cited on pp. 14, 40).

[59] G. A. Smolenskii and V. A. Isupov. "Segnetoelektricheskie Svoistva Tverdykh Rastvorov Stannata Bariya V Titanate Bariya". *Zhurnal Tek. Fiz.* 24.8 (1954), pp. 1375–1386 (cited on p. 14).

[60] G. A. Smolenskii, V. A. Isupov, A. I. Agranovskaya, and S. N. Popov. "Ferroelectrics with Diffuse Phase Transitions". *Sov. Phys. Solid State* 2.11 (1961), pp. 2584–2594 (cited on p. 14).

[61] G. Smolensky. "Ferroelectrics with diffuse phase transition". *Ferroelectrics* 53.1 (Apr. 1984), pp. 129–135 (cited on p. 14).

[62] G. Burns and B. A. Scott. "'Dirty' displacive ferroelectrics". *Solid State Commun.* 13.3 (Aug. 1973), pp. 417–421 (cited on pp. 14, 28).

[63] G. Burns. "Dirty displacive ferroelectrics". *Phys. Rev. B* 13.1 (Jan. 1976), pp. 215–226 (cited on pp. 14, 27).

[64] N. Setter and L. E. Cross. "The contribution of structural disorder to diffuse phase transitions in ferroelectrics". *J. Mater. Sci.* 15.10 (Oct. 1980), pp. 2478–2482 (cited on pp. 14, 16, 17).

[65] L. Cross. "Relaxor ferroelectrics: An overview". *Ferroelectrics* 151.1 -4 pt 1 (1994), pp. 305–320 (cited on p. 14).

[66] R. A. Cowley, S. N. Gvasaliya, S. G. Lushnikov, B. Roessli, and G. M. Rotaru. "Relaxing with relaxors: a review of relaxor ferroelectrics". *Adv. Phys.* 60.2 (Apr. 2011), pp. 229–327 (cited on pp. 14, 16).

[67] R. E. Cohen. "Materials science: Relaxors go critical". *Nature* 441.7096 (June 2006), pp. 941–942 (cited on p. 14).

[68] S.-E. Park and T. R. Shrout. "Ultrahigh strain and piezoelectric behavior in relaxor based ferroelectric single crystals". *J. Appl. Phys.* 82.4 (Aug. 1997), pp. 1804–1811 (cited on pp. 14, 18).

[69] D. Viehland, S. J. Jang, L. E. Cross, and M. Wuttig. "Freezing of the polarization fluctuations in lead magnesium niobate relaxors". *J. Appl. Phys.* 68.6 (Sept. 1990), pp. 2916–2921 (cited on p. 15).

[70] R. Pirc and R. Blinc. "Vogel-Fulcher freezing in relaxor ferroelectrics". *Phys. Rev. B* 76.2 (July 2007), p. 020101 (cited on p. 15).

[71] J. L. Tholence. "On the frequency dependence of the transition temperature in spin glasses". *Solid State Commun.* 35.2 (July 1980), pp. 113–117 (cited on p. 15).

[72] G. Burns and F. H. Dacol. "Crystalline ferroelectrics with glassy polarization behavior". *Phys. Rev. B* 28.5 (Sept. 1983), pp. 2527–2530 (cited on pp. 15, 16).

[73] A. A. Bokov and Z.-G. Ye. "Dielectric relaxation in relaxor ferroelectrics". *J. Adv. Dielect.* 02.02 (Apr. 2012), p. 1241010 (cited on pp. 15, 16, 77).

[74] A. N. Salak, M. P. Seabra, and V. M. Ferreira. "Evolution from Ferroelectric to Relaxor Behavior in the $(1-x)BaTiO_3$–$xLa(Mg_{1/2}Ti_{1/2})O_3$ System". *Ferroelectrics* 318.1 (July 2005), pp. 185–192 (cited on p. 15).

[75] P. Bonneau, P. Garnier, G. Calvarin, E. Husson, J. R. Gavarri, A. W. Hewat, and A. Morell. "X-ray and neutron diffraction studies of the diffuse phase transition in $PbMg_{1/3}Nb_{2/3}O_3$ ceramics". *J. Solid State Chem.* 91.2 (Apr. 1991), pp. 350–361 (cited on p. 16).

[76] G. Burns and B. A. Scott. "Index of refraction in 'dirty' displacive ferroelectrics". *Solid State Commun.* 13.3 (Aug. 1973), pp. 423–426 (cited on p. 16).

[77] A. E. Glazounov and A. K. Tagantsev. "Direct evidence for Vögel–Fulcher freezing in relaxor ferroelectrics". *Appl. Phys. Lett.* 73.6 (Aug. 1998), pp. 856–858 (cited on p. 16).

[78] N. Setter and L. E. Cross. "The role of B-site cation disorder in diffuse phase transition behavior of perovskite ferroelectrics". *J. Appl. Phys.* 51.8 (1980), pp. 4356–4356 (cited on pp. 16, 17, 77).

[79] *The Story of the Three Bears*. New York: F. Warne, 1900 (cited on p. 17).

[80] J. Ravez and A. Simon. "Lead-free relaxor ferroelectrics with 'TTB' structure". *C. R. Chim.* 5.3 (Mar. 2002), pp. 143–148 (cited on pp. 18, 31).

[81] W. Jo, R. Dittmer, M. Acosta, J. Zang, C. Groh, E. Sapper, K. Wang, and J. Rödel. "Giant electric-field-induced strains in lead-free ceramics for actuator applications – status and perspective". *J. Electroceram.* 29.1 (May 2012), pp. 71–93 (cited on p. 18).

[82] Y.-M. Chiang, G. W. Farrey, and A. N. Soukhojak. "Lead-free high-strain single-crystal piezoelectrics in the alkaline–bismuth–titanate perovskite family". *Appl. Phys. Lett.* 73.25 (Dec. 1998), pp. 3683–3685 (cited on p. 18).

[83] S.-T. Zhang, A. B. Kounga, E. Aulbach, H. Ehrenberg, and J. Rödel. "Giant strain in lead-free piezoceramics $Bi_{0.5}Na_{0.5}TiO_3$–$BaTiO_3$–$K_{0.5}Na_{0.5}NbO_3$ system". *Appl. Phys. Lett* 91.11 (Sept. 2007), p. 112906 (cited on p. 18).

[84] J. A. Bock, S. Trolier-McKinstry, G. D. Mahan, and C. A. Randall. "Polarization-based perturbations to thermopower and electronic conductivity in highly conductive tungsten bronze structured (Sr,Ba)Nb_2O_6: Relaxors vs normal ferroelectrics". *Phys. Rev. B* 90.11 (Sept. 2014), p. 115106 (cited on pp. 18, 32, 117).

[85] H. Fu and R. E. Cohen. "Polarization rotation mechanism for ultrahigh electromechanical response in single-crystal piezoelectrics". *Nature* 403.6767 (Jan. 2000), pp. 281–283 (cited on p. 18).

[86] M. Gröting, S. Hayn, and K. Albe. "Chemical order and local structure of the lead-free relaxor ferroelectric $Na_{1/2}Bi_{1/2}TiO_3$". *J. Solid State Chem.* 184.8 (Aug. 2011), pp. 2041–2046 (cited on pp. 18, 65, 76).

[87] M. Gröting and K. Albe. "Comparative study of A-site order in the lead-free bismuth titanates $M_{1/2}Bi_{1/2}TiO_3$ (M = Li, Na, K, Rb, Cs, Ag) from first-principles". *Journal of Solid State Chemistry* 213 (May 2014), pp. 138–144 (cited on p. 18).

[88] B. P. Burton, E. Cockayne, and U. V. Waghmare. "Correlations between nano-scale chemical and polar order in relaxor ferroelectrics and the lengthscale for polar nanoregions". *Phys. Rev. B* 72.6 (Aug. 2005), p. 064113 (cited on p. 18).

[89] S. Tinte, B. P. Burton, E. Cockayne, and U. V. Waghmare. "Origin of the Relaxor State in $Pb(B_xB'_{1-x})O_3$ Perovskites". *Phys. Rev. Lett.* 97.13 (Sept. 2006), p. 137601 (cited on pp. 18, 76).

[90] B. P. Burton, E. Cockayne, S. Tinte, and U. V. Waghmare. "First-principles-based simulations of relaxor ferroelectrics". *Phase Transit.* 79.1-2 (Jan. 2006), pp. 91–121 (cited on p. 18).

[91] P. Labbé. "Tungsten Oxides, Tungsten Bronzes and Tungsten Bronze-Type Structures". *Key Eng. Mater.* 68 (1992), pp. 293– (cited on pp. 19, 76).

[92] A. Magnéli, R. Mårin, C. M. Haug, J. Stene, and N. A. Sörensen. "Tetragonal Tungsten Bronzes of Degenerated Perovskite Type." *Acta Chem. Scand.* 5 (1951), pp. 670–672 (cited on p. 20).

[93] A. Magnéli, A. I. Virtanen, J. Olsen, A. I. Virtanen, and N. A. Sörensen. "Studies on the Hexagonal Tungsten Bronzes of Potassium, Rubidium, and Cesium." *Acta Chem. Scand.* 7 (1953), pp. 315–324 (cited on p. 20).

[94] P. B. Jamieson, S. C. Abrahams, and J. L. Bernstein. "Ferroelectric Tungsten Bronze-Type Crystal Structures. I. Barium Strontium Niobate $Ba_{0.27}Sr_{0.75}Nb_2O_{5.78}$". *J. Chem. Phys.* 48.11 (June 1968), pp. 5048–5057 (cited on pp. 19, 24, 25, 27, 28).

[95] S. C. Abrahams, P. B. Jamieson, and J. L. Bernstein. "Ferroelectric Tungsten Bronze-Type Crystal Structures. III. Potassium Lithium Niobate $K_{6-x-y}Li_{4+x}Nb_{10+y}O_{30}$". *J. Chem. Phys.* 54.6 (Mar. 1971), pp. 2355–2364 (cited on pp. 20, 22, 24, 25).

[96] M. Lundberg and M. Sundberg. "Studies of phases in the $KNbO_3$–Nb_2O_5 system by high-resolution electron microscopy and X-ray powder diffraction". *J. Solid State Chem.* 63.2 (July 1986), pp. 216–230 (cited on pp. 20–22).

[97] F. Madaro, R. Sæterli, J. R. Tolchard, M.-A. Einarsrud, R. Holmestad, and T. Grande. "Molten salt synthesis of $K_4Nb_6O_{17}$, $K_2Nb_4O_{11}$ and KNb_3O_8 crystals with needle- or plate-like morphology". *CrystEngComm* 13.5 (Feb. 2011), pp. 1304–1313 (cited on pp. 20, 21).

[98] K. Ngai and T. Reinecke. "Model of the Ferroelectric Phase Transition in the Tetragonal Tungsten-Bronze-Structure Ferroelectrics". *Phys. Rev. Lett.* 38.2 (Jan. 1977), pp. 74–77 (cited on p. 21).

[99] P. B. Jamieson, S. C. Abrahams, and J. L. Bernstein. "Ferroelectric Tungsten Bronze-Type Crystal Structures. II. Barium Sodium Niobate $Ba_{4+x}Na_{2-2x}Nb_{10}O_{30}$". *J. Chem. Phys.* 50.10 (May 1969), pp. 4352–4363 (cited on pp. 21, 22, 24, 25, 29).

[100] E. C. Subbarao, G. Shirane, and F. Jona. "X-ray dielectric, and optical study of ferroelectric lead metatantalate and related compounds". *Acta Crystallogr.* 13.3 (Mar. 1960), pp. 226–231 (cited on pp. 22, 119, 131).

[101] N. C. Stephenson. "The crystal structure of the tetragonal bronze, $Ba_6Ti_2Nb_8O_{30}$". *Acta Crystallographica* 18.3 (Mar. 1965), pp. 496–501 (cited on pp. 22, 100).

[102] T. Kolodiaznyi, H. Sakurai, M. Isobe, Y. Matsushita, S. Forbes, Y. Mozharivskyj, T. J. S. Munsie, G. M. Luke, M. Gurak, and D. R. Clarke. "Superconductivity and crystal structural origins of the metal-insulator transition in $Ba_{6-x}Sr_xNb_{10}O_{30}$ tetragonal tungsten bronzes". *Phys. Rev. B* 92.21 (Dec. 2015), p. 214508 (cited on pp. 22, 31, 32, 105, 107–109, 113, 115, 117).

[103] H. El Alaoui-Belghiti, A. Simon, M. Elaatmani, J. Reau, and J. Ravez. "TKWB-Type Lead-Free Oxyfluoride Relaxors Derived from $Ba_2NaNb_5O_{15}$". *Phys. Status Solidi A* 187.2 (Oct. 2001), pp. 549–556 (cited on p. 22).

[104] A. Reisman and F. Holtzberg. "Phase Equilibria in the System K_2CO_3–Nb_2O_5 by the Method of Differential Thermal Analysis". *J. Am. Chem. Soc.* 77.8 (Apr. 1955), pp. 2115–2119 (cited on p. 21).

[105] R. S. Roth, H. S. Parker, W. S. Brower, and D. Minor. *Alkali oxide-tantalum oxide and alkali oxide-niobium oxide ionic conductors*. Technical report. Apr. 1974 (cited on pp. 21, 22).

[106] A. B. Haugen, F. Madaro, L.-P. Bjørkeng, T. Grande, and M.-A. Einarsrud. "Sintering of sub-micron $K_{0.5}Na_{0.5}NbO_3$ powders fabricated by spray pyrolysis". *J. Eur. Ceram. Soc.* 35.5 (May 2015), pp. 1449–1457 (cited on p. 21).

[107] E. Irle, R. Blachnik, and B. Gather. "The phase diagrams of Na_2O and K_2O with Nb_2O_5 and the ternary system Nb_2O_5–Na_2O–Yb_2O_3". *Thermochim. Acta* 179 (Apr. 1991), pp. 157–169 (cited on p. 22).

[108] J. Schneck, J. C. Toledano, R. Whatmore, and F. W. Ainger. "Incommensurate phases in ferroelectric tetragonal tungsten bronzes". *Ferroelectrics* 36.1 (Oct. 1981), pp. 327–330 (cited on pp. 22, 28, 29).

[109] I. Levin, M. C. Stennett, G. C. Miles, D. I. Woodward, A. R. West, and I. M. Reaney. "Coupling between octahedral tilting and ferroelectric order in tetragonal tungsten bronze-structured dielectrics". *Appl. Phys. Lett.* 89.12 (Sept. 2006), p. 122908 (cited on p. 22).

[110] J. Als-Nielsen and D. McMorrow. *Elements of Modern X-ray Physics*. John Wiley & Sons, Apr. 2011 (cited on p. 23).

[111] P. Bak. "Commensurate phases, incommensurate phases and the devil's staircase". *Rep. Prog. Phys.* 45.6 (1982), p. 587 (cited on p. 23).

[112] R. S. Roth. "Unit-cell data of the lead niobate, $PbNb_2O_6$". *Acta Crystallogr.* 10.6 (June 1957), pp. 437–437 (cited on pp. 23, 24).

[113] M. H. Francombe and B. Lewis. “Structural, dielectric and optical properties of ferroelectric lead metaniobate”. *Acta Crystallogr.* 11 (1958), pp. 696–703 (cited on pp. 24, 25, 85).

[114] E. Ascher. “Role of particular maximal subgroups in continuous phase transitions”. *Phys. Lett.* 20.4 (Mar. 1966), pp. 352–354 (cited on p. 25).

[115] P. Labbé, M. Frey, and G. Allias. “Nouvelles données structurales sur la variété ferroélectrique du métaniobate de plomb $PbNb_2O_6$”. *Acta Crystallogr. B* 29.10 (Oct. 1973), pp. 2204–2210 (cited on pp. 25–27, 79, 81, 86, 90, 192).

[116] P. Labbé, M. Frey, B. Raveau, and J. C. Monier. “Structure cristalline de la phase ferroélectrique du niobate de plomb $PbNb_2O_6$. Déplacements des atomes métalliques et interprétation de la surstructure”. *Acta Crystallogr. B* 33.7 (July 1977), pp. 2201–2212 (cited on pp. 25, 26, 28, 86, 90).

[117] R. Mahé. “Étude structurale du métaniobate de plomb rhomboédrique. I. — Caractérisation de la maille. Analogies avec le métatantalate de plomb”. *Bull. Soc. Chim. Fr.* 11 (1966), pp. 3401–3403 (cited on pp. 26, 121, 126).

[118] R. Mahé. “Étude structurale du métaniobate de plomb rhomboédrique. II. — Positions des atomes”. *Bull. Soc. Chim. Fr.* 6 (1967), pp. 1879–1884 (cited on pp. 26, 29, 119–121, 126, 129, 191).

[119] S. S. Lopatin, E. S. Medvedev, and I. P. Raevskii. “Phase-Transition in Rhombohedral Lead Metaniobate and Solid-Solutions Based on It”. *Zhurnal Neorg. Khimii* 30.8 (1985), pp. 2102–2106 (cited on pp. 27, 29, 120, 128, 131, 132).

[120] A. M. Glass. “Ferroelectric $Sr_{1-x}Ba_xNb_2O_6$ as a fast and sensitive detector of infrared radiation”. *Appl. Phys. Lett* 13.4 (Aug. 1968), pp. 147–149 (cited on p. 27).

[121] J. Schneck and F. Denoyer. “Incommensurate phases in barium sodium niobate”. *Phys. Rev. B* 23.1 (Jan. 1981), pp. 383–388 (cited on pp. 28, 29).

[122] L. G. Van Uitert, H. J. Levinstein, J. J. Rubin, C. D. Capio, E. F. Dearborn, and W. A. Bonner. “Some characteristics of niobates having “filled” tetragonal tungsten bronze-like structures”. *Mater. Res. Bull.* 3.1 (Jan. 1968), pp. 47–57 (cited on p. 29).

[123] B. A. Scott, E. A. Giess, G. Burns, and D. F. O’Kane. “Alkali-rare earth niobates with the tungsten bronze-type structure”. *Mater. Res. Bull.* 3.10 (Oct. 1968), pp. 831–842 (cited on pp. 29, 31, 76, 98).

[124] R. R. Neurgaonkar, J. G. Nelson, J. R. Oliver, and L. E. Cross. “Ferroelectric and structural properties of the tungsten bronze system $K_2Ln^{3+}Nb_5O_{15}$, Ln = La to Lu”. *Mater. Res. Bull.* 25.8 (Aug. 1990), pp. 959–970 (cited on pp. 29, 31, 93).

[125] T. Sugai and M. Wada. "Crystal Growth and Dielectric Properties of Potassium Bismuth Niobate". *Jpn. J. Appl. Phys.* 11.12 (Dec. 1972), pp. 1863–1864 (cited on p. 30).

[126] M. Shimazu, Y. Tanokura, and S. Tsutsumi. "X-Ray Diffraction and Dielectric Studies on the $K_2BiNb_5O_{15}$-$K_2LaNb_5O_{15}$ System". *Jpn. J. Appl. Phys.* 28.Part 1, No. 10 (Oct. 1989), pp. 1877–1881 (cited on p. 30).

[127] R. R. Neurgaonkar, W. K. Cory, J. R. Oliver, E. J. Sharp, G. L. Wood, and G. J. Salamo. "Growth and optical properties of ferroelectric tungsten bronze crystals". *Ferroelectrics* 142.1 (Jan. 1993), pp. 167–188 (cited on p. 30).

[128] R. D. Shannon. "Revised effective ionic radii and systematic studies of interatomic distances in halides and chalcogenides". *Acta Crystallogr. A* 32.5 (Sept. 1976), pp. 751–767 (cited on pp. 30, 65, 90, 99, 100).

[129] N. A. Spaldin and M. Fiebig. "The renaissance of magnetoelectric multiferroics". *Science* 309.5733 (2005), pp. 391–392 (cited on p. 32).

[130] S.-W. Cheong and M. Mostovoy. "Multiferroics: a magnetic twist for ferroelectricity". *Nat. Mater.* 6.1 (Jan. 2007), pp. 13–20 (cited on p. 32).

[131] S. Picozzi and C. Ederer. "First principles studies of multiferroic materials". *J. Phys.: Condens. Matter* 21.30 (2009), p. 303201 (cited on pp. 32, 40, 43).

[132] K. Yamauchi and S. Picozzi. "Interplay between Charge Order, Ferroelectricity, and Ferroelasticity: Tungsten Bronze Structures as a Playground for Multiferroicity". *Phys. Rev. Lett.* 105.10 (Sept. 2010), pp. 107202–107202 (cited on p. 32).

[133] A. Rotaru, A. J. Miller, D. C. Arnold, and F. D. Morrison. "Towards novel multiferroic and magnetoelectric materials: dipole stability in tetragonal tungsten bronzes". *Phil. Trans. R. Soc.* 372.2009 (Feb. 2014), p. 20120451 (cited on p. 32).

[134] S. A. Reisinger, M. Leblanc, A.-M. Mercier, C. C. Tang, J. E. Parker, F. D. Morrison, and P. Lightfoot. "Phase Separation and Phase Transitions in Multiferroic $K_{0.58}FeF_3$ with the Tetragonal Tungsten Bronze Structure". *Chem. Mater.* 23.24 (2011), pp. 5440–5445 (cited on p. 32).

[135] S. Lee, R. H. T. Wilke, S. Trolier-McKinstry, S. Zhang, and C. A. Randall. "$Sr_xBa_{1-x}Nb_2O_{6-\delta}$ Ferroelectric-thermoelectrics: Crystal anisotropy, conduction mechanism, and power factor". *Appl. Phys. Lett* 96.3 (Jan. 2010), p. 031910 (cited on p. 32).

[136] S. Lee, J. A. Bock, S. Trolier-McKinstry, and C. A. Randall. "Ferroelectric-thermoelectricity and Mott transition of ferroelectric oxides with high electronic conductivity". *J. Eur. Ceram. Soc.* 32.16 (Dec. 2012), pp. 3971–3988 (cited on p. 32).

[137] C. S. Dandeneau, Y. Yang, B. W. Krueger, M. A. Olmstead, R. K. Bordia, and F. S. Ohuchi. "Site occupancy and cation binding states in reduced polycrystalline $Sr_xBa_{1-x}Nb_2O_6$". *Appl. Phys. Lett* 104.10 (Mar. 2014), p. 101607 (cited on p. 32).

[138] H. Ma, K. Lin, L. Fan, Y. Rong, J. Chen, J. Deng, L. Liu, S. Kawaguchi, K. Kato, and X. Xing. "Structure and oxide ion conductivity in tetragonal tungsten bronze $BaBiNb_5O_{15}$". *RSC Adv.* 5.88 (Aug. 2015), pp. 71890–71895 (cited on p. 32).

[139] K. Burke and L. O. Wagner. "DFT in a nutshell". *Int. J. Quantum Chem.* 113.2 (2013), pp. 96–101 (cited on p. 32).

[140] D. Sholl and J. A. Steckel. *Density Functional Theory: A Practical Introduction*. John Wiley & Sons, Sept. 2011 (cited on p. 32).

[141] K. Burke. *The ABC of DFT*. Irvine, CA: Department of Chemistry, University of California, Apr. 2007 (cited on p. 32).

[142] W. Koch and M. C. Holthausen. *A Chemist's Guide to Density Functional Theory*. 2nd Edition. Weinheim; New York: Wiley-VCH, July 2001 (cited on p. 32).

[143] R. M. Martin. *Electronic Structure: Basic Theory and Practical Methods*. Cambridge University Press, Apr. 2004 (cited on pp. 32, 37).

[144] R. P. Stoffel, C. Wessel, M.-W. Lumey, and R. Dronskowski. "Ab Initio Thermochemistry of Solid-State Materials". *Angew. Chem. Int. Ed.* 49.31 (2010), pp. 5242–5266 (cited on p. 32).

[145] K. Burke. "Perspective on density functional theory." *J. Chem. Phys.* 136.15 (Apr. 2012), pp. 150901–150901 (cited on pp. 32, 39).

[146] A. J. Cohen, P. Mori-Sánchez, and W. Yang. "Challenges for Density Functional Theory". *Chem. Rev.* 112.1 (Jan. 2012), pp. 289–320 (cited on p. 32).

[147] A. D. Becke. "Perspective: Fifty years of density-functional theory in chemical physics". *J. Chem. Phys.* 140.18 (May 2014), 18A301 (cited on p. 32).

[148] R. O. Jones. "Density functional theory: Its origins, rise to prominence, and future". *Rev. Mod. Phys.* 87.3 (Aug. 2015), pp. 897–923 (cited on p. 32).

[149] M. Born and R. Oppenheimer. "Zur Quantentheorie der Molekeln". *Ann. Phys.* 389.20 (Jan. 1927), pp. 457–484 (cited on p. 32).

[150] L. H. Thomas. "The calculation of atomic fields". *Math. Proc. Cambridge* 23.05 (Jan. 1927), pp. 542–548 (cited on p. 33).

[151] E. Fermi. "Eine statistische Methode zur Bestimmung einiger Eigenschaften des Atoms und ihre Anwendung auf die Theorie des periodischen Systems der Elemente". *Z. Phys.* 48.1-2 (Jan. 1928), pp. 73–79 (cited on p. 33).

[152] P. Hohenberg and W. Kohn. "Inhomogeneous Electron Gas". *Phys. Rev.* 136.3B (Nov. 1964), B864–B871 (cited on p. 33).

[153] W. Kohn and L. J. Sham. "Self-Consistent Equations Including Exchange and Correlation Effects". *Phys. Rev.* 140.4A (Nov. 1965), A1133–A1138 (cited on p. 33).

[154] R. Stowasser and R. Hoffmann. "What Do the Kohn-Sham Orbitals and Eigenvalues Mean?": *J. Am. Chem. Soc.* 121.14 (Apr. 1999), pp. 3414–3420 (cited on p. 34).

[155] V. I. Anisimov, J. Zaanen, and O. K. Andersen. "Band theory and Mott insulators: Hubbard *U* instead of Stoner *I*". *Phys. Rev. B* 44.3 (July 1991), pp. 943–954 (cited on p. 34).

[156] J. P. Perdew and K. Schmidt. "Jacob's ladder of density functional approximations for the exchange-correlation energy". *AIP Conf. Proc.* 577 (July 2001), pp. 1–20 (cited on p. 35).

[157] J. P. Perdew, A. Ruzsinszky, J. Tao, V. N. Staroverov, G. E. Scuseria, and G. I. Csonka. "Prescription for the design and selection of density functional approximations: More constraint satisfaction with fewer fits". *J. Chem. Phys.* 123.6 (Aug. 2005), p. 062201 (cited on p. 35).

[158] D. I. Bilc, R. Orlando, R. Shaltaf, G.-M. Rignanese, J. Íñiguez, and P. Ghosez. "Hybrid exchange-correlation functional for accurate prediction of the electronic and structural properties of ferroelectric oxides". *Phys. Rev. B* 77.16 (Apr. 2008), pp. 165107–165107 (cited on pp. 35, 38).

[159] A. D. Becke. "Density-functional thermochemistry. III. The role of exact exchange". *J. Chem. Phys.* 98.7 (Apr. 1993), pp. 5648–5652 (cited on p. 36).

[160] K. Kim and K. D. Jordan. "Comparison of Density Functional and MP2 Calculations on the Water Monomer and Dimer". *J. Phys. Chem.* 98.40 (Oct. 1994), pp. 10089–10094 (cited on pp. 36, 39).

[161] P. J. Stephens, F. J. Devlin, C. F. Chabalowski, and M. J. Frisch. "Ab Initio Calculation of Vibrational Absorption and Circular Dichroism Spectra Using Density Functional Force Fields". *J. Phys. Chem.* 98.45 (Nov. 1994), pp. 11623–11627 (cited on pp. 36, 39).

[162] A. D. Becke. “Density-functional exchange-energy approximation with correct asymptotic behavior”. *Phys. Rev. A* 38.6 (Sept. 1988), pp. 3098–3100 (cited on p. 36).

[163] C. Lee, W. Yang, and R. G. Parr. “Development of the Colle-Salvetti correlation-energy formula into a functional of the electron density”. *Phys. Rev. B* 37.2 (Jan. 1988), pp. 785–789 (cited on p. 36).

[164] J. P. Perdew, K. Burke, and M. Ernzerhof. “Generalized Gradient Approximation Made Simple”. *Phys. Rev. Lett.* 77.18 (Oct. 1996), pp. 3865–3868 (cited on pp. 36, 39, 46).

[165] J. P. Perdew, M. Ernzerhof, and K. Burke. “Rationale for mixing exact exchange with density functional approximations”. *J. Chem. Phys.* 105.22 (Dec. 1996), pp. 9982–9985 (cited on p. 36).

[166] C. Adamo and V. Barone. “Toward reliable density functional methods without adjustable parameters: The PBE0 model”. *J. Chem. Phys.* 110.13 (Apr. 1999), pp. 6158–6170 (cited on p. 36).

[167] P. M. W. Gill. “Obituary: Density Functional Theory (1927-1993)”. *Aust. J. Chem.* 54.11 (Jan. 2001), pp. 661–662 (cited on p. 36).

[168] J. Heyd, G. E. Scuseria, and M. Ernzerhof. “Hybrid functionals based on a screened Coulomb potential”. *J. Chem. Phys.* 118.18 (May 2003), pp. 8207–8215 (cited on p. 37).

[169] A. V. Krukau, O. A. Vydrov, A. F. Izmaylov, and G. E. Scuseria. “Influence of the exchange screening parameter on the performance of screened hybrid functionals”. *J. Chem. Phys.* 125.22 (Dec. 2006), p. 224106 (cited on p. 37).

[170] V. I. Anisimov and O. Gunnarsson. “Density-functional calculation of effective Coulomb interactions in metals”. *Phys. Rev. B* 43.10 (Apr. 1991), pp. 7570–7574 (cited on p. 37).

[171] S. Satpathy, Z. S. Popović, and F. R. Vukajlović. “Electronic Structure of the Perovskite Oxides: $La_{1-x}Ca_xMnO_3$”. *Phys. Rev. Lett.* 76.6 (Feb. 1996), pp. 960–963 (cited on p. 37).

[172] J. Hong, A. Stroppa, J. Íñiguez, S. Picozzi, and D. Vanderbilt. “Spin-phonon coupling effects in transition-metal perovskites: A DFT + U and hybrid-functional study”. *Phys. Rev. B* 85.5 (Feb. 2012), p. 054417 (cited on p. 38).

[173] L. Schimka, J. Harl, and G. Kresse. “Improved hybrid functional for solids: The HSEsol functional”. *J. Chem. Phys.* 134.2 (Jan. 2011), p. 024116 (cited on pp. 38, 39, 46, 115).

[174] M. Aras and C. Kilic. "Combined hybrid functional and DFT+U calculations for metal chalcogenides". *J. Chem. Phys.* 141.4 (July 2014), p. 044106 (cited on p. 38).

[175] E. Wigner and F. Seitz. "On the Constitution of Metallic Sodium". *Phys. Rev.* 43.10 (May 1933), pp. 804–810 (cited on p. 38).

[176] P. Giannozzi *et al.* "Quantum ESPRESSO: a modular and open-source software project for quantum simulations of materials". *J. Phys.: Condens. Matter* 21.39 (Sept. 2009), p. 395502 (cited on p. 38).

[177] P. M. Grant. *Electronic Properties of Rocksalt Copper Monoxide: A Proxy for High Temperature Superconductivity.* Conference talk at the 2009 APS March Meeting. Pittsburgh, PA, Mar. 2009 (cited on p. 38).

[178] N. Nosengo. "Can artificial intelligence create the next wonder material?": *Nature* 533.7601 (May 2016), pp. 22–25 (cited on p. 38).

[179] W. Kohn. "Nobel Lecture: Electronic structure of matter—wave functions and density functionals". *Rev. Mod. Phys.* 71.5 (Oct. 1999), pp. 1253–1266 (cited on p. 39).

[180] J. A. Pople. "Nobel Lecture: Quantum chemical models". *Rev. Mod. Phys.* 71.5 (Oct. 1999), pp. 1267–1274 (cited on p. 39).

[181] K. Lejaeghere *et al.* "Reproducibility in density functional theory calculations of solids". *Science* 351.6280 (Mar. 2016), aad3000 (cited on p. 40).

[182] J. Hafner. "Materials simulations using VASP—a quantum perspective to materials science". *Comput. Phys. Commun.* 177.1-2 (July 2007), pp. 6–13 (cited on pp. 39, 128).

[183] K. M. Rabe and P. Ghosez. "First-Principles Studies of Ferroelectric Oxides". *Physics of Ferroelectrics.* Topics in Applied Physics 105. Springer Berlin Heidelberg, 2007, pp. 117–174 (cited on p. 39).

[184] R. E. Cohen and H. Krakauer. "Electronic structure studies of the differences in ferroelectric behavior of $BaTiO_3$ and $PbTiO_3$". *Ferroelectrics* 136.1 (Nov. 1992), pp. 65–83 (cited on p. 39).

[185] I. Inbar and R. E. Cohen. "Origin of ferroelectricity in $LiNbO_3$ and $LiTaO_3$". *Ferroelectrics* 194.1 (1997), pp. 83–95 (cited on p. 39).

[186] K. Toyoura, M. Ohta, A. Nakamura, and K. Matsunaga. "First-principles study on phase transition and ferroelectricity in lithium niobate and tantalate". *J. Appl. Phys.* 118.6 (Aug. 2015), p. 064103 (cited on p. 39).

[187] C. J. Fennie and K. M. Rabe. "Ferroelectric transition in $YMnO_3$ from first principles". *Phys. Rev. B* 72.10 (Sept. 2005), p. 100103 (cited on pp. 39, 40).

[188] Y. Kumagai and N. A. Spaldin. "Structural domain walls in polar hexagonal manganites". *Nat. Commun.* 4 (Feb. 2013), p. 1540 (cited on p. 39).

[189] R. Machado, M. G. Stachiotti, R. L. Migoni, and A. H. Tera. "First-principles determination of ferroelectric instabilities in Aurivillius compounds". *Phys. Rev. B* 70.21 (Dec. 2004), p. 214112 (cited on p. 39).

[190] H. Djani, E. Bousquet, A. Kellou, and P. Ghosez. "First-principles study of the ferroelectric Aurivillius phase Bi_2WO_6". *Phys. Rev. B* 86.5 (Aug. 2012), p. 054107 (cited on p. 39).

[191] A. Y. Birenbaum and C. Ederer. "Potentially multiferroic Aurivillius phase $Bi_5FeTi_3O_{15}$: Cation site preference, electric polarization, and magnetic coupling from first principles". *Phys. Rev. B* 90.21 (Dec. 2014), p. 214109 (cited on p. 39).

[192] N. A. Benedek. "Origin of Ferroelectricity in a Family of Polar Oxides: The Dion—Jacobson Phases". *Inorg. Chem.* 53.7 (Apr. 2014), pp. 3769–3777 (cited on p. 39).

[193] E. E. McCabe, E. Bousquet, C. P. J. Stockdale, C. A. Deacon, T. T. Tran, P. S. Halasyamani, M. C. Stennett, and N. C. Hyatt. "Proper Ferroelectricity in the Dion–Jacobson Material $CsBi_2Ti_2NbO_{10}$: Experiment and Theory". *Chem. Mater.* 27.24 (Dec. 2015), pp. 8298–8309 (cited on p. 39).

[194] N. A. Benedek and C. J. Fennie. "Hybrid Improper Ferroelectricity: A Mechanism for Controllable Polarization-Magnetization Coupling". *Phys. Rev. Lett.* 106.10 (Mar. 2011), p. 107204 (cited on pp. 39–41).

[195] T. Birol, N. A. Benedek, and C. J. Fennie. "Interface Control of Emergent Ferroic Order in Ruddlesden-Popper $Sr_{n+1}Ti_nO_{3n+1}$". *Phys. Rev. Lett.* 107.25 (Dec. 2011), p. 257602 (cited on p. 39).

[196] H. Akamatsu *et al.* "Inversion Symmetry Breaking by Oxygen Octahedral Rotations in the Ruddlesden-Popper $NaRTiO_4$ Family". *Phys. Rev. Lett.* 112.18 (May 2014), p. 187602 (cited on pp. 39, 48).

[197] J. López-Pérez and J. Íñiguez. "Ab initio study of proper topological ferroelectricity in layered perovskite $La_2Ti_2O_7$". *Phys. Rev. B* 84.7 (Aug. 2011), p. 075121 (cited on p. 39).

[198] A. P. Levanyuk and D. G. Sannikov. "Improper ferroelectrics". *Sov. Phys. Usp.* 17.2 (Feb. 1974), p. 199 (cited on p. 39).

[199] V. Dvořák. "Improper ferroelectrics". *Ferroelectrics* 7.1 (Jan. 1974), pp. 1–9 (cited on p. 39).

[200] N. A. Hill and A. Filippetti. "Why are there *any* magnetic ferroelectrics?": *J. Magn. Magn. Mater.* Proceedings of the Joint European Magnetic Symposia (JEMS'01) 242–245, Part 2 (Apr. 2002), pp. 976–979 (cited on p. 40).

[201] C. Ederer, T. Harris, and R. Kováčik. "Mechanism of ferroelectric instabilities in non-d^0 perovskites: $LaCrO_3$ versus $CaMnO_3$". *Phys. Rev. B* 83.5 (Feb. 2011), p. 054110 (cited on p. 40).

[202] N. A. Benedek and C. J. Fennie. "Why Are There So Few Perovskite Ferroelectrics?": *J. Phys. Chem. C* 117.26 (July 2013), pp. 13339–13349 (cited on p. 40).

[203] M. T. Dove. *Structure and Dynamics: An Atomic View of Materials*. OUP Oxford, Mar. 2003 (cited on p. 41).

[204] A. Togo and I. Tanaka. "First principles phonon calculations in materials science". *Scripta Mater.* 108 (Nov. 2015), pp. 1–5 (cited on pp. 41, 47).

[205] P. Ghosez, X. Gonze, and J.-P. Michenaud. "Lattice dynamics and ferroelectric instability of barium titanate". *Ferroelectrics* 194.1 (1997), pp. 39–54 (cited on p. 41).

[206] E. Bousquet, M. Dawber, N. Stucki, C. Lichtensteiger, P. Hermet, S. Gariglio, J.-M. Triscone, and P. Ghosez. "Improper ferroelectricity in perovskite oxide artificial superlattices". *Nature* 452.7188 (Apr. 2008), pp. 732–736 (cited on p. 41).

[207] A. Matsumoto, Y. Koyama, A. Togo, M. Choi, and I. Tanaka. "Electronic structures of dynamically stable As_2O_3, Sb_2O_3, and Bi_2O_3 crystal polymorphs". *Phys. Rev. B* 83.21 (June 2011), p. 214110 (cited on p. 41).

[208] A. Togo and I. Tanaka. "Evolution of crystal structures in metallic elements". *Phys. Rev. B* 87.18 (May 2013), p. 184104 (cited on pp. 41, 48).

[209] R. Resta. "Theory of the electric polarization in crystals". *Ferroelectrics* 136.1 (Nov. 1992), pp. 51–55 (cited on pp. 41, 47).

[210] R. D. King-Smith and D. Vanderbilt. "Theory of polarization of crystalline solids". *Phys. Rev. B* 47.3 (1993), pp. 1651–1654 (cited on pp. 41, 47).

[211] R. Resta. "Macroscopic polarization in crystalline dielectrics: the geometric phase approach". *Rev. Mod. Phys.* 66.3 (July 1994), pp. 899–915 (cited on p. 41).

[212] R. Resta and D. Vanderbilt. "Theory of Polarization: A Modern Approach". *Physics of Ferroelectrics*. Topics in Applied Physics 105. Springer Berlin Heidelberg, 2007, pp. 31–68 (cited on p. 41).

[213] R. Resta. "Electrical polarization and orbital magnetization: the modern theories". *J. Phys.: Condens. Matter* 22.12 (2010), p. 123201 (cited on p. 41).

[214] N. A. Spaldin. "A beginner's guide to the modern theory of polarization". *J. Solid State Chem.* 195 (Nov. 2012), pp. 2–10 (cited on pp. 41, 42).

[215] M. V. Berry. "Quantal Phase Factors Accompanying Adiabatic Changes". *Proc. R. Soc. Lond. A* 392.1802 (Mar. 1984), pp. 45–57 (cited on p. 42).

[216] R. Resta. "Manifestations of Berry's phase in molecules and condensed matter". *J. Phys. Condens. Matter* 12 (2000), pp. 107–143 (cited on p. 42).

[217] R. Resta, M. Posternak, and A. Baldereschi. "Towards a quantum theory of polarization in ferroelectrics: The case of $KNbO_3$". *Phys. Rev. Lett.* 70.7 (Feb. 1993), pp. 1010–1013 (cited on p. 42).

[218] S. Dall'Olio, R. Dovesi, and R. Resta. "Spontaneous polarization as a Berry phase of the Hartree-Fock wave function: The case of $KNbO_3$". *Phys. Rev. B* 56.16 (Oct. 1997), pp. 10105–10114 (cited on p. 42).

[219] G. Ortiz and R. Martin. "Macroscopic polarization as a geometric quantum phase: Many-body formulation". *Phys. Rev. B* 49.20 (1994), pp. 202–211 (cited on p. 42).

[220] M. Born and K. Huang. *Dynamical theory of crystal lattices*. Clarendon Press, 1954 (cited on p. 43).

[221] P. Ghosez, J.-P. Michenaud, and X. Gonze. "Dynamical atomic charges: The case of ABO_3 compounds". *Phys. Rev. B* 58.10 (Sept. 1998), pp. 6224–6240 (cited on pp. 43, 47, 73, 76).

[222] G. Kresse and J. Hafner. "Ab initio molecular dynamics for liquid metals". *Phys. Rev. B* 47.1 (1993), pp. 558–561 (cited on p. 45).

[223] G. Kresse and J. Hafner. "Ab initio molecular-dynamics simulation of the liquid-metal–amorphous-semiconductor transition in germanium". *Phys. Rev. B* 49.20 (1994), pp. 14251–14269 (cited on p. 45).

[224] G. Kresse and J. Furthmüller. "Efficient iterative schemes for ab initio total-energy calculations using a plane-wave basis set." *Phys. Rev. B* 54.16 (Oct. 1996), pp. 11169–11186 (cited on p. 45).

[225] G. Kresse and J. Furthmüller. "Efficiency of ab-initio total energy calculations for metals and semiconductors using a plane-wave basis set". *Comp. Mater. Sci.* 6 (1996), pp. 15–50 (cited on p. 45).

[226] P. E. Blöchl. "Projector augmented-wave method". *Phys. Rev. B* 50.24 (1994), pp. 17953–17979 (cited on p. 45).

[227] G. Kresse and D. Joubert. "From ultrasoft pseudopotentials to the projector augmented-wave method". *Phys. Rev. B* 59.3 (1999), pp. 1758–1775 (cited on p. 45).

[228] H. J. Monkhorst and J. D. Pack. "Special points for Brillouin-zone integrations". *Phys. Rev. B* 13.12 (1976), pp. 5188–5192 (cited on p. 45).

[229] J. P. Perdew, A. Ruzsinszky, G. I. Csonka, O. A. Vydrov, G. E. Scuseria, L. A. Constantin, X. Zhou, and K. Burke. "Restoring the Density-Gradient Expansion for Exchange in Solids and Surfaces". *Phys. Rev. Lett.* 100.13 (Apr. 2008), pp. 136406–136406 (cited on pp. 46, 128).

[230] S. L. Dudarev, G. A. Botton, S. Y. Savrasov, C. J. Humphreys, and A. P. Sutton. "Electron-energy-loss spectra and the structural stability of nickel oxide: An LSDA+U study". *Phys. Rev. B* 57.3 (Jan. 1998), pp. 1505–1509 (cited on p. 46).

[231] K. Momma and F. Izumi. "VESTA 3 for three-dimensional visualization of crystal, volumetric and morphology data". *J. Appl. Crystallogr.* 44.6 (Oct. 2011), pp. 1272–1276 (cited on pp. 46, 103).

[232] M. I. Aroyo, A. Kirov, C. Capillas, J. M. Perez-Mato, and H. Wondratschek. "Bilbao Crystallographic Server. II. Representations of crystallographic point groups and space groups". *Acta Crystallogr.* 62.2 (2006), pp. 115–128 (cited on p. 46).

[233] M. I. Aroyo, J. M. Perez-Mato, C. Capillas, E. Kroumova, S. Ivantchev, G. Madariaga, A. Kirov, and H. Wondratschek. "Bilbao Crystallographic Server: I. Databases and crystallographic computing programs". *Z. Kristallogr.* 221.1 (2006), pp. 15–27 (cited on p. 46).

[234] M. Aroyo, J. Perez-Mato, D. Orobengoa, E. Tasci, L. F. De, and A. Kirov. "Crystallography online: Bilbao crystallographic server". *Bulg Chem Commun* 43.2 (2011), pp. 183–197 (cited on p. 46).

[235] R. P. Feynman. "Forces in Molecules". *Phys. Rev.* 56.4 (Aug. 1939), pp. 340–343 (cited on p. 46).

[236] J. R. Shewchuck. *An Introduction to the Conjugate Gradient Method Without the Agonizing Pain. Edition 1 ¼*. Aug. 1994. (Visited on 05/31/2016) (cited on p. 46).

[237] P. Pulay. “Convergence acceleration of iterative sequences. The case of SCF iteration”. *Chem. Phys. Lett.* 73.2 (July 1980), pp. 393–398 (cited on p. 46).

[238] G. P. Francis and M. C. Payne. “Finite basis set corrections to total energy pseudopotential calculations”. *J. Phys.: Condens. Matter* 2.19 (1990), p. 4395 (cited on p. 46).

[239] H. Jónsson, G. Mills, and K. W. Jacobsen. “Nudged elastic band method for finding minimum energy paths of transitions”. *Classical and Quantum Dynamics in Condensed Phase Simulations*. World Scientific Publishing Co., June 1998, pp. 385–404 (cited on p. 46).

[240] G. Henkelman, B. P. Uberuaga, and H. Jónsson. “A climbing image nudged elastic band method for finding saddle points and minimum energy paths”. *J. Chem. Phys.* 113.22 (Dec. 2000), pp. 9901–9904 (cited on p. 47).

[241] G. Henkelman and H. Jónsson. “Improved tangent estimate in the nudged elastic band method for finding minimum energy paths and saddle points”. *J. Chem. Phys.* 113.22 (Dec. 2000), pp. 9978–9985 (cited on p. 47).

[242] D. Sheppard, R. Terrell, and G. Henkelman. “Optimization methods for finding minimum energy paths”. *J. Chem. Phys.* 128.13 (Apr. 2008), p. 134106 (cited on p. 47).

[243] D. Sheppard, P. Xiao, W. Chemelewski, D. D. Johnson, and G. Henkelman. “A generalized solid-state nudged elastic band method”. *J. Chem. Phys.* 136.7 (Feb. 2012), p. 074103 (cited on p. 47).

[244] R. F. W. Bader. *Atoms in Molecules*. John Wiley & Sons, Ltd, 1990 (cited on p. 47).

[245] R. F. W. Bader. “A quantum theory of molecular structure and its applications”. *Chem. Rev.* 91.5 (July 1991), pp. 893–928 (cited on p. 47).

[246] W. Tang, E. Sanville, and G. Henkelman. “A grid-based Bader analysis algorithm without lattice bias”. *J. Phys.: Condens. Matter* 21.8 (Feb. 2009), p. 084204 (cited on p. 47).

[247] S. Gudmundsdóttir, W. Tang, G. Henkelman, H. Jónsson, and E. Skúlason. “Local density of states analysis using Bader decomposition for N_2 and CO_2 adsorbed on Pt(110)-(1 × 2) electrodes.” *J. Chem. Phys.* 137.16 (Oct. 2012), pp. 164705–164705 (cited on p. 47).

[248] M. Gajdoš, K. Hummer, G. Kresse, J. Furthmüller, and F. Bechstedt. “Linear optical properties in the projector-augmented wave methodology”. *Phys. Rev. B* 73.4 (Jan. 2006), p. 045112 (cited on p. 47).

[249] S. Baroni and R. Resta. "Ab initio calculation of the macroscopic dielectric constant in silicon". *Phys. Rev. B* 33.10 (May 1986), pp. 7017–7021 (cited on p. 47).

[250] A. Togo, F. Oba, and I. Tanaka. "First-principles calculations of the ferroelastic transition between rutile-type and $CaCl_2$-type SiO_2 at high pressures". *Phys. Rev. B* 78.13 (Oct. 2008), pp. 134106–134106 (cited on p. 47).

[251] E. Bousquet. "First-Principles study of ferroelectric oxide nanostructures". PhD thesis. Liège: Université de Liège, 2008 (cited on p. 48).

[252] B. C. Hauback, H. Fjellvåg, O. Steinsvoll, K. Johansson, O. T. Buset, and J. Jørgensen. "The high resolution Powder Neutron Diffractometer PUS at the JEEP II reactor at Kjeller in Norway". *J. Neutron Research* 8.3 (2000), pp. 215–232 (cited on p. 49).

[253] G. W. Stinton and J. S. O. Evans. "Parametric Rietveld refinement". *J. Appl. Crystallogr.* 40.1 (Feb. 2007), pp. 87–95 (cited on p. 50).

[254] G. H. Olsen, S. M. Selbach, and T. Grande. "On the energetics of cation ordering in tungsten-bronze-type oxides". *Phys. Chem. Chem. Phys.* 17.45 (Nov. 2015), pp. 30343–30351 (cited on pp. 53, 69, 77).

[255] H. T. Stokes and D. M. Hatch. "FINDSYM : program for identifying the space-group symmetry of a crystal". *J. Appl. Crystallogr.* 38.1 (Feb. 2005), pp. 237–238 (cited on pp. 54, 128).

[256] H. S. C. O'Neill and A. Navrotsky. "Simple spinels: crystallographic parameters, cation radii, lattice energies, and cation distribution". *Am. Mineral.* 68 (1983), pp. 181–194 (cited on pp. 58, 62, 67).

[257] H. Schmalzried. "Röntgenographische Untersuchung der Kationenverteilung in Spinellphasen". *Z. Phys. Chem.* 28 (1961), pp. 203–219 (cited on p. 58).

[258] A. Navrotsky and O. J. Kleppa. "The thermodynamics of cation distributions in simple spinels". *J. Inorg. Nucl. Chem.* 29.11 (Nov. 1967), pp. 2701–2714 (cited on p. 58).

[259] T. Norby. "A Kröger-Vink Compatible Notation for Defects in Inherently Defective Sublattices". *J. Korean Ceram. Soc.* 47.1 (2010), pp. 19–25 (cited on p. 58).

[260] R. M. Hazen and A. Navrotsky. "Effects of pressure on order-disorder reactions". *Am. Mineral.* 81.9-10 (1996), pp. 1021–1035 (cited on p. 66).

[261] F. Meducin, S. A. T. Redfern, Y. Le Godec, H. J. Stone, M. G. Tucker, M. T. Dove, and W. G. Marshall. "Study of cation order-disorder in $MgAl_2O_4$ spinel by in situ neutron diffraction up 1600 K and 3.2 GPa". *Am. Mineral.* 89.7 (July 2004), pp. 981–986 (cited on p. 66).

[262] F. Nestola, T. B. Ballaran, T. Balic-Zunic, F. Princivalle, L. Secco, and A. Dal Negro. "Comparative compressibility and structural behavior of spinel $MgAl_2O_4$ at high pressures: The independency on the degree of cation order". *Am. Mineral.* 92.11-12 (2007), pp. 1838–1843 (cited on p. 66).

[263] S. A. T. Redfern, R. J. Harrison, H. S. C. O'Neill, and D. R. R. Wood. "Thermodynamics and kinetics of cation ordering in $MgAl_2O_4$ spinel up to 1600 °C from in situ neutron diffraction". *Am. Mineral.* 84.3 (Mar. 1999), pp. 299–310 (cited on p. 67).

[264] G. H. Olsen, U. Aschauer, N. A. Spaldin, S. M. Selbach, and T. Grande. "Origin of ferroelectric polarization in tetragonal tungsten-bronze-type oxides". *Phys. Rev. B* 93.18 (May 2016), p. 180101 (cited on pp. 69, 99).

[265] D. Orobengoa, C. Capillas, M. I. Aroyo, and J. M. Perez-Mato. "AMPLIMODES: symmetry-mode analysis on the Bilbao Crystallographic Server". *J. Appl. Crystallogr.* 42.5 (Sept. 2009), pp. 820–833 (cited on pp. 70, 71, 110).

[266] F. Detraux, P. Ghosez, and X. Gonze. "Anomalously large Born effective charges in cubic WO_3". *Phys. Rev. B* 56.3 (July 1997), pp. 983–985 (cited on p. 73).

[267] P. S. Halasyamani and K. R. Poeppelmeier. "Noncentrosymmetric Oxides". *Chem. Mater.* 10.10 (Oct. 1998), pp. 2753–2769 (cited on p. 76).

[268] Y. Kuroiwa, S. Aoyagi, A. Sawada, J. Harada, E. Nishibori, M. Takata, and M. Sakata. "Evidence for Pb-O Covalency in Tetragonal $PbTiO_3$". *Phys. Rev. Lett.* 87.21 (Nov. 2001), p. 217601 (cited on pp. 76, 90, 103).

[269] T. A. Whittle, S. Schmid, and C. J. Howard. "Octahedral tilting in the tungsten bronzes". *Acta Crystallogr. B* 71.3 (June 2015), pp. 342–348 (cited on pp. 76, 98).

[270] H. Brusset, M. Gillier-Pandraud, and S. D. Voliotis. "Etude du polymorphisme du metaniobate de strontium $SrNb_2O_6$". *Mater. Res. Bull.* 6.1 (Jan. 1971), pp. 5–14 (cited on p. 76).

[271] S. Podlozhenov, H. A. Graetsch, J. Schneider, M. Ulex, M. Wöhlecke, and K. Betzler. "Structure of strontium barium niobate $Sr_xBa_{1-x}Nb_2O_6$ (SBN) in the composition range $0.32 \leq x \leq 0.82$". *Acta Crystallogr. B* 62.6 (Dec. 2006), pp. 960–965 (cited on pp. 77, 94, 98).

[272] J.-H. Ko, S. Kojima, S. G. Lushnikov, R. S. Katiyar, T.-H. Kim, and J.-H. Ro. "Low-temperature transverse dielectric and pyroelectric anomalies of uniaxial tungsten bronze crystals". *J. Appl. Phys.* 92.3 (Aug. 2002), pp. 1536–1543 (cited on p. 77).

[273] C. Capillas, E. S. Tasci, G. de la Flor, D. Orobengoa, J. M. Perez-Mato, and M. I. Aroyo. "A new computer tool at the Bilbao Crystallographic Server to detect and characterize pseudosymmetry". *Z. Kristallogr.* 226.2 (2011), pp. 186–196 (cited on pp. 84, 94).

[274] L. Liang, Y. L. Li, L.-Q. Chen, S. Y. Hu, and G.-H. Lu. "Thermodynamics and ferroelectric properties of $KNbO_3$". *J. Appl. Phys.* 106.10 (Nov. 2009), p. 104118 (cited on p. 86).

[275] K. R. Chakraborty, K. R. Sahu, A. De, and U. De. "Structural Characterization of Orthorhombic and Rhombohedral Lead Meta-Niobate Samples". *Integr. Ferroelectr.* 120.1 (Nov. 2010), pp. 102–113 (cited on pp. 86, 121).

[276] G. H. Olsen, M. H. Sørby, B. C. Hauback, S. M. Selbach, and T. Grande. "Revisiting the Crystal Structure of Rhombohedral Lead Metaniobate". *Inorg. Chem.* 53.18 (Sept. 2014), pp. 9715–9721 (cited on pp. 86, 119).

[277] R. Guo, H. T. Evans, Jr., and A. S. Bhalla. "Crystal structure analysis and polarization mechanisms of ferroelectric tetragonal tungsten bronze lead barium niobate". *Ferroelectrics* 206.1 (Feb. 1998), pp. 123–132 (cited on pp. 90, 97).

[278] W. M. Haynes, ed. *CRC Handbook of Chemistry and Physics*. 93rd Edition. Boca Raton, Fla.; London: CRC Press, June 2012 (cited on p. 94).

[279] S. C. Abrahams, S. K. Kurtz, and P. B. Jamieson. "Atomic Displacement Relationship to Curie Temperature and Spontaneous Polarization in Displacive Ferroelectrics". *Phys. Rev.* 172.2 (Aug. 1968), pp. 551–553 (cited on p. 99).

[280] J. P. Mulkey and F. W. Oehme. "A review of thallium toxicity". *Vet. Hum. Toxicol.* 35.5 (Oct. 1993), pp. 445–453 (cited on p. 99).

[281] N. J. Ramer and A. M. Rappe. "Application of a new virtual crystal approach for the study of disordered perovskites". *J. Phys. Chem. Solids* 61.2 (Feb. 2000), pp. 315–320 (cited on p. 101).

[282] L. Bellaiche and D. Vanderbilt. "Virtual crystal approximation revisited: Application to dielectric and piezoelectric properties of perovskites". *Phys. Rev. B* 61.12 (Mar. 2000), pp. 7877–7882 (cited on p. 101).

[283] P. Ghosez, D. Desquesnes, X. Gonze, and K. M. Rabe. "First-principles study of lattice instabilities in $Ba_xSr_{1-x}TiO_3$". *AIP Conf. Proc.* 535.1 (2000), pp. 102–110 (cited on p. 101).

[284] E. O. Chi, A. Gandini, K. M. Ok, L. Zhang, and P. S. Halasyamani. "Syntheses, Structures, Second-Harmonic Generating, and Ferroelectric Properties of Tungsten Bronzes: $A_6M_2M'_8O_{30}$ (A = Sr^{2+}, Ba^{2+}, or Pb^{2+}; M = Ti^{4+}, Zr^{4+}, or Hf^{4+}; M′ = Nb^{5+} or Ta^{5+})". *Chem. Mater.* 16.19 (Sept. 2004), pp. 3616–3622 (cited on p. 101).

[285] J. Leciejewicz. "On the crystal structure of tetragonal (red) PbO". *Acta Crystallogr.* 14.12 (Dec. 1961), pp. 1304–1304 (cited on p. 103).

[286] R. J. Hill. "Refinement of the structure of orthorhombic PbO (massicot) by Rietveld analysis of neutron powder diffraction data". *Acta Crystallogr. C* 41.9 (Sept. 1985), pp. 1281–1284 (cited on p. 103).

[287] G. Trinquier and R. Hoffmann. "Lead monoxide. Electronic structure and bonding". *J. Phys. Chem.* 88.26 (Dec. 1984), pp. 6696–6711 (cited on p. 103).

[288] G. W. Watson, S. C. Parker, and G. Kresse. "Ab initio calculation of the origin of the distortion of α-PbO". *Phys. Rev. B* 59.13 (Apr. 1999), pp. 8481–8486 (cited on p. 103).

[289] A. Georges, G. Kotliar, W. Krauth, and M. J. Rozenberg. "Dynamical mean-field theory of strongly correlated fermion systems and the limit of infinite dimensions". *Rev. Mod. Phys.* 68.1 (Jan. 1996), pp. 13–125 (cited on p. 116).

[290] G. Kotliar and D. Vollhardt. "Strongly correlated materials: Insights from dynamical mean-field theory". *Phys. Today* 57.3 (Mar. 2004), pp. 53–59 (cited on p. 116).

[291] G. Kotliar, S. Y. Savrasov, K. Haule, V. S. Oudovenko, O. Parcollet, and C. A. Marianetti. "Electronic structure calculations with dynamical mean-field theory". *Rev. Mod. Phys.* 78.3 (Aug. 2006), pp. 865–951 (cited on p. 116).

[292] K. Held. "Electronic structure calculations using dynamical mean field theory". *Adv. Phys.* 56.6 (Nov. 2007), pp. 829–926 (cited on p. 116).

[293] S. Biermann, A. Poteryaev, A. I. Lichtenstein, and A. Georges. "Dynamical Singlets and Correlation-Assisted Peierls Transition in VO_2". *Phys. Rev. Lett.* 94.2 (Jan. 2005), p. 026404 (cited on p. 116).

[294] K. Dymkowski and C. Ederer. "Strain-induced insulator-to-metal transition in $LaTiO_3$ within DFT + DMFT". *Phys. Rev. B* 89.16 (Apr. 2014), p. 161109 (cited on p. 116).

[295] P. A. Cox. *Transition Metal Oxides: An Introduction to their Electronic Structure and Properties*. Oxford: Clarendon Press, 1992 (cited on pp. 116, 117).

[296] I. Wentzell, H. Fuess, J. W. Bats, and A. K. Cheetham. "Preparation and Crystal Structure of $PbRe_2O_6$. An Example of the Re_2O_{10} Unit with No Metal-Metal Bonding". *Z. anorg. allg. Chem.* 528.9 (Sept. 1985), pp. 48–54 (cited on pp. 119, 131).

[297] W. C. Hamilton. "Significance tests on the crystallographic *R* factor". *Acta Crystallogr.* 18.3 (Mar. 1965), pp. 502–510 (cited on pp. 126, 127).

[298] E. Prince. *Mathematical Techniques in Crystallography and Materials Science*. Berlin, Heidelberg: Springer Berlin Heidelberg, 2004 (cited on p. 126).

[299] F. Galasso, G. Layden, and G. Ganung. "ANb_2O_6 and ATa_2O_6 Phases". *Mater. Res. Bull.* 3.5 (1968), pp. 397–408 (cited on p. 131).

[300] G. K. Layden. "Dielectric and Structure Studies of Hexagonal $BaTa_2O_6$". *Mater. Res. Bull.* 3.4 (1968), pp. 349–360 (cited on p. 131).

[301] H. Beck, H. Seup-Ra, R. Haberkorn, H. Kohlmann, M. Eul, T. Harmening, and R. Pöttgen. "A Study on AB_2O_6 Compounds: Part I, Synthesis, Structure, Magnetic Properties and ^{151}Eu Mössbauer Spectroscopic Data of $EuNb_2O_6$". *Z. anorg. allg. Chem.* 636.6 (May 2010), pp. 1069–1073 (cited on p. 131).

[302] H. P. Beck. "A study on AB_2O_6 compounds, Part II: the branches of the hcp family". *Z. Kristallogr.* 227.12 (Dec. 2012), pp. 843–858 (cited on p. 131).

[303] H. P. Beck. "A study on AB_2O_6 compounds, Part III: Co-ordination needs and patterns of connectivity". *Z. Kristallogr.* 228.6 (June 2013), pp. 271–288 (cited on p. 131).

[304] H. P. Beck. "A study on AB_2O_6 compounds, Part IV: on segregation, electrostatic imbalance and connectivity formulas". *Z. Kristallogr.* 229.1 (2014), pp. 24–38 (cited on p. 131).

Appendices

Published scientific papers

1. G. H. Olsen, M. H. Sørby, B. C. Hauback, S. M. Selbach and T. Grande, "Revisiting the crystal structure of rhombohedral lead metaniobate", *Inorg. Chem.* **53**, 9715-9721 (2014).

2. G. H. Olsen, S. M. Selbach and T. Grande, "On the energetics of cation ordering in tungsten-bronze-type oxides", *Phys. Chem. Chem. Phys.* **17**, 30343-30351 (2015).

3. G. H. Olsen, U. Aschauer, N. A. Spaldin, S. M. Selbach and T. Grande, "Origin of ferroelectric polarization in tetragonal tungsten-bronze-type oxides", *Phys. Rev. B* **93**, 180101(R) (2016).

Inorganic Chemistry

Article

pubs.acs.org/IC

Revisiting the Crystal Structure of Rhombohedral Lead Metaniobate

Gerhard Henning Olsen,[†] Magnus Helgerud Sørby,[‡] Bjørn Christian Hauback,[‡] Sverre Magnus Selbach,[†] and Tor Grande*[,†]

[†]Norwegian University of Science and Technology (NTNU), Høgskoleringen 1, 7491 Trondheim, Norway

[‡]Institute for Energy Technology (IFE), Instituttveien 18, NO-2007 Kjeller, Norway

Supporting Information

ABSTRACT: Lead metaniobate ($PbNb_2O_6$) can exist both as a stable rhombohedral and a metastable orthorhombic tungsten-bronze-type polymorph. Although the orthorhombic is a well-known ferroelectric material, the rhombohedral polymorph has been far less studied. The crystal structure and energetic stability of the stable rhombohedral polymorph of lead metaniobate is re-examined by powder X-ray diffraction and powder neutron diffraction in combination with ab initio calculations. We show that this structure is described by the polar space group *R*3, in contradiction to the previously reported space group *R*3*m*. The crystal structure is unusual, consisting of edge-sharing dimers of $NbO_{6/2}$ octahedra forming layers with 6- and 3-fold rings of octahedra and lead ions in channels formed by these rings. The layers are connected by corner-sharing between octahedra. Finally, the crystal structure is discussed in relation to other AB_2O_6 compounds with B = Nb, Ta.

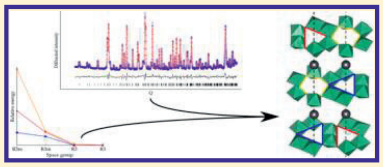

INTRODUCTION

Lead metaniobate ($PbNb_2O_6$ or PN) is one of the simplest compounds to crystallize in the tungsten-bronze-type structure.[1] The tungsten-bronze polymorph is orthorhombic (denoted o-PN) and ferroelectric with a high Curie temperature of 570 °C.[2] The paraelectric tungsten-bronze has a tetragonal crystal structure (t-PN). A large anisotropy in electromechanical coupling factors and a very low mechanical quality factor makes the material suitable for high-temperature electroacoustic applications.[3] The t-PN polymorph is, however, metastable with respect to a rhombohedral polymorph (r-PN) below a transition temperature reported at 1200−1250 °C,[4−6] and this thermodynamically stable low-temperature phase has not been reported to have attractive properties. The phase transition between the t-PN and r-PN polymorphs is reconstructive and sluggish, so the metastable tungsten-bronze phase can be obtained by quenching the material from above the r-PN to t-PN transition at 1200−1250 °C.[4]

Numerous attempts have been done to stabilize the tungsten-bronze phase, for example, by molten salt methods,[7,8] hydrothermal synthesis,[9] or formation of solid solutions.[10] The rhombohedral polymorph, on the other hand, has received comparatively little attention, although the possibility of attractive piezoelectric properties has been suggested also for this polymorph, with one work reporting a possible ferroelectric phase transition at 815 °C.[11] Still, investigations on the crystal structure and properties of the r-PN polymorph are few.[11−14] Here, we re-examine the crystal structure of r-PN by powder X-ray- and powder neutron diffraction combined with density functional theory calculations, with particular focus on determining the correct space group symmetry. We show that, contrary to previous assumptions,[12,13] *R*3*m* is not the correct space group symmetry for r-PN. On the basis of experimental and computational data, we demonstrate that the structure is described by the space group *R*3 or the closely related space group $R\bar{3}$. We argue that *R*3 is the more plausible of the two because of the reported high-temperature properties of r-PN, which indicate that the low-temperature space group symmetry is polar. The fact that the space group is polar motivates further studies of possible piezoelectric properties.

EXPERIMENTAL SECTION

Powders of lead metaniobate were prepared by conventional solid-state synthesis. PbO (Aldrich, 99.999%) and Nb_2O_5 (Aldrich, 99.99%) powders were mixed in equimolar amounts with a mortar and pestle, uniaxially pressed into 25 mm pellets and fired at 850 °C for 2 h in a sealed alumina crucible. The pellets were crushed, and pressing and firing was repeated twice, for a total of three 2 h firings at 850 °C. The sample was finally crushed to a powder and annealed for 30 min at 550 °C prior to structural analysis in order to remove possible strain from the crushing.

Powder X-ray diffraction was performed at room temperature with a Siemens D5005 diffractometer in Bragg−Brentano geometry, with Cu $K\alpha_1$ radiation, a primary graphite monochromator, and a Braun position sensitive detector. Data were collected in a 2θ range of 5°−110° with a step size of 0.015°.

Powder neutron diffraction data were collected with the PUS diffractometer at the JEEP II reactor at Institute for Energy Technology at Kjeller, Norway. Neutrons with a wavelength of 1.5555 Å were provided from a vertically focusing Ge monochromator using the (511) reflection and a takeoff angle of 90°. Data were collected at room temperature in a 2θ range of 10°−130° in steps of 0.05° with two detector banks; each contained six horizontally stacked ^{3}He-filled position sensitive detector tubes covering 20° in 2θ.[15]

Received: May 27, 2014
Published: August 28, 2014

   dx.doi.org/10.1021/ic5012378 | *Inorg. Chem.* 2014, 53, 9715−9721

Table 1. Wyckoff Sites and Atomic Positions for Each of the Five Space Groups Considered in This Work[a]

atom	$R3$	$R\bar{3}$	$R32$	$R3m$	$R\bar{3}m$
Pb1	1*a*	1*a*	1*a*	1*a*	1*a*
	(*x*,*x*,*x*)	(0,0,0)	(0,0,0)	(*x*,*x*,*x*)	(0,0,0)
Pb2	1*a*	2*c*	2*c*	1*a*	2*c*
	(*x*,*x*,*x*)	(*x*,*x*,*x*)	(*x*,*x*,*x*)	(*x*,*x*,*x*)	(*x*,*x*,*x*)
Pb3	1*a*			1*a*	
	(*x*,*x*,*x*)			(*x*,*x*,*x*)	
Nb1	3*b*	6*f*	3*e*	6*c*	6*g*
	(*x*,*y*,*z*)	(*x*,*y*,*z*)	(1/2,*y*,−*y*)	(*x*,*y*,*z*)	(*x*,−*x*,1/2)
Nb2	3*b*		3*e*		
	(*x*,*y*,*z*)		(1/2,*y*,−*y*)		
O1	3*b*	6*f*	3*d*	6*c*	6*f*
	(*x*,*y*,*z*)	(*x*,*y*,*z*)	(0,*y*,−*y*)	(*x*,*y*,*z*)	(*x*,−*x*,0)
O2	3*b*	6*f*	3*d*	3*b*	6*h*
	(*x*,*y*,*z*)	(*x*,*y*,*z*)	(0,*y*,−*y*)	(*x*,*x*,*z*)	(*x*,*x*,*z*)
O3	3*b*	6*f*	6*f*	3*b*	6*h*
	(*x*,*y*,*z*)	(*x*,*y*,*z*)	(*x*,*y*,*z*)	(*x*,*x*,*z*)	(*x*,*x*,*z*)
O4	3*b*		6*f*	3*b*	
	(*x*,*y*,*z*)		(*x*,*y*,*z*)	(*x*,*x*,*z*)	
O5	3*b*			3*b*	
	(*x*,*y*,*z*)			(*x*,*x*,*z*)	
O6	3*b*				
	(*x*,*y*,*z*)				
atomic DOF	26	13	11	16	7

[a]The notation (*x*, *x*, *x*) means *x* = *y* = *z*). The bottom line gives the atomic degrees of freedom (DOF) for each space group (i.e., the total number of free variables in the atomic coordinates). For the polar groups *R*3 and *R*3*m*, the atomic DOF is 1 less than the number of free variables due to anchoring of Pb1 at (0,0,0).

Rietveld refinements were performed with both data sets simultaneously using the Bruker AXS Topas 4.2 software, with structural data from Mahé[13] used as starting point. The data sets were refined according to the symmetry constraints of five distinct rhombohedral space groups: $R\bar{3}m$ (166), *R*3*m* (160), *R*32 (155), $R\bar{3}$ (148), and *R*3 (146). The rhombohedral setting was used for all the space groups, and Pb was anchored at (0,0,0) for the Pb1 Wyckoff position for the polar space groups *R*3*m* and *R*3 (see Table 1). The background intensity was fitted to a Chebychev polynomial, and peak shapes were fitted to a Pearson type VII profile for X-ray data and a Thompson−Cox−Hastings pseudo-Voigt profile for neutron data. Lattice parameters and atomic positions were refined according to the atomic degrees of freedom described in Table 1, and isotropic thermal displacement factors were refined under the constraint that all atoms of the same element on the same Wyckoff site have the same displacement factors.

COMPUTATIONAL DETAILS

Density functional theory (DFT) calculations were done with the VASP code.[16−19] Calculations of the exchange-correlation energy were done both within the local density approximation (LDA), and within the generalized gradient approximation (GGA) with the functionals PBE[20] and PBEsol.[21] Projector-augmented wave potentials[22,23] were used, treating 14 valence electrons for Pb ($5d^{10}6s^26p^2$), 13 for Nb ($4s^24p^64d^35s^2$), and 6 for O ($2s^22p^4$). Well-converged results were achieved when wave functions were expanded in a plane wave basis set up to an energy cutoff of 550 eV, and Brillouin zone integration was performed on a 2 × 2 × 2 Monkhorst−Pack grid.[24] For geometry optimization, lattice vectors and atomic coordinates were relaxed until the forces on the ions were less than 1×10^{-4} eV Å^{-1}.

The experimental structures, as obtained by refinement of diffraction data, were relaxed using the three functionals described above. Three different contraints were applied: (a) ionic relaxation at the experimental lattice parameters; (b) relaxation of ions and lattice vectors with the constraint that the unit cell volume be constant and equal to the experimental volume; (c) full relaxation of both ions and lattice vectors with no constraints on the unit cell volume (see Figure 2). The total energies were then compared between cells of different space group symmetries.

Lattice dynamical calculations were performed with the force constant method,[25] using VASP for calculation of Hellmann−Feynman forces and the Phonopy code for calculation of the approximate dynamical matrix and the full phonon dispersion. A 2 × 2 × 2 supercell was used, and symmetry-inequivalent atoms displaced by 0.01 Å in each direction (see Supporting Information for details).

RESULTS

Diffraction Experiments. The five space groups considered (*R*3, $R\bar{3}$, *R*32, *R*3*m*, and $R\bar{3}m$) have the same selection rules for diffraction, so the distinction between the different candidate space groups relies only on the intensities of the Bragg reflections.

X-ray and neutron diffractograms are shown in Figure 1 together with Rietveld refinements within space group *R*3, which gave the best fit both for the two data sets separately and for simultaneous refinement (individual refinements and relevant parameters are given in Supporting Information). The goodness of fit for the different space groups is summarized in Table 2 together with lattice parameters from the refinements. Space group $R\bar{3}m$ yielded the worst fit and gave rise to a systematic deviation for certain reflections between experimental data and the fit. Also, the previously reported[12] space group *R*3*m* gave systematic deviations for certain reflections, and a magnification of the representative (321) reflection is shown in the insets of Figure 1, comparing the fit for space group *R*3*m* and *R*3. Similar deviations of comparable magnitude are apparent also in other reflections throughout the *Q* range, notably the $(1\bar{4}\bar{3})$ and $(03\bar{7})$ reflections at approximately *Q* = 4.55 Å^{-1} and *Q* = 6.52 Å^{-1}, respectively (see Supporting Information). For space group *R*3,

dx.doi.org/10.1021/ic5012378 | Inorg. Chem. 2014, 53, 9715−9721

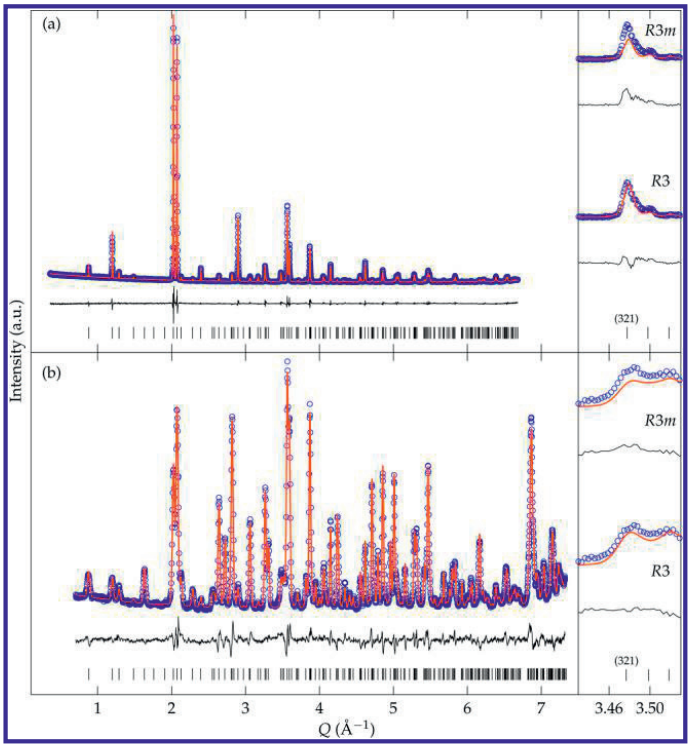

Figure 1. (a) Powder X-ray and (b) powder neutron diffractograms, showing observed (blue circles) and calculated (red line) intensity for space group *R*3, and their difference (black line) as a function of the scattering vector ($Q = 2\pi/d$). Black tick marks show the position of individual Bragg reflections. Close-up image to the right shows a comparison between refinements within space groups *R*3 and *R*3*m*.

Table 2. Lattice Parameters at Room Temperature and Quality of Fit for Joint Refinement of X-ray and Neutron Data within Each of the Five Space Groups Considered[a]

	lattice parameters		quality of fit		
space group	a (Å)	α (deg)	R_p (%)	R_{wp} (%)	χ^2
*R*3	7.17530(7)	93.9548(5)	6.62	9.05	1.89
$R\bar{3}$	7.17530(7)	93.9552(5)	6.85	9.29	1.94
*R*32	7.17508(9)	93.9566(6)	8.21	11.66	2.44
*R*3*m*	7.17521(8)	93.9555(6)	7.65	10.69	2.23
$R\bar{3}m$	7.17516(10)	93.9564(6)	8.51	11.93	2.49
*R*3*m*[12]	7.183	93.94			
*R*3*m*[14]	7.1654	93.908			

[a]Estimated standard deviations are in parentheses. Literature values for *R*3*m* (converted from hexagonal setting) are included at the bottom.

which gave the best fit, both the experimental (joint refinement of X-ray and neutron diffraction data) and the optimized atomic coordinates are given in Table 3.

For all space groups, the refined structures show distinct differences from the previously reported structures, refined in space group *R*3*m*.[13,14] The most pronounced difference is that the $NbO_{6/2}$ octahedra are far less deformed, with less variation in the Nb−O bond lengths. This will be further discussed below.

Computational Results. Additional information on the relative stability of the different space groups is obtained from the calculated energies of the candidate structures. The energies of the possible structures are shown in Figure 2a−c, corresponding to the three different relaxation constraints described above. For full relaxation with no volume constraints, the volume after relaxation is shown in Figure 2d. All energies are reported per formula unit of $PbNb_2O_6$ and given relative to the structure with the lowest symmetry, *R*3. The energy of the *R*32 structure is omitted from the figures, because this experimental structure relaxes into the higher-symmetry space group $R\bar{3}m$. Because of this apparent instability and the relatively poor goodness of fit for Rietveld refinement within this space group (Table 2), *R*32 was not considered further as a plausible space group symmetry for r-PN at ambient temperature.

For the three space groups $R\bar{3}m$, *R*3*m*, and *R*3, the calculated energies correlate with the degree of symmetry, with $R\bar{3}m$ having the highest symmetry and the highest calculated energy, *R*3*m* intermediate, and *R*3 the lowest. $R\bar{3}$, however, does not follow this trend: it has essentially the same energy as *R*3, while at the same time possessing a higher symmetry and merely half as many atomic degrees of freedom as *R*3 (Table 1). This result is the same for all the relaxation methods used. Lattice dynamical calculations similarly show negligible difference between the dynamical stability of the $R\bar{3}$ and *R*3 structures, while the *R*3*m* and $R\bar{3}m$ structures have instabilities which correlate with their higher energy (phonon dispersions are included in Supporting Information).

dx.doi.org/10.1021/ic5012378 | *Inorg. Chem.* 2014, 53, 9715−9721

Table 3. Atomic Positions and Unit Cell Parameters ($R3$, Rhombohedral Setting) Based on Joint Refinement of Diffraction Data, and after Geometry Optimization by DFT Calculations (PBEsol, Unconstrained Relaxation)[a]

	experimental				optimized		
atom	x	y	z	B_{eq} (Å^2)	x	y	z
Pb1	0	0	0	1.48(3)	0	0	0
Pb2	0.3527(4)	0.3527(4)	0.3527(4)	1.48(3)	0.3527	0.3527	0.3527
Pb3	0.6889(5)	0.6889(5)	0.6889(5)	1.48(3)	0.6764	0.6764	0.6764
Nb1	0.5338(11)	0.2006(9)	0.8384(10)	0.06(3)	0.5403	0.1965	0.8405
Nb2	0.1531(10)	0.5117(8)	0.8068(9)	0.06(3)	0.1562	0.5122	0.8123
O1	0.404(2)	0.947(2)	0.678(2)	0.40(3)	0.403	0.959	0.678
O2	0.9617(14)	0.3878(14)	0.668(2)	0.40(3)	0.9501	0.3941	0.675
O3	0.760(2)	0.773(2)	0.065(2)	0.40(3)	0.772	0.772	0.058
O4	0.055(2)	0.053(2)	0.5216(14)	0.40(3)	0.058	0.058	0.5129
O5	0.571(2)	0.580(2)	0.293(2)	0.40(3)	0.581	0.581	0.294
O6	0.292(2)	0.294(2)	0.8515(12)	0.40(3)	0.295	0.295	0.8398
a (Å)	7.17530(7)				7.15572		
α (deg)	93.9548(5)				94.0297		
V_{cell} (Å^3)	366.652(11)				363.551		

[a] B_{eq} is the isotropic thermal displacement factors, constrained to be the same for all atoms of the same element. Optimized atomic positions from DFT calculations are reported with a numerical precision corresponding to the uncertainty in the experimental data.

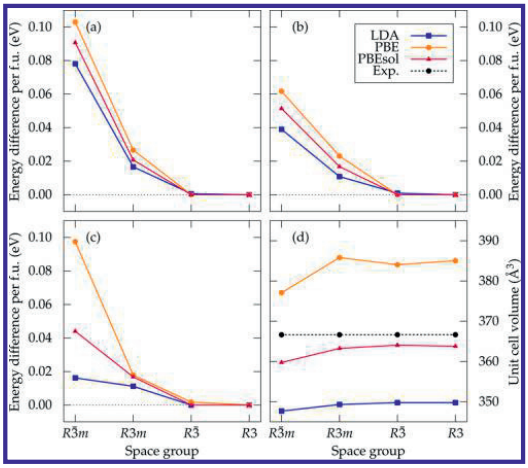

Figure 2. Calculated energy per formula unit for each of the space groups considered, after (a) ionic relaxation at experimental lattice parameters; (b) relaxation of ions and lattice vectors at constant experimental volume; (c) unconstrained relaxation of ions and lattice vectors. Energies are given relative to the lowest-energy space group $R3$. (d) Unit cell volume after unconstrained relaxation with the three functionals, including the experimental volume.

Atomic positions for the $R3$ structure, both experimental (joint refinement) and after computational optimization (full relaxation with the PBEsol functional), are given in in Table 3.

DISCUSSION

Determination of Space Group Symmetry. Both refinement of the diffraction data and comparison of DFT energies, point to either of $R\bar{3}$ or $R3$ as the most likely space group symmetries for r-PN at ambient conditions. This is in contrast to earlier works,[12,13] which conclude that the space group is $R3m$. Figure 3 gives the group−subgroup relations between all five space groups considered in this work. The path involving space group $R32$ can be excluded based on the poor

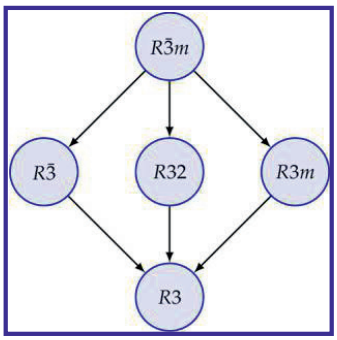

Figure 3. Group−subgroup relations between the space group symmetries considered in this study.

Rietveld fit (Table 2) and the instability with respect to force-based geometry optimization.

The difference in quality of fit is quite small between $R3$ and $R\bar{3}$, as is evident from Table 2. A reasonable way of testing the significance of this difference is by Hamilton's R-ratio test,[26] which is based on the well-known F-test. In our case, the ratio of R_{wp} factors for the $R\bar{3}$ and $R3$ refinements is $\mathcal{R} = 1.027$. For the joint refinement, the total number of (hkl) reflections is 730, with 60 parameters refined for $R3$ and 47 for $R\bar{3}$ (the difference of 13 corresponding to the difference in atomic degrees of freedom, as given in Table 1). From Hamilton's table,[26] we read off $\mathcal{R}_{13,670,0.005} = 1.023$, meaning that the probability of $R3$ actually being a better model than $R\bar{3}$ for this refinement, is higher than 0.995. The same result is obtained if the X-ray and neutron diffraction data is refined and tested individually, so we conclude that $R3$ is a significantly better model than $R\bar{3}$.

In addition to the rhombohedral space group symmetries shown in Figure 3, one could in principle also consider refinements within further subgroups of $R3$ and $R\bar{3}$, that is, the trigonal groups $P3$ (143), $P3_1$ (144), $P3_2$ (145), and $P\bar{3}$ (147). $P3_1$ and $P3_2$, however, can be excluded, as the 3-fold screw axes are not compatible with the stacking pattern found in this

dx.doi.org/10.1021/ic5012378 | Inorg. Chem. 2014, 53, 9715−9721

structure (further described below). $P3$ and $P\bar{3}$, although possible from a structural point of view, do not yield a better fit than $R3$, despite a higher number of refined parameters for the trigonal groups. Because of this, we see no reason not to keep the rhombohedral lattice centering, restricting the possible space groups to those shown in Figure 3.

A general observation for all energy calculations is that $R\bar{3}m$ has the highest energy, $R3m$ intermediate, and $R\bar{3}$ and $R3$ are essentially at the same, lowest energy. This is true for all methods of geometry optimization, and for all functionals, as shown in Figures 2a−c. In practice, the experimental $R3$ structure relaxes toward $R\bar{3}$ symmetry, and the distinction between them is ultimately a matter of tolerance during the symmetry analysis.[27] For the constrained relaxations (Figure 2a,b), the $R3$ structure is regarded as having $R\bar{3}$ symmetry for tolerances higher than 3×10^{-4} if relaxed with PBE, and 3×10^{-2} if relaxed with PBEsol. For the unconstrained relaxation (Figure 2c), the threshold values are 5×10^{-4} for LDA and 1×10^{-3} for PBEsol. In other words, the structures relaxed using PBEsol give the largest structural differences between $R3$ and $R\bar{3}$, although the two space groups are hard to distinguish in all cases.

The graphs in Figure 2 confirm certain well-known properties of the functionals used.[28] LDA has an inherent tendency to overbind, which is reflected in a relaxed cell volume which is smaller than the experimental volume by around 5%, as seen in Figure 2d. The PBE functional, on the other hand, slightly overcorrects this deviation, producing a unit cell volume which is around 5% larger than the experimental value. The PBEsol functional is intended to improve on PBE for equilibrium properties of solids such as bond lengths and lattice parameters, and the volume calculated with PBEsol comes very close to the experimental volume. This difference between the functionals is also reflected in the energies for the different space groups. As spontaneous polarization in solids requires a certain volume for the displacement of ions, the underbinding PBE functional is expected to favor polar space groups more than the overbinding LDA. For all calculations, PBE gives the largest energy difference between the polar $R3$ and the nonpolar $R\bar{3}m$, and LDA the smallest. The effect of this is most pronounced for the unconstrained relaxations, as shown in Figure 2c.

Although the diffraction data is convincing, $R3$ and $R\bar{3}$ are still so similar in structure and energy that care must be taken to properly distinguish between them. The difference between the space group symmetries $R3$ and $R\bar{3}$ is the presence of an inversion center in the latter, making the space group nonpolar. This is obviously important for applications of the material, because, for example, pyro- and ferroelectricity requires a polar space group. Lopatin[11] suggested that a rhombohedral $R3m$ polymorph might transform to the nonpolar space group $R\bar{3}m$ at high temperatures, based on an observed contraction of the polar axis (hexagonal [001] direction, rhombohedral [111] direction) upon heating to 815 °C, followed by normal thermal expansion. Such an anisotropic thermal expansion would be expected to accompany the transition from a polar to a nonpolar space group (e.g., from $R3m$ to $R\bar{3}m$ or from $R3$ to $R\bar{3}$), whereas a transition between two polar (or two nonpolar) space groups is likely to be much more subtle. To explain the anisotropic thermal expansion reported by Lopatin,[11] it is therefore required that the ambient-temperature space group be polar. This, in addition to the statistical significance of the R_{wp} factors from the refinement, makes $R3$ the most probable space group symmetry.

Description of the Crystal Structure. The main characteristic features of the crystal structure of r-PN are illustrated in Figure 4. Rhombohedral lead metaniobate is not a "layered" structure in the usual sense, although it is natural to picture it as being built from layers due to the anisotropy in crystal structure, polyhedral connectivity, and bonding. The fundamental building blocks are *dimer* units, made up of two edge-sharing $NbO_{6/2}$ octahedra as shown in Figure 4a. The dimers are corner-linked, creating layers or sheets, as shown in Figure 4b. The layers have a point group symmetry which is nearly hexagonal, although, as will be further discussed below, the point group symmetry of the crystal is trigonal due to the stacking sequence and the polyhedral connectivity between layers.

Three different kinds of rings of corner- and edge-sharing octahedra can be identified in the layers: one hexagonal and two triangular rings that are symmetrically inequivalent. In Figure 4b, the hexagonal ring (yellow) is in the middle, surrounded by six triangular rings (red and blue). Each of the triangular rings is pointing either up (red) or down (blue) within the plane of the figure, thereby distinguishing the two types. In a single layer of ideal hexagonal symmetry ($P6/mmm$), the two triangular rings would be equivalent.

The layers are stacked as shown in Figure 4c, with a repeating sequence of three layers. The rings in each layer form channels parallel to the hexagonal c axis. Lead cations are positioned inside these channels, between the layers. In the three-dimensional structure, every hexagonal ring has a triangular ring both above and below. This stacking sequence, with mixing of hexagonal and triangular rings, lowers the symmetry of the crystal from the ideal 6-fold, to the 3-fold symmetry observed. It can be noted that each of the three rings is associated with one of the three Wyckoff positions for lead in space group $R3$ (Table 1).

In addition to the stacking sequence, the polyhedral connectivity itself introduces tilts and distortions that prevent the ideal hexagonal symmetry from being realized. Between the layers, only corner-sharing connects the $NbO_{6/2}$ octahedra, whereas both corners and edges are shared within the layers. It is not possible to connect the layers, as shown in Figure 4c, without introducing symmetry-breaking distortions of the octahedra.

The octahedral deformation in the crystal structure reported here, is much less than reported in the previous work by Mahé.[13] He pointed out the large variation in Nb−O bond lengths, but remarked that this variation was not significant considering the experimental uncertainty in the oxygen positions. The uncertainty in oxygen positions in Mahé's work[13] was on the order of 0.1 Å, while here it is an order of magnitude less (Table 3), as a consequence of the neutron scattering cross section of oxygen being comparable to those of lead and niobium.

Structures built from $BO_{6/2}$ dimer units are well-known for niobates and tantalates of AB_2O_6 stoichiometry, with A = Ca, Sr or Ba.[29] In particular, the hexagonal high-temperature form of $BaTa_2O_6$[30] bears a resemblance to the layer-like structure of r-PN described here, with a combination of dimers and corner-sharing octahedra. The hexagonal $BaTa_2O_6$ structure is arguably even more complex than r-PN, containing both three-, five- and six-membered rings. Half of the $TaO_{6/2}$ octahedra in hexagonal

dx.doi.org/10.1021/ic5012378 | Inorg. Chem. 2014, 53, 9715−9721

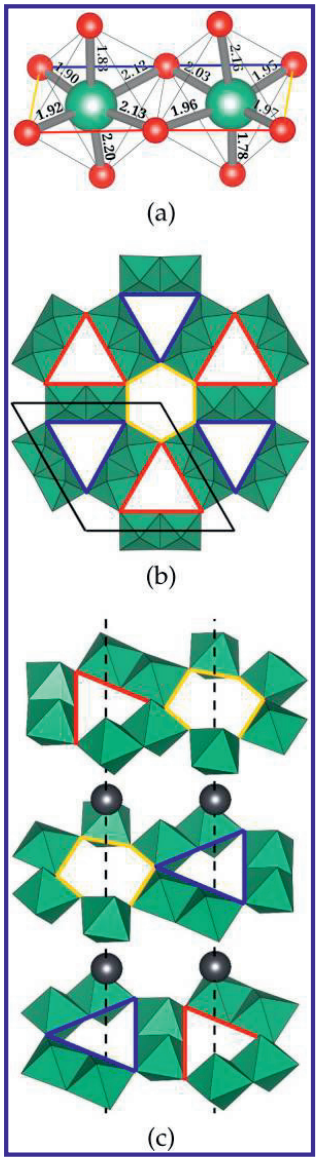

Figure 4. Layered structure of PN: (a) Single dimer consisting of two edge-sharing $NbO_{6/2}$ octahedra. Experimental Nb−O bond lengths for space group *R*3 given in Å; edges colored as in (b) and (c). (b) Single layer showing the hexagonal rings (yellow) and the two types of triangular rings (red and blue). Black line marks one hexagonal unit cell. (c) Stacking sequence of layers. The layers are stretched apart along the hexagonal (001) axis for clarity. Lead ions (gray spheres) are situated inside channels formed by openings in the layers. Figure created with VESTA.[34]

$BaTa_2O_6$ share only corners with other octahedra, while in the r-PN structure, every $NbO_{6/2}$ octahedron is part of a dimer.

The particular crystal structure found in r-PN is not commonly encountered and is rather unique. It was not reported to exist for other compounds in a recent review[31] of AB_2O_6 compounds, although $PbRe_2O_6$ has previously been reported[32] as isotypic with r-PN, with space group $R\bar{3}m$. $PbTa_2O_6$ has also been reported[33] to exist in a nonferroelectric rhombohedral form, analogous to r-PN, but no detailed structural study of this compund has to our knowledge been performed.

The presence of a polar space group symmetry in r-PN is interesting, because it is a requirement for pyro- and ferroelectricity. It thereby opens up for possible device applications, such as in piezoelectric sensors.

CONCLUSION

The ambient-temperature phase of lead metaniobate has been investigated by powder X-ray diffraction and powder neutron diffraction in combination with ab initio DFT calculations. It is found that the space group symmetry of r-PN is most likely the polar group *R*3, in contrast to previous assumptions of *R*3*m* being the correct space group for this structure. Furthermore, the new data on atomic positions in r-PN shows a structure with significantly less deformation of the $NbO_{6/2}$ octahedra than in previous works. Rhombohedral lead metaniobate has a highly anisotropic structure and is conveniently described as being built from layers. Within the layers, $NbO_{6/2}$ octahedra share edges to form dimers, which are connected by corner-sharing, at the same time forming triangular and hexagonal rings in the layers. The layers are connected by corner-sharing, with the rings in each layer forming channels that accommodate the lead cations.

ASSOCIATED CONTENT

Supporting Information

Rietveld refinements of powder diffraction data within different space groups, as well as X-ray and neutron diffraction data refined separately. Lattice parameters from geometry optimization by DFT are also given, along with full phonon dispersions for the space group symmetries considered. This material is available free of charge via the Internet at http://pubs.acs.org/.

AUTHOR INFORMATION

Corresponding Author

*E-mail: tor.grande@ntnu.no.

Notes

The authors declare no competing financial interest.

ACKNOWLEDGMENTS

The Research Council of Norway (NFR project no. 209337) and The Faculty of Natural Sciences and Technology, Norwegian University of Science and Technology (NTNU) are acknowledged for financial support. Computational resources were provided by NOTUR (The Norwegian Metacenter for High Performance Computing) through the project nn9264k.

REFERENCES

(1) Lines, M. E.; Glass, A. M. *Principles and applications of ferroelectrics and related materials*; Oxford University Press: Oxford, U.K., 2001.
(2) Goodman, G. *J. Am. Ceram. Soc.* **1953**, *36*, 368−372.
(3) Gallego-Juárez, J. A. *J. Phys. E: Sci. Instrum.* **1989**, *22*, 804−816.
(4) Francombe, M. H. *Acta Crystallogr.* **1956**, *9*, 683−684.
(5) Rivolier, J.-L.; Ferriol, M.; Cohen-Adad, M.-T. *Eur. J. Solid State Inorg. Chem.* **1995**, *32*, 251−262.

(6) Lee, H. S.; Kimura, T. *J. Am. Ceram. Soc.* **1998**, *81*, 3228−3236.
(7) Kimura, T.; Machida, M.; Yamaguchi, T.; Newnham, R. E. *J. Am. Ceram. Soc.* **1983**, *66*, c195−c197.
(8) Li, C. C.; Chiu, C. C.; Desu, S. B. *J. Am. Ceram. Soc.* **1991**, *74*, 42−47.
(9) Lu, C.-H.; Chyi, N. *Mater. Lett.* **1996**, *29*, 101−105.
(10) Sahini, M. G.; Grande, T.; Fraygola, B.; Biancoli, A.; Damjanovic, D.; Setter, N. *J. Am. Ceram. Soc.* **2014**, *97*, 220−227.
(11) Lopatin, S. S.; Medvedev, E. S.; Raevskii, I. P. *Russ. J. Inorg. Chem.* **1985**, *30*, 2102−2106.
(12) Mahé, R. *Bull. Soc. Chim. Fr.* **1966**, 3401−3403.
(13) Mahé, R. *Bull. Soc. Chim. Fr.* **1967**, 1879−1884.
(14) Chakraborty, K. R.; Sahu, K. R.; De, A.; De, U. *Integr. Ferroelectr.* **2010**, *120*, 102−113.
(15) Hauback, B. C.; Fjellvåg, H.; Steinsvoll, O.; Johansson, K.; Buset, O. T.; Jørgensen, J. *J. Neutron Res.* **2000**, *8*, 215−232.
(16) Kresse, G.; Hafner, J. *Phys. Rev. B* **1993**, *47*, 558−561.
(17) Kresse, G.; Hafner, J. *Phys. Rev. B* **1994**, *49*, 14251−14269.
(18) Kresse, G.; Furthmüller, J. *Comput. Mater. Sci.* **1996**, *6*, 15−50.
(19) Kresse, G.; Furthmüller, J. *Phys. Rev. B* **1996**, *54*, 11169−11186.
(20) Perdew, J. P.; Burke, K.; Ernzerhof, M. *Phys. Rev. Lett.* **1996**, *77*, 3865−3868.
(21) Perdew, J. P.; Ruzsinszky, A.; Csonka, G. I.; Vydrov, O. A.; Scuseria, G. E.; Constantin, L. A.; Zhou, X.; Burke, K. *Phys. Rev. Lett.* **2008**, *100*, 136406−136406.
(22) Blöchl, P. E. *Phys. Rev. B* **1994**, *50*, 17953−17979.
(23) Kresse, G.; Joubert, D. *Phys. Rev. B* **1999**, *59*, 11−19.
(24) Monkhorst, H. J.; Pack, J. D. *Phys. Rev. B* **1976**, *13*, 5188−5192.
(25) Togo, A.; Oba, F.; Tanaka, I. *Phys. Rev. B* **2008**, *78*, 134106−134106.
(26) Hamilton, W. C. *Acta Crystallogr.* **1965**, *18*, 502−510.
(27) Stokes, H. T.; Hatch, D. M. *J. Appl. Crystallogr.* **2005**, *38*, 237−238.
(28) Hafner, J. *J. Comput. Chem.* **2008**, *29*, 2044−2078.
(29) Galasso, F.; Layden, G.; Ganung, G. *Mater. Res. Bull.* **1968**, *3*, 397−408.
(30) Layden, G. K. *Mater. Res. Bull.* **1968**, *3*, 349−360.
(31) Beck, H. P. *Z. Kristallogr.* **2013**, *228*, 271−288.
(32) Wentzell, I.; Fuess, H.; Bats, J. W.; Cheetham, A. K. *Z. Anorg. Allg. Chem.* **1985**, *528*, 48−54.
(33) Subbarao, E. C.; Shirane, G.; Jona, F. *Acta Crystallogr.* **1960**, *13*, 226−231.
(34) Momma, K.; Izumi, F. *J. Appl. Crystallogr.* **2011**, *44*, 1272−1276.

PCCP

PAPER

View Article Online
View Journal | View Issue

Cite this: *Phys. Chem. Chem. Phys.*, 2015, **17**, 30343

On the energetics of cation ordering in tungsten-bronze-type oxides†

Gerhard Henning Olsen, Sverre Magnus Selbach and Tor Grande*

Received 27th August 2015,
Accepted 19th October 2015

DOI: 10.1039/c5cp05119c

www.rsc.org/pccp

Oxides with the tetragonal tungsten bronze (TTB) structure are well-known ferroelectrics that show a large flexibility both with respect to chemical composition and cation ordering. Two of the simplest compounds in this family are lead metaniobate ($PbNb_2O_6$ or PN) and strontium barium niobate ($Sr_xBa_{1-x}Nb_2O_6$ or SBN). While PN is a classical ferroelectric, SBN goes from ferroelectric to relaxor-like with increasing Sr content, with a polar direction different from that in PN. The partially occupied sublattices in both systems give the possibility for cation order–disorder phenomena, but it is not known if or how this influences the polarization and ferroelectricity. Here, we use density functional theory (DFT) calculations to investigate how cation and cation vacancy ordering influences the energetics of these compounds, by comparing both the energy differences and the barriers for transition between different cation configurations. We extend the thermodynamic model of O'Neill and Navrotsky, originally developed for cation interchange in spinels, to describe the order–disorder phenomenology in TTB oxides. The influence of order–disorder processes on the functional properties of PN and SBN is discussed.

1 Introduction

In the family of ferroelectric oxides based on $BO_{6/2}$ octahedra, oxides with the tetragonal tungsten bronze (TTB) structure form the second largest group after the perovskites.[1] The simplest of these compounds is lead metaniobate, $PbNb_2O_6$ or PN, which has a high Curie temperature of 570 °C.[2] It is, however, only stable at temperatures above 1200–1250 °C, and metastable with respect to a rhombohedral polymorph below this temperature range.[3–5] A lead-free analogue to PN is strontium barium niobate, $Sr_xBa_{1-x}Nb_2O_6$ or SBN, which is apparently stable in the TTB structure down to ambient temperature, although with a lower T_C of 70–200 °C, depending on composition.[6,7]

Both PN and SBN have the general formula $(A1)_2(A2)_4C_4(B1)_2(B2)_8O_{30}$, with five formula units in the unit cell, and space group symmetry $P4/mbm$ in the aristotype structure. The A1 and A2 sites form, respectively, pentagonal and square channels that run parallel to the tetragonal axis, and which accommodate the Pb^{2+}, Sr^{2+} and Ba^{2+} cations. The C sites form narrow triangular channels, and are usually vacant, as only a few cations such as Li^+ and Nb^{5+} are small enough for these sites.[8,9] The B1 and B2 sites are symmetrically different octahedral positions, and are fully occupied by Nb^{5+} in both PN and SBN. With all A-site cations divalent and Nb in the pentavalent state, as is the case in PN and SBN, charge neutrality requires that 5 out of 6 A-sites are occupied.

While PN and SBN are similar in terms of structure, there are fundamental differences in the behaviour of the two compounds. PN is a classical ferroelectric, while SBN is ferroelectric for barium-rich compositions, but becomes relaxor-like for strontium contents higher than approximately $x = 0.6$.[10] The ferroelectric transitions are also different in terms of symmetry: while SBN remains tetragonal at all temperatures, with a spontaneous polarization in the [001] direction below T_C,[6] PN has an in-plane polarization along the [110] direction referred to the aristotype cell, leading to an orthorhombic distortion in the ferroelectric state.[11] The explanation of this difference, or indeed the mechanism for ferroelectricity in general, is not fully understood for these compounds. It has been suggested that in the ferroelectric state, the main contribution to the polarization is displacement of Nb^{5+} along [001] for SBN, and in-plane displacement of the A-site cations for PN.[12] This difference could be related to the stereochemically active $6s^2$ lone pair on Pb^{2+}, in analogy with the perovskite titanates of lead and barium.[13] Nevertheless, the picture is less clear for TTB compounds, due to the significantly more complicated structure.

In addition to the complexity of the crystal structure itself, the partial occupancies in the tungsten-bronze oxides give rise to the possibility of cation order–disorder phenomena. Non-convergent ordering is well known in spinels with AB_2O_4 stoichiometry, but has to our knowledge never been addressed

Department of Materials Science and Engineering, Norwegian University of Science and Technology (NTNU), NO-7491 Trondheim, Norway.
E-mail: tor.grande@ntnu.no; Tel: +47 735 94084

† Electronic supplementary information (ESI) available: Derivation of thermodynamic equations, energetics data in tabular form and data on crystal structures. See DOI: 10.1039/c5cp05119c

for materials with the TTB-type crystal structure. In spinels, the cation exchange between the tetrahedral and octahedral sublattices can be thought of as a chemical reaction,[14] and the cation distribution can thus be modelled as a simple chemical equilibrium.[15–17] The tungsten-bronzes are similar to the spinels in terms of cation distribution between two non-equivalent sublattices, so a similar hypothesis should also apply here. Intuitively, the larger ionic radius of Ba^{2+} relative to Sr^{2+} and Pb^{2+} implies that the former will preferentially occupy the larger pentagonal sites, which has also been found experimentally.[6,18] However, even this simple effect of atomic size is not obvious: large cations preferentially occupy the larger octahedral sites in 4–2 spinels, while the opposite is actually true for 2–3 spinels.[16] There is therefore no guarantee that a simple argument based on atomic size also holds for a different crystal structure such as the TTB-type.

In this study, we examine the differences between the tungsten-bronze-type oxides PN and SBN by density functional theory (DFT) calculations. Particular attention is given to the effect of cation ordering between the A1 and A2 sites, and the effect of this on energetic stability. This line of thinking has previously been applied to perovskite relaxors,[19,20] but no first-principles study of cation ordering in TTB materials has to our knowledge been done. In our work, we seek to study the energetics of order–disorder effects in the paraelectric state of the materials, where sufficient cation mobility may occur only during synthesis far above T_C. The influence of cation ordering on polarization and lattice instabilities due to ferroelectric order is not included in this study, but will be followed up in future work. For computational treatment of these effects, we employ a supercell approach which makes it possible to sample several different cation configurations. We analyze the energy landscape between the configurations, consider the plausibility of cation ordering in tungsten-bronze-type oxides, and discuss possible reasons for the relaxor properties of strontium-rich compounds in the SBN system.

2 Methodology

2.1 Combinatorial aspects

An analysis is made of the different orderings possible in ANb_2O_6-type tungsten-bronzes. Starting with a single unit cell containing 45 atoms (5 formula units of ANb_2O_6), there are 6 sites among which to distribute 5 cations (or, equivalently and more convenient, six sites among which to distribute 1 vacancy). The four pentagonal (P) sites are equivalent, as are also the two square (S) sites (see Fig. 1a), so for a single unit cell, there are only two unique configurations.

A more realistic approach is to look at the possible configurations in a $1 \times 1 \times 2$ supercell, by doubling the unit cell in the c direction. In such a cell, there are a total of 12 A-sites (pentagonal and square), as shown in Fig. 1b. Among these 12 sites, there are 10 atoms and 2 vacancies to be distributed. For the rest of this discussion we focus on distribution of the vacancies, and count and name the configurations according to the following scheme:

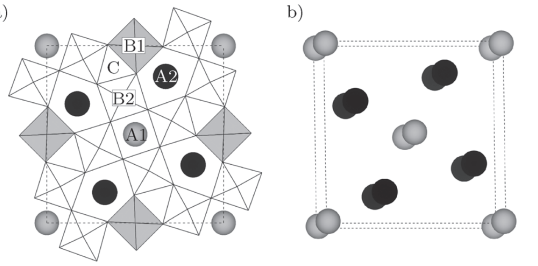

Fig. 1 (a) Projection along the c axis of the tetragonal tungsten-bronze unit cell in the *P4/mbm* aristotype, with labels for the different cation sites. The A1 and A2 sites are represented by grey and black spheres, respectively, while the B1 and B2 sites are shown as grey and white octahedra. (b) Supercell with a doubled c axis, showing only the A1 and A2 sites with the same colors as in panel (a). Figures created with the aid of VESTA.[21]

- The two vacancies can be distributed between square and pentagonal sites in three ways: both pentagonal (PP), both square (SS), or one of each (SP).
- If the first vacancy is located on a square site, there are three possible ways to place the second vacancy on another square site: on the other square site in the same layer; diagonally in the layer above; or directly above the first. Hence, there are three SS configurations.
- If the first vacancy is located on a pentagonal site, there are five possible ways to place the second vacancy on another pentagonal site: two in the same layer (next to the first or diagonally opposite from it); the same two positions in the layer above; or directly above the first. Hence, there are five PP configurations.
- If the first vacancy is located on a square site and the second on a pentagonal, they can either be in the same layer, or in different layers. Hence, there are two SP configurations.
- We use a triplet [*hkl*] to describe the (approximate) vector between the two vacancies. For example, two pentagonal vacancies within the same layer can be designated as PP[100] or PP[110] configurations, depending on whether the vacancies are "nearest neighbours" within the unit cell, or diagonally opposite from each other, respectively.

This scheme leads to a total of 10 unique configurations for each composition. These are summarized in Table 1, which

Table 1 The 10 cation configurations possible for the $1 \times 1 \times 2$ supercell considered in this work, showing the systematic name, local space group symmetry, and a sketch of the configuration (cations represented by grey spheres, vacant sites white)

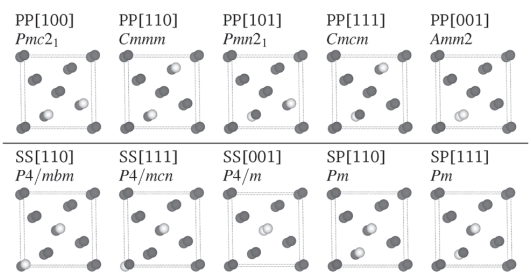

gives the systematic name for each configuration, and the local space group symmetry arising from the cation ordering.[22] As the table shows, the five PP configurations lead to local orthorhombic space group symmetries, the three SS configurations preserve the tetragonal symmetry (with SS[110] even preserving the aristotype space group *P*4/*mbm*), and the two SP configurations lead to local monoclinic symmetry. The 10 configurations for a 1 × 1 × 2 supercell also include the two configurations possible for a single unit cell: PP[001] is identical to a single unit cell with the vacancy on a pentagonal site, while SS[001] is identical to a single unit cell with the vacancy on a square site.

In principle it is possible to extend the investigation to even larger supercells, such as 1 × 1 × 3 or 1 × 1 × 4, but this was not performed. Possible effects of increasing the supercell size is included in the discussion.

2.2 Thermodynamic model

To gain insight into the possibility of cation ordering, we extend the thermodynamic model of O'Neill and Navrotsky[16] for the cation distribution in spinels. The fundamental assumption, introduced by Schmalzried[14] and elaborated by Navrotsky and Kleppa,[15] is that the interchange of cations between two distinct sublattices can be viewed as a chemical equilibrium:

$$[\mathrm{A}v](\mathrm{A}_4)\mathrm{Nb}_{10}\mathrm{O}_{30} \rightleftharpoons [\mathrm{A}_{1+x}v_{1-x}](\mathrm{A}_{4-x}v_x)\mathrm{Nb}_{10}\mathrm{O}_{30}, \quad (1)$$

where [A] denotes a cation A on an A1 or square site, (A) denotes a cation A on an A2 or pentagonal site, and v denotes a cation vacancy. This also introduces an interchange parameter, x, which ranges from 0 (all vacancies on square sites, *i.e.*, SS configurations) to 1 (all vacancies on pentagonal sites, *i.e.*, PP configurations). It is then assumed that the free energy of the cation interchange reaction (1) can be expressed as

$$\Delta G_{\mathrm{int}}(x) = \alpha x + \beta x^2 + RT\sum_s b_s \sum_i x_{i,s} \ln x_{i,s}, \quad (2)$$

where the last term on the right side is the entropy of mixing for an ideal solution, with $x_{i,s}$ being the fractional occupancy of species i on site s, and b_s the multiplicity of site s. This is a purely configurational entropy contribution, *i.e.* it is assumed that all other entropy changes following reaction (1) are negligible. The enthalpy consists of two terms, one linear and one quadratic in the interchange parameter x, as was proposed by O'Neill and Navrotsky[16] as an expansion of the original model by Navrotsky and Kleppa.[15] Effects of volume and non-configurational entropy are neglected. The energy difference between different configurations with the same degree of cation interchange is not taken into account at this stage, so all SS configurations are for now assumed to be degenerate, and the same applies for the PP and SP configurations. A simple differentiation of the entropy part shows that maximal configurational entropy is obtained for $x = 2/3$. This is analogous to AB_2O_4 spinels, which also have a maximal configurational entropy for $x = 2/3$ when x is the fraction of B cations on tetrahedral sites (this is referred to as a random spinel).

By writing out (2) for the TTB structure (see ESI† for details), and differentiating with respect to x, the following expression is found for equilibrium conditions:

$$\ln K = \ln\frac{x(1+x)}{(1-x)(4-x)} = -\frac{\alpha + 2\beta x}{RT}, \quad (3)$$

where K can be recognized as the equilibrium constant for the simplified cation exchange reaction [v] + (A) ⇌ (v) + [A], using the same notation as in (1). Eqn (3) gives the relation between temperature and degree of inversion once the enthalpy coefficients α and β are determined. This can be done experimentally by determining x from refinement of diffraction data at different T, although it could be challenging to obtain high-quality data at temperatures high enough for the cation mobility to be appreciable. Here, we will instead estimate the parameters by calculating the enthalpy term in (2) from first principles for cation configurations with different x.

2.3 Computational details

A non-polar SBN unit cell was created by starting from structural data from literature[18] and searching for pseudosymmetry[23] in the non-polar space group *P*4/*mbm* (127). The end members of the SBN system, $SrNb_2O_6$ (SN) and $BaNb_2O_6$ (BN), were modelled by replacing all Sr and Ba in the unit cell with only one of the two elements, and setting the lattice parameters a and c to the values extrapolated from the polynomial expressions given by Podlozhenov *et al.*[18] For PN, lattice parameters from Labbé[12] were used, after extracting the pseudosymmetric *P*4/*mbm* structure from the experimental space group *Amm*2 as described above.

Total energies were obtained by density functional theory (DFT) calculations with the VASP code,[24–27] where the exchange–correlation energy was calculated with the gradient-corrected PBEsol functional.[28] Core electrons were described by the projector-augmented wave (PAW) method,[29,30] with pseudopotentials treating 10 valence electrons for Sr ($4s^24p^65s^2$) and Ba ($5s^25p^66s^2$), 14 for Pb ($5d^{10}6s^26p^2$), 13 for Nb ($4s^24p^64d^35s^2$) and 6 for O ($2s^22p^4$). Valence electrons were described by wave functions expanded in plane waves up to an energy cutoff of 550, which gave well converged lattice parameters in test calculations. Brillouin-zone integration was done on a 2 × 2 × 6 Monkhorst–Pack mesh[31] for the 45-atom TTB unit cell, and reduced to a 2 × 2 × 3 mesh for the 90-atom supercells. Atomic positions and lattice vectors were relaxed until the forces on the ions were less than 0.01 eV Å^{-1}.

For estimation of the energy barrier between differently ordered configurations, we performed climbing-image nudged elastic band calculations.[32,33] For each composition, we considered two diffusion paths: between the configurations PP[100] and PP[101]; and between SS[110] and SS[111]. Both consist of a single cation diffusing from one layer to another inside the pentagonal and square tunnels, respectively. The minimum energy paths (MEPs) were found by considering 3 intermediate images between the endpoints, and optimizing atomic positions until the forces on the ions were less than 0.05 eV Å^{-1}.

3 Results

3.1 Energy landscape of cation configurations

We have calculated the total energy of BN, SN and PN in all 10 configurations considered above, and the results are shown in Fig. 2. Both the energy of the initial structures, and the energy after optimisation of ionic positions and lattice parameters, are shown. The two configurations that correspond to a single unit cell, PP[001] and SS[001], are the least energetically favourable among the initial structures, and for all three compounds, it is one of these two configurations that has the highest energy initially. The relative energies of the configurations change, however, when ionic relaxation is taken into account. Especially for BN, the initial configurations of highest energy are the ones that gain most by relaxation, giving an overall energy landscape which is quite flat. Subsequent relaxation of the unit cell volume and change of lattice parameters does not contribute as much, as the main energy gain lies in the relaxation of the ionic positions.

For SN and PN, the energy landscape is not quite as flat as for BN, although for both compounds there are several configurations that are very close in energy. The effect of volume relaxation is even lower for SN and PN than for BN, contributing very little to the total energy gain upon optimization of the structure. The effect of ionic relaxation is significant, making the total energy gain larger, at the most around 3.8 eV. The energy for the fully relaxed structures is summarized in Fig. 3a, where dashed lines mark the range of energies for each composition. In general, there is no single configuration, or a few configurations, that stand out as significantly more plausible than the others for any of the three compounds.

The change in the unit cell volume following the relaxation of lattice parameters is shown in Fig. 3b. The volume change is positive in almost all cases, and as large as up to 2% with respect to the initial volumes. Some trends are evident: for BN, the expansion is largest for the PP configurations, where Ba^{2+} completely occupies the narrow square channels, and smaller and slightly negative for the SS configurations. This is as expected, as the large Ba^{2+} cations preferentially occupy pentagonal sites, and will expand the lattice if forced into the smaller square sites. A closer inspection of the lattice parameters shows

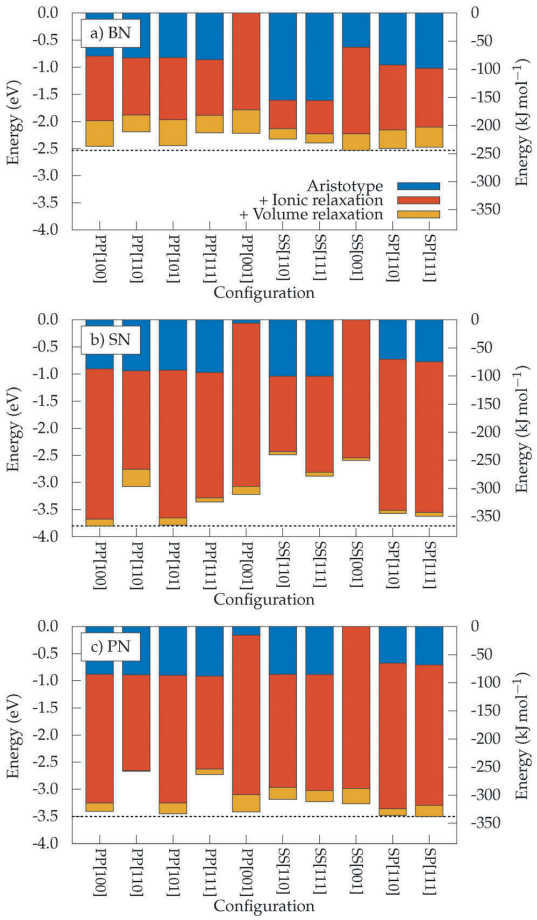

Fig. 2 Relative energy per unit cell ($A_5B_{10}O_{30}$) of the different configurations for (a) BN, (b) SN and (c) PN. The blue bars labeled "Aristotype" show the energies of the initial structures, with space group symmetry as described in Table 1. The red and yellow bars show the additional energy contribution from relaxation of ionic positions and unit cell volume, respectively. The zero level is set at the highest initial energy for each composition (configurations PP[001] or SS[001]).

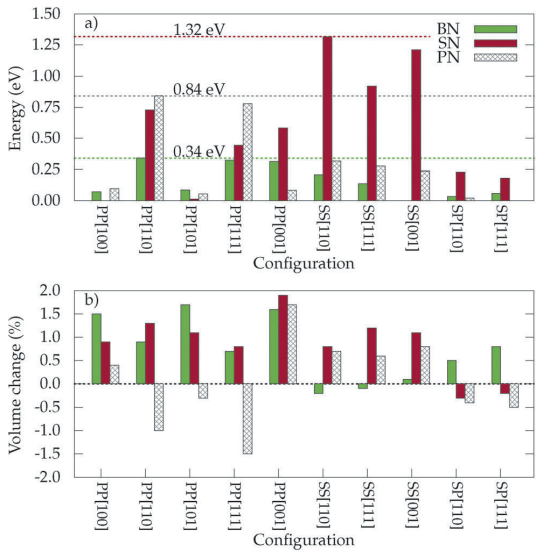

Fig. 3 (a) Relative energy per unit cell ($A_5B_{10}O_{30}$) of the fully relaxed structures, corresponding to the total energy shown in Fig. 2. The lowest-energy structure is used as reference state for each compound (SS[001] for BN, PP[100] for SN and SP[111] for PN). Dashed lines mark the highest-energy configuration for each composition. (b) Volume change corresponding to the relaxed structures in panel a, showing the difference in unit cell expansion associated with different cation configurations.

that the volume change for BN comes from an expansion of the a and b parameters, and a contraction of c with respect to the initial values. Also for SN and PN, the a and b parameters mostly expand (the sole exception being PP[110] for PN, where they slightly contract), while the c parameter either expands or contracts.

3.2 Transition barriers between cation configurations

Due to the similarity in energetic stability between the different configurations, we calculated the energy barriers for transitions between some of these configurations in order to get an impression of how the configurations compare also kinetically. Two cases were considered, namely diffusion of A^{2+} cations in the two different types of channels in the structure. To visualize these cases, the unit cell is shown again in Fig. 4a (left panel) together with an alternative view emphasizing the pentagonal and square channels (right panel). Fig. 4b illustrates a perspective view of the channel shapes, with grey and black arrows defines the diffusion paths through the square and pentagonal channels, respectively. Fig. 4c shows the minimum energy path (MEP) for these two diffusion processes, where the end configurations are the PP[100] and PP[101] configurations for the pentagonal channel case, and SS[110] and SS[111] for the square channel case. As expected, the energy maximum midway along the path is higher for the square channel than for the pentagonal channel, as the square channels are narrower. In Fig. 4d, the height of the energy barriers are compared for the two cases in all three compositions, and the larger size of Ba^{2+} relative to Sr^{2+} and Pb^{2+} is again manifested in the increased transition barrier. The height of the barriers is significant, and dominates over the energy differences between the start and end points, as demonstrated in Fig. 4c.

3.3 Application of the thermodynamic model

As stated above, the thermodynamic model we employ here does not take into consideration the energetic differences between configurations with the same value of the cation interchange parameter x. In an attempt to meet this problem, we fitted the enthalpic part of eqn (2) to Boltzmann averages of the energies for each x:

$$\langle E\rangle(T) = \frac{\sum_n E_n e^{-E_n/k_B T}}{\sum_n e^{-E_n/k_B T}}, \quad (4)$$

where E_n is the energy of configuration n, and the sums are over configurations with the same value of x (*i.e.*, the PP, SS and SP configurations are averaged separately). In this way, at zero kelvin the energies are identical to the single lowest energy for each x, while at finite temperatures there is also a contribution to the energy from population of configurations with higher energy.

Fitting the energies of the fully relaxed structures to eqn (2) as described above leads to the plot shown in Fig. 5a. As is evident from this plot, the energies for each x spread out significantly, especially for the PP cases (x = 1.0), as was also seen in Fig. 3a. Fits to eqn (2) for T = 0 K and T = 1800 K are both displayed in Fig. 5a, in order to get an impression of how much the higher-energy configurations contribute for each x at finite temperatures. In general, this contribution is small, and α and β show very little variation with temperature.

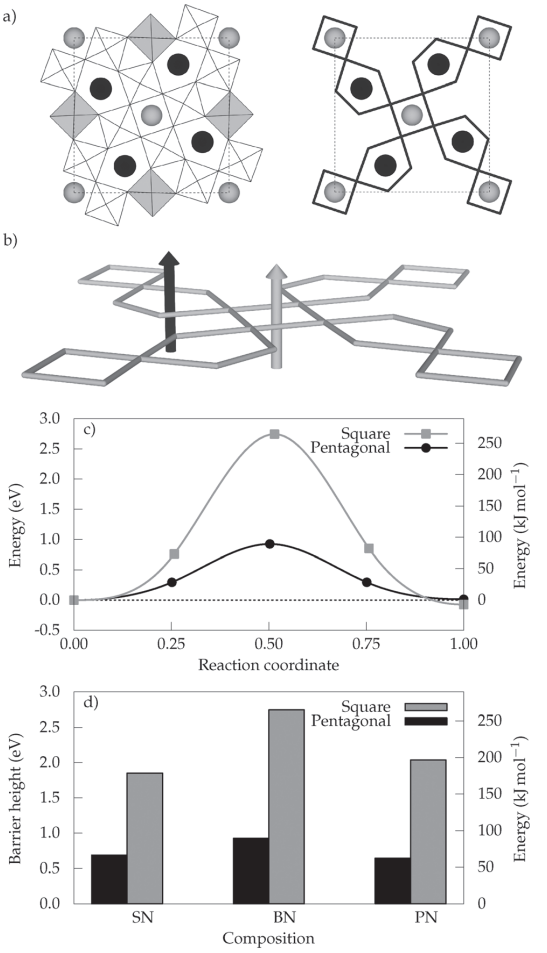

Fig. 4 (a) Projection of TTB unit cell along c (left), highlighting the shape of the channels considered for diffusion (right). (b) Perspective view of diffusion paths through the square (grey arrow) and pentagonal (black arrow) channels. (c) Minimum energy paths (MEP) for cation diffusion through square and pentagonal channels in BN. The square channel diffusion is represented by the transition SS[110] to SS[111], while the pentagonal channel is represented by PP[100] to PP[101]. The dashed line marks the energy of the initial configuration in the diffusion process. (d) Comparison of the barrier heights for the MEPs for all three compositions.

The entropic part of (2) is purely configurational, and is shown in Fig. 5b. For comparison, the configurational entropy of a simple spinel is also given, and both are normalized with respect to the number of sites in the structure. It is noteworthy that both the spinel and the tungsten-bronze-type structure possess a maximal configurational entropy for x = 2/3 with the definitions of x used here, which is therefore predicted to be

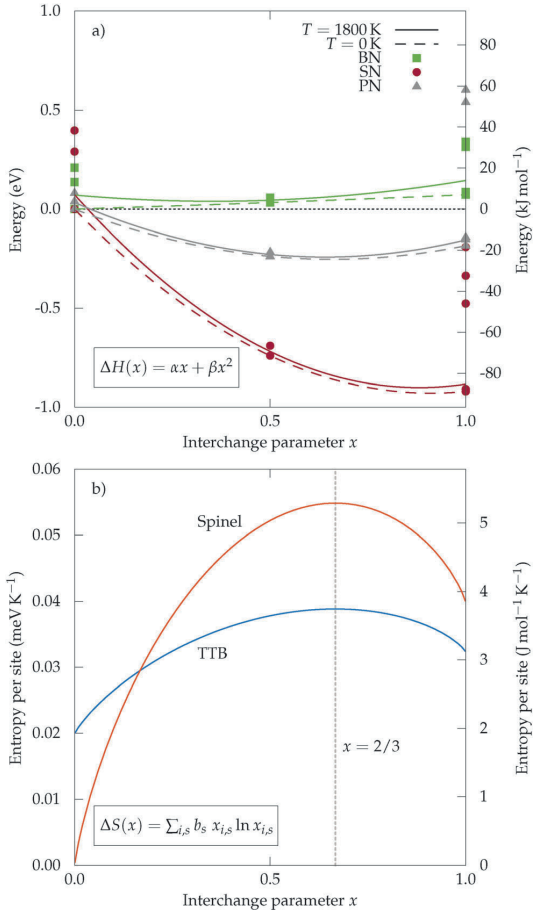

Fig. 5 (a) Calculated total energies (points) plotted against the interchange parameter x as defined in reaction (1). x = 0 corresponds to the three SS configurations, x = 0.5 to the two SP, and x = 1 to the five PP configurations. The energy is given per unit cell, corresponding to reaction (1), with the lowest energy configuration at x = 0 used as reference. Lines show fits to the enthalpic part of eqn (2), where dashed lines represent zero temperature (only the lowest energy for each x is used) and dashed lines represent T = 1800 K through a Boltzmann average of the energies for each x. (b) Configurational entropy as a function of the degree of inversion for the TTB structure considered in this work, compared to the configurational entropy of a simple spinel. Values are normalized per site (three for spinel and six for TTB), to make it possible to compare the entropy between two structures with different stoichiometry. In both structures, maximal configurational entropy occurs at x = 2/3.

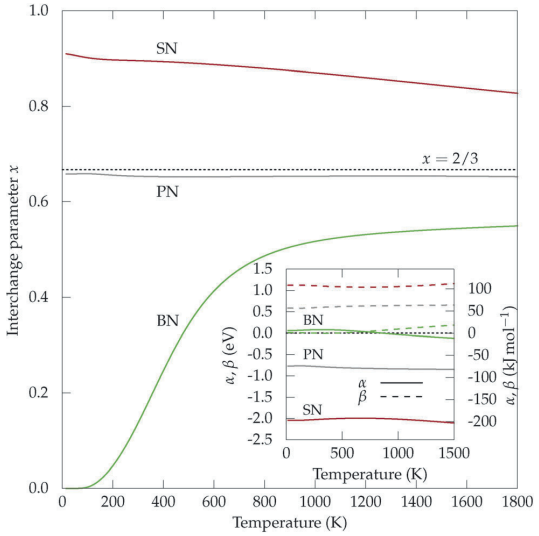

Fig. 6 Degree of cation interchange as a function of temperature for BN, SN and PN, calculated from eqn (3). The high-temperature limit x = 2/3, corresponding to maximal configurational entropy, is marked with a dotted black line. Inset plot shows the temperature dependency of the fitting parameters α (solid lines) and β (dashed).

the high-temperature limit of x in both structure types. However, the difference between maximum and minimum configurational entropy is almost three times larger for spinel than for the TTB structure. This is justified by the fact that a normal spinel (x = 0) can be defined as having zero configurational entropy, as both sublattices are fully occupied by only one cation. For the TTB structure, on the other hand, there is always a mixed occupancy between cations and vacancies on at least one of the sublattices, and so the configurational entropy is never zero. This means that there is less driving force for disordering for the TTB structure than for spinels, and that enthalpic effects can be expected to dominate the tungsten-bronze-type oxides also at higher temperatures.

Using α and β obtained above, we calculate the degree of cation interchange, x in (1), as a function of temperature. The result is plotted in Fig. 6, which also gives the temperature dependence of α and β (inset panel). For BN, both α and β are quite small, which means that entropy is the main factor that governs the degree of cation inversion. BN therefore has a prominent temperature dependency, while both PN and SN, which have much more distinct minima in enthalpy (Fig. 5a), show only a weak dependency of x on temperature (Fig. 6). As is also the case for spinels,[16] α and β are of similar magnitude, but with opposite sign (inset of Fig. 6).

4 Discussion

4.1 Possibility of cation ordering in tungsten-bronze-type oxides

As Fig. 3a demonstrates, the energy differences between different cation configurations are quite small, with a maximal difference of 1.32 eV per unit cell (0.263 eV or 25.4 kJ mol^{-1} per formula unit) for fully relaxed SN, and less for the other compositions. This is somewhat unexpected, as Ba^{2+} is significantly larger than Sr^{2+} and Pb^{2+}, so especially the PP configurations, with more cations in the narrow square channels, would be expected to lie high in energy for BN. This is the case for the initial structures

(blue bars in Fig. 2a–c), where two of the SS configurations have a much lower energy than the others, as expected from atomic size considerations. After relaxation of the structure is taken into account, the energy landscape is relatively flat, with energy differences smaller for BN than for both SN and PN. The main contribution to this energy landscape flattening comes from the ionic movements (red bars in Fig. 2a−c), and only to a lesser extent from volume change (yellow bars). Although the energetic contribution from volume change is larger for BN than for SN and PN, the volume change itself is not systematically larger for BN, as seen in Fig. 3b.

The flatness of the energy landscape, particularly for BN, is striking, see Fig. 2. This difference in behaviour of BN relative to SN and PN can be rationalized from the relative size of the cations and the coordination environment inside the channels. The square channels are formally 12-coordinated and similar to the A-sites in ABO_3 perovskites. The pentagonal channels are formally 15-coordinated, although in practice both the square and pentagonal coordination polyhedra are to some degree distorted and the effective coordination number is therefore less than the formal value. This distortion of A-site coordination polyhedra happens to a larger degree for Sr^{2+} and less for Ba^{2+}, since Sr^{2+} is significantly smaller than Ba^{2+} (ionic radii of 1.58 Å and 1.74 Å, respectively, when extrapolating Shannon values[34] to CN = 15). Sr^{2+} therefore has higher ability to shift towards an off-centered position in the channel, thus obtaining a smaller effective coordination number than Ba^{2+}. This enhanced ability to off-center and distort the structure enables the SN configurations to relax further towards their local energy minima than BN, where full relaxation is partially restricted by the large Ba^{2+} ions. In the case of Pb^{2+}, additional contributions may result from covalent bonding between Pb and O.

Although the energy differences shown in Fig. 3a are small, the transition barriers between configurations are large, on the order of 1.0–2.5 eV. This is far above the thermal energy at synthesis conditions, which is on the order of 0.1–0.2 eV. We have only looked at transitions corresponding to diffusion within the square or pentagonal channels, *i.e.*, transitions that do not change the value of x. We expect that since the channel cross-sections are larger than the openings between the channels, transitions that change x will have even higher barriers than those investigated at present.

Although our zero-kelvin DFT calculations indicate that the structure is not able to explore its entire configurational space, the situation might be very different at higher temperatures. During cooling from synthesis temperatures of typically 1300–1400 °C, it is possible that certain configurations are ''frozen in'' and persist to lower temperatures, where the different local space group symmetries (some of which are polar, *cf.* Table 1) can aid in the nucleation of the ferroelectric phase. This is similar to the scheme suggested for the lead-free perovskite relaxors studied by Gröting *et al.*,[19] where it was concluded that the small energy differences between different A-site configurations are not sufficient to create long-range order, but that short-range ordering may still be possible. Locally ordered regions that freeze in at high temperature in the paraelectric state, will most likely influence the nature of the ferroelectric ground state. For example, the relatively flat energy landscape predicted for BN might allow more of a long-range cooperativity in the ferroelectric phase, while the larger energetic differences between configurations of SN could lead to less long-range ordering in the ferroelectric state. This could in turn be an explanation for the tendency for SBN materials to become more relaxor-like for Sr-rich compositions. For PN, although more similar to SN in terms of energetics and cation radius, we expect the stereochemically active $6s^2$ lone pair on Pb^{2+} to play a significant role in the ferroelectric transition, and this might trump the contribution from energetics which would otherwise have made the material more similar to SN.

The volume change shown in Fig. 3b is, in effect, the ΔV associated with reaction (1). Volume change for order–disorder processes has been addressed previously in the case of spinels.[35] In general, the order–disorder volume $\Delta V = V_{\mathrm{disorder}} - V_{\mathrm{order}}$ for spinels can be positive or negative, but more often positive, and largest (up to 5%) when the disordering process involves changes in coordination numbers of the cations. Largely normal spinels such as $MgAl_2O_4$ tend to become more inverse with increasing pressure, and it has been observed that this compound disorders more with temperature under high-pressure conditions.[35,36] However, at ambient temperature, high pressure alone has only a negligible effect on the cation distribution,[37] which is also one of the assumptions in the thermodynamic model employed in this work.

4.2 Analogy to spinels and adaptation of O'Neill–Navrotsky model

As stated in the introduction, it should be possible to exploit the similarities between TTBs and spinels in the phenomenological analysis of order–disorder processes. A central question in this respect concerns the transferability of the O'Neill–Navrotsky model. First, it is assumed that non-configurational contributions to the entropy of reaction (1) are negligible. This works well for the interchange process in spinels, and we have made the same assumption here. In addition to the configurational entropy, there could in principle be a contribution from change in vibrational entropy. Since the cation configurations differ with respect to local space group symmetry (Table 1), the number of vibrational modes will also be different, with more modes for configurations of lower symmetry. We do not attempt here to explicitly include this presumably small entropy contribution in the thermodynamic model.

Accepting the premise of configurational entropy only, the conceptually most important difference between TTBs and spinels is revealed by the entropy plot shown in Fig. 5b: since at least one of the sublattices in TTB has a mixed occupancy for all x, the configurational entropy is never zero. In other words, there is no value of x for which the structure must necessarily be fully ordered. This is in contrast to spinels, where a normal spinel ($x = 0$) must be perfectly ordered, while an inverse spinel ($x = 1$) can be either ordered or disordered, depending on how the A and B cations distribute over the octahedral sites (the latter is not given by the value of x). Even a ''random'' spinel ($x = 2/3$)

can have different degrees of order, even though the configurational entropy is at a maximum for this degree of inversion. For TTBs, however, any degree of inversion can have varying degrees of order, so there is no *a priori* reason for $x = 0$ to be defined as the ground state.

In light of the above considerations, it is clear that x in itself is not a measure of the degree of disorder, but should merely be though of as a parameter describing the distribution of cations between two sublattices. Order–disorder can take place on each of these sublattices. In a spinel, a transition from normal to (partially or completely) inverse, must necessarily be accompanied by disorder, and so it is expected that the parameter α always be positive for spinels. This is indeed found to be the case,[16,38] so the negative values obtained for α for the TTB materials (inset of Fig. 6) may seem counter-intuitive when compared to α values for spinels. However, once it is realized that reaction (1) is not in itself a disordering process, a negative α is not problematic: it merely reflects the fact that a cation interchange from the SS configurations towards the SP (and possibly PP) configurations is energetically favoured—to a large degree for SN; to a somewhat lesser degree for PN; and for BN, the flat energy landscape is reflected in the very small values of α and β.

Turning to the plot of x as a function of temperature (Fig. 6), the different behaviour of BN, SN and PN can be understood in light of the above considerations. For BN, x increases with temperature, since the lowest-energy configuration at zero temperature has $x = 0$. The contribution from configurational entropy acts to push the structure towards a higher degree of cation interchange at higher temperature, similar to the behaviour of normal spinels. As the energy landscape for BN is so flat, the effect of entropy is large, and x rapidly approaches 2/3 when the temperature increases. For SN, however, the energy differences between the configurations are much larger, with a pronounced enthalpy minimum at around $x = 0.9$, which does not change significantly with temperature, as shown in Fig. 5a. The effect of increased temperature is therefore to push x towards a slightly lower value, giving the behaviour of decreasing x shown for SN in Fig. 6. PN is intermediate between BN and SN in terms of how deep the enthalpy minimum is (Fig. 5), but as this minimum is located at around $x = 0.65$, very close to the high-temperature limit of $x = 2/3$, the temperature dependence of x becomes extremely weak for this compound, resulting in the almost flat curve for PN in Fig. 6.

The use of a thermodynamic model provides a more complete picture of the behaviour of BN, SN and PN at realistic temperatures, as compared to simply calculating the zero-kelvin energy of the different configurations. It should be kept in mind that the transition barriers between configurations are high. The development of x with temperature (Fig. 6) represents the true equilibrium state, while in reality the relaxation time for cation ordering will increase exponentially upon reduction of temperature, and a certain configuration will eventually freeze in, as has also been shown for spinels.[38] The main finding is that the preferred value of x differs significantly for BN and SN, which is likely connected to the gradual change in dielectric and ferroelectric properties with changing Sr/Ba-ratio in the SBN system. The strong temperature dependence of x for Ba suggests that changes in the cation configuration due to thermal history is most likely to occur at high Ba content.

In this study, we have only sampled three different values of x, namely 0 (the SS configurations), 0.5 (SP) and 1 (PP), *via* a total of 10 configurations. These are all the possibilities accessible using a $1 \times 1 \times 2$ supercell, while a larger supercell would make it possible to sample more of configurational space (*e.g.*, a $1 \times 1 \times 3$ supercell would give access to configurations with $x = 0.33$ and $x = 0.67$, as well as more configurations with $x = 0$ and $x = 1$). However, already when using a $1 \times 1 \times 2$ supercell, we see a substantial variation of the energies between different configurations of the same x value, and a sampling of more x values would not necessarily improve significantly on the model. At the same time, an advantage of larger supercells would be to remove artifacts from the periodic boundary conditions. The supercells used here contain two octahedral layers, and therefore have a repeat distance of nearly 8 Å along the shortest dimension (the c axis). Larger cells would be advantageous to eliminate all artificial ordering of vacancies, although it is not known if this contribution is significant. In any case, larger supercells would lead to many more configurations to investigate, and also make each configuration significantly more computationally demanding.

5 Conclusion

The energetics of cation ordering in oxides with tetragonal tungsten bronze (TTB) oxides was investigated by *ab initio* DFT calculations. It was found that different degrees of cation interchange between the A1 and A2 sublattices are preferred for the TTB metaniobates of barium, strontium and lead. Furthermore, a thermodynamic model was developed for the phenomenology of cation interchange in TTB oxides, based on the model developed for spinels by O'Neill and Navrotsky. Due to the relatively small energy differences between several of the configurations, there is little driving force for long-range cation ordering. For barium metaniobate, the configurational energy landscape is very flat, and a certain temperature dependence of the cation ordering is to be expected. Due to quite high barriers for transitions between different configurations, we suggest that certain configurations will be "frozen in" during synthesis, and that different local configurations, some of which lead to polar space group symmetries, can act as seeds for nucleation of the ferroelectric phase below T_C.

Acknowledgements

The Research Council of Norway (NFR project no. 209337) and The Faculty of Natural Sciences and Technology, Norwegian University of Science and Technology (NTNU) are acknowledged for financial support. Computational resources were provided by NOTUR (The Norwegian Metacenter for High Performance Computing) through the project NN9264K. Sandra Helen Skjærvø

(NTNU), Ulrich Aschauer and Nicola A. Spaldin (ETH Zurich) are acknowledged for insightful discussions.

References

1 M. E. Lines and A. M. Glass, *Principles and applications of ferroelectrics and related materials*, Oxford University Press, New York, 2001.
2 G. Goodman, *J. Am. Ceram. Soc.*, 1953, **36**, 368–372.
3 M. H. Francombe, *Acta Crystallogr.*, 1956, **9**, 683–684.
4 M. G. Sahini, T. Grande, B. Fraygola, A. Biancoli, D. Damjanovic and N. Setter, *J. Am. Ceram. Soc.*, 2014, **97**, 220–227.
5 G. H. Olsen, M. H. Sørby, B. C. Hauback, S. M. Selbach and T. Grande, *Inorg. Chem.*, 2014, **53**, 9715–9721.
6 P. B. Jamieson, S. C. Abrahams and J. L. Bernstein, *J. Chem. Phys.*, 1968, **48**, 5048–5057.
7 A. A. Ballman and H. Brown, *J. Cryst. Growth*, 1967, **1**, 311–314.
8 M. Lundberg and M. Sundberg, *J. Solid State Chem.*, 1986, **63**, 216–230.
9 F. Madaro, R. Sæterli, J. R. Tolchard, M.-A. Einarsrud, R. Holmestad and T. Grande, *CrystEngComm*, 2011, **13**, 1304–1313.
10 A. M. Glass, *J. Appl. Phys.*, 1969, **40**, 4699–4713.
11 M. H. Francombe and B. Lewis, *Acta Crystallogr.*, 1958, **11**, 696–703.
12 P. Labbé, M. Frey, B. Raveau and J. C. Monier, *Acta Crystallogr., Sect. B: Struct. Crystallogr. Cryst. Chem.*, 1977, **33**, 2201–2212.
13 R. Cohen, *Nature*, 1992, **358**, 136–138.
14 H. Schmalzried, *Z. Phys. Chem.*, 1961, **28**, 203–219.
15 A. Navrotsky and O. J. Kleppa, *J. Inorg. Nucl. Chem.*, 1967, **29**, 2701–2714.
16 H. O'Neill and A. Navrotsky, *Am. Mineral.*, 1983, **68**, 181–194.
17 H. O'Neill and A. Navrotsky, *Am. Mineral.*, 1984, **69**, 733–753.
18 S. Podlozhenov, H. A. Graetsch, J. Schneider, M. Ulex, M. Wöhlecke and K. Betzler, *Acta Crystallogr., Sect. B: Struct. Sci.*, 2006, **62**, 960–965.
19 M. Gröting, S. Hayn and K. Albe, *J. Solid State Chem.*, 2011, **184**, 2041–2046.
20 M. Gröting and K. Albe, *J. Solid State Chem.*, 2014, **213**, 138–144.
21 K. Momma and F. Izumi, *J. Appl. Crystallogr.*, 2011, **44**, 1272–1276.
22 H. T. Stokes and D. M. Hatch, *J. Appl. Crystallogr.*, 2005, **38**, 237–238.
23 C. Capillas, E. S. Tasci, G. de la Flor, D. Orobengoa, J. M. Perez-Mato and M. I. Aroyo, *Z. Kristallogr.*, 2011, **226**, 186–196.
24 G. Kresse and J. Hafner, *Phys. Rev. B: Condens. Matter Mater. Phys.*, 1993, **47**, 558–561.
25 G. Kresse and J. Hafner, *Phys. Rev. B: Condens. Matter Mater. Phys.*, 1994, **49**, 14251–14269.
26 G. Kresse and J. Furthmüller, *Comput. Mater. Sci.*, 1996, **6**, 15–50.
27 G. Kresse and J. Furthmüller, *Phys. Rev. B: Condens. Matter Mater. Phys.*, 1996, **54**, 11169–11186.
28 J. P. Perdew, A. Ruzsinszky, G. I. Csonka, O. A. Vydrov, G. E. Scuseria, L. A. Constantin, X. Zhou and K. Burke, *Phys. Rev. Lett.*, 2008, **100**, 136406.
29 P. E. Blöchl, *Phys. Rev. B: Condens. Matter Mater. Phys.*, 1994, **50**, 17953–17979.
30 G. Kresse and D. Joubert, *Phys. Rev. B: Condens. Matter Mater. Phys.*, 1999, **59**, 11–19.
31 H. J. Monkhorst and J. D. Pack, *Phys. Rev. B: Solid State*, 1976, **13**, 5188–5192.
32 G. Henkelman, B. P. Uberuaga and H. Jónsson, *J. Chem. Phys.*, 2000, **113**, 9901–9904.
33 G. Henkelman and H. Jónsson, *J. Chem. Phys.*, 2000, **113**, 9978–9985.
34 R. D. Shannon, *Acta Crystallogr., Sect. A: Cryst. Phys., Diffr., Theor. Gen. Crystallogr.*, 1976, **32**, 751–767.
35 R. M. Hazen and A. Navrotsky, *Am. Mineral.*, 1996, **81**, 1021–1035.
36 F. Meducin, S. a. T. Redfern, Y. Le Godec, H. J. Stone, M. G. Tucker, M. T. Dove and W. G. Marshall, *Am. Mineral.*, 2004, **89**, 981–986.
37 F. Nestola, T. B. Ballaran, T. Balic-Zunic, F. Princivalle, L. Secco and A. Dal Negro, *Am. Mineral.*, 2007, **92**, 1838–1843.
38 S. a. T. Redfern, R. J. Harrison, H. S. C. O'Neill and D. R. R. Wood, *Am. Mineral.*, 1999, **84**, 299–310.

PHYSICAL REVIEW B **93**, 180101(R) (2016)

Origin of ferroelectric polarization in tetragonal tungsten-bronze-type oxides

Gerhard Henning Olsen,[1,2] Ulrich Aschauer,[2,3] Nicola A. Spaldin,[2] Sverre Magnus Selbach,[1] and Tor Grande[1,*]

[1]*Department of Materials Science and Engineering, NTNU, Norwegian University of Science and Technology, NO-7491 Trondheim, Norway*

[2]*Materials Theory, ETH Zurich, Wolfgang-Pauli-Strasse 27, CH-8093 Zurich, Switzerland*

[3]*Department of Chemistry and Biochemistry, University of Bern, Freiestrasse 3, CH-3012 Bern, Switzerland*

(Received 22 March 2016; revised manuscript received 22 April 2016; published 9 May 2016)

The origin of ferroelectric polarization in tetragonal tungsten-bronze- (TTB-) type oxide strontium barium niobate (SBN) is investigated using first-principles density functional calculations. We study in particular the relationship between the polarization and the cation and vacancy ordering on alkali-earth metal lattice sites. Lattice dynamical calculations for paraelectric structures demonstrate that all cation configurations that can be accommodated in a $1 \times 1 \times 2$ supercell result in a single unstable polar phonon, composed primarily of relative Nb-O displacements along the polar axis, as their dominant instability. The majority of the configurations also have a second octahedral tilt-mode instability which couples weakly to the polar mode. The existence of the tilt mode is strongly dependent on the local cation ordering, consistent with the fact that it is not found experimentally. Our results suggest that ferroelectricity in the SBN system is driven by a conventional second-order Jahn-Teller mechanism caused by the d^0 Nb^{5+} cations, and demonstrate the strong influence of the size of Sr and Ba on the lattice distortions associated with polarization and octahedral tilting. Finally, we suggest a mechanism for the relaxor behavior in Sr-rich SBN based on Sr displacement inside pentagonal channels in the TTB structure.

DOI: 10.1103/PhysRevB.93.180101

Ferroelectric oxides with a tetragonal tungsten-bronze (TTB) structure have been known since 1953 [1], and their polar properties are both widely studied and used in applications. One of the simplest TTB compounds, lead metaniobate ($Pb_5Nb_{10}O_{30}$ or PN), is commercially available and attractive for high-temperature piezoelectric sensor applications. In spite of their popularity, however, a fundamental explanation of the mechanism leading to spontaneous polarization in TTBs is still missing. One possible origin is Nb^{5+}, which is a ferroelectrically active cation in perovskites owing to a second-order Jahn-Teller mechanism enabled by its d^0 electron configuration [2,3]. Fundamental studies on TTBs are challenging, partly due to multiple competing phases: PN, for example, is, at ambient temperature, metastable in the TTB structure with respect to a rhombohedral polymorph [4–6]. Most other tungsten-bronze oxides are solid solutions with structural and chemical disorder, consistent with many of them being relaxor ferroelectrics [7–9].

The aristotype unit cell with the general formula $(A1)_2(A2)_4C_4(B1)_2(B2)_8O_{30}$ has six sites available for A-type cations and ten for B-type cations. The structure is highly anisotropic, with the A1 and A2 sites forming channels along the c direction. The A1 sites are formally 12-coordinated and similar to the A sites in perovskites, while the A2 sites are pentagonal and formally 15-coordinated. The B1 and B2 sites are octahedrally coordinated, with corner-sharing BO_6 octahedra forming the structural framework. Many niobates and tantalates crystallize as TTBs where Nb or Ta resides on the octahedral B sites. The A sites can accommodate a wide range of cations, from alkali and alkaline-earth metals to p block cations such as Pb^{2+} and Bi^{3+}. The triangular, 9-coordinated C sites can only accommodate small cations such as Li^+ and Nb^{5+} and are therefore often completely vacant, while the A sites can be partially or completely filled [10–12]. Due to this flexibility, disorder in TTBs takes place both through site interchange and partial occupancy.

We choose the simple $(Sr_xBa_{1-x})_5Nb_{10}O_{30}$ (SBN) as a model system for investigating the ferroelectric polarization in TTBs. The divalent cations Sr^{2+} and Ba^{2+} occupy the A1 and A2 sites, with one of the six total A sites unoccupied to maintain electroneutrality [10]. Only intermediate SBN compositions ($0.25 < x < 0.75$) are accessible by conventional synthesis methods, while the end members are metastable with respect to other more stable polymorphs [13,14]. SBN materials with a TTB structure have attractive electro-optical properties, such as high second harmonic yield and good pyroelectric performance [15], and they are also of interest as lead-free ferroelectrics [16,17]. Ba-rich SBN compositions are classical ferroelectrics with a sharp dielectric maximum at T_C and Curie-Weiss behavior in the paraelectric state, while Sr-rich compositions are relaxor ferroelectrics with a broad dielectric maximum and a strong frequency dispersion in dielectric permittivity [7]. The transition is gradual, but relaxor behavior dominates for compositions with $x > 0.50$ [7,9,15]. The mechanism triggering this crossover is not known, although a recent study found relaxor behavior in TTBs to correlate with the existence of incommensurate superstructures [9]. Here, we present first-principles calculations of the stability and lattice dynamics of the end-point compounds of SBN, $Ba_5Nb_{10}O_{30}$ (BN) and $Sr_5Nb_{10}O_{30}$ (SN). We study ten different cation-vacancy configurations, and in each case calculate the structural ground state and its associated spontaneous polarization. Based on the behavior of the end members, we discuss how the Sr/Ba ratio affects the properties of SBN, with particular focus on the ferroelectric mechanism and how it is influenced by different A-site cation sizes.

Structural data for BN and SN with TTB structure were taken from our previous work [18] where we calculated the high-symmetry paraelectric structures for the ten distinct cation configurations that can be accommodated in a $1 \times 1 \times 2$

*tor.grande@ntnu.no

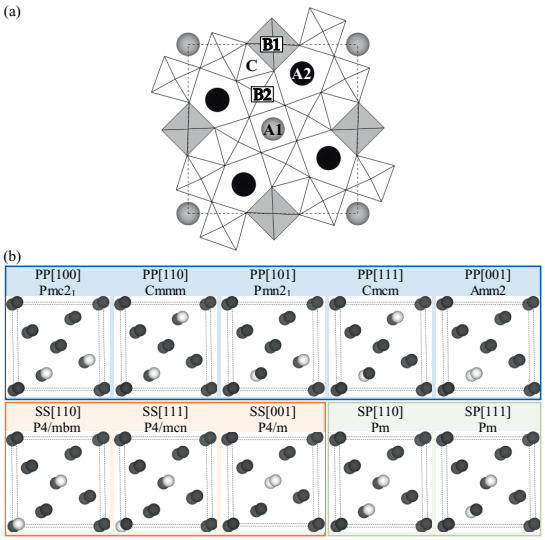

FIG. 1. (a) Projection along c of the aristotype tetragonal tungsten-bronze (TTB) unit cell with space group symmetry $P4/mbm$ and general formula $(A1)_2(A2)_4C_4(B1)_2(B2)_8O_{30}$. (b) The ten cation configurations possible for a $1 \times 1 \times 2$ supercell. Each entry gives the systematic name, local space group symmetry, and a sketch of the configuration (cations gray, vacancies white). Boxes separate orthorhombic (PP), tetragonal (SS), and monoclinic (SP) configurations. Figures created with VESTA [20].

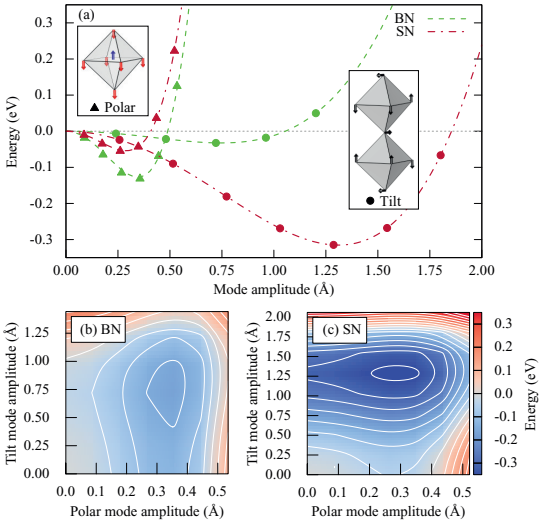

FIG. 2. (a) Potential energy curves for $Ba_5Nb_{10}O_{30}$ (BN) and $Sr_5Nb_{10}O_{30}$ (SN) in the SS[001] configuration, showing energy lowering from freezing in polar and tilt-mode instabilities independently from the paraelectric structure. Points show calculated energies, and lines are polynomial fits to $\Delta E = \alpha Q^2 + \beta Q^4$ where Q is the mode amplitude ($Q = 1$ Å means that $Q^2 = \sum_i u_i^2 = 1$ Å where u_i is the distortion of atom i and the sum is over all atoms in a unit cell). Insets show the structural distortions associated with the phonons. (b) and (c) Contour plots for BN and SN, respectively, showing the weak coupling between the polarization and tilt modes (SS[001] configuration).

supercell of the aristotype unit cell [Fig. 1(a)]. The configurations are shown in Fig. 1(b), along with their space group symmetries [19] and a label indicating the location of the vacancies. The nomenclature describes whether the two vacancies are located on pentagonal A2 sites (P) or on square A1 sites (S), as well as the approximate vector between the vacancies ([100], etc.) [18]. Vacancy ordering lowers the symmetry from the aristotype space group $P4/mbm$ to either tetragonal (SS configurations), orthorhombic (PP), or monoclinic (SP) space group symmetries [Fig. 1(b)].

Starting from these ten paraelectric structures, we calculated the phonon instabilities and the fully relaxed ground states using density functional theory as implemented in the VASP code [21]. We used the gradient-corrected Perdew-Burke-Ernzerhof exchange-correlation density functional optimized for solids (PBEsol) [22] and the projector-augmented wave method [23] with standard VASP potentials and valence electron configurations $4s^24p^65s^2$ for Sr, $5s^25p^66s^2$ for Ba, $4s^24p^64d^35s^2$ for Nb, and $2s^22p^4$ for O. Wave functions were expanded in plane waves up to an energy cutoff of 550 eV, and reciprocal space integrals were done on a $2 \times 2 \times 3$ Monkhorst-Pack grid [24] for the 90-atom supercells. All structures were relaxed until the forces on all ions converged to below 10^{-4} eV Å^{-1}. Phonon calculations were performed with the finite displacement method as implemented in the PHONOPY code [25,26], with displacements of 0.01 Å used for calculation of the force constants. Spontaneous polarization in periodic structures was calculated using the Berry phase method [27–29], and Born effective charges (BECs) were obtained using the linear response routines in VASP.

Phonon calculations for the paraelectric structures reveal imaginary frequency phonons, corresponding to structural instabilities, for all ten configurations of both BN and SN. The phonon with the highest imaginary frequency is in all cases a polar mode with Γ^- symmetry, corresponding to the displacement pattern illustrated in the left inset of Fig. 2(a). The mode consists primarily of a cooperative displacement along the tetragonal c direction of all Nb ions relative to the surrounding oxygens in the NbO_6 octahedra. This is a polar mode, similar to the soft mode responsible for the ferroelectric transition in perovskite ferroelectrics [30], and produces a polarization along c. Consistent with the imaginary frequency of the mode, we find that displacing the atoms according to the eigenvector of the polar mode (we refer to this as "freezing in" the mode in what follows) lowers the energy in all cases. The energy lowering as a function of mode amplitude [31] is shown in Fig. 2(a) for BN and SN in the SS[001] configuration. A nonpolar mode consisting of octahedral tilting around axes in the xy plane [Fig. 2(a), right inset] is also present in all cases. This mode has a smaller imaginary frequency than the polar mode for both compounds in all configurations. The energy lowering associated with the tilt mode is significantly larger for SN than for BN, as shown in Fig. 2(a). The tilt mode also lowers the energy more than the polar mode for SN, despite having a lower imaginary frequency. Simultaneous freezing in

of the polar and tilt modes [Figs. 2(b) and 2(c)] show that the coupling between the modes is weak for both compounds.

We systematically search for the dynamically stable ground state of each configuration of both compounds by freezing in the polar mode, which always has the largest imaginary frequency of the unstable modes, at a mode amplitude close to the energetic minimum. We then relax the structures, allowing the volume and cell parameters to change. After repeating the phonon calculations for the relaxed polar structures, no further instabilities are found in nine of the 20 cases. In the remaining 11, a second, nonpolar instability persists, its eigenvector qualitatively identical to the tilt mode found in the paraelectric structures. After also freezing in this mode, relaxing the structures, and repeating phonon calculations, we obtain the stable ground state structure for both compounds in all configurations. The relative energies of all the configurations are shown in Figs. 3(a) and 3(b). The energy landscape is different for the two compounds: The SS[001] configuration has the lowest ground state energy for BN, while for SN the lowest energy is obtained for PP[100]. No single configuration has a substantially lower energy than the others, especially for SN, where PP[101] and SS[111] are particularly close in energy to the lowest-energy configuration. Consistent with the fixed-volume mapping of unstable modes shown in Fig. 2, the energy relaxation following the polar distortion is more pronounced for BN, while the tilt mode has a larger impact on the ground state energy for SN. For SN there are large energy differences between the paraelectric structures, but the substantial contribution from tilt-mode distortions reduces these differences. The resulting spontaneous polarizations are shown in Fig. 3(c) and compared to literature data. Several of the paraelectric reference structures have polar space group symmetries [Fig. 1(b)], but none allow a polarization along z. We focus here on the polarization component along the tetragonal axis, P_z, which results from freezing in the unstable polar phonon. For the majority of the configurations, BN has a larger P_z compared to the same configuration for SN. Eleven of the 20 ground state structures have tilt-mode instabilities, but the polar nature remains in all cases.

We now turn to understanding the chemical bonding which stabilizes the polarization. In Figs. 4(a) and 4(b) we show the charge density for the paraelectric and ground state structures for BN and SN in the SS[001] configuration. This configuration is suitable for comparing the effects of polar and tilt-mode instabilities, in addition to being the true 0-K ground state for SN. At the chosen isosurface value, we see a distinct "necking" between Nb and O in the direction of the polar distortion, pointing to a covalent bonding between the atoms. As further evidence for the role of Nb-O covalency, we calculate BECs (Z^*) [32] for all configurations of both compounds in their paraelectric states (see Supplemental Material [33]). Consistent with the charge density visualization in Figs. 4(a) and 4(b), the BECs for Nb and O along c are large, exceeding $+9$ for Nb and -7 for oxygen, in comparison to their respective formal charges of $+5$ and -2. The values are similar to BECs reported for $KNbO_3$ and $NaNbO_3$, following the trend of Z^* being proportional to the formal charge of the B-site cation [32,34]. The variation in BEC between BN and SN is minor, pointing to a similar degree of Nb-O covalency in the two compounds, which is also indicated by their similar

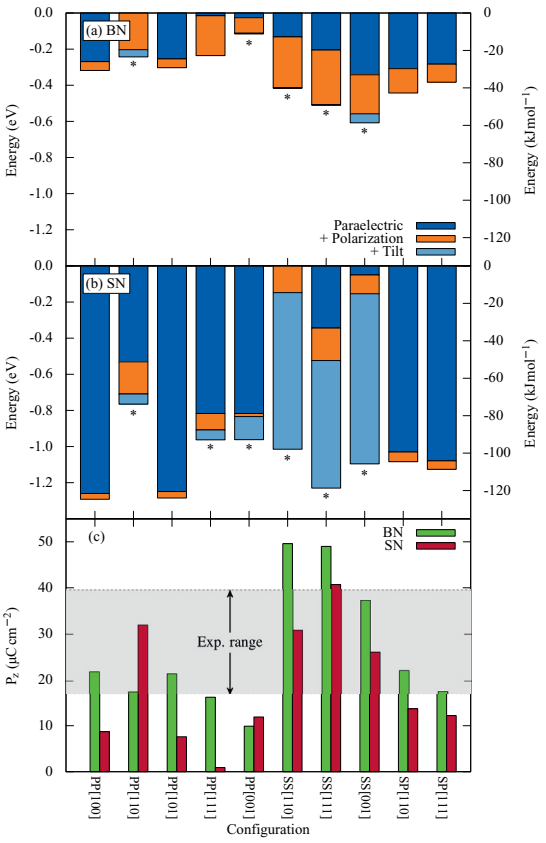

FIG. 3. Energy landscape for (a) $Ba_5Nb_{10}O_{30}$ (BN) and (b) $Sr_5Nb_{10}O_{30}$ (SN), showing the stepwise energy lowering from freezing in the unstable phonons in sequence. All configurations have a polar instability ("Polarization"), while 11 of 20 (marked with *) have a secondary tilt-mode instability ("Tilt") after freezing in the polar mode. Energies are per 45-atom unit cell, with the zero level set to the highest-energy paraelectric structure ("Paraelectric"). (c) Spontaneous polarization for BN and SN in their fully relaxed ground states. P_z is the polarization along the tetragonal c direction. The shaded region marks values reported by Glass [15].

electronic densities of states [33]. In addition, the BECs for Ba and Sr are similar and close to the formal charge of $+2$, demonstrating that these ions do not significantly change their covalency in the ferroelectric transition.

Our results point to a conventional ferroelectric mechanism in which polarization arises from off centering of d^0 Nb^{5+} ions in the NbO_6 octahedra, which is in turn stabilized by the resulting enhanced Nb-O covalency. Partial covalency is well known as the origin of ferroelectricity in perovskite oxides [35–37], and is classified as a second-order Jahn-Teller effect [2]. The charge densities we obtain for BN and SN [Figs. 4(a) and 4(b)] are visually similar to those found experimentally for the prototype ferroelectrics $BaTiO_3$ and $PbTiO_3$ [38], and the large BECs we find are close to previous calculations for Nb and O in $KNbO_3$ [32]. The interpretation

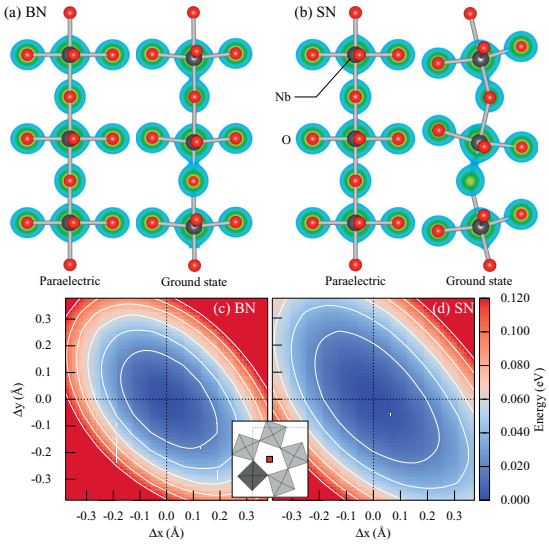

FIG. 4. (a) and (b) Charge density plots for $Ba_5Nb_{10}O_{30}$ (BN) and $Sr_5Nb_{10}O_{30}$ (SN) in paraelectric and ground state structures (isosurface value 0.15 r Å^{-3}). (c) and (d) Potential energy surfaces for the A2-site cation in BN and SN in the paraelectric SS[001] configuration (energy per 45-atom unit cell). The reference position of the cation is in the middle of each plot, and the inset shows the location and size of the mapped area (red square).

of large BECs is that additional covalency associated with the polar distortion occurs through electron transfer from O $2p$ to the formally empty Nb $4d$ orbitals, thereby enhancing the charge transfer compared to simple ionic displacement with nominal charges. The calculated P_z [Fig. 3(c)] show that the polarization is robust with respect to cation-vacancy disorder, and that a significant polarization persists for all ten configurations for both compounds. This is also evident from the charge densities [Figs. 4(a) and 4(b)] which demonstrate that the off centering of Nb^{5+} is significant even for the ground state of SN in the SS[001] configuration, where the tilt-mode amplitude is large. Octahedral tilting in TTBs is otherwise restricted by the connectivity in the xy plane, which prevents tilting around the z axis. Tilts around axes in the xy plane are, however, possible, and often lead to a $\sqrt{2} \times \sqrt{2} \times 2$ supercell relative to the aristotype [8,39], in line with a recent group-theoretical analysis [40]. A $\sqrt{2} \times \sqrt{2} \times 2$ supercell was also reported for pure SN with a TTB structure [41], although for intermediate SBN compositions, doubling of the c parameter has to our knowledge not been reported.

It is generally accepted that chemical or structural disorder is necessary for relaxor properties [7], and both are possible in SBN due to Sr^{2+}, Ba^{2+}, and vacancies occupying the same sublattices. In disordered perovskite relaxors the two cations occupying the same sublattice are always aliovalent, examples being B-site disordered $PbMg_{1/3}Nb_{2/3}O_3$ (PMN) [7,42] and A-site disordered $Bi_{1/2}Na_{1/2}TiO_3$ (BNT) [17,43]. In PMN and BNT the cation ratios are fixed by electroneutrality, whereas in SBN the A-site composition can be varied continuously and relaxor properties emerge gradually for higher Sr content. This points to a different relaxor mechanism for SBN than for the perovskites. We investigate the possible role of the A-site cations in SBN by displacing Ba and Sr away from their relaxed positions in the A2 channels and mapping the potential energy surface (PES) as shown in Figs. 4(c) and 4(d). The PES is flatter for SN than for BN, which is explained by Sr^{2+} being smaller than Ba^{2+}. Due to the restrictions imposed by the octahedral connectivity, and the fact that not all cation configurations in SBN produce tilted ground states, the TTB structure cannot compensate for this by octahedral tilting. Based on this, we suggest that Sr^{2+} is able to displace inside the A2 channels under application of an electric field, thereby producing an additional dielectric response which creates a diffuse phase transition for Sr-rich SBN. Sr preferentially occupies the A1 sites in SBN [18,44], but for $x > 0.40$, Sr must also occupy A2 sites. For $x > 0.50$, the amount of Sr on A2 is high enough for this displacement effect to be appreciable, and we propose that this induces relaxor behavior. The mechanism is different from perovskite relaxors in which cation ordering determines the type of dielectric response [45]. The properties demonstrated here should apply also to other TTB oxides with [001] polarization.

In conclusion, we have shown that the ferroelectric polarization in BN and SN with TTB structure originates from a single polar instability. Charge densities and Born effective charges point to a conventional ferroelectric mechanism in the form of a second-order Jahn-Teller effect acting on the d^0 Nb^{5+} cations. A second unstable mode leads to tilting of the NbO_6 octahedra in the xy plane. The ferroelectric polarization is robust with respect to cation-vacancy disorder, even when the ground state involves significant octahedral tilting. We suggest that this ferroelectric mechanism is present for all compositions of SBN, and that relaxor behavior emerges as an additional contribution for high Sr content due to the smaller Sr^{2+} displacing inside the pentagonal channels.

G.H.O., S.M.S., and T.G. acknowledge financial support from the Research Council of Norway (NFR Project No. 209337) and NTNU, Norwegian University of Science and Technology. U.A. and N.A.S. acknowledge financial support from ETH Zurich and the ERC Advanced Grant program, No. 291151. Computational resources were provided by ETH Zurich (Euler cluster) and Notur, The Norwegian Metacenter for High Performance Computing (Abel cluster) through Project No. NN9264K.

[1] G. Goodman, J. Am. Ceram. Soc. **36**, 368 (1953).
[2] P. S. Halasyamani and K. R. Poeppelmeier, Chem. Mater. **10**, 2753 (1998).
[3] N. A. Hill, J. Phys. Chem. B **104**, 6694 (2000).
[4] M. H. Francombe, Acta Crystallogr. **9**, 683 (1956).
[5] M. G. Sahini, T. Grande, B. Fraygola, A. Biancoli, D. Damjanovic, and N. Setter, J. Am. Ceram. Soc. **97**, 220 (2014).

[6] G. H. Olsen, M. H. Sørby, B. C. Hauback, S. M. Selbach, and T. Grande, Inorg. Chem. **53**, 9715 (2014).
[7] L. E. Cross, Ferroelectrics **76**, 241 (1987).
[8] P. Labbe, Key Eng. Mater. **68**, 293 (1992).
[9] X. Zhu, M. Fu, M. C. Stennett, P. M. Vilarinho, I. Levin, C. A. Randall, J. Gardner, F. D. Morrison, and I. M. Reaney, Chem. Mater. **27**, 3250 (2015).
[10] P. B. Jamieson, S. C. Abrahams, and J. L. Bernstein, J. Chem. Phys. **48**, 5048 (1968).
[11] P. B. Jamieson, S. C. Abrahams, and J. L. Bernstein, J. Chem. Phys. **50**, 4352 (1969).
[12] S. C. Abrahams, P. B. Jamieson, and J. L. Bernstein, J. Chem. Phys. **54**, 2355 (1971).
[13] M. H. Francombe, Acta Crystallogr. **13**, 131 (1960).
[14] K. L. Keester, R. R. Neurgaonkar, T. C. Lim, and E. J. Staples, Mater. Res. Bull. **15**, 821 (1980).
[15] A. M. Glass, J. Appl. Phys. **40**, 4699 (1969).
[16] J. Ravez and A. Simon, J. Solid State Chem. **162**, 260 (2001).
[17] V. V. Shvartsman and D. C. Lupascu, J. Am. Ceram. Soc. **95**, 1 (2012).
[18] G. H. Olsen, S. M. Selbach, and T. Grande, Phys. Chem. Chem. Phys. **17**, 30343 (2015).
[19] H. T. Stokes and D. M. Hatch, J. Appl. Crystallogr. **38**, 237 (2005).
[20] K. Momma and F. Izumi, J. Appl. Crystallogr. **44**, 1272 (2011).
[21] G. Kresse and J. Furthmüller, Phys. Rev. B **54**, 11169 (1996).
[22] J. P. Perdew, A. Ruzsinszky, G. I. Csonka, O. A. Vydrov, G. E. Scuseria, L. A. Constantin, X. Zhou, and K. Burke, Phys. Rev. Lett. **100**, 136406 (2008).
[23] G. Kresse and D. Joubert, Phys. Rev. B **59**, 1758 (1999).
[24] H. J. Monkhorst and J. D. Pack, Phys. Rev. B **13**, 5188 (1976).
[25] A. Togo and I. Tanaka, Scr. Mater. **108**, 1 (2015).
[26] A. Togo, F. Oba, and I. Tanaka, Phys. Rev. B **78**, 134106 (2008).
[27] R. D. King-Smith and D. Vanderbilt, Phys. Rev. B **47**, 1651(R) (1993).
[28] R. Resta, Rev. Mod. Phys. **66**, 899 (1994).
[29] N. A. Spaldin, J. Solid State Chem. **195**, 2 (2012).
[30] M. T. Dove, Am. Mineral. **82**, 213 (1997).
[31] D. Orobengoa, C. Capillas, M. I. Aroyo, and J. M. Perez-Mato, J. Appl. Crystallogr. **42**, 820 (2009).
[32] P. Ghosez, J.-P. Michenaud, and X. Gonze, Phys. Rev. B **58**, 6224 (1998).
[33] See Supplemental Material at http://link.aps.org/supplemental/10.1103/PhysRevB.93.180101 for Born effective charges (BECs) and electronic densities of states (DOSs).
[34] F. Detraux, P. Ghosez, and X. Gonze, Phys. Rev. B **56**, 983 (1997).
[35] H. D. Megaw, Acta Crystallogr. **5**, 739 (1952).
[36] I. B. Bersuker, Phys. Lett. **20**, 589 (1966).
[37] R. Cohen, Nature (London) **358**, 136 (1992).
[38] Y. Kuroiwa, S. Aoyagi, A. Sawada, J. Harada, E. Nishibori, M. Takata, and M. Sakata, Phys. Rev. Lett. **87**, 217601 (2001).
[39] B. A. Scott, E. A. Giess, G. Burns, and D. F. O'Kane, Mater. Res. Bull. **3**, 831 (1968).
[40] T. A. Whittle, S. Schmid, and C. J. Howard, Acta Crystallogr., Sect. B **71**, 342 (2015).
[41] H. Brusset, M. Gillier-Pandraud, and S. D. Voliotis, Mater. Res. Bull. **6**, 5 (1971).
[42] S. Tinte, B. P. Burton, E. Cockayne, and U. V. Waghmare, Phys. Rev. Lett. **97**, 137601 (2006).
[43] M. Gröting, S. Hayn, and K. Albe, J. Solid State Chem. **184**, 2041 (2011).
[44] S. Podlozhenov, H. A. Graetsch, J. Schneider, M. Ulex, M. Wöhlecke, and K. Betzler, Acta Crystallogr., Sect. B **62**, 960 (2006).
[45] N. Setter and L. E. Cross, J. Appl. Phys. **51**, 4356 (1980).

B

Structural data from literature

Tables B.1 and B.2 give the reported structural data (lattice parameters and atomic positions) used as starting point for the Rietveld refinements in Chapters 9 and 6, respectively. Nomenclature: WP, Wyckoff position; Occ., occupancy; B_{iso}, isotropic thermal displacement factors.

Table B.1 — Atomic positions for r-PN reported by Mahé[118] (space group $R3m$, transformed from hexagonal to rhombohedral setting). Lattice parameters: $a = 7.183$ Å, $\alpha = 93.94°$ (uncertainty in lattice parameters and atomic positions corresponds to the number of significant digits). The structure is visualized in Figure 9.1.

Atom	WP	x	y	z	Occ.	B_{iso}
Pb1	1*a*	0	0	0	1	0.47
Pb2		0.357	0.357	0.357	1	0.47
Pb3		0.668	0.668	0.668	1	0.47
Nb	6*c*	0.507	0.164	0.815	1	0.7
O1	6*c*	0.387	0.959	0.702	1	2
O2	3*b*	0.737	0.021	0.737	1	3
O3		0.034	0.531	0.034	1	3
O4		0.618	0.343	0.618	1	3
O5		0.243	0.901	0.243	1	3

Table B.2 — Atomic positions for TTB-PN reported by Labbé[115] (space group *Amm*2, transformed from the original *Cm*2*m* setting). Lattice parameters: $a = (3.870 \pm 0.005)$ Å, $b = (17.65 \pm 0.02)$ Å, $c = (17.92 \pm 0.02)$ Å. The structure is visualized in Figure 2.12(b).

Atom	WP	x	y	z	Occ.	B_{iso}
Pb1	4*e*	1/2	0.3278(7)	0.0282(11)	1	4.0(2)
Pb2		1/2	0.006(3)	0.1970(13)	1/2	2.7(5)
Pb3		1/2	0.4832(10)	0.3452(13)	1/2	2.7(5)
Pb4		1/2	0.2549(11)	0.2504(14)	1/2	1.5(3)
Nb1	2*a*	0	0	0	1	0.9(3)
Nb2		0	0	0.500(2)	1	1.4(4)
Nb3	4*d*	0	0.1807(10)	0.1095(13)	1	1.2(4)
Nb4		0	0.3180(10)	0.3935(13)	1	1.1(4)
Nb5		0	0.3942(13)	0.1802(14)	1	2.2(5)
Nb6		0	0.1100(10)	0.3198(13)	1	0.8(3)
O1	2*b*	1/2	0	0	1	3
O2		1/2	0	1/2	1	3
O3	4*e*	1/2	0.151(9)	0.110(9)	1	3
O4		1/2	0.299(8)	0.395(9)	1	3
O5		1/2	0.402(8)	0.182(8)	1	3
O6		1/2	0.119(8)	0.297(8)	1	3
O7	4*d*	0	0.083(9)	0.092(9)	1	3
O8		0	0.139(9)	0.213(8)	1	3
O9		0	0.221(7)	0.001(9)	1	3
O10		0	0.279(9)	0.135(9)	1	3
O11		0	0.417(9)	0.073(8)	1	3
O12		0	0.081(9)	0.427(8)	1	3
O13		0	0.209(8)	0.334(8)	1	3
O14		0	0.331(8)	0.281(8)	1	3
O15		0	0.433(8)	0.390(9)	1	3
O16	2*a*	0	0	0.735(12)	1	3
O17		0	0	0.252(12)	1	3